Polyamine and Schiff base metal complexes incorporated in mesostructured templated porous silicas: tentative application in selective oxidation

Wen-Juan Zhou

No d'ordre : ……

No attribué par la bibliothèque : ……

THESE

pour obtenir le grade de

Docteur de l'Université de Lyon – Ecole Normale Supérieure de Lyon

Spécialité : Chimie

Laboratoire de Chimie

École Doctorale de Chimie de Lyon

présentée et soutenue publiquement le 18 September 2009

par Madame Wen-Juan ZHOU

Polyamine and Schiff base metal complexes incorporated in mesostructured templated porous silicas: tentative application in selective oxidation

Directeur de thèse: Monsieur Laurent BONNEVIOT et Monsieur Ming-Yuan HE

Après avis de: Monsieur Jean-Luc BLIN, rapporteur
Monsieur Peng WU, member/ rapporteur

Devant la Commission d'Examen formée des membres suivants :

Monsieur Dong-Yuan ZHAO, member
Monsieur Peng WU, member/ rapporteurs
Madame Belén ALBELA, member
Monsieur Yan-Qin WANG, member
Monsieur Yi-Meng WANG, member

Acknowledgment

First, and foremost, I would like to express my thanks to the cooperation program between Ecoles Normales Supérieures and East China Normal University (ECNU) in the education and training of graduate students. It brought me the opportunity to carry out my doctoral study in Ecole Normale Supérieure de Lyon (ENS-Lyon) and ECNU. I am sincerely grateful to the directors of this program in both French side and Chinese side. Particularly, I would like to give my thanks to the Chinese director, Mme. Yun-Hua Qian, for her remarkable management of this cooperation program, and especially for her personal advice, kind encouragement and firm support for me.

Then I would like to express my great gratitude to my two supervisors, Prof. Laurent Bonneviot (ENS-Lyon, France) and Prof. Ming-Yuan He (ECNU, China), for their offers of carrying my research and study in their groups.

I am grateful to my French supervisor, Prof. Laurent Bonneviot for his responsible supervision, patient discussion and timely encouragement during my Ph.D. study in ENS-Lyon, in particular for his great help on paper-writing and thesis-writing stages. His rigorous attitude and persistent pursuit of perfection in science have deeply impressed me. I am also grateful to Dr. Belén Albela of ENS, for her specific guidance throughout my searching, working, paper-writing and thesis-writing stages. Belén not only afforded me much help in my work but also influenced me imperceptibly by her nice personality. She is an extremely nice lady, and always warmhearted and optimistic. I enjoy every moment of working with Laurent and her.

I am also sincerely indebted to my Chinese supervisor, Prof. Ming-Yuan He, for his wise direction, sagacious suggestions and solid supports. He is a respectable scientist with great insights. He sets a perfect example for me, and I admire him so much. I also would like to thank Prof. Peng Wu, for his prompt helps and earnest supports.

I would like to show appreciations to my French colleagues for their specific helps in my experiments here. Many thanks to Mme. Martine Simon in ENS-Lyon for helping me on IR measurement, to Prof. Edouard Garbowski of Université Lyon 1 for providing UV-visible spectroscopy, to Dr. Philippe Maurin for his assistance with HPLC (ENS-Lyon), to Dr. Pascal Perriat for TEM measurement (INSA-Lyon), to Mme. Noëlle Cristin and Mme. Pascale

Mascuman for N_2 sorption and ICP-MS measurement (IRCE-Lyon), and to Dr. Fabien Miomandre for providing eletrochemical measurement (ENS-Cachan).

I would like to thank my other colleagues both in ENS-Lyon and in ECNU for their accompanies and helps, and they are Marion Giraud, Sébastien Abry, Stépanie Calmettes, Kun Zhang, Anissa Bendjeriou, Christophe Aronica, Delphine Pitrat, Giacri Veronique, Lin Fang and others.

I hope to thank the following persons in ENS-Lyon who have helped me in my administrative issues and/or facilitated my work in ENS-Lyon or ECNU. They are Prof. Philippe Sautet, the director of Chemistry Laboratory (ENS), Mme. Nadine Donguy of the service of international relations (ENS), Mr. Jean-Louis Duclos and Mr. Jan Matas, the former and current director of department of international relations (ENS), Mr. Christian Melkonian, the computer and network administrator of Chemistry Laboratory (ENS), Mme. Fatima Benmedjahed and Mr. Kevin Pollet-Guiffray, the former and current secretary of chemistry Laboratory (ENS), Prof. Jia-Xin Lu and Prof. Pin-Gang He, the former and current director of Chemistry Laboratory (ECNU), and Ran Du, the secretary of Chemistry department (ECNU).

I want to express my personal appreciation to Prof. Wei Dong of ENS-Lyon. He is the Ph.D. supervisor of my husband, and during our stay in France he took care of us very much like our dear family. I would like to thank his hospitality and helps for us. I also want to thank Prof. Myroslav Holovko of National Academy of Sciences of Ukraine and Prof. XiaoBin Zhang of Hunan University for some inspiring talks and impressive discussions during their visit in ENS-Lyon.

Special thanks go to the jury members of my thesis defense. I would like to thank five referees, Prof. Jean-Luc BLIN of Université Henri Poincare, France, Prof. Peng Wu of ECNU, Prof. Bo Tu of Fudan University, Dr. Belén Albela of ENS-Lyon, and Prof. Yi-Meng Wang of East China Normal University for their reading my thesis and providing constructive comments. Besides them, I also want to give my sincere thanks to Prof. Dong-Yuan Zhao of Fudan University, Prof. Yan-Qin Wang of East China University of Science and Technology, and Prof. Pin-Gang HE of ECNU for their presence and questions.

Last, but not least, I would like to thank my family. I am deeply indebted to my parents for their deepest love and unqualified moral support. I would like to thank my husband Dr.

Shuang-Liang Zhao. He is always nearby to support me, listen to me and encourage me. He is also my best friend, sharing my happiness and sadness, influencing me by his aspiring and optimistic spirit.

Abstract

Novel materials were designed from hybrid organic-inorganic silica-based mesoporous materials containing Cu(II) complexes and were applied in selective oxidation reactions. The localization of the metal sites was controlled using three different organosilane-ligands and two different synthetic routes, either the one-pot synthesis or the post-synthesis grafting.

The organosilanes were: N-(2-aminoethyl)-3-aminopropyltrimethoxysilane (L^1), N-salicylaldimine-propylamine-trimethoxysilane (L^2) and N-(salicylaldimine) -(N'-propyltrimethoxyl silane)-diethylenetriamine, (L^3). In addition, Ni(II) ion was used as structural probe. The Ni(II)-L^1, Cu(II)-L^1 and Cu(II)-L^2 complexes were co-condensed with sodium silicate using the one-pot synthetic route in the presence of cetyltrimethylammonium tosylate as templating agent to built well-ordered periodic mesoporous organosilicas (PMOs) of MCM-41 type. The as-made materials were submitted to treatments using a mixture of chlorotrimethylsilane and hexamethyldisilazane or an appropriate amount of HCl washing to extract template and maintain the mesoporous structure. The Ni(II)-L^1, Cu(II)-L^1 or Cu(II)-L^3 complexes have been also grafted in the preformed mesoporous silica and evenly distributed using the a molecular stencil patterning technique. A multiple technique approach has been applied to thoroughly investigate the structure and morphology of the material as well as the coordination of the metal sites, using XRD, TEM, N_2 sorption isotherms, elemental analysis, TGA, DRUV, FT-IR and EPR spectroscopies. In addition, the chemical accessibility and the leaching properties of the metal sites were tested using isothiocyanate (SCN^-) as a ligand probe, metal displacement of Ni(II) by Cu(II) ions or resistance to acidic leaching. Apart from the known channel species obtained from grafting that are solution-like, two different framework species were identified from their structural and chemical properties: the accessible and non-accessible ones, named "embedded" and "showing on" sites, respectively. The catalytic activity in phenol hydroxylation using hydrogen peroxide as oxidant and catechol oxidation reactions using dioxygen as oxidant depends on the metal location. The grafted Cu(II)-L^3 complex exhibited the best catalytic activities and was working in water solutions. The conversion and selectivity into valuable products, catechol and hydroquinone, were investigated in function of time, temperature, pH and substrate to oxidant ratio. Catalyst recycling has been also investigated.

Key words: one-pot synthesis; molecular surface engineering; hybrid mesoporous materials; polyamine ligands; Schiff-base ligands; copper(II) complexes; nickel(II) complexes; phenol hydroxylation.

Résumé

De nouveaux matériaux ont été conçus à partir de matériaux hybrides organique-inorganiques mésoporeux renfermant des complexes de Cu(II). Ils ont été mis en œuvre comme catalyseurs dans des réactions d'oxydation sélective. La localisation des sites du métal a été contrôlée en utilisant trois ligands synthétiques le type organosilane et deux stratégies différentes, c. àd.,une synthèse dite "one-pot", et un greffage post-synthètique.

Les organosilanes ont été le N-(2-aminoéthyl)-3-aminopropyltriméthoxysilane (L^1), le N-propylamine-salicylaldimine-triméthoxy-silane (L^2) et le de N-(salicylaldimine)-(N'-propyltriméthoxylsilane)-diéthylènetriamine (L^3). En outre, l'ion Ni(II) a été utilisé comme sonde structurale. Selon la synthèse "one-pot", les complexes Ni(II)-L^1, Cu(II)-L^1 et Cu(II)-L^2 ont été co-condensés avec du silicate de sodium en présence d'un tensoactif, le cétyltriméthylammonium tosylate. Ce dernier avait le rôle de gabarit structurant pour la construction d'organosilices mésoporeuses périodiques (PMOs), de structure bien ordonnée de type MCM-41. Ces matériaux ont ensuite été soumis à des traitements mis au point pour préserver la structure mésoporeuse utilisant un mélange de chlorotriméthylsilane et hexaméthyldisilazane ou une quantité appropriée de HCl aqueux (lavage) pour extraire le tensio-actif. Dans les greffages post synthétiques, les complexes Ni(II)-L^1, Cu(II)-L^1 ou Cu(II)-L^3 ont été liés de façon covalent à la surface de silice mésoporeuse préformée selon une distribution uniforme mettant en œuvre une technique dite de pochoir moléculaire. Une caractérisation multitechnique approfondie fut mener pour vérifier la structure et la morphologie du matériau et pour déterminer le site de coordination du métal (XRD, TEM, isothermes d'adsorption-désorption d'azote, analyse élémentaire, ATG, spectroscopies DRUV, FT-IR et RPE). De plus, l'accessibilité chimique du site métallique et le relargage du métal ont été testés en utilisant 1) l'isothiocyanate (SCN^-) comme ligand sonde, 2) l' échange des ions Ni(II) par les ions Cu (II) d'ions ou encore 3) la résistance à la lixiviation acide. Outre les sites métalliques des canaux obtenus par greffage et trés ressemblant à des sites "en solution", deux autres sites ont été mis en évidence. Ils sont tous les deux situés dans les murs des pores. L'un non accessible, est appelé "site enlisé", l'autre est "site émergenant". L'activité catalytique en hydroxylation du phénol par le peroxyde d'hydrogène et oxydation du catéchol par le dioxygène dépend de la localisation du métal. Les complexes Cu(II)-L^3 greffés présentent les meilleures activités catalytiques et fonctionnent dans l'eau. La conversion et la sélectivité en produits valorisables comme le catéchol et l'hydroquinone, ont été étudiées en fonction du temps, de la température, du pH et du rapport substrat /oxydant. Enfin, le recyclage du catalyseur a également été étudié.

Mots clés: synthèse « one-pot » ; ingénierie moléculaire de surface; matériaux hybrides mésoporeux; ligands polyaminés; ligands de type base de Schiff; complexes du Cu(II); complexes du Ni(II); hydroxylation du phénol.

摘　要

本论文报道了含铜（II）配合物的有机-无机杂化介孔新型材料以及这些材料应用于选择性氧化反应中。金属在材料中的位置是通过三种不同的有机硅烷配体和两种合成路线控制的，或者是一步合成或者后合成嫁接法。三种有机硅烷分别是 N-(2-氨乙基)-3-氨丙基三甲氧基硅烷 (L^1), N-水杨基醛二胺-氨丙基三甲氧基硅烷 (L^2) 和 N-(水杨基醛二胺)-(N'-氨丙基三甲氧基硅烷)-二乙烯三胺 (L^3)。另外，镍(II) 离子被用作结构探针。Ni(II)-L^1, Cu(II)-L^1 或者 Cu(II)-L^2 配合物与硅酸钠缩合，通过一步合成路线以甲苯磺酸十六烷基三甲基铵为模板剂，合成出具有 MCM-41 类型的有序周期性介孔有机无机硅烷材料（PMOs）。 这些一步合成的原材料通过混合试剂三甲基氯硅烷和六甲基二硅胺烷或者适当的盐酸萃取模板剂，并且所得材料依然保持介孔六方结构。Ni(II)-L^1, Cu(II)-L^1 或者 Cu(II)-L^3 配合物以“分子模版图案方式”嫁接在成型的介孔硅材料以使得配合物能够均匀的分布在介孔硅材料的内表面。一系列的表征方法用于彻底的研究材料的结构和形态以及金属的配位状态，如 XRD，N_2 吸附脱附等温线，元素分析，差热热重法（TGA），固体紫外漫反射（DRUV），傅立叶红外和电子顺磁共振光谱（EPR）。此外，金属的可接触性和金属的可移去性质通过异硫氰酸盐（SCN^-）作为配体，Ni(II) 替换 Cu(II)或者酸洗来测试。除了嫁接在孔道内的物种与其溶液中配位状态一致外，两种墙壁内的物种通过它们的结构和化学性质识别出：一种为不可接触 “嵌入”在墙壁内，另一种为可接触 “显示”在墙壁上。材料在以双氧水为氧化剂的苯酚的羟基化和以氧气为氧化剂的邻苯二酚的催化活性与金属在材料中的位置紧密相关。结果发现嫁接于 Cu(II)-L^3 配合物的材料显示了最好的催化活性且是以水为溶剂。转化率和对有价值的邻苯二酚和对苯二酚产物的选择性进行了考察，结果发现它们与反应时间，温度，pH 以及底物和氧化剂的比例有关。催化剂的循环也进行了研究。

关键词：一步合成法；“分子模版图案”；介孔杂化材料；多聚胺配体；席夫碱配体；金属铜（II）配合物；金属镍（II）配合物；苯酚羟基化。

Contents

Chapter 1 General introduction

1.1 History of heterogeneous catalyst

Nowadays, more than 90 % of the manufacturing processes through the world involve catalysis, since it makes the manufacture of desirable products safer and cheaper. Catalysis is also increasingly implied in atmospheric depollution and in the design of environmentally compatible new technologies. The catalytic converter of automobiles is among examples of atmospheric pollution reduction in the most wildly spread. In the field of chemistry, catalysis is more and more considered one of the central tools for the development of green chemistry to reduce energy consumption and tackle the problem of waste in fine and specialty chemical industries by reducing reaction temperature, replacing stoichiometric reagents and improving selectivity. Furthermore, it is also related in the pursuit of new ways of generating energy either by harnessing solar radiation or making use of exothermal conversion of abundant hydrocarbons such as methane, or small molecules such as the oxides of carbon.

In fact, catalysis is a chemical process in which the rate of reaction is increased in the presence of molecular ions, polymers or any solid additives called catalyst. This additive of course participates into the chemical pathways leading from the reactant to the formation of the products but it is regenerated at the end of the chemical route. As a consequence, it can be used again and again as far as it does not undergo alteration, called ageing. Therefore, it does not affect the thermodynamic of the reaction and can be used in a tiny amount. In addition, it allows to run a given reaction at lower temperature, saving energy during a chemical process.[1] Furthermore, the catalyst may favor one route among the possible routes that usually end on different products.[2] Consequently, the production of one chemical among the other can be favored, changing the so-called selectivity toward the desired product and minimizing wastes. Indeed, catalysis implies one or several molecular steps of the reaction, changes the nature of the intermediate that are hardly characterized. Therefore, research in catalysis implies ⅰ) theoretical modelisation on well defined catalytic systems, ⅱ) kinetics

studies and iii) development of catalytic systems. The actual thesis pertains to the third kind.

There are three kinds of catalysts, homogeneous, heterogeneous catalysts and enzymes classified from the kinetic behavior and the phases included in the process. Homogeneous catalysts work in the same phase as the reactants. By contrast, heterogeneous catalysts work in a different phase, usually this is a solid while the reaction medium is liquid or gaseous. Enzyme are proteins manufactured inside the living cells and functioning under quite mild conditions, *i.e.*, room temperature. They are considered as a separate group that is not studied here though they have been taken as an inspiring model for the choice of active sites in this thesis. Indeed, those sites not always characterized at the molecular level are fascinating since they provide ultimate energy saving, selectivity, molecular efficiency in clean media for most of reactions that a chemist can dream off. By comparison homogeneous catalysis, a pure product of man made molecular engineering, provides high molecular control and selectivity on a relatively large panel of reactions, but in rather harsh conditions (toxic solvents, controlled atmospheres, high pressure etc) with drastic separation problems, and limitation in scaling up the production. On the contrary, heterogeneous catalysis provides easy separation, on-line process, large scale production (often use in petroleum refining). However, it suffers of limited molecular control and usually poor selectively, most likely because it involves the surfaces that are very difficult to characterize. The ideal situation would be to develop catalysts as clean as enzymes, as controlled and selective as homogeneous catalysts and as productive as heterogeneous catalysts. To develop molecular control in the surface of solids is the main aim of this thesis. However, the route is long and heterogeneous catalysis is an old story early recognized though various Nobel Prize awards.

The beginning of the use of heterogeneous catalysis can date back to the early studies of alcohol dehydration over alumina and alcohol oxidation over platinum metal. The application of heterogeneous catalysts on industrial process emerged in 1900s with the requirement of increasing the reaction rate and reaching the maximal yield of a desired product. An important discovery, by the father of the hydrogenation process, Paul Sabatier, is the catalytic hydrogenation at the beginning of the twentieth century. He introduced a trace of

nickel as a catalyst to facilitate and accelerate the addition of hydrogen to unsaturated molecules of gaseous hydrocarbon. For this work Sabatier shared the 1912 Nobel Prize in chemistry. Meanwhile, Wihelem Normann took a patent in Germany in 1902 and in Britain in 1903 on the hydrogenation of liquid oils in presence of nickel catalyst: this was the beginning of what is now world wide industry. The landmark in the history of applied catalysis is certainly the successful synthesis of ammonia from nitrogen and hydrogen in the presence of a reduced magnetite (Fe_3O_4) catalyst using a high-pressure process discovered by Fritz Haber in 1909. In that time, he invented a process for the large-scale production of ammonia for use in nitrogen fertilizer. Then Carl Bosch and Alwin Mittasch at the laboratories of Badische Anilin & Soda Fabrik (BASF) in Germany improved this catalyst and made ammonia commercially available in large quantities in the years preceding World War I. For considerable contribution, Haber and Bosch both won the Nobel Prize in chemistry in 1918 and 1931, respectively, for their work on iron catalysts. Their so-called Haber-Bosch process held tremendous impact, since it made possible a huge increase in agricultural production and thus underpinned the 20^{th} century's massive population boom. After 1930s, catalysis using modified clays, microporous and mesoporous solids played a growing role in the petroleum industry and clean technology. In 1930s, acid-treated clays of montmorillonite type improved the petroleum cracking process. Then, Houdry developed the fixed-bed catalytic process of cracking crude oil to obtain petrol, now known as the Houdry process. The earlier thermal cracking technology was able to break down heavy hydrocarbon fractions into a much wider range of lighter fractions, in particular, a higher proportion of unsaturated hydrocarbon gases. After 1970s, the leading actor of catalysis in the industrial chemistry belongs to zeolite family.[3] These crystalline microporous aluminosilicates exhibited strong catalytic activity and high selectivity to the desired products, in addition with easy separation and high recover. As a landmark in this field, Mobil Oil Company in 1975 discovered one of most versatile zeolites, the ZSM-5 zeolite. It was successfully employed as acid catalyst in the manufacture of methanol to gasoline (MTG) in 1980s, which opened a window for synthetic fuel. In 1990s, the titanium silicate analogue of ZSM-5 (TS-1) firstly reported by ENichem Company[4] provided a convincing heterogeneous alternative for the catalytic conversion of phenol into catechol and hydroquinone,

which is an important industrial reaction for production of fine chemicals. However, its application is limited by the relatively small pore opening (*ca*. 0.56 nm)[5] and weak diffusion of the reactants and products in and out of the catalyst. In 1990s, mobile scientists and Japanese scientists reported for the first time a new type of porous silicate characterized by channel diameter ranging from 2.5 nm to 10 nm, high surface area (~ 1000 $m^2 \cdot g^{-1}$) and high thermal stability (~ 550 °C).[6, 7] These features compared to zeolites opened opportunities for the inclusion of bulkier guest molecules such as organometallic compounds and even enzymes for the design of immobilized homogeneous catalytic sites in confined space that may conveniently be organically tailored.

Until now, a vast number of metal complexes have been included inside the mesoporous silica through post-functionalization, *i.e*. mere physical deposition or covalent grafting.[8] For the former route, high metal loading can be reached (> 5 %). However, low metal dispersion is produced with low recyclability mainly because of the weak interaction of the metal with the support and high leaching problems. By contrast, covalent grafting is based on the formation of direct oxo bridges, "Si-O-Si", between the tether of functions and the support, which generate efficient, robust and more recyclable catalysts. However, the modification of the complex structure under grafting may alter the catalytic activity.[9] In addition, the strong covalent grafting process may easily create non-homogeneous metal distribution in the pore network of the solid. One of the alternatives is to graft very tiny amount of species at low temperature for prolongated period of time, which is not efficient. Another approach consists in the design of a method that specifically overcomes the diffusion problem. This method called "molecular stencil patterning" (MSP) has been recently developed in the laboratory.[10] It is based on the preparation of the surface according to a regular pavement pattern taking advantage of the repulsive charge of the quaternary long chain surfactant molecules that occupy the mesopore channel of the material at the end of the synthesis. This will be described in the literature survey.

Another alternative strategy consists to introduce directly the organic function in the synthesis of the siliceous framework. This has been reported for the first time in 1999, leading to a new type of materials referred to as periodic mesoporous organosilicas (PMOs).[11-13] PMOs have been prepared through so-called one-pot synthesis also known as

the co-condensation method since it involves a mixture of silicate precursor and organosilsesquioxane molecules in the presence of templating surfactant. They are unique as their channel walls contain both inorganic and organic fragments. These fragments are statistically distributed in the framework of the inorganic component, and do not occupy the void space of the channel after the removal of surfactant. Thus, this new synthetic approach extends the realm of mesoporous materials to "chemistry of the channel walls". Combining, chemistry in the wall and in the channel may provide, particularly if metals are at stake, a great deal of possibility to design materials with redox, optical, charge-transport and magnetic properties. However, it requires the development of the "in wall chemistry" from organic to organometallic chemistry.

To our best knowledge, the first report on a catalytic active metal complex introduced directly in the one-pot synthetic route of a templated mesoporous silicate of MCM-41 type came from Corma *et al.* in 2004.[14] It implied a very large vanadium salen type of complex, where its location in the wall was not really proved. Anyhow, the material was catalytically active in the cyanosilylation reaction. Probably, the second paper in this field came from our laboratory with organophosphine rhodium type of complex.[15] In this study, a through investigation of this SBA-3 based solid clearly evidenced the location of the complex in the wall. In this case, hydrogenation catalytic activity was found close to that of the homogenous catalysts. However, Corriu *et al.* showed that Co(II) and Cu(II)-cylam complexes may be fully embedded in the wall and rendered inaccessible in the large wall of SBA-15 materials.[16-18] Since it appears that the cationic accessibility depends on the synthetic procedure, one question raises on the structural parameter that controls this property. This problem is treated in this thesis.

1.2 Aims and objectives of this Research

In the framework of the above context it appears that catalysis needs well-defined solids in the pore of which high molecular control over the catalytic (metal) sites is achieved together with a given accessibility to molecule and eventual reactants. In addition, one of the most difficult tasks for catalysis is oxidation reactions. To tackle the problem, the metal system cho-

sen here were nickel(II) and copper(II) ions that both provide a lot of possible spectroscopic characterizations of the sites. Moreover, and particularly for copper, there is a lot of examples of proteins containing this metal that is active in oxidation catalysis.[19-21] Already, two articles have been published this year in the laboratory on this subject.[22, 23] They concern grafted species using the MSP technique. Here, nickel has been used as a spectroscopic probe to investigate the location of the ethylenediamine like complexes in the wall of a 2D hexagonal periodic mesoporous silica of MCM-41 type. Comparison of copper and nickel and a search for accessibility control using different ligands has been also treated, for such a kind of framework sites. Finally, reactivity of the copper containing solids has been tested on hydroxylation of phenol into catechol and hydroquinone.

The porous solids were thoroughly investigated using a multitechnique approach, where texture and porosity and metal environment of the complexes, as well as the catalytic activity, have been at stake using XRD, TEM, IR, N_2 sorption isotherm, EPR spectroscopy, diffuse reflectance UV-visible spectroscopy, cyclic voltammetry, GC and HPLC, characterization tools.

1.3 Structure of manuscript

This thesis is composed of six chapters. The first chapter is the general introduction. The second chapter is the bibliography survey concerning mesoporous materials, metal complex functionalized mesoporous materials, characterization techniques and various applications. The third chapter presents the experimental work. The fourth chapter is related to the incorporation of nickel ethylenediamine complexes in the pore wall of nanostructured porous silica via one-pot synthesis, in which nickel (II) complex is used as a probe to monitor the metal location in the mesoporous material. The fifth chapter is related to the incorporation of copper ethylenediamine and Schiff base complexes in a nanostructured porous silica. It is composed of three parts: 1) the properties of Cu(II) ethylenediamine complex depending on its location in the mesoporous material, *i.e.*, redox properties and catalytic properties; 2) preparation and characterization of Schiff-base copper(II) complexes with 2N2O coordination type incorporated in mesoporous silica *via* the one-pot synthesis route; 3) for compar-

ison, another Schiff-base copper(II) complexes with 3N1O coordination type have been grafted on a mesoporous material according to the molecular stencil patterning technique. Both types of materials with immobilized Schiff-base copper(II) complexes are also submitted to catalytic oxidation tests. Finally, the sixth chapter contains the general conclusions and perspectives.

Chapter 2 Literature survey

2.1 Silica-based mesoporous materials

Silica-based porous materials have witnessed an intense research activity over the past decades on chemistry,[24] physics, biology,[25, 26] theory,[27, 28] simulation and medicine,[29, 30] due to their tailor-made pore sizes and shapes which can lead to different behaviors of active species in the porous materials as their bulk behaviors. In chemistry, they have been broadly applied on selective adsorption,[31, 32] chemical sensing,[33] shape-selective catalysis,[34] nanotechnology and separation.[35] Recently, porous materials in the form of membranes have been applied on the microreactors field.[36] In addition, the low dielectric constant and high modulus make porous materials useful for microelectronic packaging.[37]

According to the International Union for Pure and Applied Chemistry (IUPAC) nomenclature,[38] on the basis of pore size (diameter), porous materials can be divided into three categories: microporous materials (< 2 nm), mesoporous materials (2-50 nm), and macroporous materials (> 50 nm). Well-known members of microporous class are zeolites, which consist of aluminosilicate minerals. Zeolites with very regular pore structure of molecular dimensions possess the ability to selectively sort molecules, which is known as "molecular sieves". A zeolite may be thought as being built up from $[SiO_4]^{4-}$ tetrahedra, each oxygen being shared by two tetrahedra, and the substitution of aluminium giving $[AlO_4]^{5-}$ ions. One excess negative charge introduced by each aluminium atom can be balanced through Brønsted acid like proton or Lewis acid such as a metal ion. Zeolites were firstly discovered in the nature but they are rarely pure and showing various degrees of contamination by other minerals, metals, quartz, or other zeolites, which excludes them from many important commercial applications where uniformity and purity are essential. Synthetic zeolites with pure compositions and defined structure were emerged and firstly synthesized by Sainte Claire Deville in 1862.[39] Synthetic zeolites having a general formula $M_v(AlO_2)_x(SiO_2)_y \cdot ZH_2O$ have been synthesized using organic molecules as structure-directing agents in the synthesis process. Today, around 100 different types of zeolites

are known. They have been widely used in industry process as catalysts like H-ZSM-5 and TS-1. However, except in a few systems, the mechanism of their formation is poorly understood and a real design of an open framework is difficult to reach. Furthermore, their applications are limited by the relatively small pore opening. Indeed, pore enlargement has been one of the main aspects in zeolite chemistry. In the 1990s,[6, 40] the discovery of the M41S family of silica-based mesoporous materials with an open-framework and well-defined geometry opened a new domain in the research of porous materials. These new mesoporous materials present two important properties: high surface per unit mass and large pore size above 2 nm. The larger pore size compared to that of zeolites allows them to be host for the inclusion of bulkier guest molecules such as enzymes and organometallic compounds.[25, 26] In the synthesis process, supramolecules were firstly used as structure-directing agents, replacing the organic molecules which are largely employed in the synthesis of zeolites. With different supramolecules and synthesis conditions, various structures of silica-based mesoporous materials have been prepared in the past decades. Their formation mechanisms, although still a matter of discussion, are understood in principle. Besides silica-based mesoporous materials, non-silica based mesoporous materials have also been reported: mesoporous carbons,[41, 42] metal oxides (e.g., titanium, aluminum, zirconium, tin, manganese, niobium),[43, 44] metal sulfides (e.g., germanium),[45, 46] and metal phosphates (e.g., aluminum, zirconium),[47-49] for satisfying different practical needs. In this work, we will focus on silica based mesoporous materials.

2.1.1 Early steps of mesoporous materials

The first examples of mesoporous materials were reported by Mobile scientists[6, 50] and Japanese researchers[7, 40] in the early 1990s through a supramolecular- templating strategy, which has been a big breakthrough in materials synthesis. Three M41S mesophases, namely, MCM-41 (hexagonal, *p*6mm), MCM-48 (cubic, *I*a3d), and MCM-50 (lamellar, *p*2) were synthesized from the hydrolysis and condensation of tetraethyl orthosilicate (TEOS) in the presence of ionic surfactants (C16- alkyltrimethylammonium halides) as structure-directing agents (SDA) under basic conditions, and their structures are shown in **Figure 2.1**. These

three types of mesoporous materials can be obtained by varying the surfactant/silicon ratio. At a surfactant/Si ratio of less than 1, the predominant product appears to be the hexagonal phase, MCM-41. When the ratio is beyond 1, a cubic phase (MCM-48) can be produced. As this ratio further increases, a lamellar phase (MCM-50) is formed. Besides the surfactant C16-alkyltrimethylammonium halides, other surfactants with different carbon chain length (C8- C14 alkyltrimethylammonium chloride) as well as auxiliary hydrophobic swelling agents have been used as structure-directing agents in the synthesis process, leading to M41S like materials with various pore sizes. They show a regularly ordered pore arrangement and a very narrow pore-size distribution that varies from 1.5 nm to 10 nm.

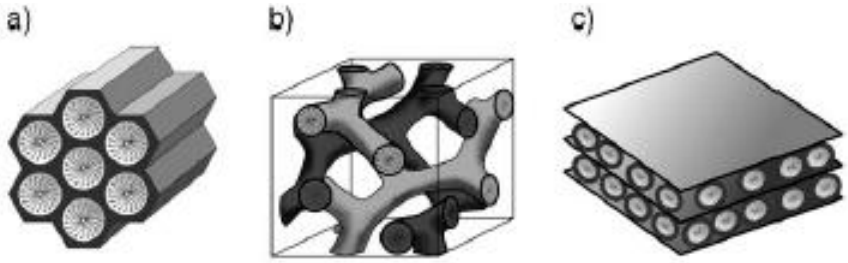

Figure 2.1 Structures of mesoporous M41S materials: a) MCM-41 (2D hexagonal, space group *p*6mm), b) MCM-48 (cubic, space group *Ia3d*), and c) MCM-50 (lamellar, space group *p*2).[6]

2.1.2 Synthesis of mesoporous materials

After the first reports by Mobile scientists and Japanese researchers, various other silicate sources such as fumed silica and sodium silicate have been successfully used for the preparation of M41S like materials, taking economy and easy preparation into consideration. In addition, counterion *p*-toluene-sulfonate replacing halides in the surfactant of C16-trimethylammonium has also been used to successfully synthesized MCM-41 like material named LUS.[51]

In the synthesis of M41S like materials, the supramolecular-templating approach can be considered as a molecular imprinting method in which polymerization process takes place around the template forming complex ordered periodic structures. According to this idea, polymers, cationic, anionic, and neutral amphiphiles with various chain lengths as supramolecular templates and auxiliary hydrophobic swelling agents have been successfully

used to prepare ordered mesostructured materials with various structures and pore sizes.[52-56] The detailed description concerning these materials will be presented in section 2.1.3.

The removal of the template from the as-made material is usually achieved through either calcination[6] or solvent-extraction,[11, 12, 57] *i.e.*, using ethanol, acid ethanolic solution or on ion-exchange agent (NaCl or NH_4Cl). The choice of the best approach to be employed on the as-made solid should be done according to practical needs. The calcination approach leads to an important loss of silanol groups of the internal surface which make the surface less functioned for further grafting other groups, causes shrinkage of the pore sizes and is also economically and ecologically unfavorable. The solvent-extraction approach can keep a maximal number of silanol groups. However, the obtained structure is easy to collapse in aqueous solution at high temperature. Some authors have reported that partial silylation or capping the internal surface with hydrophobic groups such as trimethylsilyl (TMS) can increase their aqueous-thermal stability.[58, 59] Generally, solvent-extraction and capping are very favorable for the mesoporous materials functionalized with organic groups in order to keep the organic functions.[15] In addition, supercritical fluids such as CO_2 have been applied to mesoporous silica, resulting in an increase of the hydrolytic stability of the surface groups.[60]

2.1.3 Different types of mesoporous materials

Nowadays, mesoporous materials have become a big family. Here, a table considering the most representative mesoporous materials is given: the structure-directing agent (SDA) used, synthesis conditions, silica source, dimensionality crystal system, space group and mean pore size (ϕ) are reported (**Table 2.1**). Among these mesoporous materials, MCM-41, SBA-15 and HMS are the most widely used. SBA-15 which possesses a very large pore size of *ca*. 7.8 nm can be a good host for the inclusion of large molecules.[55] HMS which presents a less structured hexagonal structure is difficult to monitor the change in the framework or in the channel.[61] In this thesis, we will focus on MCM-41 type of materials since they possess a well-defined structure (2D hexagonal), controllable pore size (homo-

geneous diffusion regime), high thermal and mechanical stability and the synthesis of these materials are highly reproducible.[6] In particular, we will use LUS (Laval University Silica), which is a 2D hexagonal (*p*6mm) mesostructured silica which has been developed in our group.[51] The high specific surface allows high loading of active sites. Moreover, the ordered mesostructure of the solid facilitates the control of the internal pore surface and the framework.

Table 2.1 Physical properties of various mesoporous silica materials.

Sample code	SDA [a]	Silica source [b]	conditions	Dimensionality crystal system, and space group	ϕ^c (nm)	Reference
MCM-41	CTACl, CTABr	TEOS	alkaline	2D hexagonal (*p6mm*)	3.7	Beck *et al*.[6]
MCM-48	CTACl, CTABr	TEOS	alkaline	Cubic (*Ia3d*)	3.5	Beck *et al*.[6]
MCM-50	CTACl, CTABr	TEOS	alkaline	Lamellar (*p*2)		Beck *et al*.[6]
FSM-16	CTACl	δ-$Na_2Si_2O_5$	alkaline	2D hexagonal (*p6mm*)	2.8	Inagaki *et al*.[62]
SBA-3	CTABr + HBr	tetraalkyl orthosilicate	acid	2D hexagonal (*p6mm*)	2.8	Huo *et al*.[54]
SBA-15	PEO-PPO-PEO	TEOS	aicd	2D hexagonal (*p6mm*)	8.5	Zhao *et al*.[55]
HMS	Dodecylamine, tetradecylamine	TEOS	alkaline	hexagonal (disordered)	2.8	Zhang *et al*.[61]
MSU-2	PEO	TEOS	neutral	Hexagonal (disordered)	3.5	Bagshaw *et al*.[53]
KIT-1	CTACl	Na_2SiO_3	acid	hexagonal (disordered)	3.5	Ryoo *et al*.[52]
LUS	CTATos	Na_2SiO_3	alkaline	2D hexagonal (*p6mm*)	3.7	Bonneviot *et al*. [51]

a: CTA^+: cetyltrimethylammonium, PEO-PPO-PEO: poly(ethylene oxide)- poly (propylene oxide)-poly(ethylene oxide); PEO: biodegradable polyethylene oxide; Tos: p-toluene-sulfonate; **b**: TEOS: tetraethyl orthosilicate; **c** : mean pore size report.

2.1.4 Formation mechanism

Two main formation mechanisms have been proposed for the M41S series of materials. The first mechanism proposed by Beck *et al*. is known as liquid crystal templating (LCT),[6] as

shown in **Figure 2.2**. In the pathway ①, ordered liquid crystalline arrays form before the addition of silicate species. In this case, the surfactant liquid-crystal phase serves as template. And then silicate species nucleates and grows within the surfactant tubules. Further hydrolysis and condensation of silicates lead to an ordered array of surfactant-inorganic composites. In the pathway ②, silicate species in solution play a more active role in directing the formation of the hexagonal ordering mesophase through the charge balance with the surfactant ions. In this mechanism, a large enough concentration of surfactant is needed to form the liquid crystal phase. The second proposed mechanism is called cooperative self-assembly suggested by Stucky *et al.*,[63] as shown in **Figure 2.3**. In this mechanism, the mutual interaction between the cationic surfactant (S^+) and partially hydrolyzed silicates creates well-ordered supramolecular aggregates. The partially hydrolyzed silicates are believed to serve both as charge balancing groups and to facilitate the ordering of the supramolecular structures. Therefore, the concentration of surfactant can be as low as the critical micelle concentration (CMC). In **Figure 2.3**, prior to silicate addition, the surfactant is in a dynamic equilibrium between spherical or cylindrical micelles and single molecules as shown in the stage of the precursor solutions (**Figure 2.3**(**A**)). After the addition of the silica source, the multicharged silicated species displace the surfactant counterions to form organic-inorganic ion pairs which reorganize first into a silicatropic mesophase followed by silica cross-linking as shown in the ion exchange part (**Figure 2.3**(**B**)). The nature of the mesophase, *i.e.* hexagonal or lamellar, is controlled by the multidentate interaction via the interface packing density (**Figure 2.3**(**C**)). Comparing these two mechanisms with experimental data, the presence of hexagonal, lamellar and cubic mesoporous silicates that are analogues to liquid crystalline phases existing in a pure surfactant solution supports the former mechanism. However, the dependence of the mesostructure on the precursor concentration and the absence of some mesostructures with liquid crystalline counterparts seem to support the latter mechanism. Even in these cases, the general consensus currently seems to be that the second mechanism is the correct for most of the syntheses even if there is still some controversy on its details.

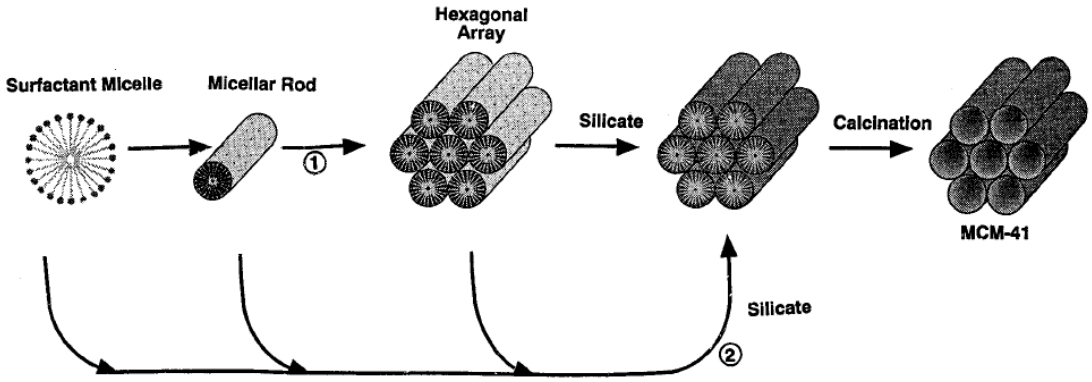

Figure 2.2 Liquid-crystalline templating mechanism.[6]

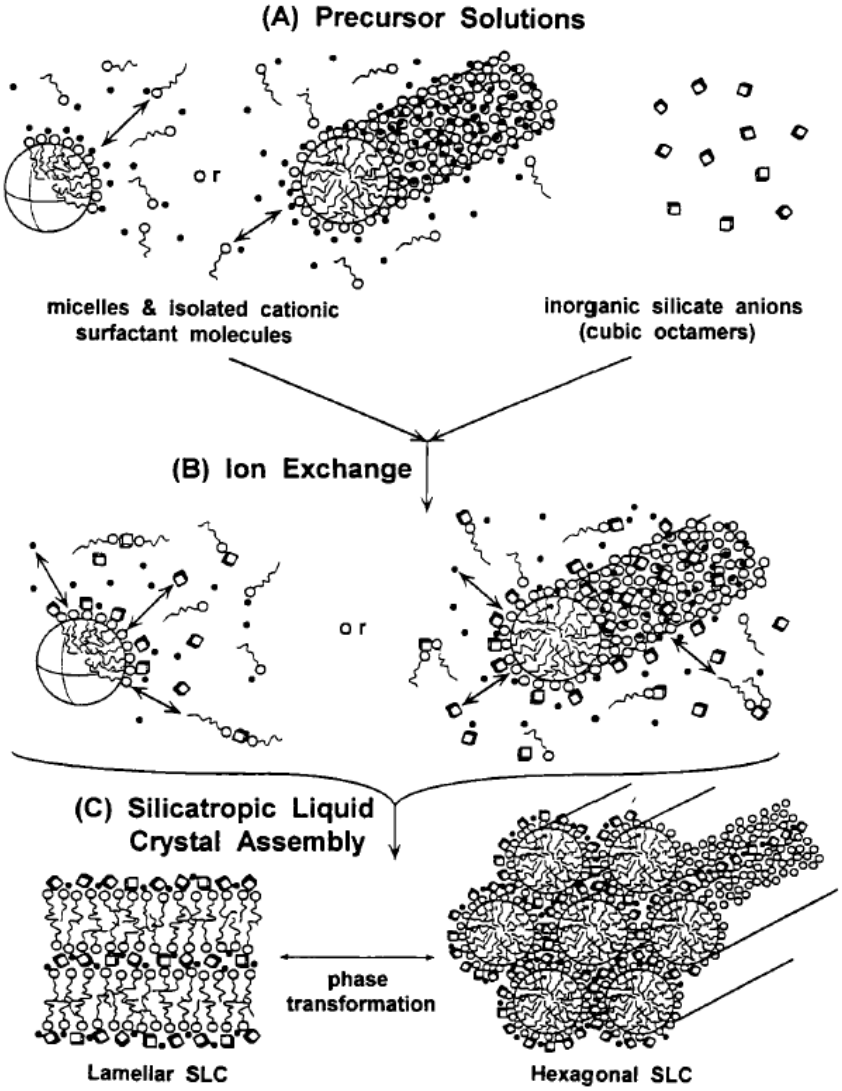

Figure 2.3 Cooperative templating mechanism.[63]

The cooperative organization process is not limited to ion pairs formed by quaternary ammonium surfactants (S^+) and anionic inorganic species (I^-), (S^+I^-) (**Figure 2.4a**). It can be generalized to other three pathways:

1) halides counterion-mediated ($S^+X^-I^+$, X^-= Cl^-, Br^-). The preparation takes place under acidic conditions (pH≈ 2), whereby the silica species are positively charged. Thus a mediator ion X^- is necessary to be added to produce an interaction between the surfactant and the silica (**Figure 2.4b**).

2) alkali metal counterion-mediated ($S^-M^+I^-$, M^+ = Na^+, K^+). In this case, it is possible to work in basic media, whereby the surfactant is negatively charged. A mediator ion M^+ is required for ensuring interaction between the equally negatively charged silica species (**Figure 2.4c**).

3) anionic surfactant such as phosphonates, sulphonates and carboxylates (S^-) and cationic precursors (I^+), (S^-I^+; **Figure 2.4d**).

Furthermore, other nonionic surfactants are used for the synthesis of mesoporous materials, such as neutral monomers (S^0), (S^0I^0 pathway), non-ionic alkyloligoethylene (N^0), (N^0I^0 pathway; **Figure 2.4e**), or ion pairs pathway ($S^0(XI)^0$; **Figure 2.4f**).

Besides aforementioned non-covalent interactions (electronic interactions, van der Waals or H-bondings), in the so-called ligand-assisted liquid-crystal templating mechanism, covalent bonds are formed between the inorganic precursor species and the organic surfactant molecules followed by self-assembling of the surfactant.[64] Generally, non-covalent interactions are favorable for a successful synthesis of mesostructured materials.

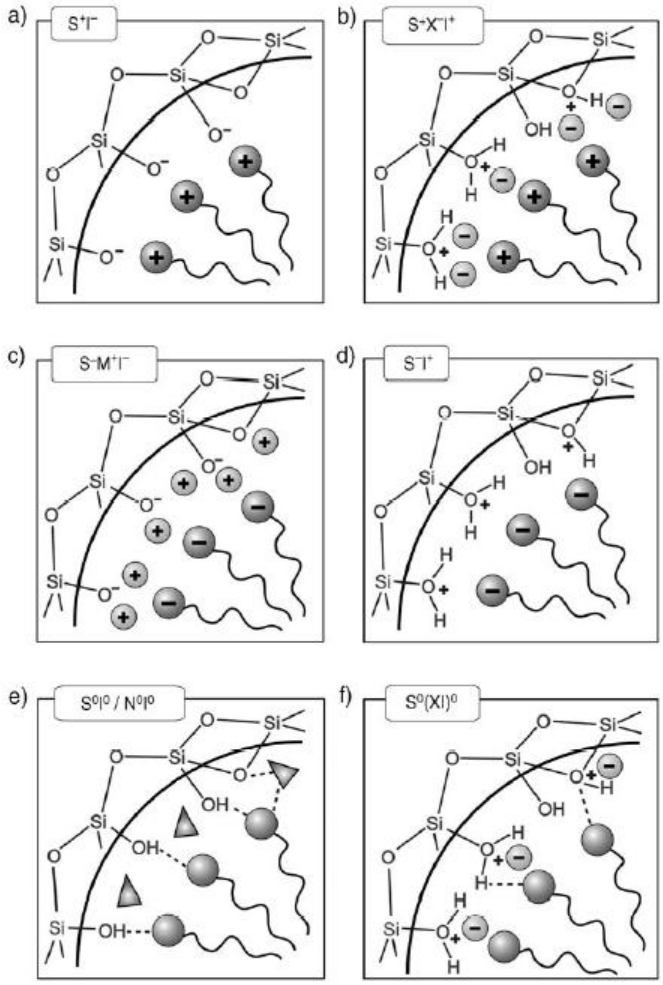

Figure 2.4 Interactions between the inorganic species and the headgroup of the surfactant with consideration of the possible synthetic pathway in acidic, basic, or neutral media. Electrostatic: S^+I^-, $S^+X^-I^+$, $S^-M^+I^-$, S^-I^+; through hydrogen bonds: S^0I^0/N^0I^0, $S^0(XI)^0$.[65]

2.1.5 Textual properties

2.1.5.1 Morphology control

The morphology of mesoporous materials can be controlled by changing the synthesis pH, the template, the reaction time, the synthesis temperature and the solvent. Various morphologies such as thin films, membranes, curved shapes,[66a] patterns,[66b] fibers, spheres[66, 67] and monoliths[68, 69] have been developed since the final application of the material will impose a preferable morphology. Generally, for the morphologies of thin films, membranes, fibers and spheres, the ($S^+X^-I^+$) approach has been successfully employed since the $S^+X^-I^+$ interaction is weaker in acidic synthesis.[70] Monoliths can be prepared using non-ionic sur-

factants such as Pluronic copolymers.[68] Solvent evaporation techniques, growth from solution and alternative deposition techniques have also been employed to synthesize mesoporous materials with different morphologies. MCM-41 materials have been successfully synthesized with the aforementioned morphologies such as sphere[67] and monolith morphologies (**Figure 2.5**).[69, 71]

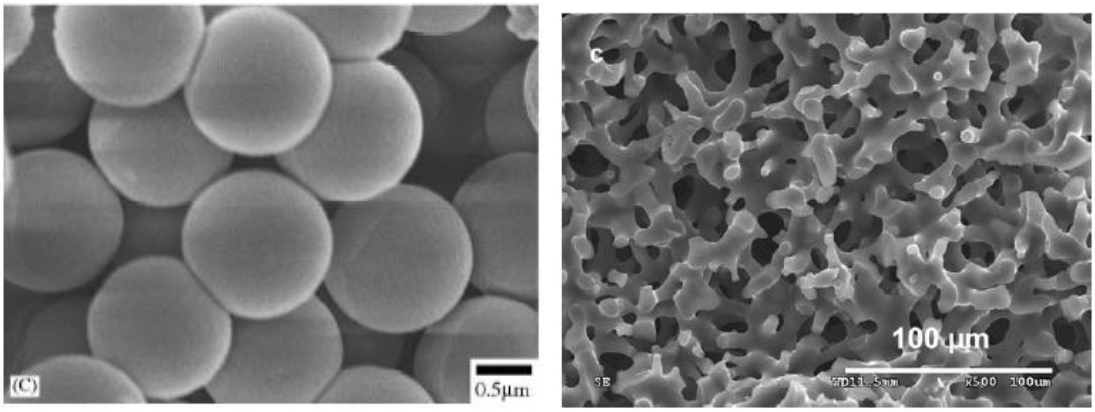

Figure 2.5 SEM images of spheres of MCM-41 samples synthesized in basic conditions with methanol as cosolvent.[67] SEM images of monoliths prepared by spinodal decomposition.[71]

2.1.5.2 Adjustable pore size

The pore size of mesoporous materials can be adjusted above 2 nm through various approaches for satisfying the need of applications such as catalysis, sensors and drug delivery. Different general approaches have been reported: 1) post-synthesis treatments;[72, 73] 2) the use of surfactants with different chain length;[74] 3) the use of polymers as templates,[55]such as poly(ethylene oxide) and polyalkylene oxide blocks; 4) swelling agents incorporated in the formed micelles, such as 1,3,5-trimethylbenzene,[75-77] amine,[78] triisopropylbenzene,[74] mesitylene[6] and tetraalkylammonium[79]; 4) tetraethoxysilane (TEOS) served as both swelling agent and a silica source[80]; 5) high temperature during synthesis or post-synthesis treatment[73, 79, 81]; 6) suitable pH of synthesis, reaction time and calcination conditions.

In many cases, swelling agents are considered to be responsible for the enlargement of the pore sizes. However, in high temperature synthesis, the swelling action is not contributed from the original swelling agents added but from the hexadecyldimethlyamine that is

generated in situ by the decomposition of part of the surfactant cations.[73, 81, 82]

Combining the aforementioned different treatments and synthesis factors, the aim is to tune much larger mesopores with relatively narrow pore size distributions. For the pore size of MCM-41, it can be enlarged to 11 nm with a narrow pore-size distribution reported by Sayari *et al*. using *N*,*N*-dimethylhexadecylamine as expander.[78]

2.1.5.3 High silanol density

The specific density of silanol groups per gram of silica depends on many factors such as the synthesis conditions, surface area and the method used to remove the template (SDA). Generally, mesoporous materials possess a high density of the silanol groups especially in the internal surface due to incomplete condensation of silica source during the sol-gel synthesis. Concentrations of between 1.4 and 1.9 groups/nm^2 have been determined for the cubic MCM-48.[83] For MCM-41, a concentration between 2 and 3 groups/nm^2 has been reported.[84] In particular, the silanol density of a LUS silica (MCM-41 type), which is going to be used in this work, is about 4.4 groups/nm^2.[85]

In the surface of MCM-41, there are mainly three types of silanol groups: free silanol (≡SiOH), geminal silanol (=Si(OH)$_2$) and hydrogen-bonded silanol groups (**Figure 2.6**). The first two can be used to graft functional groups, whereas, the last one is less accessible to modification.[84]

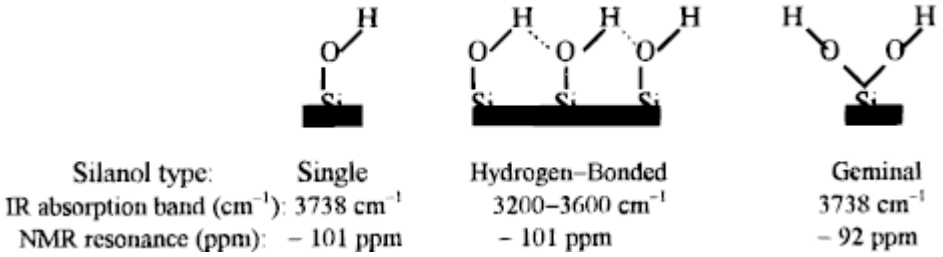

Figure 2.6 Schematic representation of the three types of SiOH groups in siliceous MCM-41 and their characteristics.[84]

A coin has two sides. Silanol groups can be used for grafting functions like organic groups or metal complexes. However, in some cases, silanol groups may induce negative effects such as in hydrothermal stability[15, 58] and in catalysis[86, 87] (*vide infra*). Therefore,

partial silylation of surface silanols may be required to some extent depending on the application of the material. This will be discussed later (*cf.* Chapter 4).

2.1.6 Characterization

Mesoporous materials are generally characterized by a variety of techniques, such as X-ray diffraction (XRD), N_2 sorption measurements, electron diffraction (ED), transmission electron microscopy (TEM), scanning electron microscopy (SEM), Fourier transform infrared (FT-IR) spectroscopy and silicon nuclear magnetic resonance (^{29}Si NMR), to name just a few. Among these techniques, XRD, FT-IR and N_2 sorption measurements are very important measurements to characterize the structure and the textual properties of mesoporous materials. In the following, the main characteristics of LUS, the mesoporous silica that has been used in this work, are presented.

2.1.6.1 X-ray diffraction (XRD)

X-ray diffraction (XRD) is one of the most important characterization tools used in solid state chemistry and materials science. Each crystalline solid has its unique characteristic X-ray powder diffraction pattern which can be used to determine its structure and as a "fingerprint" for its identification. For example, LUS is a hexagonal structured material with long-range ordered pores (**Figure 2.7A**). The XRD pattern shows four peaks assigned to <100>, <110>, <200> and <210> reflections (**Figure 2.7**). In fact, these peaks reflect the hexagonal unit of structure, for example, the <100> reflection corresponds to the diffracting planes of the two layers of hexagonal structure (**Figure 2.7A**). The spacing between diffracting planes d_{100} can be obtained from the Bragg's law: $2d\sin\theta = n\lambda$ (θ is the incident angle, n is any integer, and λ is the wavelength of the beam). The L or a_0 which is the lattice factor (**Figure 2.7A**), *i.e.*, the distance between the center of two hexagons and can be calculated from $a_0 = 2*d_{100}/3^{1/2}$.

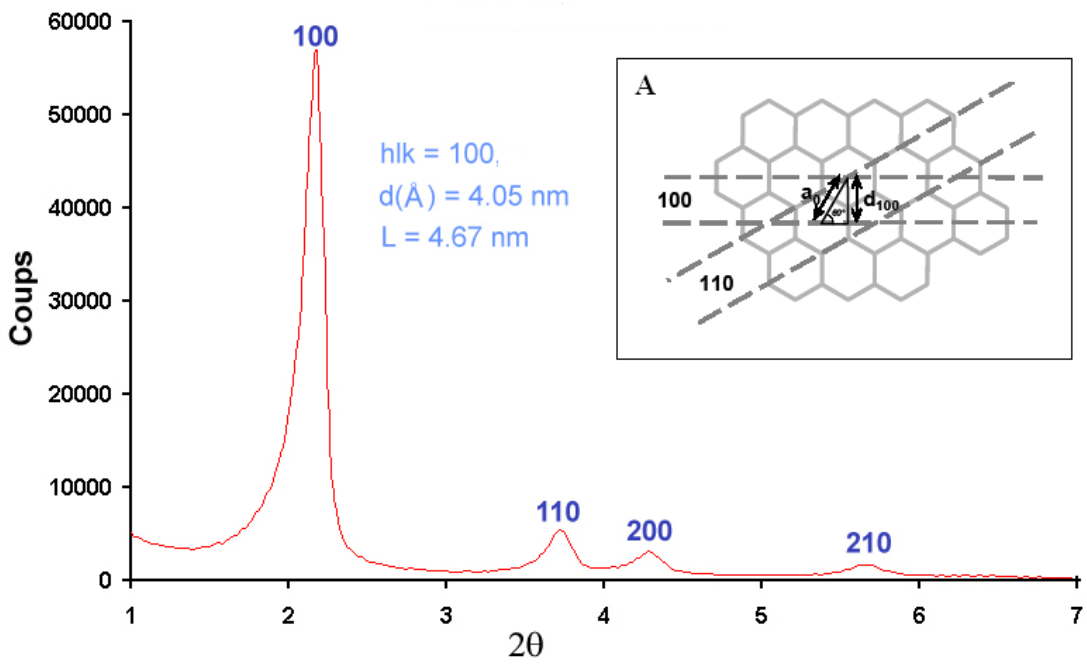

Figure 2.7 XRD patterns of as-made LUS. Internal Figure A: arrangement of pores and plans reticular Miller indices (100) and (110) for a symmetric hexagonal structure (part A).

2.1.6.2 Fourier transform infrared spectroscopy (FT-IR)

Fourier Transform Infrared Spectroscopy (FT-IR) is a spectroscopic technique that deals with the middle infrared region of the electromagnetic spectrum (400 - 4000 cm^{-1}). Each covalent bond of organic functions and inorganic species exhibits a characteristic frequency of vibration in FT-IR spectroscopy which can be used to identify its component. The vibration forms of molecules are primary two types: 1) stretching vibration (ν), 2) bending vibration (δ). Generally, stretching vibration modes are observed at higher frequency than that of bending vibrations for a same covalent bond.

The main FT-IR features of as-made LUS are presented in **Figure 2.8** and **Table 2.2**. The absorption bands observed are attributed to the vibrations from both silica and template (SDA). The characteristic absorption bands of silica are the following: bending vibration δ(O-Si-O) of valence angle of tetrahedral SiO_4 located at 450 cm^{-1}, symmetric stretching ν_s(Si-O) of tetrahedral SiO_4 located at 800 cm^{-1}, asymmetric stretching ν_{as}(Si-O) of tetrahedral SiO_4 located at 950 - 1300 cm^{-1} range, stretching ν(O-H) of H_2O of silanol groups in the surface of silica located at 3000 - 3600 cm^{-1} range. The template (hexadecyltrimethylammonium *p*-tolunensulfonate (CTATos) exhibit bands at 2850 cm^{-1} and

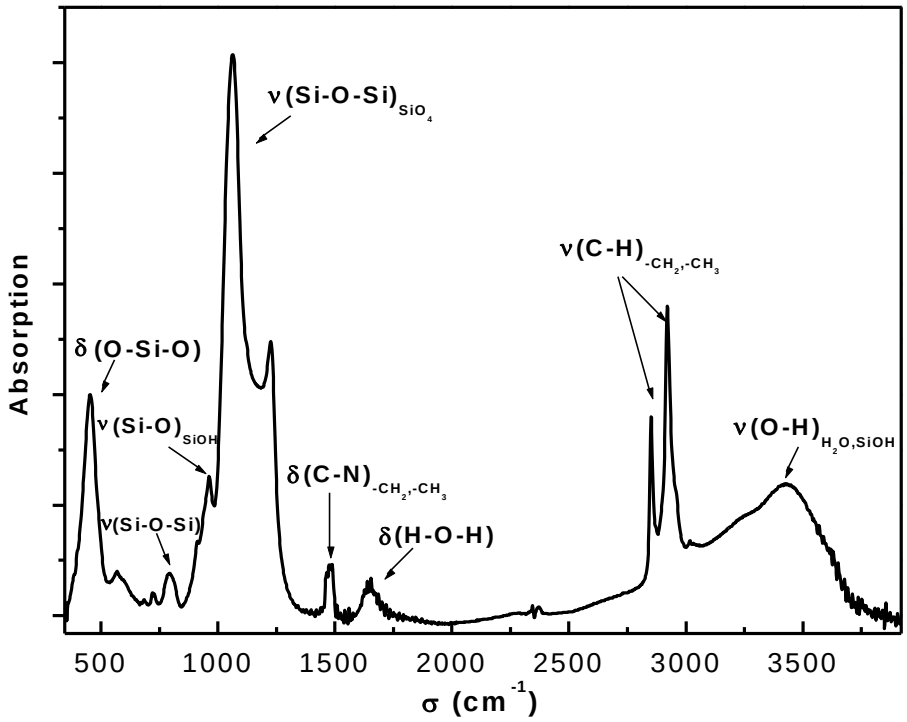

Figure 2.8 IR spectra of as-made LUS.

Table 2.2 FT-IR data for an as-made LUS.

Wavelength (cm^{-1})	Vibration
450	δ(O-Si-O) of valence angle of tetrahedral SiO_4
800	ν_s(Si-O) of tetrahedral SiO_4
950	ν(Si-O) of silanol groups (≡SiOH)
970～1300	ν_{as}(Si-O) of tetrahedral SiO_4
1477	δ_{as} (N-C) of CTA^+
1500	δ(C-H) of $–CH_2$ and $–CH_3$ groups from CTA^+ [a]
1650	δ(H-O-H) of H_2O
2852, 2920	ν_s(C-H) and ν_{as}(C-H) of $-CH_2$ groups from CTA^+
3000 - 3600	ν(O-H) of H_2O and silanol groups (≡SiOH)

a: CTA^+: hexadecyltrimethylammonium

2918 cm^{-1} which are assigned to the symmetric stretching ν_s(C-H) and asymmetric stretching ν_{as}(C-H) stretching vibrations of the $-CH_2-$ groups of the template (CTA^+), respec-

tively, and band at 1477 cm^{-1} which is attributed to asymmetric bending δ(N-C) of the template (positively charged head). In addition, FT-IR spectra also can be used to quantify species by an adequate treatment of spectra, such as amount of template, amount of trimethylsilyl, which will be presented in the next chapter.

2.1.6.3 N_2 sorption isotherm

N_2 sorption measurements have been used to determine the physical textural properties including surface area, pore size distribution and pore volume per gram. This technique is based on the physical adsorption of gas (generally N_2) on the internal and external surface of the solid. N_2 sorption analysis works under a constant temperature (usually 77 K), by measuring the amount of gas adsorbed at each relative pressure (compared to the atmospheric pressure). The adsorption-desorption isotherm can be thus obtained. The isotherm of the mesoporous materials here studied is of type IV according to the IUPAC classification.[38]

The isotherm of calcined LUS is depicted in **Figure 2.9** and the pore size distribution is shown in the insert. Each step of the adsorption isotherm can be interpreted as follows:

- region **A**: the adsorption at very low relative pressure, $P/P_0 < 0.05$, is due to monolayer adsorption of liquid N_2 on the walls of the pores. In addition, the rapid increase of N_2 adsorption observed ($P/P_0 < 0.05$) is most probably due to the presence of micropores.
- region **B**: $0.05 < P/P_0 < 0.3$, it corresponds to the multi-layer adsorption of liquid N_2 on the walls of mesopores.
- region **C**: $0.3 < P/P_0 < 0.5$, an rapid augment of adsorption is due to the capillary condensation on the walls of mesopores. The starting point of the hysteresis loop corresponds to the liquid N_2 condensation in the smallest mesopores, the end of the loop is relative to the filling of the largest mesopores with liquid N_2.
- region **D**: $0.5 < P/P_0 < 0.95$, the adsorption of liquid N_2 takes place on the extra surface; $0.95 < P/P_0 < 1$, we think it is due to the N_2 adsorption between the grains of solid.

Different theoretical models can be applied to analyze the experimental data. Among the

theories, Barrett-Joyner-Halenda (BJH)[88] and Broekhoff-De Boer (BdB)[89] approaches are widely used for calculation of the pore size. The pore volume is calculated from the maximal amount of adsorbed liquid nitrogen around $P/P_0 = 0.98$. The calculation of the surface area is based on the BET (Brunauer, Emmett and Teller) theory which was developed in 1938 based on Langmuir adsorption model.[90]

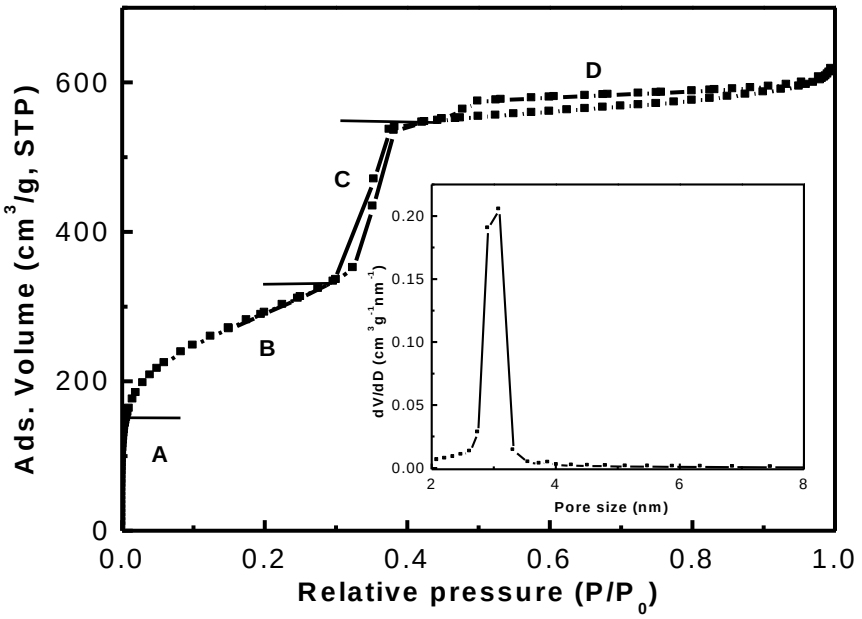

Figure 2.9 Nitrogen adsorption-desorption isotherm of calcined LUS and pore size distribution using BJH method (insert).

2.2 Mesoporous materials immobilizing organic groups

The field of organic-inorganic hybrid mesoporous materials bridges chemistry (organic, inorganic, organometallic, and polymer) to materials science. In fact, the idea of combing the properties of organic and inorganic compounds to form unique materials is relatively old and started with the beginning of the industrial era. But only recently, more extensive and systematic studies have been used to make hybrid organic-inorganic materials for many applications, such as catalysis, optics, sensing, separations and microelectronics.

Silica-based mesoporous materials are the good candidates for supporting organic functions due to their large pores sizes above 2 nm and abundant silanol groups on the surface. A number of studies to locate functions on mesoporous silica are reported. Functions can be

located either in the channels or in the pore walls. Three main approaches are available for the synthesis of porous hybrid materials starting from type of organoalkoxysilane units (**Figure 2.10**): 1) grafting (post-synthesis) approach, the subsequent modification of the pore surface of a purely inorganic mesostructured silica; 2) co-condensation approach (or one-pot synthesis), the simultaneous condensation of corresponding silica and organosilicas precursors; 3) co-condensation (one-pot synthesis) approach, the incorporation of organic groups as bridging components directly and specifically into the pore walls by the use of bisilylated single-source organosilicas precursors (PMOs).

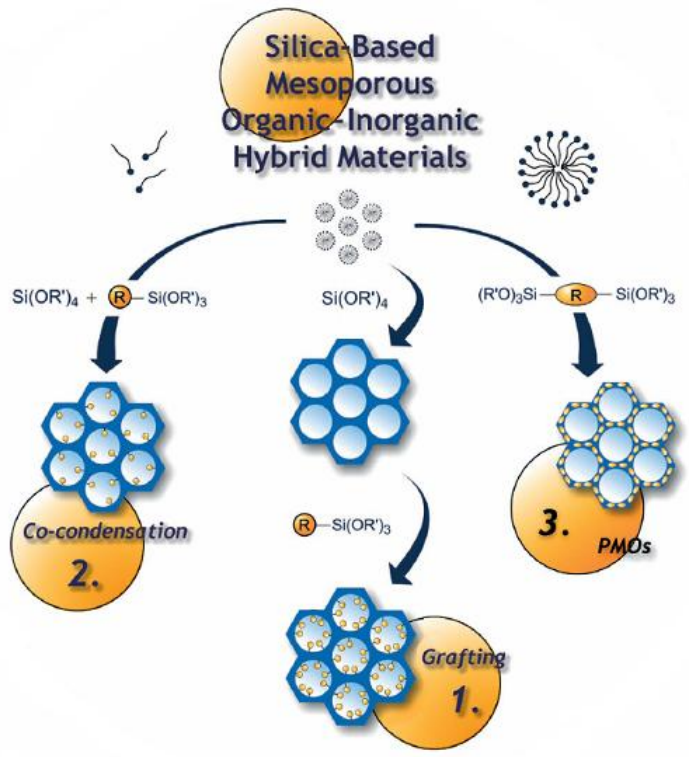

Figure 2.10 Three synthesis approaches for mesoporous hybrid materials.[65]

2.2.1 Grafting method

2.2.1.1 Grafting with passive surface groups

Grafting approach or post-synthesis is based on the reaction of organosilanes with free silanol (≡Si-OH) and geminal silanol [=Si(OH)$_2$] groups on the surface of the mesostructured silica using an appropriate solvent, *e.g.*, toluene or cyclohexane, under reflux conditions (**Figure 2.11**). Silica-based mesoporous materials have been functionalized with low reactiv-

ity groups, such as, trimethylchlorosilane, chloroalkyldimethysilanes, disiloxane $[Si(CH_3)_3]_2O$, disilazane agents of the type $HN(SiR^1R_2^2)_2$ ($R^{1,2}$ = H, Me, Ph, vinyl, ^{n}Bu, ^{n}Oct).[91] The functionalized mesoporous materials exhibit a reduction of pore size and pore volumes compared to the initial mesoporous material. The silanol groups in these materials are passivated, the surface hydrophobicity is increased and thereby the stability to moisture and mechanical compression is improved. This technique can be also applied to the design of multifunctional mesoporous materials. Shanks *et al*. have reported the multifuntionalized mesoporous silica (SBA-15 type) with sulfonic acid and hydrophobic organic groups (Et-Si≡) exhibiting a high catalytic conversion for the esterification reaction, which is most probably due to the hydrophobic environment provided by the organic groups.[87]

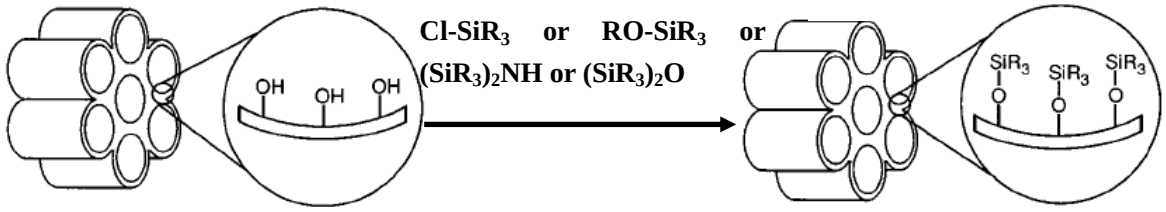

Figure 2.11 Grafting (post-synthesis) for organic modification of mesoporous silica phases with various organosilanes.[91]

2.2.1.2 Grafting with reactive surface groups

A number of reactive silane-coupling agents have been grafted on mesoporous silica in the aim of various applications. These reactive agents are olefins, nitriles, alkylthiols, alkyl amines, alkyl halides, epoxides, and other surface groups.[91] Olefins, such as vinyl groups, can be modified by bromination or hydroboration. Alkylthiols can be oxidized to sulfonic acid, and nitriles can be hydrolyzed to form carboxylic acids. Alkyl halides can introduce other functions by nucleophilic substitution. Functionalized mesoporous silica with the above agents can be used as absorbents, *e.g*., thiol-functionalized MCM-41, amino-functionalized MCM-41 and SBA-15 for absorption toxic metals, vinyl-MCM-41 for sorption organics, reported by Mercier, Pinnavaia,[92] Feng,[93] Su,[94] Stein,[91] Yoshitake[95] and their co-workers. They have been also used for catalytic reactions, *e.g*., sulfonic acid-functionalized mesoporous material as catalyst for esterification of glycerol with fatty

acids[87, 96] and bisphenol-A synthesis,[97, 98] amino functionalized mesoporous materials as catalyst for the Knoevenagel reaction.[99]

Using this approach, the occupation of the channel space by the organic functions in some cases takes place at the external surface and near the pore openings of the material which is problematic. However, this method does not compromise the mesoporous structure.

2.2.2 Co-condensation method (one-pot synthesis)

Co-condensation of a tetraalkoxysilane [$(RO)_4Si$ (R=Et, Me)] and one or more organosilanes of the type $(RO)_3SiR'$ (R=Et, Me) in the presence of supramolecular molecules as structure directing agents (SDA) is an alternative method to produce hybrid mesoporous materials with organic functions in the framework (**Figure 2.12**). A large number of substituents R' of the $(RO)_3SiR'$ organosilane has been reported: 3-aminopropyl, 2-cyanorthyl-, 3-chloropropyl, ethyl-, propyl-, mercaptopropyl-, phenyl-, vinyl-, to a name few.[91] Like the hydrolysis and condensation of tetraalkoxysilane, *e.g.*, preparation of MCM-41 or SBA silica phases, the sol-gel chemistry of organotriakoxysilanes depends on the trialkoxylsily group R of $(RO)_3SiR'$, size, length and steric hindrance of the organic groups R' of $(RO)_3SiR'$, water quantity and pH.[100] Hybrid mesoporous materials with organically modified surfaces can be prepared through a S^+I^-, $S^+X^-I^+$, S^0I^0, and N^0I^0 pathways (**Figure 2.4**).[65, 91] A very interesting work using the S^-I^+ pathway has been reported by Che and co-workers, where the ammonium-functionalized silicas can be synthesized using the chiral anionic surfactant N-acyl-L–alanate. After calcination, mesoporous silicas with helical chirality can be formed.[101]

Generally, the content of organosilane in the modified silica phases can reach 40 mol %, and still maintain an ordered meosoporous structure. The template removal can be achieved either via treatment with ethanol or an acidic ethanolic solution or through ion-exchange (NaCl or NH_4Cl). However, calcination is not suitable in most cases.

If grafting and co-condensation methods are compared, organo-units are generally more homogeneously distributed in materials synthesized with co-condensation methods, and

pore blocking is not a problem in the co-condensation approaches.

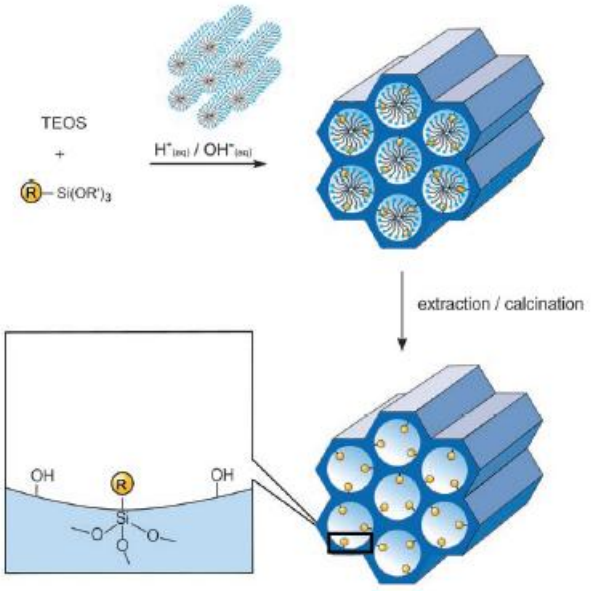

Figure 2.12 Co-condensation method (one-pot synthesis) for the organic modification of mesoporous pure silica phases. R=organic functional group.[65]

2.2.3 Preparation of periodic mesoporous organosilicas (PMOs) by co-condensation (one-pot synthesis) approach

The periodic mesoporous organosilicas (PMOs) were born in 1999 in three groups, *i.e.*, Inagaki,[11] Ozin[12] and Stein[13]. The synthesis approach of PMOa also profits of the supramolecular templating technique. They were synthesized through co-condensation of bis(trialkoxysilyl)organic units $(RO)_3Si\text{-}R'\text{-}Si(OR)_3$ in the presence of structure-directing agents (**Figure 2.13**). These bridged silsesquioxanes are hexafuntional molecules with six hydrolysable and polymerizable groups, thus they can quickly undergo hydrolysis even in dilute solutions. The nature of the R' group in the $(RO)_3Si\text{-}R'\text{-}Si(OR)_3$ units for the synthesis of PMOs can vary from ethane, ethylene and methylene to ferrocene, 1,4-phenylene, thiophene and benzene. The obtained PMOs possess high surface areas (> 600 $m^2 \cdot g^{-1}$), large pore size (> 2 nm) and a type IV isotherms determined by N_2 sorption measurements. The framework of PMOs is composed of silica and organic units which are homogeneously distributed in the pore wall. Even crystal-like pore walls of PMOs have been observed by Inagaki and co-workers using benzene-bridged organosilane $[(RO)_3Si\text{-}C_6H_4\text{-}Si(OR)_3]$[102].

PMOs have been applied in chromatography, host-guest chemistry, separations and catalysis, due to the periodic and uniform arrangement of mesopores, the narrow mesoporous size distribution and the presence of functional organic groups in the framework.

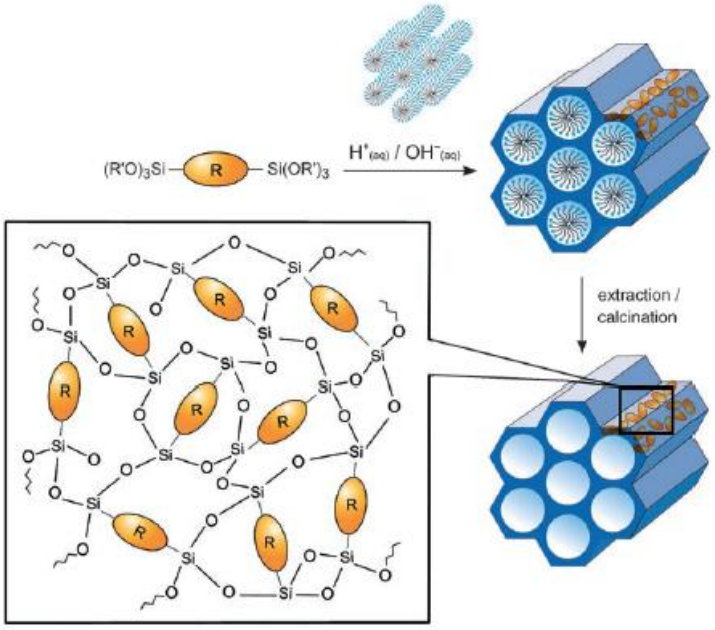

Figure 2.13 General synthetic pathway to PMOs that are constructed from bissilylated organic bridging units using the co-condensation method (one-pot synthesis). R=organic function.[65]

2.3 Incorporation of metals in mesoporous materials

Incorporation of metals in mesoporous materials has been largely developed for catalytic applications, since the introduction of metals allows fine-tuning of acidity or redox properties, like in zeolites and amorphous aluminosilicates. Various metals have been introduced in the mesoporous materials, such as B, Ga, Ti, V, Al, and transition metals (Ni, Cu, Mn, Co, Fe).[49] There are numerous of approaches for the introduction of metals into mesoporous materials. Here, we present two types: 1) introduction of metal ions without organic ligands, in which the final materials consist of metal oxides and silica; 2) introduction of metal ions with organic ligands, in which the obtained materials are composed of metal complexes and silica.

2.3.1 Without organic ligands

Metal salts as precursors. We have seen that metal modification of the composition of mesoporous materials is possible by the one-pot synthesis or post-treatment. In the one-pot synthesis, metal salts are added in the initial gel. The post-treatment can be performed either by impregnation or by ion-exchange; both cases the reaction takes place between the metal salt and the initially prepared silica mesoporous material. The resulting materials from these two different methods are not necessarily identical. The one-pot synthesis can typically lead to a relatively homogeneous distribution of the metal ion, whereas, the post-treatment primarily modify the pore surface and thus result in the increase of the metal concentration mainly on the surface. The post-treatment also can be performed through a grafting method. Tilley *et al*. were pioneered in the approach to prepare single-site "grafted catalysts" by using a technique that they designate as precursor route.[103, 104] For example, using (^{i}PrO)Ti[OSi(^{t}Bu)$_3$]$_3$ and Ti[OSi(^{t}Bu)$_3$]$_4$ as precursor, which are respectively grafted on MCM-41 and SBA-15, respectively, catalysts with single sites (OH)-Ti-(OSi)$_3$ and Ti-(OSi)$_4$ can respectively be obtained. Using this approach, orther mesoporous materials with single-site metal centers, such as, Ti, Cr, Fe and V, have been obtained.

Metal complexes as precursors. There are also some examples to show that an adequate choice of the metal precursor in the post-treatment can increase the metallic dispersion in the mesoporous material. Che *et al*. have observed that during the adsorption of Ni(NH$_3$)$_x$(H$_2$O)$_{(6-2x)}$ complexes on SiO$_2$, the metal complex loose the aquo ligands which are replaced by ≡SiO$^-$ from the surface of the silica.[105] In addition, the mono-dentate NH$_3$ ligand can be easily replaced by a water molecule during drying and calcination, which may lead to condensation of the complexes by olation or oxolation, resulting in the formation of nickel phyllosilicates and nickel hydroxide on the final material.[106] By the contrast, the use of the bidentate ligand (ethylenediamine, en) instead of NH$_3$ can lead after calcination to a relatively higher amount of isolated Ni species better dispersed in the silica.[107]

2.3.2 With organic ligands

Hybrid materials composed of silica and metal complexes can possess advantages both

from metal complexes and from the insoluble supports, such as, a heterogeneous silica catalyst with metal complexes as active sites, which present an easy separation and recovering because of the solid support. There are four methods for placing metal complexes into mesoporous materials, *i.e.*, encapusulating, exchanging, post-synthesis (grafting) and one-pot synthesis. Encapusulating and exchanging methods are on electrostatic interactions between the complexes and the support, which are weak interactions, the anchored complexes are thereby usually easily leached during the reaction process. Post-synthesis and one-pot synthesis methods are nowadays very popular for immobilizing complexes on solids due to the formation of stable covalent bonds ≡Si-O-Si-R' (R': functional group) between the functions and the solids. Different grafted metal complexes are described, such as salen metal complexes of Ni(II), Co(II) and Cu(II), phosphine-type complexes of Rh(III) and Pd(II), complexes of Mo(VI) and W(VI) with chiral ligands and Cu(II) and Co(II) complexes with salicylaldimine ligand. In this section, we will focus on the incorporation of polyamine and Schiff-base metal complexes, in particular Ni(II) and Cu(II), either by post-synthesis or by one-pot synthesis. A special attention will be devoted to the characterization of the copper species by electron paramagnetic resonance (EPR) spectroscopy.

2.3.2.1 Incorporation by grafting

Grafting metal complexes into the channel of mesoporous materials generates the active centers in the solid. On the other side, silica-based mesoporous material can offer confinement and changeable chemical environment (hydrophilic- hydrophobic), as shown in **Figure 2.14**. In some cases, the activity of the hybrid material can even be enhanced compared to that of homogeneous complex due to the confinement effect of the support and the surface properties (hydrophilic or hydrophobic). In addition, oligomerization of the complexes often observed in homogeneous catalysis, which can deactivate the catalyst, can be avoided in the hybrid materials.

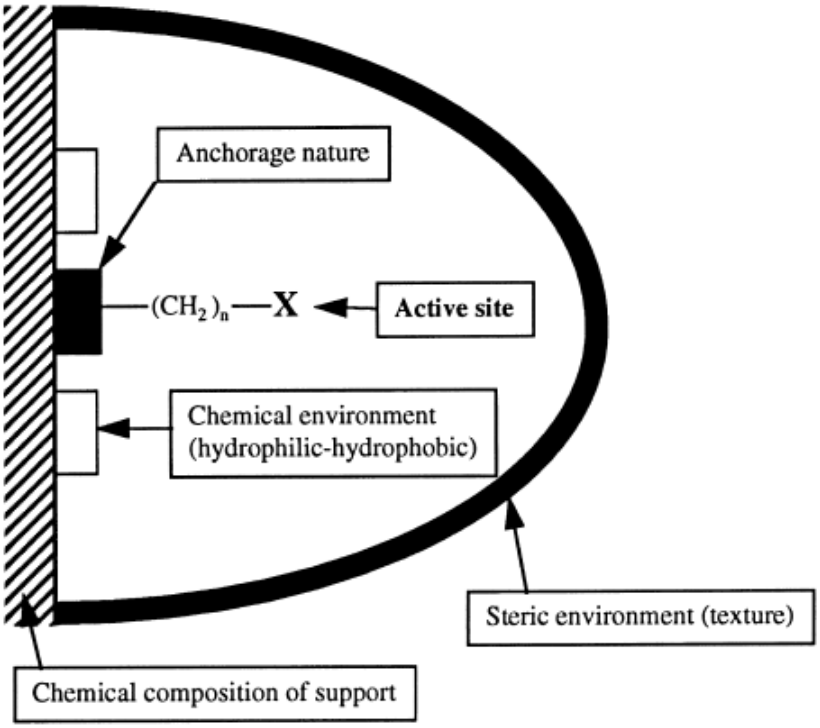

Figure 2.14 Design of hybrid organic-inorganic mesoporous materials.

There are various strategies for grafting metal complexes into mesoporous materials. Herein, we divide them into two types: indirect grafting and direct grafting. In the direct grafting, the complex possessing an alkoxylsilane arm directly reacts with an initially prepared mesoporous material. By contrast, in the indirect grafting, the ligand with an alkyltrialkoxysilane $(OR)_3SiR'$ is firstly grafted in the solid and then coordinated to a metal ion in the second step.

2.3.2.2 Indirect grafting

Some examples from the literature have been selected to illustrate this approach. Groups of Liu and Yoshitake have reported the grafting of aminopropylsilanes [(*N*-[3-trimethoxysilyl)propyl]-ethylenediamine and N-[3-(trimethoxysilyl)-propyl]- diethylenetriamine] on MCM-41.[31, 108] The grafted amino-ligands are then complexed with a metal ion [Cu(II), Fe(III), Ni(II)]. These obtained materials have been applied on sorption of arsenate ions in the wastewater.

In 1999, the group of Brunel has reported functionalized MCM-41 with halogenopopyltrialkoxysilanes (chloropropyltrialkylsilane and iodopropyltrimethoxysilane) and aminopropyltrialkoxysilane by post-synthesis method. The grafted halogeno organic moieties were further modified by nucleophilic substitution of other functions like various amines, leading to salen type of ligands grafted on the silica. Finally, Mn(II) was complexed to the ligand on the silica, obtaining a functionalized MCM-41 with a metal complex .[99]

Stack *et al*. have reported the functionalization of SBA-15 with Mn(II) bis-phen complexes using a metal-template or a metal-exchange method [phen: ethyl 4-(3-(triethoxysilyl)propy lthio) -1,10- phenanthroline-3-carboxylate].[9] In the first method a bis-phen Cu(I) complex already grafted on SBA-15 is used as template. Then the grafted Cu(I) in the grafted is exchanged with $Mn(II)(CF_3SO_3)_2$, leading to the functionalized SBA-15 with bis-phen Mn(II) complex (**Figure 2.15**, right part). In the latter method, the ligand was randomly with the grafted on the surface, then $Mn(II)(CF_3SO_3)_2$ was complexed to the grafted ligand. Comparison of the imprinted material with the material synthesized by random grafting of the ligand show that the template method creates more reproducible sites. The imprinted material presents a higher product selectivity in epoxydation, a more efficient use of oxidant and a higher reactivity than the homogeneous analogue. By contrast, the random grafted manganese material presents both bis-phen Mn(II) complex and mono-phen Mn(II) compexes, the latter coordinated to the silanolate groups on the surface (**Figure 2.15**, left part).

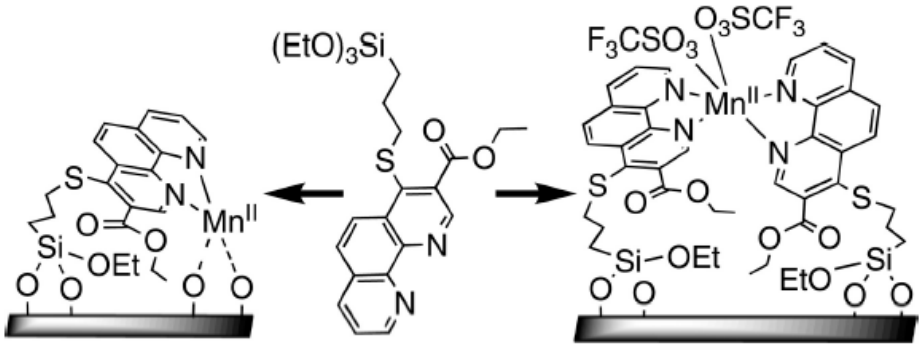

Figure 2.15 Various metal species on SBA-15 by indirect grafting.[9]

The use of a grafting post-treatment often leads to a heterogeneous distribution of the introduced complexes. To handle this problem, a novel approach has been developed in our group, the so-called "Molecular Stencil Patterning" (MSP) technique.[109, 110,22] It consists of a consecutive grafting method which has been proved to be efficient for dual fictionalizations on the surface of MCM-41 (**Figure 2.16**). The surfactant molecules present in the as-made silica the patterning during the grafting of the first function (trimethylsilyl groups) which serves as the isolation group. Then the second function (organic ligand) is introduced after displacement of the remaining template. The key point is that the amount of the first (trimethylsilyl) group introduced can be well controlled since the template removal can be accurately performed. Consequently, the second function can be isolated by the first function at different distances. Finally, the metal ion is complexed with the grafted ligand, obtaining the bifunctionalized material with a homogeneous distribution of the complex on the solid.

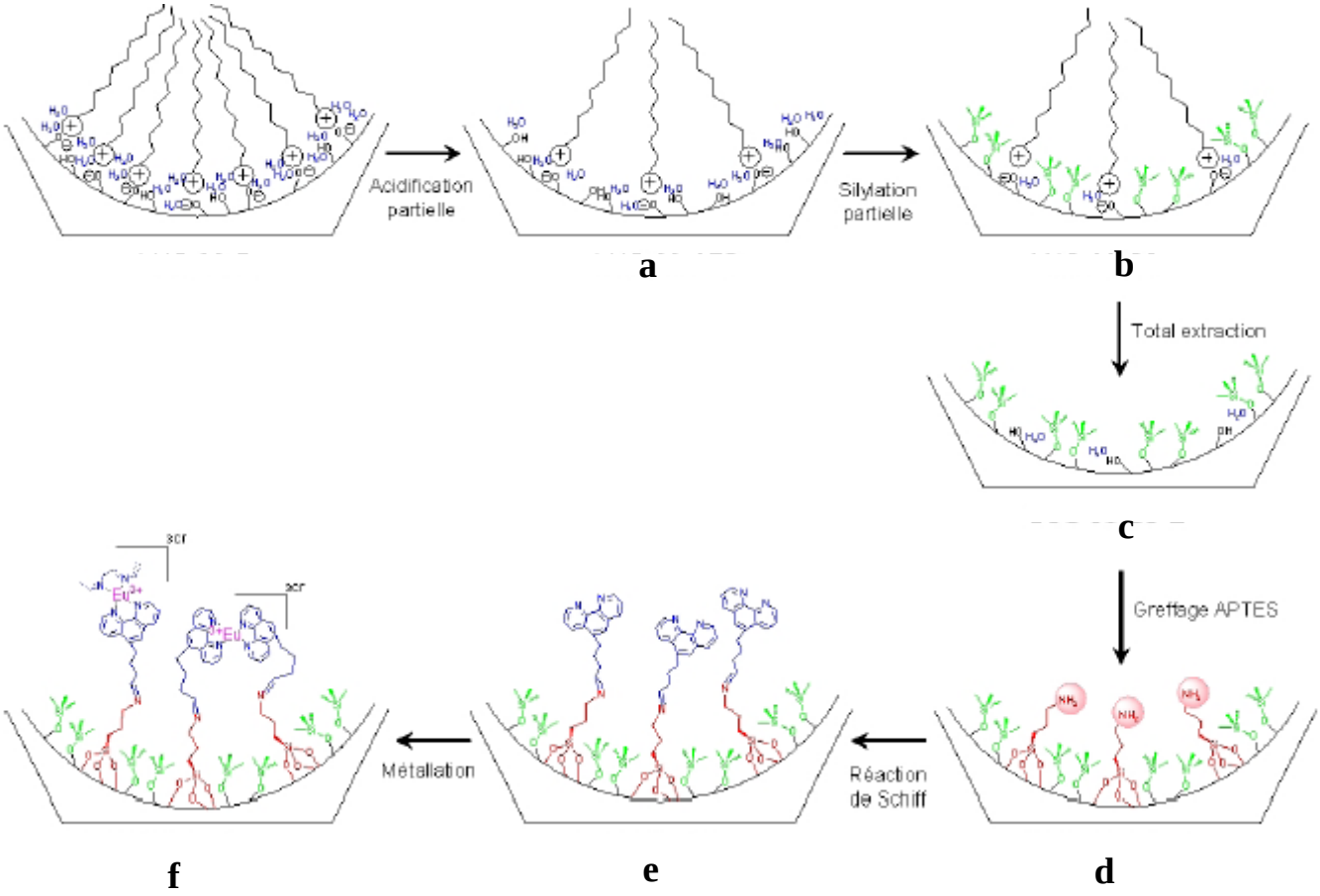

Figure 2.16 "Molecular stencil patterning" (MSP) technique for synthesis dual function groups. a) partial acidification; b) partial trimethylsylilation; c) total extraction of surfactant; d) grafting of 3-aminopropyltriéthoxysylane; e) Schiff reaction for grafting of

5-butanal-1,10-phenanthroline; f) incorporation of europium and complexation with 1,10-phenanthroline.[109]

2.3.2.1.2 Direct grafting

In direct grafting, complexation of the metal ion with the ligand occurs at the molecular level, different from the indirect grafting where the metal ion reacts with the solid which possesses the ligand. Therefore, in this method, the risk of modification of the metal complex can be minimized. Typical synthesis processes are described in the following.

Johnson *et al*. have synthesized a ferrocenyl precursor, which was anchored to the surface of a mesoporous silica MCM-41 support in a one-step reaction[111] (**Figure 2.17**).

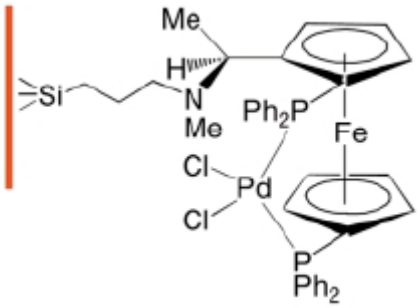

Figure 2.17 Functionalized MCM-41 with bis(phenylphosphino)ferrocenyl- dichloropalladiumpropyl *via* direct grafting of the metal precusor.[111]

Che *et al*. have reported that a chromium (III) binaphthyl Schiff base complex was immobilized on modified MCM-41.[112] The MCM-41 was firstly functionalized with aminopropyl groups on the surface. Then, the chromium (III) complex is formed by coordinated to the terminal NH_2 group of the surface-bound tether *via* simple addition (**Figure 2.18**).

Kureshy *et al*. have described the covalent bonding of a chiral Mn(III) salen complex in modified MCM-41 and SBA-15 with 3-aminopropyltriethoxysilane as a reactive tether (**Figure 2.19**).[113] Calcined MCM-41 and SBA-15 can be firstly functionalized 3-aminopropyltriethoxysilane and then the Mn(III) salen complex is introduced by a S_N2 substitution of amine and chloro. The obtained materials present a high catalytic activity for enantioselective epoxidation of nonfunctionalized alkenes and can be recycled several times.

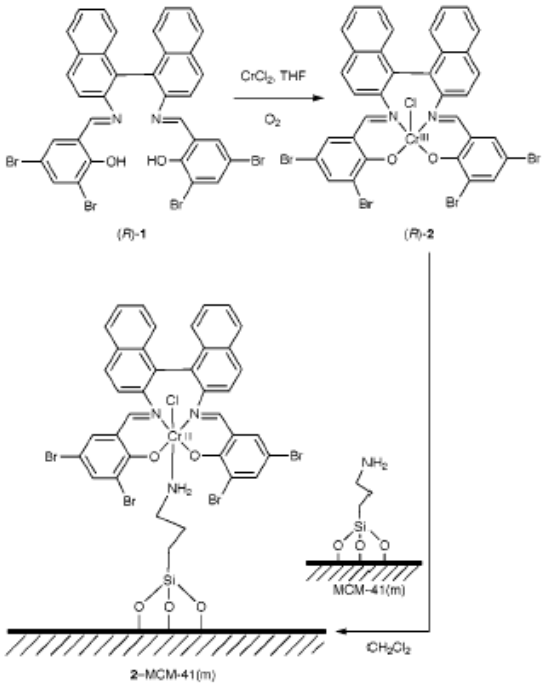

Figure 2.18 Heterogenization of a chromium Schiff base complex on MCM-41.[112]

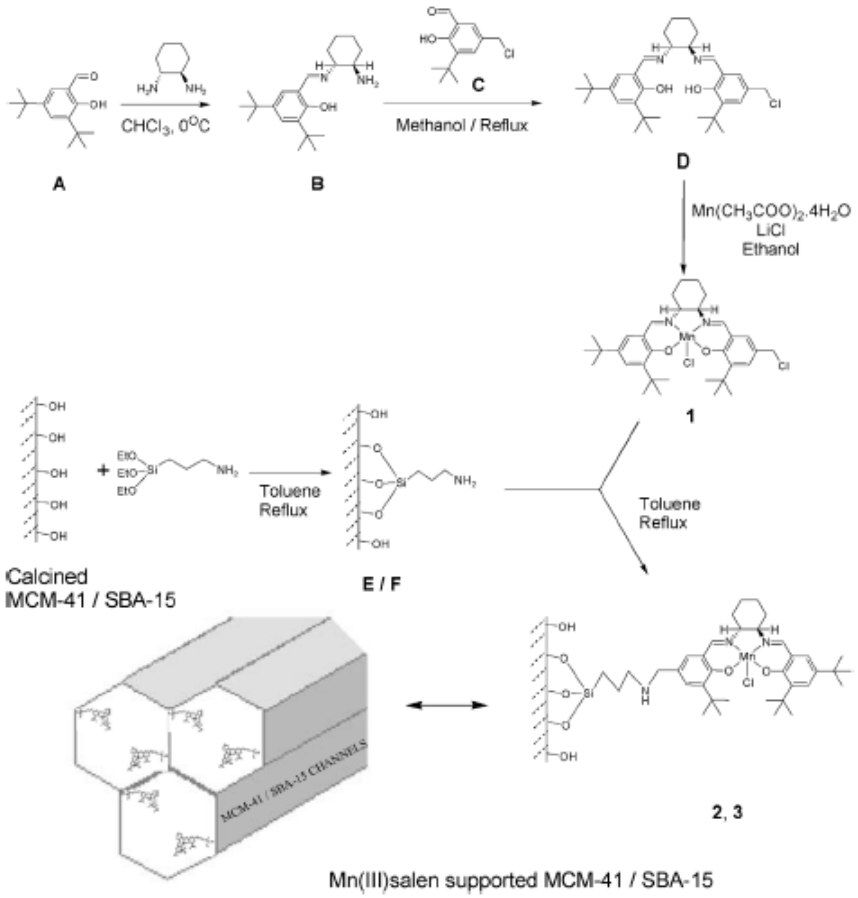

Figure 2.19 Synthesis of Mn(III) salen supported on MCM-41/SBA-15.

2.3.2.2 Incorporation by one-pot synthesis

The channel walls containing both metal complexes and inorganic substances in hybrid materials provide some advantages: 1) quicker diffusion of reactants in comparison to the occupation of channel by metal complexes grafted, 2) potential interesting electronic, optical, charge-transport and magnetic properties.

Hybrid materials containing metal complexes in the pore wall have been synthesized using the co-condensation of silica source and organosilica precusors in the presence of supramolecular templating agent by sol-gel chemistry. The silica source most common used is tetraethoxysilane (TEOS). Using a co-solvent is added to the aqueous solution, such as methanol or ethanol. This type of materials presents a large surface area and a narrow pore size distribution. Hybrid materials can be prepared via $S^{+}I^{-}$ pathway as described for PMOs materials possessing vanadyl Schiff base complexes and palladium carbapalladacycle complexes (100 %) in the presence of cetyltrimethylammonium bromide (CTABr) under basic conditions (**Figure 2.20**). They can also be synthesized via $S^{0}I^{0}$ pathway, such as metal 1,4,8,11-tetraazacyclotetradecane (cyclam) complex in the pore wall (*vide infra*).[17] Indeed, the preparation conditions need to take care of the stability of the metal complexes and to avoid leaching of the metal. The process of surfactant removal has to be adapted to not only keep the mesostructure but also maintain the metal coordination environment as in the homogeneous complex. The surfactant removal can be achieved via ethanol or acid ethanolic solution treatment, but the acid content need to be controlled to avoid metal leaching.

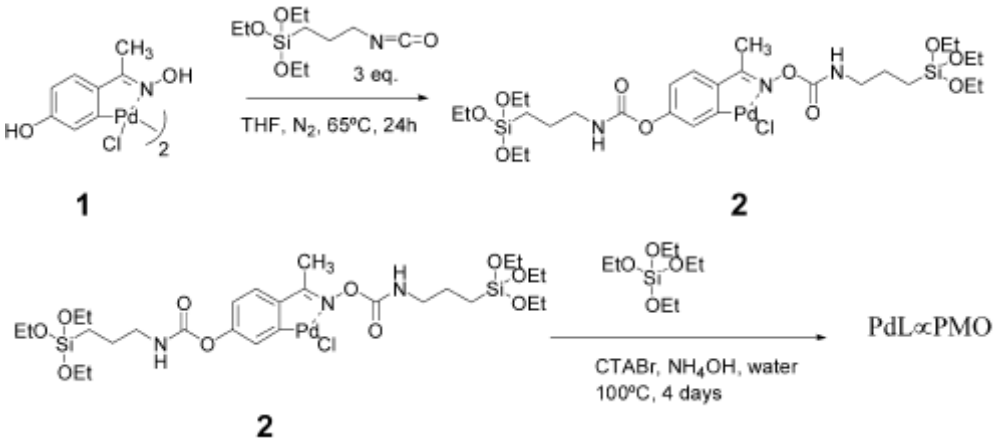

Figure 2.20 Procedure to prepare several PdL∝PMOs by varying the **2** to TEOS molar ratio.

2.3.3 Incorporation of metal-amino complexes into silica materials

Amino groups include aliphatic amines, aromatic amines, polyamines and cyclic polyamines. Polyamines are organic compounds containing two or more primary amino groups such as ethylenediamine, ethylenetriamine and spermine. They can be used as bidentate or tridentate ligands for the coordination with transition metals such as Ni(II) and Cu(II). Cyclic polyamines like 1,4,8,11-tetraazacyclotetradecane, 1,4,7,10-tetraazacyclododecane and 1-(3,5,7-trinitro- 1,3,5,7-tetrazocan-1-yl)ethanone can be used as tetradentate ligand. There are a lot of examples for immobilizing of metal-amino complexes on mesostructured silica by post-synthesis as described above, while there is a few of examples by one-pot synthesis of mesoporous silica containing metal-amino complexes with more than one alkyltrialkoxysilane arms. In this section, we will present these one-pot synthesized hybrid materials.

Metal-amino complexes have been introduced in silica through co-condensation with a silica source *via* one-pot synthesis. Karakassides *et al*. have reported that under neutral conditions Cu(II)-ethylenediamine-containing MCM-41 can be synthesized by a sol-gel approach using tetramethoxysilane (TMOS) as silicon source and the copper-ethylenediamine precursor $Cu[(CH_3O)_3Si(CH_2)_3NHCH_2CH_2NH_2]_2$, $[Cu(AAPTMS)_2]$, AAPTMS = N-(2-aminoethyl)-3-aminopropyltriymethoxysilane. The as-made materials have been characterized by EPR spectroscopy, showing the presence of a mixture of $Cu(AAPS)^{2+}$ and $Cu(AAPS)_2^{2+}$ species. Both studies of Mercier *et al* and Karakassides *et al*. suggest that neutral conditions are not optimal for metal ion coordination when the synthesis of ethylenediamine (**en**) functionalized mesoporous materials is at stake.

Corriu *et al*. have synthesized a new type of mesoporous hybrid materials containing cyclam moieties inside the framework complexed to transition metal ions such as Cu(II) or Co(II).[16-18] These syntheses are performed under neutral conditions using a metal-cyclam precursor with either SiH_3 or $Si(OEt)_3$ hydrolisable groups, tetraethoxysilane (TEOS) as silica source and methanol as cosolvent. Two different transition metals can be selectively incorporated, one on the framework and the other in the channel pores. The cyclam complex in the framework of the mesostructured silica is quite stable and no decomplexation is possible using a large excess of ligand.

Indeed, pH is one of the determining factors during the one-pot synthesis of hybrid materials containing metal complexes with amino-ligands. For instance, the pK_1 and pK_2 of ethylenediamine are 7.56 and 10.71, respectively. Thus if the pH of the solution is below the pK_a of ethylenediamine, the amino group can be protonated, thus losing the coordination ability. On the other hand, in order to avoid complex degradation during the synthesis process, temperature is another important factor to take into consideration, since stability constants of complexes can dramatically vary with temperature.

2.3.4 Incorporation of metal-Schiff base complexes into silica materials

A Schiff base, with general formula $R_1R_2C=N-R_3$, is a functional group that contains a carbon-nitrogen double bond (C=N) with the nitrogen atom connected to an aryl or alkyl group (R_3). Schiff bases are among the most used N-ligands, because the basicity of the sp^2-hybridized N lone pair, although lower than that of amines (sp^3 hybridization), is well suited to complex metal ions. The family of Schiff base ligand is known as salen and salicylaldimine ligand. The first salen-type Schiff base metal complexes were synthesized in 1933 by condensation of salicylaldehyde and ethylenediamine with various metal salts (**Figure 2.21**). Salicylaldimine ligand can be seen as the half of a salen ligand and is synthesized by the reaction of equivalent salicylaldehyde with only one monoamino group. Although the imine group is prone to undergo an acid-catalyzed hydrolysis, reverting to the corresponding salicylaldehyde and amine reactants in the presence of water, the stability of the Schiff base group increases considerably upon coordination with a metal ion and formation of the Schiff base-metal complex. Different from the Schiff base ligand, the Schiff base-metal complex can be used in wet solvents or even in aqueous media without undergoing decomposition.

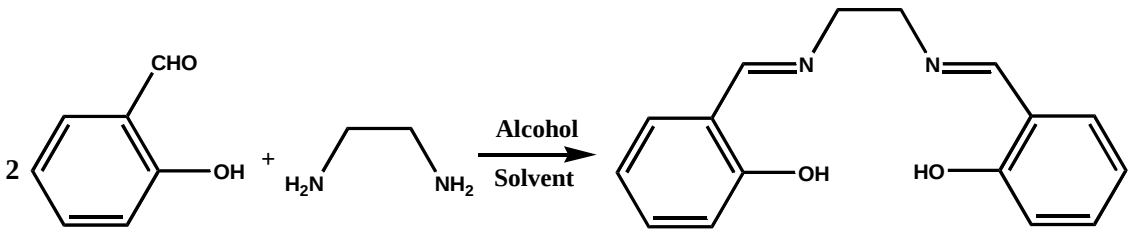

Figure 2.21 Synthesis route of salen.

Schiff bases are known to be among the most convenient and attractive ligands for complexes. The reasons are the following: 1) the two donor atoms, N and O, of the Schiff base exert two opposite electronic effects: the imine nitrogen is a soft donor and accordingly will stabilize the low oxidation state of the metal atom state whereas the phenolate oxygen is a hard donor known to stabilize higher oxidation states; 2) steric and electronic effects around the metal ion can be finely tuned by an appropriate selection of bulky and /or electron withdrawing or donating substituents into the Schiff base. Various Schiff base complexes are primarily with transition metals such as Mn, Cu, Fe, Cr, Co, V, Ti, Ru, Al, Zn and Au.[114] They exhibit a distorted square planar or square pyramidal geometry depending on the tetradentate N_2O_2 or pentadentate N_2O_2X coordination around the metal center.[114-116] Salen-metal complexes are widely used as catalysts for oxidation reactions which will be presented latter.

Converting homogeneous metal-salen complexes into heterogeneous catalysts is a general trend. The approaches for incorporating metal-salen complexes onto mesoporous silica are grafting or one-pot synthesis mentioned above. Among them, few examples of one-pot synthesized hybrid materials are reported. Here, we would like to present these examples.

The group of Baiker was the first to claim the immobilization of salen complexes [cobalt(salen) and copper(salen)] on silica xero- and aerogels, which was achieved *via* sol-gel method using a precursor N, N'-ethylenebis(salicylidenaminato) (salen) metal complex which was co-condensed with tetraethoxysilane (TEOS) under acid conditions (**Figure 2.22**).[117] The Schiff base ligands used contain only a single imine group, and the actual complexes reported were bis(salicylidenaminate) complexes of Co(III) and Cu(II) which lack of bridge connection between two nitrogen atoms. The obtained hybrid materials are proved to possess imine bond and metal complexes. Aerogels have been tested on the catalytic aerobic allylic oxidation of α- and β-isophorone (α- and β-IP) to ketoisophorone (KIP) and exhibit a much lower activity than the homogeneous analogue.[118] The authors suggest that the differences in the activities of homogeneous and heterogeneous systems may be associated to the phenomenon of site isolation leading to different reaction pathways. Indeed, due to the poor characterization of the hybrid materials, the coordination environment around the metal could be different from that proposed, *i.e.*, [2(NO)], which could be the

reason for the lower catalytic activity compared to the homogeneous analogue.

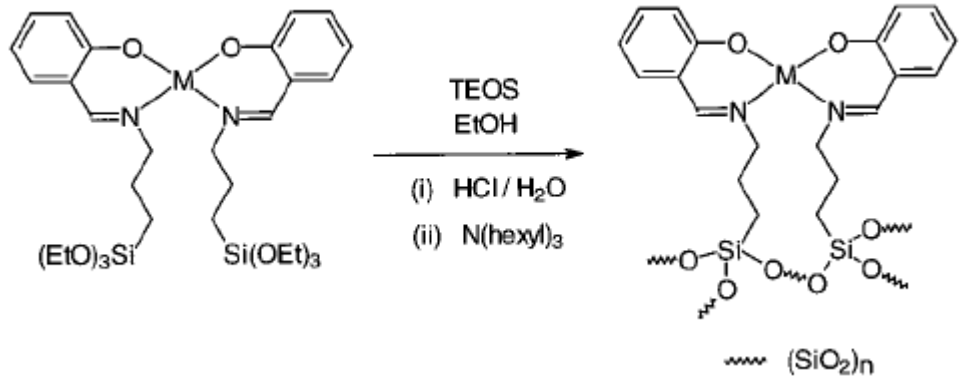

Figure 2.22 Immobilization via the sol-gel process of silyl ether modified salen catalysts in a silica gel [M = Co, Cu].[117]

Corriu *et al*. have synthesized hybrid materials containing Cu(II) or Co(II) Schiff base complexes covalently linked to the silica matrix (SBA-15) by two Si-C bonds using two routes via one-pot synthesis in acid conditions (**Figure 2.23**). The first (route **A**) corresponds to the hydrolysis and polycondensation of a bis-silylated metal Schiff base complex. The second (route **B**) consists of the hydrolysis and polycondensation of a bis-silylated Schiff base followed by the complexation with metal. It was found that these two routes lead to different results on metal environments and catalytic reactivity. For the hybrid material synthesized via the route A, the Cu(II) complex is in a trigonal bipyramidal geometry, whereas, it possesses a geometry between a square planar pyramid and a trigonal bipyramid if route **B** is used. In addition, only the materials prepared via the route **A** are efficient for dioxygen sorption. Authors think that the reason of such a behavior is probably due to the difference of geometry around the metal centers. Indeed, in the route **A**, Cu(II) complexes are already formed and then they were carried on the hydrolysis process, avoiding the modification of the metal coordination. However, in the route **B**, the metal complexation process is in the final step, which most probably can lead to multiple Cu(II) coordination states on the solid, and even some polymer Cu(II) species on the solid surface. The various Cu(II) species can provide negative effects or positive effects on the dioxygen sorption. Furthermore, this example reminds us again the advantages of the direct introduction of the metal complexes.

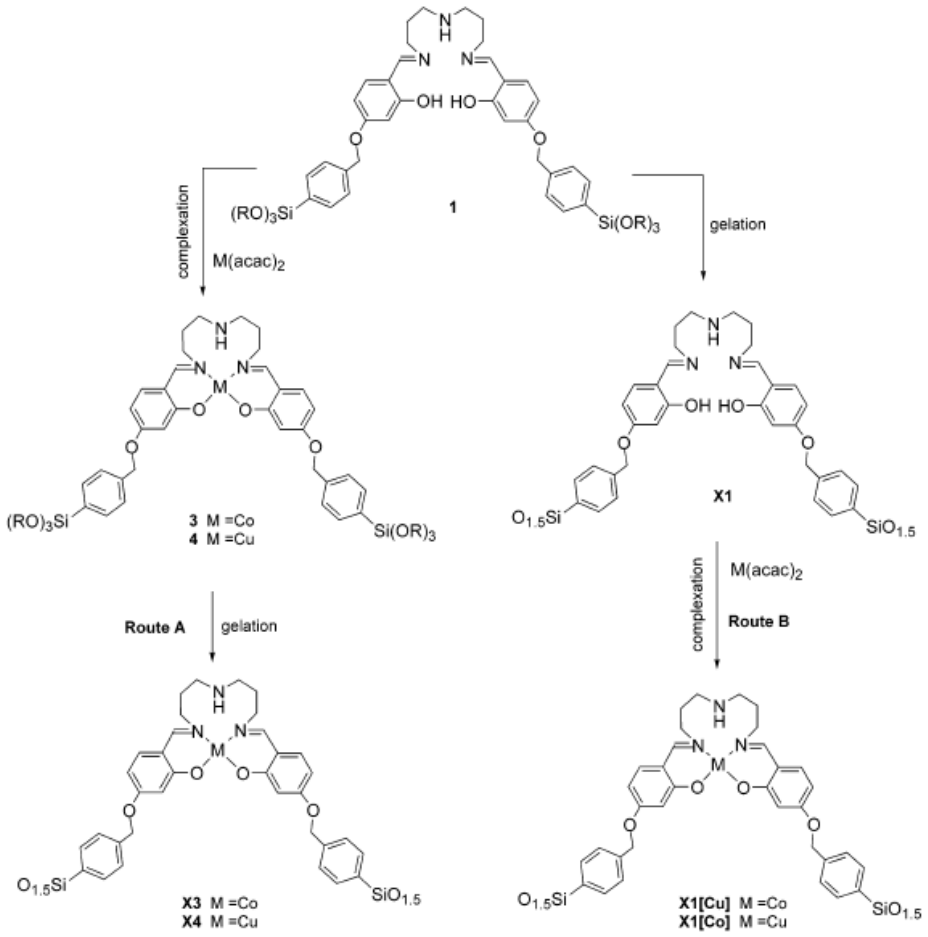

Figure 2.23 Two synthesis routes of hybrid materials containing Cu(II) or Co(II).

Corma *et al*. have synthesized hybrid materials incorporating chiral vanadyl Schiff base complexes in the framework by one-pot synthesis, obtaining materials VO(salen)@PMO and VO(salen)@ChiMO (**Figure 2.24**). The synthesis of the PMOs was performed like for MCM-41 using cetyltrimethylammonium bromide as template under basic conditions, and with the addition of ethanol as co-solvent in order to increase the solubility of the salen complex in the aqueous gel.[119-121] The obtained PMOs materials [VO(salen)@PMO and VO(salen)@ChiMO] possess a well-ordered hexagonal mesostructure as determined by XRD characterization and BET surface areas of 900 $m^2 \cdot g^{-1}$ and pore sizes of *ca*. 4.2 nm from the Ar isotherm adsorption. The Salen-vanadyl complex is maintained under the basic synthesis conditions which was confirmed by the following characterizations: 1) the PMOs materials exhibit similar absorption bands on UV-visible spectra as the metal precursors; 2) absorption bands assigned to the vibrations of imine and metallosalen were observed in

FT-IR spectra; 3) a T^3 peak attributed to Si atoms of $–CH_2$-Si(OSi≡)$_3$ is presented in MAS ^{29}Si NMR. PMOs showed catalytic activity for cyanosilylation reaction and this catalyst can be recycled several times.

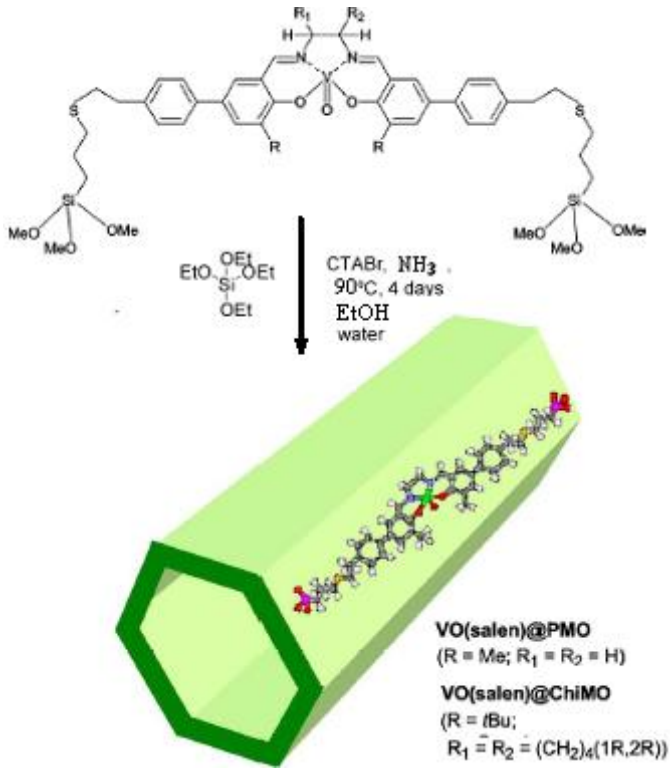

Figure 2.24 Preparation of VO(salen)@PMO and VO(salen)@ChiMO. Synthesis conditions: TEOS, NH_3, CTAB, H_2O, EtOH, 90 °C, 4 days.[119]

2.3.5 Characterization

The characterization of hybrid mesoporous materials immobilizing metal complexes is related to two aspects: 1) characterization of solids' textures; 2) characterization of metal coordination environments. For the first part, the textual characterization of solids can be performed by a panel of techniques, such as XRD, N_2 sorption measurements and IR spectroscopy, which have been presented before. Indeed, they can also provide indirect information about the presence of grafted metal complexes. For example, functionalized mesoporous material in the channel usually exhibits a reduced pore size, pore volume and surface area compared to the material before functionalization. In the FT-IR spectra new bands corresponding to the silanol groups on the surface diminish. For the second part, the metal

complex can be characterized by UV-vis-NIR diffuse reflectance, Raman and electronic paramagnetic resonance (EPR) spectroscopies. Among them, EPR spectroscopy can only monitor paramagnetic species, such as Cu(II) species, which can provide the information about the environment and the geometry of complexes. In the following, this technique will be introduced.

2.3.5.1 Electronic paramagnetic resonance (EPR) spectroscopy

EPR is a valuable technique, both because of its high sensitivity ([spin] ~10^{-8} mol/L) and its general capability to identify unambiguously paramagnetic species which contain unpaired electrons, such as O^-, O_2^-, Cu^{2+}, Fe^{3+} etc. It can reveal the oxidation state, electronic configuration and coordination number of a paramagnetic ion. This technique has been used in catalytic chemistry (monitoring of the oxidative state of an ion during a reaction for metal complexes in solution or immobilized on a solid, etc), biological systems (enzyme, DNA, protein etc), food production (beer, wine, milk, etc). Here, we will focus on this technique and its characterization on Cu(II) species.

Principle

EPR is an absorption spectroscopy in which radiation having frequency in microwave region is absorbed by paramagnetic species to induce transition between magnetic energy level of electrons with unpaired spin ($S = n/2 \neq 0$, S: total spin of the system, n: the number of unpaired electrons) (**Figure 2.25**). Each electron processes a magnetic moment and a spin quantum number S = 1/2, with magnetic components $m_s = +1/2$ and $m_s = -1/2$. In the presence of an external magnetic field with strength B_0, the electron's magnetic moment aligns itself either parallel ($m_s = +1/2$) or antiparallel ($m_s = -1/2$) to the field. The separation between $m_s = +1/2$ and $m_s = -1/2$ state is $\Delta E = g_e \mu_B B_0$, where g_e is the electron's so-called g-factor, B_0 is the magnetic field, μ_B is the Bohr magneton. An unpaired electron can move between energy levels by either absorbing or emitting electromagnetic radiation of energy $\varepsilon = h\nu$ such that the resonance condition, $\varepsilon = \Delta E$, is obeyed. Therefore, the fundamental equation of EPR spectroscopy is obtained: $h\nu = g_e \mu_B B_0$. In practice, the frequency

(ν) of radiant energy is usually fixed to approximately 9.5 GHz in X-band EPR, and the external magnetic field (B_0) is varied until that the gap between the $m_s = +1/2$ and $m_s = -1/2$ energy states matches the energy of microwaves (**Figure 2.25**).

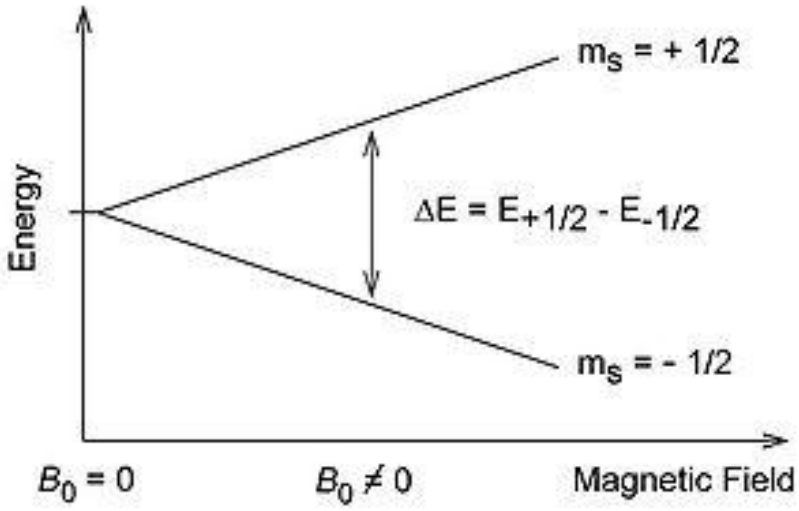

Figure 2.25 Energy-level diagram for S=1/2 and no zero-field splitting.

g-value For a free electron in vacuum, g is equal to 2.0023. In chemical systems, the *g*-value reflects the unpaired electron occupying an orbital which may be more or less localized on a single atom or may be heavily delocalized across a molecular or radical. Therefore, g-value can be smaller or bigger than that of a free electron in chemical systems.

In an isotropic system, the g directions in the x, y and z axes are equivalent and only one $g = g_x = g_y = g_z$ can be observed [**Figure 2.26** (**a**)]. However, many systems are anisotropic [**Figure 2.26** (**b**), (**c**)]. Under these conditions, the g value depends on the direction between the magnetic field and the principal (Z) axis of the system. For complexes of copper (II), there are mainly two principal *g*-values, $g_{\|}$ and $g_{\perp}$; when the magnetic field and molecular axes are alined, the signal appears at $g_{\|}$ [**Figure 2.26** (**b**)]; when they are perpendicular it appears at $g_{\perp}$ [**Figure 2.26** (**c**)]. For a rhombic system three different g-values can be observed (g_x, g_y, g_z) [**Figure 2.26** (**d**)].

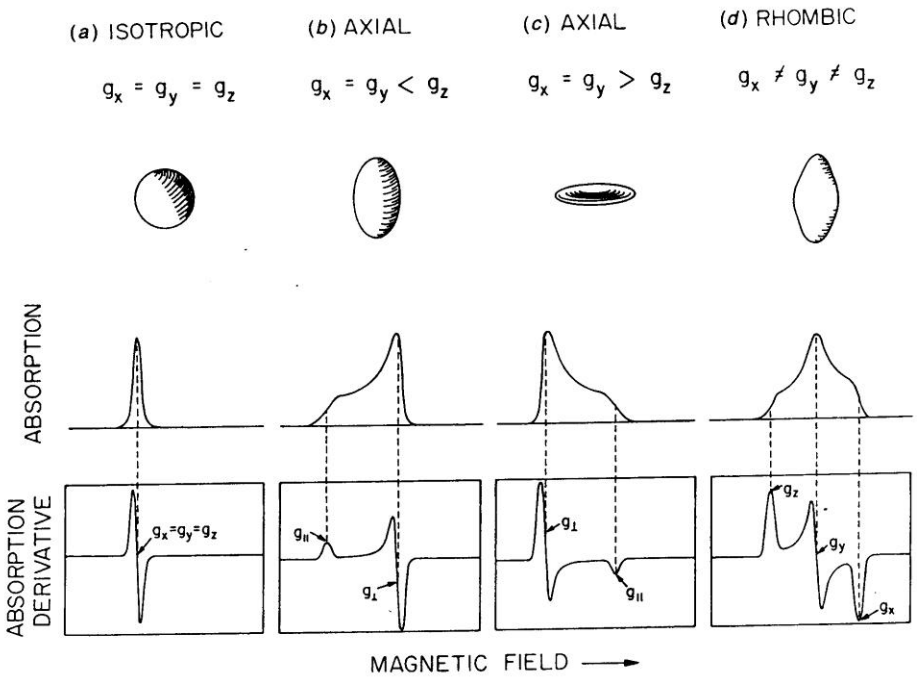

Figure 2.26 Resonance pattern depending on the g tensor symmetry.[122]

Hyperfine structure The EPR spectra of Cu(II) complexes usually show additional fine structure (**Figure 2.27**). In fact, the Cu atom on which the unpaired spin is centred has a nucleus which possesses a nuclear spin, *I*. The nucleus of spin *I* gives rise to a splitting of the EPR line into $2I + 1$ components (**Figure 2.27**). For Cu, *I* is equal to 3/2, and 4 lines can be therefore observed in the EPR spectrum. The hyperfine coupling constant A is usually higher for the g_{II} than for $g_\perp$.

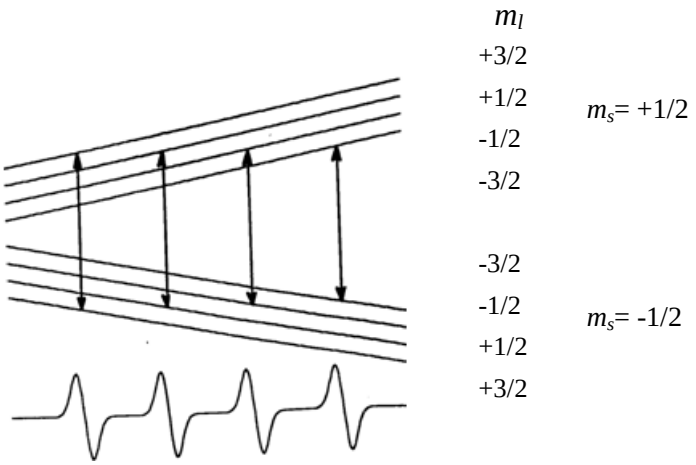

Figure 2.27 Hyperfine splitting of the m_s = -1/2→+1/2 transition due to the interaction with the nuclear spin *I* = 3/2. The four resulting transitions are equally spaced.

Relation between $g_{\|}$ and the Cu^{2+} coordination state

g-value, $g_{\|}$ and hyperfine coupling constant, $A_{\|}$, are correlated with the coordination mode of the complex. A good example can be given from the report of Sakurai and coworkers.[123] They have studied several copper(II) complexes with a CuN_4 type coordination mode and with various geometries. The relationship between $g_{\|}$ and $A_{\|}$ is presented in **Figure 2.28**. For copper(II) complexes with square-planar or axially-coordinated square-planar or distorted square-planar geometries, in most cases, g-values are similar, whereas, the hyperfine parameters $A_{\|}$ values decrease for Cu(II) complexes with axially-coordinated square-planar geometry compared to these with square-planar or distorted square-planar geometries. Furthermore, copper complexes with tetrahedral geometry exhibit higher $g_{\|}$ and smaller $A_{\|}$ values in comparison to these of square-planar geometry. Even for a given geometry, an increase of $g_{\|}$ is followed by a decrease of $A_{\|}$. In fact, $A_{\|}$-value is related to the delocalization of the unpaired electron on the copper nucleus where while $g_{\|}$ is strongly affected by the ligand field strength. We can take ethylenediamine complexes of copper(II) with different number of ligands, $[Cu(H_2O)_6]^{2+}$, $[Cu(en)(H_2O)_4]^{2+}$, $[Cu(en)_2(H_2O)_2]^{2+}$, as examples.[124] In all these cases, the hyperfine coupling (I = 3/2) of copper(II) complexes is easily characterized (**Figure 2.29**). The higher the stability constant of copper(II) complex, the lower the $g_{\|}$-values and the higher the $A_{\|}$-value: $g_{\|}$ = 2.400 and $A_{\|}$ = 128x10^{-4} (cm^{-1}) for $[Cu(H_2O)_6]^{2+}$, $g_{\|}$ = 2.281 and $A_{\|}$ = 181x10^{-4} (cm^{-1}) for $[Cu(en)(H_2O)_4]^{2+}$, $g_{\|}$ = 2.209 and $A_{\|}$ = 203x10^{-4} (cm^{-1}) for $[Cu(en)_2(H_2O)_2]^{2+}$ (**Table 2.3**).

Using a plot of A_z *vs* g_z ($A_z \equiv A_{ll}$, $g_z \equiv g_{ll}$), Peisach and Blumberg have discriminated defined ranges parameters for CuN_4, CuN_2O_2, CuO_4 types of coordination in natural metalloenzymes. Some of us has used this type of diagrams to characterize copper complexes in mesoporous silicas like in the present study.[22] The ranges of Az ~ 180-200 x 10^{-4} cm^{-1} and g_z ~ 2.19-2.25CuN_4 are generally for CuN_4 species, Az ~ 160-190 x 10^{-4} cm^{-1} and g_z ~ 2.21-2.25common for $Cu(N_3O)$ species. However, the domains for various coordination states overlap and do not provide unequivocal answer.

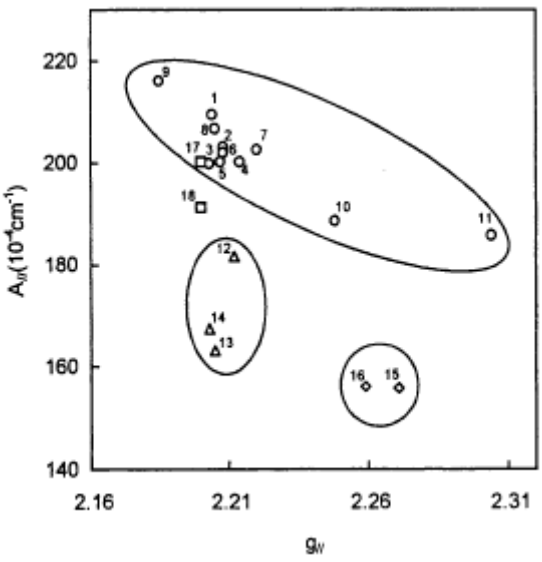

Figure 2.28 Relation between g_{ll}-values and A_{ll}-values for a CuN_4 complex.[123] (○) square-planar, (△) axially-coordinate square-planar, (◇) tetrahedral, (□) distorted square-planar. 1. (ethylenediamine)$_2$; 2. (*N*-Methyl-ethylenediamine)$_2$; 3. (*N*,*N*-dimethyl-ethylenediamine)$_2$; 4. (*N,N'*-dimethyl-ethylenediamine)$_2$; 5. (*N*-ethylene-ethylenediamine)$_2$; 6. (*N*-Propyl-ethylenediamine)$_2$; 7. (1,3-trimethylenediamine)$_2$; 8. (trans-1,2-cyclohexanediamine)$_2$; 9. 1,4,8,11-tetraazacyclotetradecane; 10. $(NH_3)_4$; 11. (pyridine)$_4$; 12. (diethylenetriamine)$_2$; 13. tetraethylenepentamine; 14. pentaethylenehexamine; 15. (1,10-phenanthroline)$_2$; 16. (2,2'-bipyridine)$_2$; 17. triethylenetetramine; 18. 1,4,7,10-tetraazacyclododecane.

The g tensor contains also a lot of information on the ground state and the symmetry of the complexes. In the case of copper(II), which is a d^9 ion, there is a strong tendency for Jahn-Teller distortion that is easily characterize by EPR. For $g_{\|} > g_{\perp}$ (**Figure 2.6(b)**) that stands for a $d_{x^2-y^2}$ ground state, copper is either in a pure square planar coordination (no ligand in the z axis) or in an elongated octahedral environment. It fits also the case of pentacoordinated square pyramid arrangement. When $g_{\|} < g_{\perp}$ [**Figure 2.26(c)**], the unpaired electron occupies in the d_z^2 orbital, the copper of complex is rather in compressed tetragonal or trigonal bipyramid situation.[125] The latter case fits also with a compressed octahedral environment through this is not often observed.

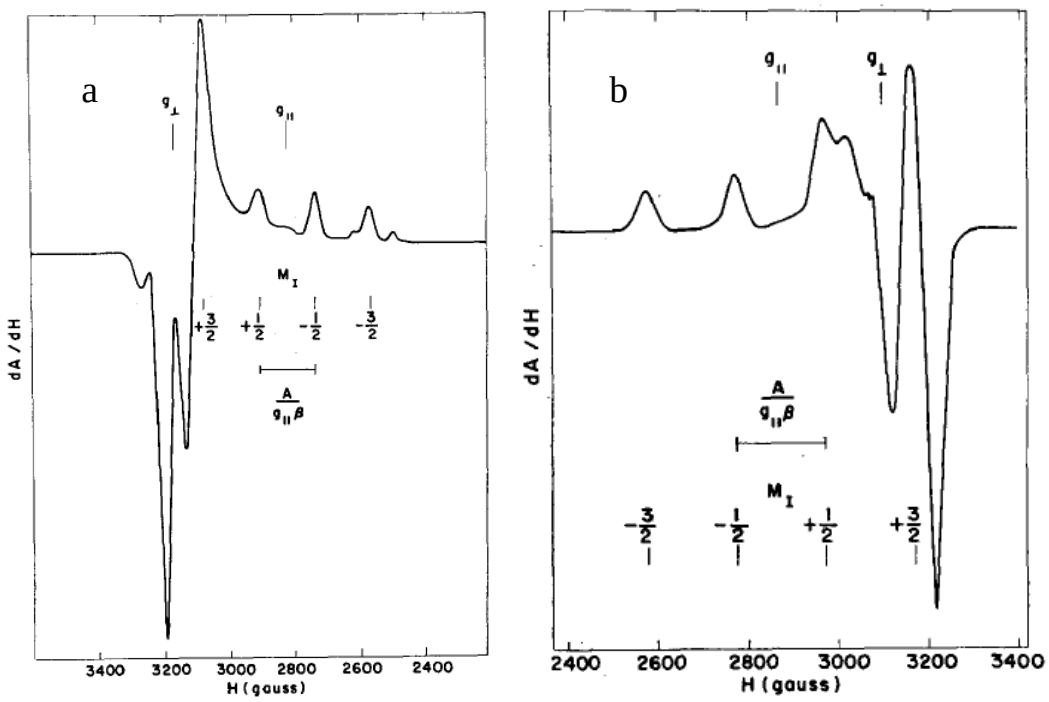

Figure 2.29 EPR spectra of (a) $[Cu(en)(H_2O)_4]^{2+}$ at -150 °C in 60 % glycerine/40 % water with en/Cu(II) = 0.83. The total Cu(II) concentration is 0.02M with roughly 68 % as $[Cu(en)(H_2O)_4]^{2+}$, 24 % as $Cu(H_2O)_6^{2+}$, and 8 % as $[Cu(en)_2(H_2O)_2]^{2+}$; (b) 0.02 M $[Cu(en)_2(H_2O)_2]^{2+}$ at -150 and $[Cu(en)_2(H_2O)_2]$ (b) at -150 °C in 60 % glycerine/40% water with en/Cu(II)= 2.25.[124]

Table 2.3 Spin-Hamiltonian parameters for copper (II) complexes

Copper(II) complex	$g_{\|\|}$	$g_{\perp}$	$A_{\|\|}$ (cm^{-1})
$[Cu(H_2O)_6]^{2+}$	2.400	2.099	128 x 10^{-4}
$[Cu(en)(H_2O)_4]^{2+}$	2.281	2.058	181 x 10^{-4}
$[Cu(en)_2(H_2O)_2]^{2+}$	2.209	2.047	203 x 10^{-4}

2.4 Applications of mesoporous materials modified with metal complexes

Mesostructured hybrid materials containing metal complexes are potential candidate for a large number of applications on catalysis, sensing, adsorption, enzymatic reaction and separation. Here, we mainly focus on their applications on catalysis, enzymatic reactions and adsorption, especially for the mesostructured hybrid materials immobilizing met-

al-polyamine complexes and metal-Schiff base complexes.

2.4.1 Catalysis

Two catalytic reactions using grafted complexes on inorganic supports have been selected and will be described in the following: 1) hydroxylation of phenol with supported Cu(II) solids; 2) cyanosilylation of aldehyde with supported vanadyl complexes.

2.4.1.1 Hydroxylation of phenol with supported Cu(II) materials

Catalytic hydroxylation of phenol is one of the challenges in the industrial chemistry, specially to afford tunable selectivity between catechol and hydroquinone and also to minimize the formation of byproducts (so-called "tars") which are the mixture of oligomers or polymers of phenol or products. So far, various heterogeneous catalysts have been employed to increase the conversion of phenol and the selectivity to diphenols. Here, a special attention is given to the hydroxylation of phenol with H_2O_2 by copper(II)-containing catalysts. The catalysts reported in the literature are mainly mesoporous silicas supporting copper oxide, such as CuSBA-15, CuMCM-41, CuHMS, hydrotalcites containing Cu and copper phosphate, while only a few examples of functionalized catalysts with Cu(II) complexes are described. The characteristics of some copper(II) catalysts for phenol hydroxylation are presented in **Table 2.4**. Various key parameters, such as reaction temperature, substrate/H_2O_2 molar ratio, phenol conversion, H_2O_2 efficient selectivity and tar selectivity are listed. However, comparison in term of phenol conversion and selectivity are difficult since different experimental conditions are used for each catalytic system as we going to show (*vide infra*).

Mapolie *et al*. have reported funtionalized mesoporous silica (MCM-41) and amorphous silica with bis(*N, N'*-ethylenebis(salicylidenaminato)) metal (Cu^{2+}, Co^{2+}, Ni^{2+}) complexes [*N, N'*-ethylenebis(salicylidenaminato), sal]. The supported [Cu(sal)] acts as catalyst for hydroxylation of phenol using H_2O_2 as oxidant under a constant flow of oxygen (**Figure 2.30**).[126] For mesoporous silica and amorphous silica immobilizing Cu(II) complexes, they both shows activity towards hydroxylation of phenol, and when MCM-41 is used as sup-

port, a higher activity of phenol conversion than the amorphous silica is observed. The

Table 2.4 Catalytic activity of Cu(II)-containing solids reported in the literature.

Catalysis	T(°C)	pH [a]	phenol Conv.%	phenol: H_2O_2 [b]	Cat/HQ [c]	H_2O_2 Eff.% [d]	Tar sel [e,e'] %	Ref.
Cu(sal)_MCM-41 [f]	110	4	54.5	1:1	0.32	--	--	Mapolie *et al.*[126]
	110	5	66.0	1: 1	0.24	--	--	
	110	6	76.0	1: 1	0.32	--	--	
Cu(sal)_SiO_2 [f]	110	2	62.5	1: 1	1.23	--	--	Mapolie *et al.*[126]
	110	4	45.2	1: 1	1.12	--	--	
	110	5	40.0	1: 1	1.14	--	--	
	110	6	47.8	1: 1	1.32	--	--	
Cu-HMS [g]	80	H_2O	38.7	1: 1	1.9	--	--	Fu *et al.*[127]
CuSBA-15 [h]	60	H_2O	59.4	1: 2	2.71	46.7	--	Wang *et al.*[128]
CuMCM-41 [i]	80	H_2O	--	--	2.31	--	--	Sobczak *et al.*[129]
CuCMM [j]	70	H_2O	25.1	3: 1	0.66	75.4	--	He *et al.*[130]
	70	H_2O	28.5	1: 1	0.99	28.5	--	
CuNaY [k]	60	H_2O	50.3	1: 1	2.26	38.6 [e]	25.3	Lee *et al.*[131]
	50	H_2O	47.9	1: 1	2.30	35.5	29.7	
	50	H_2O	17.4	3: 1	2.77	60.2	9.9	
CuNiAl2-1 [l]	65	5	22.6	2: 1	1.8	45.2	--	Kannan *et al.*[132]
		5	40.3	1: 1	1.6	39.8	--	
CuCo31 [m]	65	5	22.1	2: 1	3.4	44.7	--	Kannan *et al.*[133]
		7	20.8	2: 1	4.5	41.6	--	
		9	0	2: 1	0	--	--	
CuAlCO3-HTLc [n]	60	7	53.5	1: 1	1.64	--	--	Wu *et al.*[134]
		5	25	1: 1	1.29	--	--	
		9	1.8	1: 1	2.03	--	--	
$Cu_2(OH)PO_4$ [o]	80	H_2O	28.3	3: 1	1.12	84.6 [e']	19.1	Xiao *et al.*[135]
	80	H_2O	48.5	1: 1	1.22	49.7	--	

a: buffer aqueous solution or water; **b**: CAT: catechol, HQ: hydroquinone, CAT:HQ molar ratio; **c**: phenol/H_2O_2 molar ratio; **d**: the efficiency conversion of H_2O_2 was calculated as follows: H_2O_2 eff.

conv.%=100 x H_2O_2 (mol) consumed in formation of diphenols and benzoquinone/H_2O_2 (mol) converted; **e**: tar selectivity %= [1- ($[CAT]_f$ +$[HQ]_f$ + $[BQ]_f$)/($[phenol]_i$ - $[phenol]_f$)] x 100 %, i: initial, f: final; [e'] The amount of tar was determined on product samples from which the catalyst was removed by filtration and the volatile products by evaporation in vacuo. **f**: [phenol]=0.22mol/L, 1 atm O_2; **g**: [phenol]=1mol/L, t : 4h; **h**: [phenol]=1mol/L, pH=7(water), phenol: Cu=448, t : 4h; **i**: phenol (13 g), H_2O (10 g), catalyst (0.2 g); **j**: [phenol]=0.7mol/L, phenol: Cu=653, t : 4h; **K**: [phenol]=0.15mol/L, t : 3h; **l**: [phenol]= 1.06mol/L, phenol: Cu=100, t : 2h; **m**: [phenol]=1.06mol/L, phenol: Cu=100, t : 2h; **n**: [phenol]=1.06mol/L, phenol: Cu=100, t: 1 h; **o**: [phenol: Cu]=22: 1, t: 4h.

product hydroquinone is preferred than catechol when MCM-41 was used as the support, which is attributed to the shape selectivity of the porous channel of MCM-41. However, these results are in contradiction with previous reports, for example, catechol was produced in higher selectivity than hydroquinone using the catalysts of CuSBA-15, CuMCM-41 and CuHMS where the Cu(II) ion is in the framework or extra framework.[127-129] They investigated pH effect on functionalized MCM-41 and amorphous silica. The highest conversion of phenol using functionalized MCM-41 with Cu(II) complex is 76.0 % at pH = 6 buffer solution, while for functionalized amorphous silica the highest conversion is 62.5%t at the pH=2 buffer solution (**Table 2.4**). The metal-salicylidenamine complexes grafted on MCM-41 lost their catalytic activity after first run. However, other important information, such as H_2O_2 efficient conversion and tar selectivity (or diphenols selectivity) can not be found in this paper. Furthermore, the metal coordination state is poorly characterized, such as the exact coordination stats of metals. In addition, we can not know whether these reaction processes are heterogeneous processes or homogeneous processes, since the reaction temperature is very high at 110 °C, which probably results in the decomposition of grafted complexes.

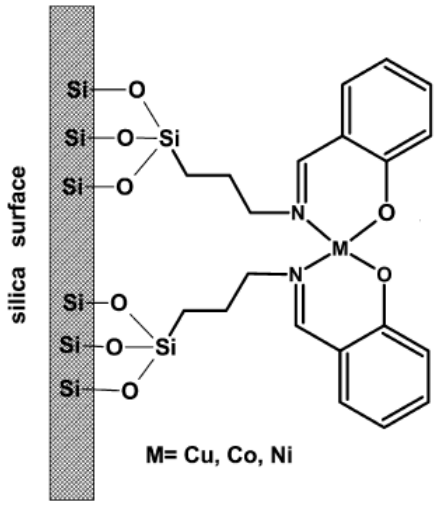

Figure 2.30 Synthetic route of the supported salicylaldimine complex [Cu(sal)].[126]

Copper oxide supported on porous silica, *i.e.*, CuSBA-15,[128] CuMCM-41,[129] CuHMS,[127] CuCMM,[130] CuNaY,[131], hydrotalcites containing Cu, *i.e.*, CuNiAl2-1,[132] CuCo31,[133] CuAlCO3-HTLc[134] and copper phosphate, *i.e.*, $Cu_2(OH)PO_4$,[135] have been used as catalysts for hydroxylation of phenol with H_2O_2. Catechol is produced in higher selectivity than hydroquinone, except over CuCMM. H_2O_2 concentration (phenol/H_2O_2 molar ratio) has a strong influence on phenol conversion. The suitable H_2O_2 addition is that phenol: H_2O_2 = 1 or 2 or 3. pH exhibit an significant influence on both phenol conversion and catechol/hydroquinone (Cat/HQ) molar ratio as reported by Wu *et al*. and Kannan *et al* (**Table 2.4**).[132-134] Generally, basic conditions are not favorable for hydroxylation of phenol, while the neutral or slight acid conditions have the positive effect on hydroxylation of phenol, which is related to the formation and stabilization of hydroxyl radical (OH·) in the reaction. The majority of these catalysts lost the activity after first run which is most probably due to the formation of tar. The activity can be recovered in a second run by regeneration of calcination.[135, 136] However, the activity of CuNaY and CuCMM can be maintained after the first run only by solvent washing and drying the catalyst after the reaction.

2.4.1.2 Cyanosilylation of aldehyde catalyzed by supported vanadyl

complexes

In the catalyst aspect, there are many approaches to optimize the catalyst in order to obtain the best catalytic activity. Here, we take the work of Baleizão *et al.* as example. They have studied the cyanosilylation reaction of aldehydes with trimethylsilyl cyanide (TMSCN) (**Figure 2.31**) over hybrid materials containing vanadyl(salen) complexes. In particular, the effects of support, hydrophobic/hydrophilic properties of the surface, chain length of tether, location of complexes, *i.e.*, in the channel (grafting, **Figure 2.32**)[14] or in the framework (one-pot synthesis, **Figure 2.24**) [119, 121], have been extensively investigated.

For functionalized hybrid materials with vanadyl complexes in the channel, *i.e.*, VOsalen@SiO_2, VOsalen@ITQ-2 and VOsalen@MCM-41, the synthesis has been performed through the reaction of grafted mercaptopropysilyl groups on the solids with a terminal carbon-carbon double bond pending alkyl chains of various lengths attached to the *para* position of the salen ligand (**Figure 2.32**).[14] However, when they were used as enantioselective catalysts for the aforementioned reaction lower ee values were found compared to solution. After variation of the tether length, the solvent and the silylation of the free silanol group, the optimized enantioselective catalyst was found to be the vanadyl salen complex anchoring the trimethylsilyl modified amorphous silica with the longest alkyl chain of the series (C_{11}). Under optimal conditions (CH_3Cl_3 as solvent and 0 °C) for the reaction of benzaldehyde (1.64 mmol) with trimethylsilyl cyanide (3 mmol) in the presence vanadium complex anchored on silica (100 mg, 0.04 mmol/g of vanadium), the enantiomeric excess was 85 %, slightly lower compared to the analogous complex (90 %). The heterogenised catalyst can be reused up to three times by simple filtration, retaining a large part of the activity of the fresh catalyst.

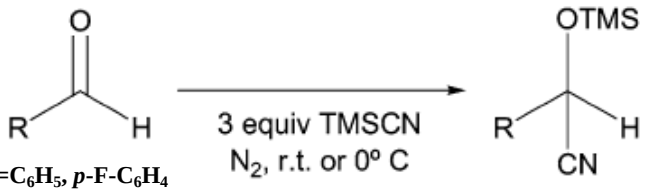

R=C_6H_5, *p*-F-C_6H_4
***p*-(CH_3O)-C_6H_4**
n-C_5H_{11}

Figure 2.31 Cyanosilylation reaction of aldehydes with TMSCN over hybrid materials containing vanadyl(salen) complexes.[14]

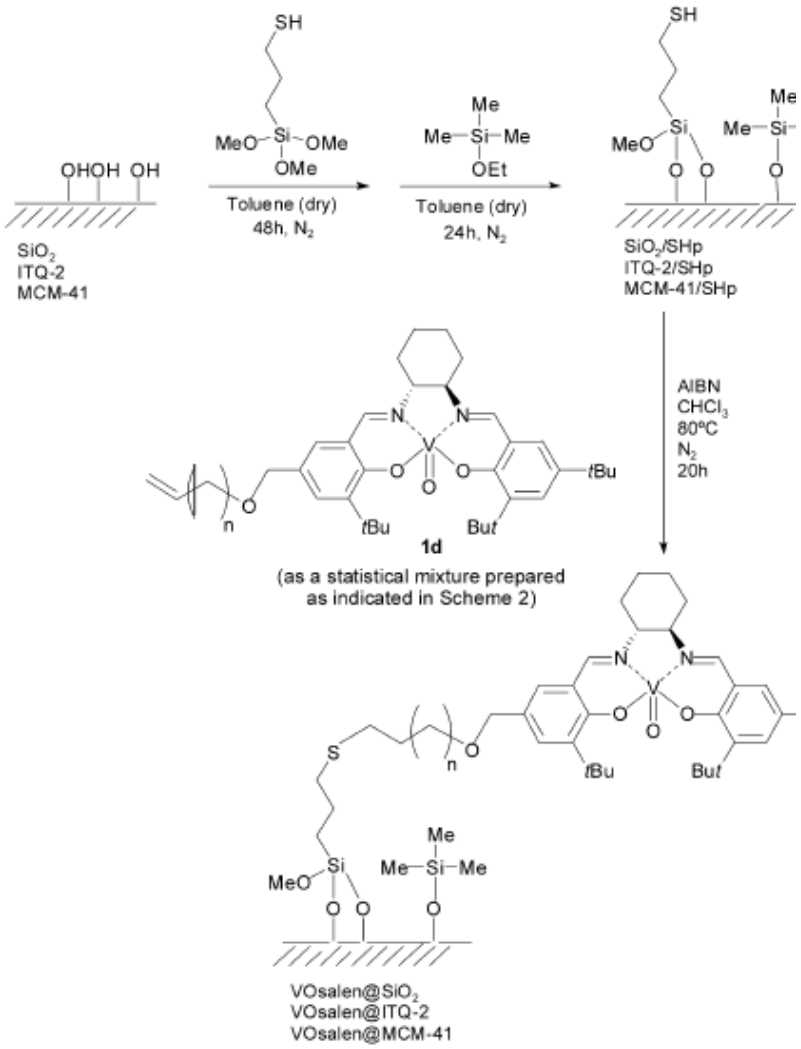

Figure 2.32 Preparation procedure for the covalent attachment of a chiral vanadyl-salen complex on amorphous silica, mesoporous silica and delaminated ITQ-2 zeolite.[14]

For functionalized hybrid material with complexes in the framework, *i.e.*, VO(salen)@ChiMO, it has been prepared through the co-condensation of chiral vanadyl(salen) complexes having two terminal trimethoxysilyl groups peripheral to the ligand and tetraethoxysilane (TEOS) in one-pot synthesis (**Figure 2.24**).[119] VO(salen)@ChiMO exhibited activity toward cyanosilylation of benzaldehyde with 30 % ee for the carbonyl addition, which is much lower than the homogenous analogue (90 % ee). However, in this case, the silylation of VO(salen)@ChiMO do not produce any positive effect on the enantioselectivity of the catalyst, that is a slightly decreased, which is contrast with the above study.[14]

2.4.2 Enzymatic reaction

In the biological systems, the transport, the stockage and the activation of molecules or some specific functions (O_2, C-C, C-H) are key living chemical process. They involve some particular sites of proteins containing usually a metal, which are named metallo-proteins. Their mode of action involves transition metals ions (Fe, Cu, Co, Ni and Mn), whose immediate environment condition their reactivity and become an intense research subject in coordination chemistry.[137] Catechol Oxidase is a copper metalloprotein involved in dioxygen storage and activation for oxidation processes.[137-140] It presents a type-3 copper active site,[141] consisting in a dicopper core in which each metal ion is chelated by three amino groups (provided by three histidines), water molecules, peroxo or oxo bridges depending on the oxidation state of copper.[142, 143] Basically, these sites contain distorted pentacoordinated copper environment. They have been extensively used as model to design homogeneous catalysts for oxidation.[144-146] The catalytic cycle proposed for oxidation of substrates consider two copper centers that are far apart in the reduced form, and then upon activation of dioxygen the metallic centers become closer thanks a peroxo brige.[139, 143]

The current models simulate this system mostly at the structural level and immediate vicinity of the metal which is the enzymatic pocket. However, the confinement effect of the enzymatic pocket is seldom considered in the biomimetic models. Mimicking the environment of the active site of a metalloenzyme is a research subject at the interface of coordination chemistry and materials science. Here, several examples of placing metal complexes on silica for mimicing catechol oxidase over oxidation of catechol are given.

Louloudi and co-workers have studied series of grafted biomimetic copper complexes on amorphous silica for mimicing the function of catechol oxidase.[147-151] They have reported a immobilized copper (II) monomer on silica that can exhibit activity for the oxidation of 3,5-di-*t*-butylquinone using of O_2 oxidant.[147] The biomimetic material consists on a Cu(histidine)$_2$ [histidine: Boc-His(Boc)-CONH-$(CH_2)_3Si(OEt)_3$] complex grafted on a silica matrix. It was synthesized through hydrolysis and co-condensation of the histine-ligand with tetraethoxysilane via a sol-gel procedure. The Cu(II) ion is coordinated to two inequivalent grafted ligands on the resulting hybrid material. The Cu(II) material exhibits catalyt-

ic activity for 3,5-di-*t*-butylquinone (DTBQ) formation in the presence of O_2.

The same research group has later synthesized the silicas grafted macrocyclic L_1 and L_2 ligands with 3N2O and 5N donor atoms *via* post-synthesis.[149] The organic ligands L_1, L_2 or grafted species $L_1{\cdot}SiO_2$ or $L_2{\cdot}SiO_2$ coordinated with Cu(II), leading to the formation of di-nuclear copper complexes $Cu_2(L_1)$, $Cu_2(L_2)$, $Cu_2(L_1){\cdot}SiO_2$ and $Cu_2(L_2){\cdot}SiO_2$ (**Figure 2.33**). The heterogenised $Cu_2(L_1){\cdot}SiO_2$ and $Cu_2(L_2){\cdot}SiO_2$ materials exhibited a higher conversion of 3,5-di-*t*-butylcatechol (DTBC) than the corresponding homogeneous copper(II) complexes $Cu_2(L_1)$ or $Cu_2(L_2)$, respectively. This result may be due to the positive contribution of support SiO_2.

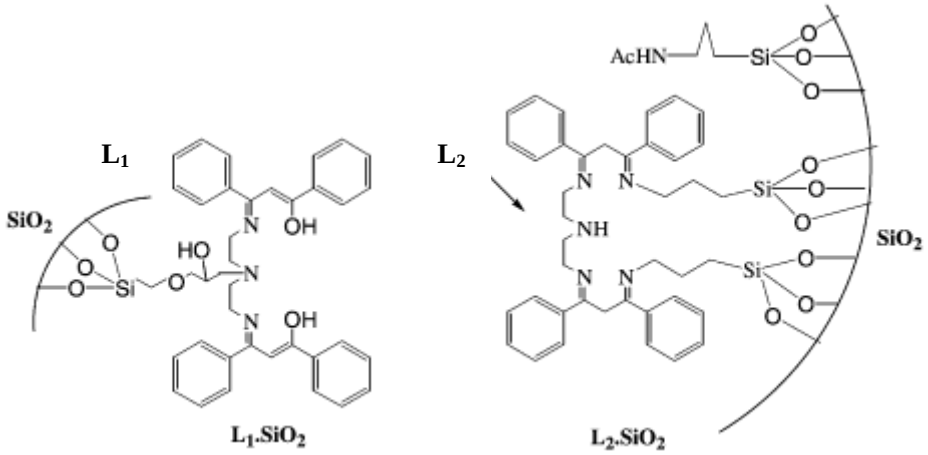

Figure 2.33 Structure of L_1 and L_2 ligand.[149]

Mou and co-workers have synthesized and characterized a hydroxo-bridged dinuclear phenanthroline cupric complex, $[(phen)_2Cu\text{-}OH\text{-}Cu(phen)_2](ClO_4)_3$ (HPC, phen=phenanthroline), dispersed in MCM-41 and sodium zeolite Y (**Figure 2.34**). They used spectroscopic techniques (FT-IR, UV-visible, EPR and EXAFS) to characterize and study the catalytic activities of immobilized HPC on the oxidation of DBTC to DBTQ to mimic the functionality of catechol oxidases. It was found that HPC complexes can adsorb only on the outside surface of the Y zeolite due to its smaller pore size. The EXAFS spectrum gave 3.51 Å for the Cu⋯Cu distance in HPC encapsulated in the nanochannels of Al-MCM-41 mesoporous solids, which is comparable to the O⋯O distance of two hydroxyl groups of DBTC, and this made a simultaneous coordination of the diol group to the dicupric center possible. The resulting complex then allows the transfer of two electrons from DTBC to the

dicupric center leading to the production of DTBQ, which is depicted in the reaction scheme (**Figure 2.34**). The nanochannels of calcined Al-MCM-41 mesoporous solids provide stability, due to confined space and surface charge, which could prevent excessive separation of the dinuclear cupric centers after removal of the hydroxo bridge during the catalytic process.

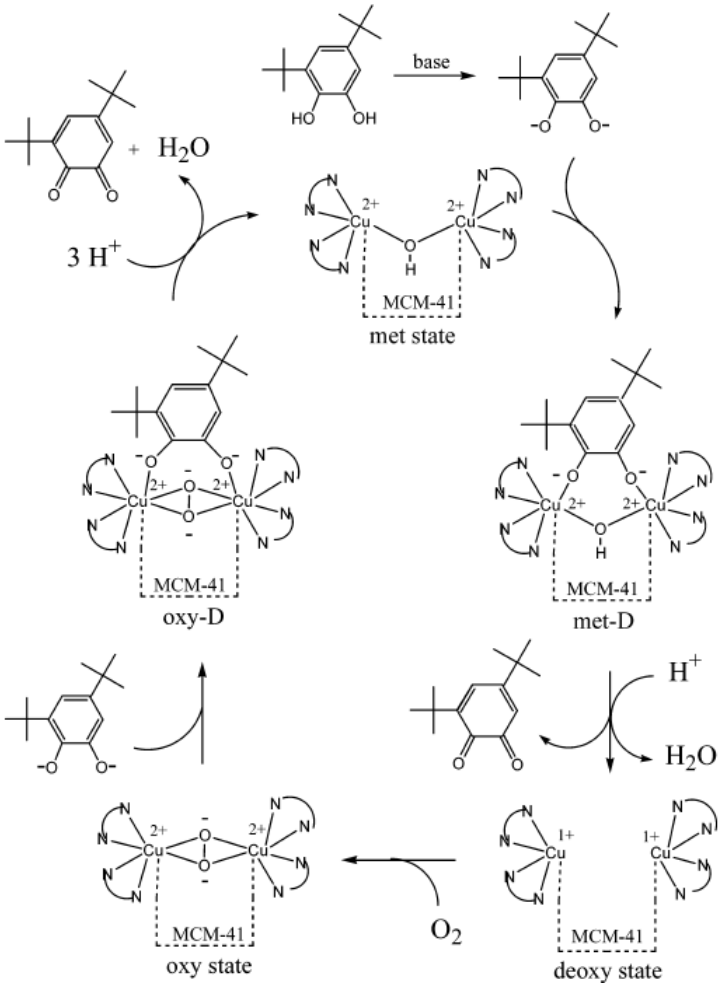

Figure 2.34 Catalytic cycle for oxidation of 3,5-di-*t*-butylcatechol in the presence of dioxygen by dinuclear copper complexes encapsulated in the nanochannels of MCM-41 mesoporous materials.[152]

2.4.3 Adsorption

Organic-inorganic mesoporous hybrid materials have been largely reported as sorbents to absorb toxic metal in water. There are few examples on functionalized mesoporous materials with metal complexes worked as sorbents.

MCM-41 grafted nickel(II) amino-complexes have been used as sorbents for the selective removal of a pharmaceutical drug (Naproxen) from water via single component adsorption equilibria measurements at ambient conditions. Preliminary performance tests showed that this type of material can adsorb at ppm level from aqueous solution. Furthermore, no metal leaching was found in this grafting strategy. DFT calculations suggest that the interaction between sorbate and sorbent generate a metal complex.

Yoshitake *et al*. have reported that Fe^{3+}, Co^{2+}, Ni^{2+} and Cu^{2+} fixed by diamino-funtionalized MCM-41 and MCM-48 can behavior as adsorption centers for arsenate ions.[31] Different metal-diamino complexes show different adsorption capacities towards arsenate. Fe^{3+} and Co^{2+} were superior to the other cations.

4.1 Strategy and choices of this work

Our objective is to develop novel strategies and methodologies on the synthesis of multifunctional catalysts using of mesostructured hybrid materials incorporating metal complexes. The goal is to learn how to control, hydrophobicity, metal accessibility and catalytic activity with the best molecular control as possible. Specifically, this thesis will investigate the potentiality of one-pot synthesis versus postsynthesis methodologies.

The one-pot synthesis will necessitate the use of metal complexes with at least two condensable alkoxysilane groups. These complexes will also be used in the postsynthesis route. Here, two different types of metal complexes have been chosen, one is a charged complex, *i.e*., a metal-polyamine complex, and the other is a neutral complex, *i.e*., a metal salicylaldimine complex, at least in the molecular state as shown in **Figure 2.35**. The former is rather hydrophilic, whilst, the latter is more hydrophobic due to the presence of aromatic rings. Thus, they will be expected to exhibit different properties when they were incorporated into mesoporous hybrid materials by one-pot synthesis. Furthermore, Ni(II)-$\mathbf{L^1}$ complex can be well characterized through UV-visible absorption bands. Cu(II)-$\mathbf{L^1}$ complex and Cu(II)-$\mathbf{L^2}$ complex are active in EPR spectra. Thus, these features are very useful to monitor the metal coordination state on the hybrid materials. In addition, Cu(II)-$\mathbf{L^2}$ complex are known to possess catalytic properties for oxidation reactions.

In addition, there are many synthesis approaches for the one-pot synthesized hybrid materials, but these approaches are usually using tetraalkyl orthosilicate (TEOS) as silica source and co-solvents (like methanol), which are expensive silica source and environmental unkindly solvent. In our synthesis condition, the sodium silicate solution will be considered as the silica source which is a very low coast source of silica and organic free. Cetyltrimethylammonium tosylate (CTATos) will be used as the surfactant instead of cetyltrimethylammonium halides since CTATos is also the cheapest cationic surfactant source commercially available.

Finally, phenol hydroxylation, which is one of the challenges in the industrial chemistry, specially to afford tunable selectivity between catechol and hydroquinone and diminish of byproducts such as tars, will be carried out using hybrid material incorporating Cu(II) -L^2 complex. Furthermore, tetradentate-Schiff base copper(II) complex [Cu(L^3)(CH_3COO)] (L^3: N-(salicylaldimine)-(N'-propyltrimethoxylsilane)-diethylenetriamine) with a 3N1O coordination sphere, which presents a higher affinity to Cu(II) than the bidentate L_2 with a 2x 1N1O type of coordination sphere, will be immobilized on mesoporous materials using the "molecular stencil patterning" technique. This type of material will be investigated in the catalytic hydroxylation of phenol.

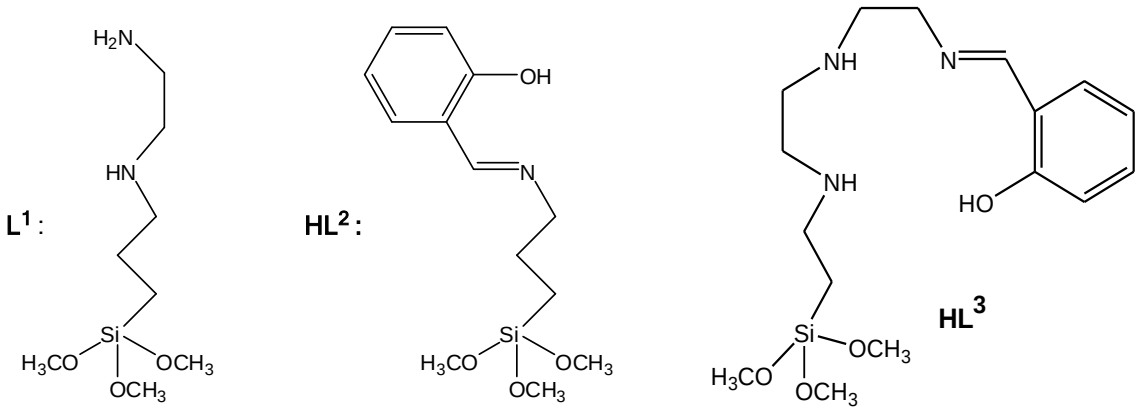

Figure 2.35 Three ligands (**L^1**, **HL^2** and **HL^3**) used in this thesis.

Chapter 3 Experimental part

3.1 Commercial products and treatment

3.1.1 Solvents

Solvents used in this dissertation are gathered in **Table 3.1**. They are used as received except cyclohexane and toluene. Cyclohexane and toluene were treated under agron atomosphere by adding 4 Å molecular sieves which were pretreated at 500 °C for absorbing the water traces of solvents.

Table 3.1 Solvents used in this dissertation.

Solvent	Purity	Provider
Toluene	>99,8%	SDS – CarloErba
Acetonitrile	>99,5%	SDS – CarloErba
Dichloromethane	>99,95%	SDS – CarloErba
Cyclohexane	>99%	SDS – CarloErba
Acetone	>99,8%	SDS – CarloErba
Technical ethanol	96%	Elvetec Services
Ethyl alcohol anhydrous (plus for HPLC	>99.5%	Carlo Erba
Absolute methanol	>99%	Carlo Erba
Petroleum ether		SDS – CarloErba
Ethyl acetate	>99%	SDS – CarloErba
Deionized water		Deionized by reverse osmosis

3.1.2 Reagents

The main reagents used are summarized in **Table 3.2**, where their source and purity is specified. They were used as received.

Table 3.2 Reagents used in this dissertation.

Product	Purity	Provider
Nickel (II) nitrate hexahydrate	99%	Acros
Copper (II) nitrate trihydrate	99%	Acros
Copper (II) acetate monohydrate	99%	Acros
Potassium thiocyanate	99 %	Sigma-Aldrich
Potassium phosphate monobasic	99 %	Acros
Di-sodium hydrogen phosphate (anhydrous)	>99 %	Merck
Sodium hydroxide	>99%	Acros
Tetramethylammonium hydroxide pentahydrate	≥ 95.0 %	Aldrich
Sulfuric acid	95 - 97 %	Fluka
Hydrochloric acid in water	1 N	Acros
Potassium iodide	99 %	Aldrich
Potassium dichromate	99 %	Avocado
Tetrabutylammonium hexafluorophosphate	puriss	Fluka
Polystyrene (average molar mass: 250 000)	puriss	Acros
Iotect	99 %	Prolabo
Ludox HS-40	40% SiO_2	Aldrich
Cetyltrimethylammonium tosylate	> 99%	Merck
N-propylethylenediamine	99%	Acros
Ethylenediamine	99%	Aldrich
Triethylamine	≥ 99 %	Sigma-Aldrich
N'-isopropyldiethylenetriamine, techinque	75 %,	Aldrich
3-aminopropyl-trimethoxysilane	95 %	Acros
N-(2-aminoethyl)-3-aminopropyltriymethoxysilane	97%	Acros
Chlorotrimethylsilane	98%	Acros
Hexamethyldisilazane	98%	Acros
Hexamethyldisiloxane	98%	Acros
Sodium *p*-toluenesulfinate	95%	Aldrich

Salicylaldehyde	98 %	Avocado
Phenol	≥ 99 %	Sigma-Aldrich
Catechol	99 + %	Acros
Hydroquinone	≥ 99 %	Fluka
1,4-benzoquinone	> 99.5 %	Fluka
3,5-di-*t*-butylcatechol	99%	Acros
3,5-di-*t*-butylquinone	98%	Acros
Naphthalene	99%	Aldrich
Hydrogen peroxide (H_2O_2) solution in water	50 wt %	Aldrich

3.1.3 Gas

The specifications of the gas used are collected in **Table 3.3**.

Table 3.3 Gas used in this dissertation.

Gas	Quality	Provider	Utilization	Treatment
Argon	α	Air Liquid	Protection gas for synthesis	Cartridge filtration multifonctions: dehydration, deoxygenation, dehydrocarbon
Nitrogen	U	Air Liquid	Working gas for TGA	No
Air	Industrial	Air Liquid	Working gas for TGA	No

3.2 Glossary of the nomenclature

Abbreviation of names and nomenclature of samples used in this dissertation are respectively presented in **Table 3.4** and

Table 3.5.

Table 3.4 Abbreviation of names used in this dissertation.

Abbreviation	Full name
PMOs	Periodic mesoporous organosilicas
TMS	Trimethylsilyl
CTATos	Cetyltrimethylammonium tosylate
Pren	*N*-propylethylenediamine
en	Ethylenediamine
L^1	N-(2-aminoethyl)-3-aminopropyltriymethoxysilane
L^2	N-salicylaldimine-propylamine-trimethoxysilane
L^3	N-(salicylaldimine)-(N'-propyltrimethoxylsil ane)-diethylenetriamine
L^3_{ref}	N-(salicylaldimine)-(N'-isopropyl)-diethylenetriamine
CTMS	Chlorotrimethylsilane
HMDSA	Hexamethyldisilazane
HMDSO	Hexamethyldisiloxane
TMAOH	Tetramethylammonium hydroxide
MSP	Molecular stencil patterning
DTBC	3,5-di-*t*-butylcatechol
DTBQ	3,5-di-*t*-butylquinone
CAT	Catechol
HQ	Hydroquinone
BQ	1,4-benzoquinone

Table 3.5 Nomenclature of samples in this dissertation.

Nomenclature	Reaction or remark
M-	Modified Laval University Silica, MCM-41 type, synthesized at 60 ºC
M1'-, M2'-	Normal Laval University Silica, synthesized at 130 ºC, number corresponding to the number of the synthesis
-OP	Prepared according to the one-pot synthesis
-X	Initial metal/SiO_2 * 100 % (mol/mol) percent in sol-gel
-Y	Initial Ligand/ metal molar ratio in sol-gel
-H	Use 1 of eq. HCl (1 mol·L^{-1}) (HCl / CTATos = 1) to extract the template (CTATos)
-2H	Use 2 of eq. HCl (1 mol·L^{-1}) (HCl / CTATos = 2) to extract the template (CTATos)
-TA	Template extraction method using a mixture of CTMS and HMDSA with simultaneous capping by trimethylsilyl (TMS)
-TO	Template extraction method using a mixture of CTMS and HMDSO with simultaneous capping by TMS
-HTA	Template extraction method using HCl and then a mixture of CTMS and HMDSA to extract remaining template and simultaneously cap by TMS
-T	Template extraction method using CTMS with simultaneous capping by TMS
-EP	Partial extraction of the template

-EPS	Partial trimethylsilylation by HMDSA on the partial template-containing materials
-ES	HCl extraction of template in partial by silylated materials
-neu	Basic neutralization using TMAOH
-SCN	Use of KSCN to test a coordination vacancy to the grafted metal complex on the solids
-CuN	Wash using TMAOH, and then complexed using $Cu(NO_3)_2$
-CuNH	Wash using TMAOH, then neutralize HCl, finally complex using $Cu(NO_3)_2$

Three examples of nomenclature:

1) M-OP-0.3Ni($2L^1$)

Mesoporous material synthesized in the presence of Ni(II) complex (L^1/Ni = Y = 2 and Ni/SiO_2 = **X** = 0.3 % in sol -gel) according to the one-pot synthesis at 60 ºC.

2) M-OP-0.3Ni($2L^1$)-TA

As-made M-OP-0.3Ni($2L^1$) sample after template extraction using a mixture of CTMS and HDMSA.

3) M-OP-0.3Ni($2L^1$)-H

As-made M-OP-0.3Ni($2L^1$) sample after template extraction using 1 of eq. HCl (HCl / CTATos = 1).

3.3 Experimental part

3.3.1 Synthesis of Ni(II) complexes

- Synthesis of Ni(II)-Pren complexes with various Pren/Ni (Y = 1-18) molar ratios in aqueous solution

Nickel (II) nitrate hexahydrate (0.1215g, 0.41 mmol) was dissolved in aqueous solution (30 mL). Then, *N*-propylethylenediamine (Pren) (0.052 mL, 0.104 mL, 0.156 mL, 0.208 mL, 0.312 mL, 0.468 mL, 0.936 mL, Pren/Ni = 1, 2, 3, 4, 6, 9, 18, respectively) was dropwise added. The resulting solution was stirred at room temperature. Colored solutions of **1-Pren** (green), **2-Pren** (blue), **3-Pren** (light violet), **4-Pren** (violet), **6-Pren** (violet), **9-Pren** (violet) and **18-Pren** (violet) were formed, respectively.

- Synthesis of Ni(II)-en complexes with various en/Ni (Y =1 - 4) molar ratios in aqueous solution

Ni(II)-**en** complexes were synthesized using the same procedure as described for Ni(II)-**Pren** complexes. Colored solutions of **1-en** (green), **2-en** (blue), **3-en** (violet) and **4-en** (violet) were formed.

- Synthesis of Ni(II)-L^1 complexes with various L^1/Ni (Y =1-18) molar ratios in aqueous solution

Ni(II)-**L^1** complexes were synthesized using the same procedure as described for Ni(II)-Pren complexes. Colored solutions of **1-L^1** (green), **2-L^1** (blue), **3-L^1** (light violet), **4-L^1** (violet), **6-L^1** (violet), **9-L^1** (violet) and **18-L^1** (violet) were formed.

- Synthesis of $Ni(Pren)_2(C_7H_7SO_2)_2$, complex 1

N-propylethylenediamine (Pren) (0.16 mL, 3 eq) was added into the aqueous solution (8 mL) of nickel (II) nitrate hexahydrate (0.1215g, 0.41 mmol), and then an aqueous solution (4 mL) of sodium *p*-toluenesulfinate (0.15 g, 2 eq) was added. After 2 days, blue crystals of **complex 1** were produced by slow evaporation of solvent.

- Synthesis of $Ni(Pren)_2(NO_3)_2$, complex 2, and $Ni(Pren)_3(NO_3)_2$, complex 3

Nickel (II) nitrate hexahydrate (0.1215g, 0.41 mmol) was dissolved in anhydrous ethanol (5 mL). Then, *N*-propylethylenediamine (Pren) (0.104 mL, 0.156 mL, Pren/Ni = 2, 3, respectively) was dropwise added and stirred at room temperature. Blue crystals of **complex 2** precipitated in 2 days. Violet crystals of **complex 3** precipitated in one week.

3.3.2 Synthesis of Cu(II)-L (L = L^2, L^3) complexes

3.3.2.1 Synthesis of L^2

A closed two necked flask with a condenser was vacuumed in room temperature and then filled with argon. The same procedure was repeated for three times. Salicylaldehyde (0.57 mL, 5 mmol) and ethyl alcohol anhydrous (22 mL) was introduced in the flask. 3-aminopropyl-trimethoxysilane (0.90 mL, 5 mmol) was then dropwise added. The resulting mixture was stirred under reflux for 6 h in the argon atmosphere. The obtained yellow

product was checked by ^{1}H NMR spectra.

3.3.2.2 Synthesis of HL^{3}_{ref} and HL^{3}

A closed two necked flask with a condenser was firstly vacuumed at room temperature and then filled with argon. The same procedure was repeated for three times. Salicylaldehyde (1.09 mL, 10 mmol or 0.11 mL, 1 mmol) and absolute ethanol (50 mL) were respectively injected in the flask. Then, (3-trimethoxylsilylpropyl)-diethylenetriamine (2.71 mL, 10 mmol) or N'- isopropyldiethylenetriamine (0.22 mL, 1 mmol) was dropwise introduced in the flask. The mixture was stirred under reflux for 6 h in the argon atmosphere. The obtained yellow products were vacuumed and washed with a mixture solvent of petroleum ether and ethyl acetate (7: 2) and then vacuumed. The final products **HL^{3}** and **HL^{3}_{ref}** were analyzed by measuring their ^{1}H NMR spectra.

^{1}H NMR data:

L	**H**C=N	Aromatic proton		-NHCH2CH2NHCH2CH2N=				Propyl protons			Ethoxy protons	
				N**H**	NHC**H**$_2$	CH$_2$NH	C**H**N=					
						C**H**$_2$						
L^2	8.40	7.28-7.35	6.89-7.03					3.63	1.81-1.93	0.72-0.81	3.63	1. 62–1. 34
L^3_{ref}	8.29	7.29-7.40	6.93-7.02		2.94-3.04	3.62	3.62	1.15	4.0			
L^3	8.28	7.25-7.36	6.80-7.00	2.24	2.66	2.96	3.43	0.58	1.57	2.61	1.18-1.37	3.63-3.71

3.3.2.3 Synthesis of $[Cu(L^2)]^+$ and $[Cu(L^2)_2]$ complexes

The above mixture was evaporated at 40 ºC through vacuum, and was reduced to 10 mL. The flask was then equipped with a constant funnel. An ethanolic solution (40 mL) of copper acetate monohydrate (0.476 g, 2.4 mmol or 0.952 g, 4.8 mmol) was dropwise added through the constant funnel into the flask. The mixture was stirred under reflux for 2 h under argon atmosphere. Then **1-L^2** and **2-L^2** (**Y** = **L^2**/Cu = 1 and 2, respectively) complexes were formed in the ethanolic solution (48.5 mL).

3.3.2.4 Synthesis of [Cu(L^3_{ref})(OAc)] and [Cu(L^3)(OAc)]

An ethanolic solution (10 mL) of **HL^3** (0.308 g, 0.73 mmol) or **HL^3_{ref}** (0.199 g, 0.81 mmol) was added in a flask. Then, copper acetate monohydrate (0.15 g, 0.74 mmol or 0.17 g, 0.81 mmol) in absolute ethanol (15 mL, 10 mL) was dropwise added in the flask. The resulting mixture was stirred under reflux for 2 h in the argon atmosphere. Dark blue solutions containing **Cu(L^3)(CH_3COO)** and **Cu(L^3_{ref})(CH_3COO)** complexes were formed.

3.3.3 One-pot synthesis of mesoporous hybrid materials

The sodium silicate solution was prepared as follows: Ludox (187 mL) was added to sodium hydroxide (32 g) in deionised water (800 mL) and stirred at 40 ºC until clear.

3.3.3.1 Synthesis of M-OP-XNi(YL^1) and M-OP-XCu(YL^1) [Ni(YL^1)@PMOs, Cu(YL^1)@PMOs]

A sodium silicate solution (40 mL) was stirred at 60 ºC for 1 h. A second solution of cetyltrimethylammonium tosylate (CTATos, 1.8 g) in deionised water (50 mL) was stirred during 1 h at 60 ºC. A solution of metal complex ($Ni(NO_3)_2$, 0.24 mg; $Cu(NO_3)_2$, 0.25 mg; **X** = Metal/SiO_2*100 % = 1 %, **Y** = Ligand/metal) in deionized water (8 mL) was added to the first solution, stirring until homogeneous. The resulting solution was dropwise added to the second one during 20 minutes. The sol-gel formed, was stirred at 60 ºC for 24 h. After filtration and washing with deionised water (200-300 mL), the as-made solids were dried at 60 ºC for 2 days. M-OP-XNi(YL^1) (X = 1, Y = 1, 2, 3 and X = 0.3, Y = 2) and M-OP-XCu(YL^1) (X = 1, Y = 1, 3) were obtained.

3.3.3.2 Synthesis of M-OP-XCu(YL^2) [Cu(YL^2)@PMOs]

A sodium silicate solution (40 mL) was stirred at 60 ºC for 1 h. A second solution of hexadecyltrimethylammonium *p*-tolunensulfonate (CTATos, 1.8 g) in deionised water (50 mL) was stirred during 1 h at 60 ºC. An ethanolic solution of 1.8 mL (n_{Cu} = 0.09 mmol), 3 mL (n_{Cu} = 0.15 mmol) or 8.5 mL (n_{Cu} = 0.42 mmol) Cu(II)-**L^2** complex (**Y** = Ligand/metal = 2)

was respectively added to the first solution, stirring until homogeneous. The resulting solution was dropwise added to the second one during 20 minutes. The sol-gel formed was stirred at 60 ºC for 24 h. After filtration and washing with deionised water (200-300 mL), the as-made solids were dried at 60 ºC for 2 days. M-OP-0.1Cu($2L^2$), M-OP-0.3Cu($2L^2$) and M-OP-0.5Cu($2L^2$) samples were respectively obtained.

3.3.4 One-pot synthesis of metal-free material (M)

Mesoporous silica (**M)** with metal-free was prepared in the same composition molar ratio and conditions as the hybrid materials except the addition of a complex. Therefore, **M** was prepared as follows: a sodium silicate solution (40 mL) was stirred at 60 ºC for 1 h. A second solution of cetyltrimethylammonium tosylate (CTATos, 1.21 g) in deionised water (60 mL) was stirred at 60 ºC for 1 h. Then, the first solution was dropwise added to the second one during 30 minutes. The resulting sol-gel was heated in the closed flask at 60 ºC for 24 h. After filtration and washing with deionised water (approximately 180 mL), the as-made solid was dried at 80 ºC for 18 h.

3.3.5 Template (surfactant) extraction

3.3.5.1 Method TA

The solid (1.0 g) was first dried at 40 ºC under argon flow for one hour, and then vacuumized at 40 ºC for one supplementary hour. Toluene (40 mL) was added; the mixture was stirred until homogeneous at room temperature. Then, HMDSA (1.98 mL, 9.50 mmol) and CTMS (1.20 mL, 9.10 mmol; n_{HMDSA}: n_{CTMS}: $n_{sufactant}$=6: 6: 1) were added. This mixture was stirred for 2 h at 60 ºC. After filtration the solid was finally washed with toluene (10 mL x 2), ethanol (10 mL x 2) and acetone (10 mL x 2), and dried at 60 ºC. The obtained materials are M-OP-XNi(YL^1)-TA (X = 1, Y = 1, 2, 3 and X = 0.3, Y = 2), M-OP-XCu(YL^1)-TA (X = 1, Y = 1, 3) and M-OP-XCu(YL^2)-TA (X = 0.1, 0.2 and 0.5, Y = 2).

3.3.5.2 Method T

Only CTMS was used to remove the surfactant of solid (0.50 g), in a molar ratio of TMSCl: Surfactant = 1. Other procedure is similar to the method TA. The obtained material is M-OP-XNi(YL^1)-T (X = 1, Y = 3).

3.3.5.3 Method TO

A mixture of two silanes was used, HMDSO and CTMS, to remove the surfactant of as made solid (0.15 g), in a molar ratio equal of TMSCl: HMDSO: surfactant = 36: 36: 1. The procedure is similar to the method TA. The obtained material is M-OP-XNi(YL^1)-TO (X = 1, Y = 3).

3.3.5.4 Method H

The solid (0.4 g) was added into a flask with a condenser. Then technical ethanol (25 mol) and HCl (1mol·L^{-1}, 0.54 mL, HCl: surfactant = 1:1) were respectively added. The mixture was stirred at 40 ºC for 1 h. After filtration and washing with technical ethanol (50 mL x 4) and acetone (50 mL x 2), the solids were dried at 60 ºC for 1 day. The obtained materials are M-OP-XNi(YL^1)-H (X = 0.3, Y = 2), M-OP-XCu(YL^1)-H (X = 1, Y = 3) and M-OP-XCu(YL^2)-H (X = 0.1, 0.2 and 0.5, Y = 2).

3.3.6 Post-synthesis of hybrid materials (“MSP” technique)

3.3.6.1 Synthesis of M’ (at high temperature, *i.e.* 130 °C)

A classical LUS was prepared in the same way as **M** except that the autoclave process was performed at 130 ºC, obtaining M’.[51, 153]

3.3.6.2 Partial surfactant extraction of M’

M’ (10 g) was placed in a round flask, and then ethanol (400 mL, 96%) and hydrochloric acid 1 mol L^{-1} (6.8 mL, 0.5 eq) were added. The mixture was stirred at 40 ºC for 1 h. After filtration and washing with ethanol (100 mL x 2) and acetone (50 mL x

2) the solid was dried at 80 ºC for 20 h. Material M'-EP (7.1 g) was obtained.

3.3.6.3 Partial silylation of M'-EP

M'-EP (6.8 g) was added into a round bottom three-neck flask, and then dried at 130 ºC for 1 h under argon flow and during 2 h under vacuum. Cyclohexane (170 mL) and HMDSA (30 mL, 30 eq.) were added under argon. The mixture was refluxed for 18 h. The obtained solid was finally washed with cyclohexane (2 x 30 mL), ethanol (2 x 60 mL) and acetone (2 x 60 mL), and then dried at 80 ºC for 18 h. This sequence of steps was repeated twice. Partially silylated material M'-EPS (7.1 g) was obtained.

3.3.6.4 Extraction of remaining surfactant of M'-EPS

M'-EPS (2 g) was placed in a round flask, and then ethanol (86 mL, 96%) and hydrochloric acid (1.28 mL, 1 eq, 1 mol/L) were added. The mixture was stirred at 0 ºC for 1 h. After filtration and washing with ethanol (50 mL) and acetone (50 mL) the obtained solid was dried at 80 ºC for 20 h. The same procedure was repeated again. Finally, material M'-ES (1.4 g) was obtained.

3.3.6.5 Grafting complex onto M'-EPS

M'-ES (0.5 g) was dried at 130 ºC under argon flow during 1 h, and then vacuumized at 130 ºC during 2 h. A solution of metal complex (0.028 mmol of $Ni(NO_3)_2$ in Ni-L^1 complexes, 0.029 mmol of $Cu(NO_3)_2$ in Cu-L^1 complexes, 0.74 mmol of $Cu(OAc)_2$ in Cu-L^3 complexes, Y = L/metal = 1, 2, or 3) in 2 mL anhydrous ethanol was added together with 40 mL of toluene into the flask. The resulting mixture was stirred at 60 ºC for 18 h under argon. The obtained solids were finally washed with toluene (50 mL) and ethanol (25 mL), and then dried at 60 ºC. M1'-ES-Ni(YL^1) (Y = 2, 3), M1'-ES-Cu(YL^1) (Y = 2) and M2'-ES-Cu(L^3) were obtained.

3.3.7 Metal exchange

3.3.7.1 Metal exchange 1

M-OP-Ni(3L^1)-TA (0.08 g) was placed in a round flask, then ethanol (5 mL) and TMAOH (3 mL, 0.1 M) were added. The mixture was stirred at 0 ºC for 30 minutes and filtered. The resulting solid was washed with abundant ethanol until neutralization of the filtered solution. The solid was then treated with an ethanolic solution (10 mL) of copper (II) nitrate (0.08 g, 10 eq, n_{Cu}: n_{Ni}=10). The mixture was stirred at 0 ºC for 5 h. After filtration, the obtained solid was finally washed with ethanol (200 mL) and dried at 60 ºC for 12, obtaining material M-OP-Ni(3L^1)-TA-CuN. For M-OP-Ni(L^1)-TA and M-OP-Ni(2L^1)-TA the treatment with TMAOH was not performed; after reaction with the copper nitrate solution, the solids M-OP-Ni(L^1)-TA-CuN (0.07 g) and M-OP-Ni(2L^1)-TA-CuN (0.07 g) were respectively obtained.

3.3.7.2 Metal exchange 2

M-OP-Ni(3L^1)-TA (0.10 g) was placed in a round flask, then ethanol (5 ml) and HCl (10 eq, n_{HCl}: $2n_N$= 10) were added obtaining a solution of pH 1.02. The mixture was then stirred at 0 ºC for 30 minutes and filtered. The resulting solid was washed with ethanol (100 ml). Then this solid was treated with an ethanolic (10 ml) solution of TMAOH (0.1 M, 12 eq, n_{TMAOH}: $2n_N$= 12), the final pH is 13. The mixture was stirred at 0 ºC for 30 minutes, then washed with ethanol for several times until that the filtrated solution is neutral. The solid was then treated with an ethanolic solution (10 mL) of copper (II) nitrate (0.10 g, 10 eq, n_{Cu}: n_{Ni}=10). The mixture was stirred at 0 ºC for 5 h. After filtration, the obtained solid was finally washed with ethanol (200 mL) and dried at 60 ºC for 12 h. The M-OP-Ni(3L^1)-TA-CuNH (0.06 g) solid was finally obtained.

3.3.7.3 Metal exchange 3

i) decomplexation: M1'-ES-Ni(2L^1) (0.09 g) was placed in a round flask, then ethanol (5 mL) and HCl (0.32 mL, 1 mol L^{-1}) were added. The mixture was then stirred at 0 ºC for 1 h. The obtained solid was washed with ethanol (200 mL) and dried at 60 ºC for 12 h, obtaining the M1'-ES-Ni(2L^1)-H (0.06 g) material.

ii) neutralization: M1'-ES-Ni($2L^1$)-H (0.6 g) was treated with TMAOH (1.6 mL, 0.1N) in ethanol (10 mL) at 0 ºC for 1 h. The obtained solid was washed with ethanol (200 mL) and dried at 60 ºC for 12 h, obtaining the M1'-ES-Ni($2L^1$)-neu (0.06 g) material.

iii) complexation with Cu(II): M1'-ES-Ni($2L^1$)-neu (0.3 g) in ethanol (8 mL) was reacted with $Cu(NO_3)_2 \cdot H_2O$ (0.2 g) and stirred at 0 ºC for 1 h 30. The final solid was washed with ethanol (200 mL) and then dried at 60 ºC for 12 h, obtaining M1'-ES-Ni($2L^1$)-HCu (0.37 g).

3.3.7.4 Metal exchange 4

M1'-ES-Ni($2L^1$) (0.08 g) was placed in a round flask, and then an ethanolic solution (10 mL) of $Cu(NO_3)_2 \cdot H_2O$ (0.08 g, 10 eq, n_{Cu}: n_{Ni}=10) was added. The mixture was stirred at 0 ºC for 5 h and then filtered. The obtained solid was finally washed with ethanol (200 mL) and dried at 60 ºC for 12 h. Material M1'-ES-Ni($2L^1$)-CuN (0.04 g) was obtained.

3.3.8 Metal displacement

3.3.8.1 Metal displacement 1

Solid (0.10 g, M-OP-Cu(YL^1)-TA, M-OP-XCu(YL^2)-H) was placed in a round flask, then ethanol (5 mL) and HCl (1 $mol \cdot L^{-1}$, HCl/Ligand = 1) were added. The mixture was then stirred at 40 ºC for 1 h and filtered. The resulting solid was washed with ethanol (200 mL) and dried at 60 ºC for 12 h. The final solids, M-OP-Cu(YL^1)-HH (Y = 3) and M-OP-XCu(YL^2)-HH (X = 0.1, 0.2 and 0.5, Y = 2), were obtained.

3.3.8.2 Metal displacement 2

M-OP-XCu(YL^2) (0.04 g) was placed in a round flask, then technical ethanol (5 mL) and HCl (1 $mol \cdot L^{-1}$, 2 eq, HCl: surfactant = 2) were added. The mixture was then stirred at 40 ºC for 1 h, then filtered, washed with abundant ethanol, and dried at 60 ºC. The final solids M-OP-XCu(YL^2)-2H (X = 0.1, 0.2 and 0.5, Y = 2) were obtained.

3.3.9 Catalytic tests

3.3.9.1 Oxidation of DTBC

The activity of catalysts was tested on the oxidation of 3,5-di-*t*-butylcatechol (DTBC). In a typical reaction, catalyst (0.0088 mmol of Cu, M-OP-Cu(YL^1) or M1'-ES-Cu(YL^1)) was added into a mixture of acetonitrile solution (2 mL) of DTBC (0.1 mol·L^{-1}, 0.2 mmol) and naphthalene (0.1 mol·L^{-1}, 0.2 mmol, internal standard) and triethylamine (5 μL). The mixture was stirred at room temperature under open air for 6 h, and aliquots were taken during the reaction and analyzed by GC. The yield of products was estimated from the peak areas based on the internal standard technical.

3.3.9.2 Hydroxylation of phenol

Phenol hydroxylation experiments were run in a 50 mL two necked flask with a condenser. In a standard run, phenol (0.1g, 1.1 mmol), catalyst [Cu: phenol = 1:100, M-OP-XCu(YL^2) or M2'-ES-Cu(L^3)] and buffer solution (7 mL) and H_2O_2 (50 % aqueous) were orderly added. The reaction was taken at 80 ºC for 2 h. The phenol and the products catechol (CAT), hydroquinone (HQ) and 1, 4-benzoquinone (BQ) were analyzed by HPLC. H_2O_2 conversion was determined by the following methods:

1) The H_2O_2 conversion was determined by iodometry method.
2) The efficiency conversion of H_2O_2 was calculated as follows: H_2O_2 eff. conv.=100 x H_2O_2 (mol) consumed in formation of diphenols and benzoquinone/H_2O_2 (mol) converted.

3.3.10 Preparation of phosphate buffer solution

pH = 7. 0.68 g of KH_2PO_4 and 40 mL of 0.1 mol/L NaOH were introduced in a 100 mL volumetric flask. Distilled water was added until a total volume of 100 mL. [KH_2PO_4] = 0.05 mol/L

pH = 6. 2.085 g of KH_2PO_4 and 0.353 g of Na_2HPO_4 were introduced in a 250 mL volumetric flask. Distilled water was added until a total volume of 250 mL. [KH_2PO_4] = 0.06

mol/L

pH = 5. 0.2 mol/L of NaOH was added into 100 mL of KH_2PO_4 (0.2 mol/L). Distilled eater was added to adjust the pH until 5 controlled by pH-meter.

3.4 Analytical Techniques

Single-crystal X-ray: Single-crystal X-ray study of **complex 1** was carried out using a Nonius KappaCCD and the related analysis software.[154] No absorption correction was applied to the data sets. The structure has been solved by direct methods using the SIR97 program[155] combined with Fourier difference syntheses and refined against *F* using reflections with [$I/\sigma(I) > 3$] with the CRYSTALS program.[156] All atomic displacements parameters for non-hydrogen atoms have been refined with anisotropic terms. The hydrogen atoms were theoretically located on the basis of the conformation of the supporting atom or found by Fourier Difference.

XRD: low angle X-ray powder diffraction experiments have been carried out using a Bruker (Siemens) D5005 diffractometer using Cu Kα monochromatic radiation.

IR: infrared spectra were recorded from KBr pellets using a Mattson 3000 IRTF spectrometer.

UV-visible spectroscopy: liquid UV-visible spectra were recorded using a Vector 550 Bruker spectrometer; solid diffuse reflectance UV-visible spectra were recorded from aluminium cells with Suprasil 300 quartz windows, using a PerkinElmer Lambda 950 and PE Winlab software.

Nitrogen sorption isotherms at 77 K were determined with a volume device Micromeritics ASAP 2010M on solids that were dried at 80 ^{o}C under vacuum overnight.

TGA measurements were collected from Al_2O_3 crucibles on a DTA-TG Netzsch STA 409 PC/PG instrument, under air (30 mL/min), with a 25-1000 ºC (10 ºC /min) temperature increase.

pH-meter (Meterlab pHM210) was calibraded in aqueous solultion, so that the pH measured for the EtOH-H_2O is only indicative.

EPR spectra were recorded using a Brucker Elexsys e500 X-band (9.4 GHz) spectrometer with a standard cavity. Quantification of Cu(II) species was performed using crystals of $CuSO_4.5H_2O$ as calibration reference.

TEM Imaging and analytical studies were performed on a JEOL 2010F microscope equipped with a field emission gun and operating at 200 kV. EDX (Energy Dispersive X-ray analysis) was performed thanks to a dispersive X-ray system (INCA-Oxford equipment) with a detector owing a polymer ultra-thin window.

^{1}H NMR spectra were recorded on a Bruker Avance 300 NMR spectrometer.

Electrochemical measurements Cyclic voltammetry of Cu(II) precursor [**Cu(2L^1)**] and one-pot synthesized material [**M-OP-Cu(3L^1)-TA**] and grafting material [**(M'-PS-Cu(2L^1)**] was performed with a CH Instruments 600B potentiostat in a three-electrode cell. The working electrode was prepared by taking a 1: 1 weight ratio of complex precursors or hybrid materials and fine graphite and dispersed in 1 mL of water, which was ultrasonicated for 10 min. Several aliquots of this dispersion and added 5 µL of 5 % polystyrene were coated on platinum disk (1 mm diameter). A platinum wire was used as the auxiliary electrode, and an $AgNO_3$|Ag electrode was used as the reference. This latter was checked vs. ferrocene as recommended by IUPAC ($E^{Ø}_{Fe}$ = 0.100 V). The electrolyte was a solution of tetrabutylammonium hexafluorophosphate (TBAP, 0.1 M) in CH_2Cl_2, and the scan rate was 0.4 $V \cdot s^{-1}$. Solutions were deaerated by argon bubbling for 10 min prior to each sequence of measurements.

GC analyses were performed on a Shimadzu GC-14B chromatograph equipped with a FID detector, a CP-sil-5CB column (30 m x 0.25 mm). Nitrogen was used as carrier gas (initial temperature 80 °C, heating rate 10 °C min^{-1} up to 280 °C).

HPLC analyses were performed on a LC/MS Agilent 1100SLT. The working condition is following: Column-ZORBAX-SB-C18 of dimension 4.6 mm x 250 mm, Protect-5 microns; loop size-8 μl; temperature of column-room temperature; UV detector-245 nm and 280 nm; mobile phase – water (10 mmol/L formic acid, 60 %) and acetonitrile (40 %); flow rate-0.2 mL/min.

3.5 Original data from elemental analysis

Table 3.6 Elemental data of samples in this dissertation.

Sample	SiO_2 %	C %	H %	N %	S %	Cl %	Ni %	Cu %
Complex 1		44.41		8.95			9.44	
Complex 2		35.78		22.07			12.07	
Complex 3		31.14		21.60			15.53	
M	41.92	35.03	7.42	2.01				
M-TA	86.19	12.43	3.59	<0.1				
M-H	87.22	12.41	3.58	0.1				
M1’	51.58	32.70	6.59	2.03				
M2’	51.62	33.89	6.72	1.99				
M1’-EP	90.34	7.80	2.37	<0.1	<0.2			
M1’-EPS	77.4	19.7	4.4	0.7				
M1’-ES	89.67	7.72	2.40	<0.1				
M2’-ES	89.67	7.72	2.40	<0.1				
M-OP-0.3Ni(L^1)	52.68	30.41	6.56	2.23	<0.2		0.61	
M-OP-Ni(L^1)	53.04	30.77	6.73	2.40			1.68	
M-OP-Ni($2L^1$)	54.78	28.93	6.31	2.97			1.56	
M-OP-Ni($3L^1$)	53.53	30.65	6.65	3.3	0.71			1.53
M-OP-Cu(L^1)	56.8	27.30	5.96	2.21				1.80
M-OP-Cu($3L^1$)	51.02	31.16	6.54	3.22	0.88			1.67
M-OP-0.1Cu($2L^2$)	51.58	33.30	6.76	1.97	<0.3			0.24
M-OP-0.2Cu($2L^2$)	53.41	31.94		2.17	0.87			0.35
M-OP-0.5Cu($2L^2$)	53.27	32.09		1.79	<0.3			0.94
M-OP-0.3Ni($2L^1$)-H	86.63	2.43	1.90	1.01	<0.2		0.88	
M-OP-Ni(L^1)-TA	85.17	11.77	3.43	1.08			2.24	
M-OP-Ni($2L^1$)-TA	81.82	12.46	3.51	2.01	<0.2		1.79	
M-OP-Ni($3L^1$)-TA	78.00	13.39	3.78	2.44	<0.2	1.35	1.91	
M-OP-Cu(L^1)-TA	86.55	11.25	3.15	1.02	0.29			
M-OP-Cu($3L^1$)-TO	75.18	13.02	3.64	2.23	<0.2	5.54		1.21
M-OP-Cu($3L^1$)-TA	80.45	12.91	3.62	2.27	<0.2	0.94		2.33
M-OP-Cu($3L^1$)-HTA	80.41	10.9	3.25	2.36		0.92		2.51

M-OP-Cu(3L^1)-H	83.70	5.97	2.58	2.60	<0.2			2.50
M-OP-0.1Cu(2L^2)-H	89.62	3.04	1.57	0.27				0.31
M-OP-0.2Cu(2L^2)-H	83.49	7.95	2.18	1.74				0.52
M-OP-0.5Cu(2L^2)-H	80.44	4.34	1.60	0.56				1.06
M-OP-0.2Cu(2L^2)-TA	85.95	12.02		<0.3	0.35			
M-OP-0.5Cu(2L^2)-TA	86.09	13.86		0.33	<0.3			
M1'-PS-Ni(2L^1)	80.7	12.1	3.0	3.5			2.5	
M1'-PS-Ni(3L^1)	76.1	12.6	3.3	4.6			2.3	
M1'-PS-Cu(2L^1)	79.71	11.15	2.78	3.53				2.55
M2'-PS-Cu(L^3)	81.88	13.82		1.92				2.79
M-OP-0.3Ni(2L^1)-HH							0.58	
M-OP-Ni(L^1)-TA-CuN							2.1	1.1
M-OP-Ni(2L^1)-TA-CuN							1.7	1.6
M-OP-Ni(3L^1)-TA-CuN							1.9	3.1
M-OP-Ni(3L^1)-TA-CuNH							1.4	4.9
M-OP-Ni(3L^1)-TA-SCN	79.61	13.22	3.72	2.56	0.67		1.99	
M-OP-Cu(L^1)-TA-H								1.95
M-OP-Cu(3L^1)-TA-H								2.25
M-OP-Cu(3L^1)-HH								2.27
M-OP-0.5Cu(2L^2)-HH								0.04
M1'-PS-Ni(3L^1)-SCN	76.61	1257	3.09	4.6	1.83		2.14	
M1'-PS-Ni(2L^1)-H							0.2	--
M1'-PS-Ni(2L^1)-HCu							0.1	4.8
M1'-PS-Ni(2L^1)-CuN							0.4	3.9
M2'-PS-Cu(L^3)-R								2.17
M-OP-0.2Cu(2L^2)-HR								0.41

Organization

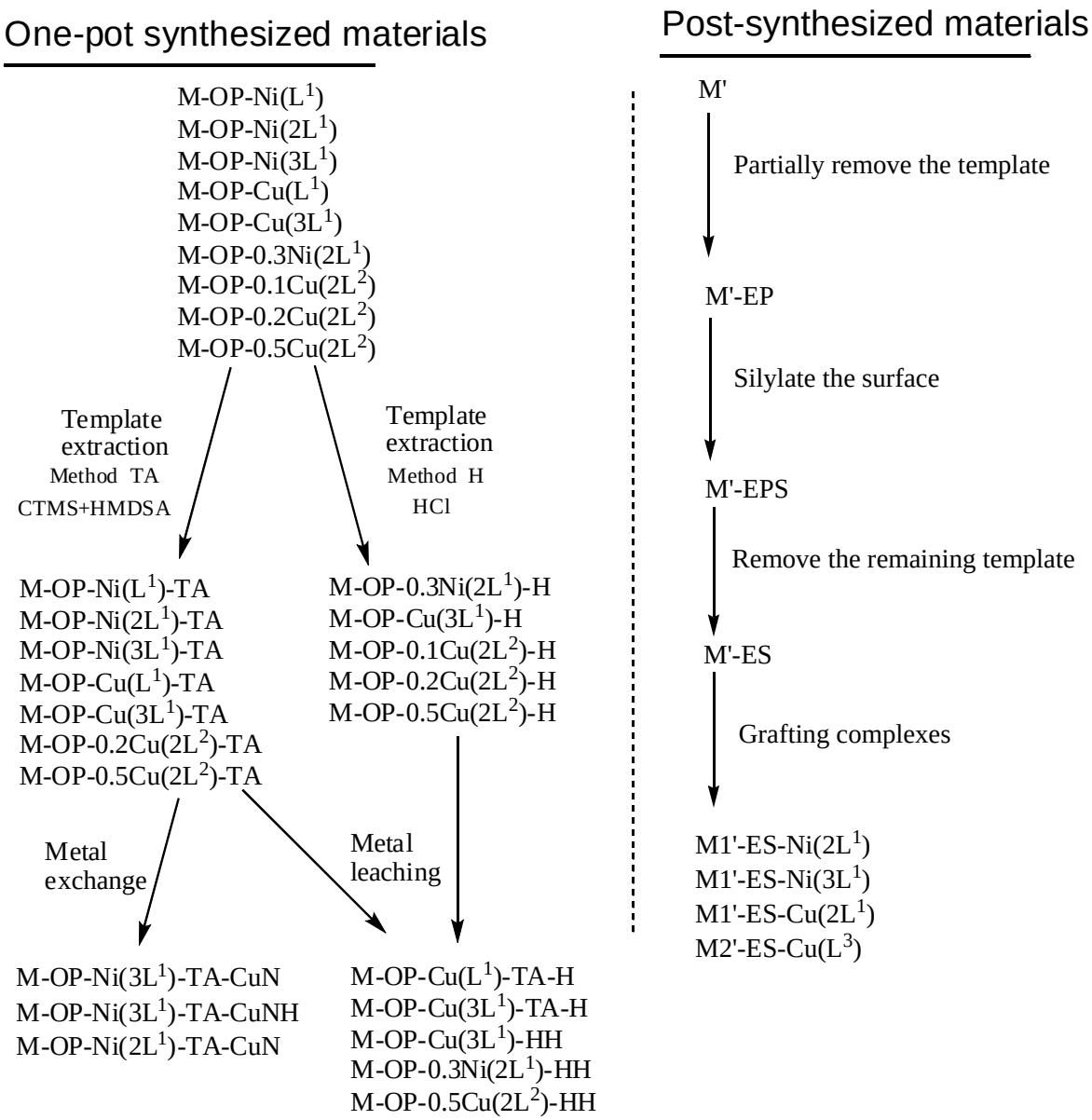

Chapter 4 Incorporation of nickel ethylenediamine complexes in the wall of a nanostructured porous silica: Nickel (II) used as a probe

4.1 Introduction

In recent years, much attention has been paid on preparation and characterization of new PMOs. Corriu *et al*. have synthesized a new type of mesoporous hybrid materials containing cyclam moieties inside the framework complexed to transition metal ions such as Cu(II) or Co(II).[16-18] These syntheses are performed under neutral conditions using a metal-cyclam precursor with either SiH_3 or $Si(OEt)_3$ hydrolisable groups, tetraethoxysilane (TEOS) as silica source and methanol as cosolvent. Two different transition metals can be selectively incorporated, one on the framework and the other in the channel pores. The cyclam complex in the framework of the mesostructured silica is quite stable and no metal decomplexation occurs even using a large excess of cyclam ligand for extracting metal in the framework.[18] Mercier *et al*. have prepared a HMS mesoporous silica with the 1,4-bis-[3-(trimethoxysilyl)propyl]ethylenediamine ligand, *bis*(TMSP)en, incorporated inside the framework under neutral conditions and using TEOS as silica source.[157] The obtained PMOs material possess a less ordered structure as shown in XRD patterns, which prevents good monitoring any change in the materials. They were used as sorbents for metal adsorption. However, they exhibit a low metal adsorption ability: less than 10 % of the ligand can be used to complex Cu(II) ions and less than 1 % to complex Ni(II) or Zn(II) ions. Furthermore, Karakassides *et al*. have reported that under neutral conditions Cu(II)-ethylenediamine-containing MCM-41 can be synthesized by a sol-gel approach using tetramethoxysilane (TMOS) as silicon source and the copper-ethylenediamine precursor $Cu[(CH_3O)_3Si(CH_2)_3NHCH_2CH_2NH_2]_2$, $[Cu(L^1)_2]$, L^1 = N-(2-aminoethyl)-3-amino-propyltriymethoxysilane.[158] The as-made materials have been characterized by EPR

spectroscopy, showing the presence of a mixture of $Cu(L^1)^{2+}$ and $Cu(L^1)_2^{2+}$ species. Both studies of Mercier *et al* and Karakassides *et al* suggest that neutral conditions are not optimal for metal ion coordination when the synthesis of ethylenediamine (en) functionalized mesoporous materials is at stake. In addition, no conclusions have been drawn concerning the low metal exchange ability observed in the PMOs materials. Thus, it could not know the precise information on the coordination of the transition metal in previous works.

We propose to tackle the problem in the actual chapter using Ni(II) ions complexed with bidentate ethylenediamine-like ligand to probe embedded or grafted complexes sites in mesostructured porous silicas. Indeed, $Ni(en)_x(H_2O)_{6-2x}(NO_3)_2$ (x=1-3) are well characterized by their UV-visible absorption bands.[159] In addition, the nitrate counterion exhibits also a well-defined absorption both in UV-visible and in IR regions. These features are very useful to monitor any change in the coordination of Ni (II)-ethylenediamine (en) complexes and in the nature of counterions when unknown environments are at stake. These are the reasons to choose $[Ni(L^1)x]$ complexes as a probe to investigate the peculiarities of framework complex sites *versus* grafted complex sites in a siliceous matrix.

From a structural point of view, *N*-(2-aminoethyl)-3-aminopropyltrimethoxysilane (L^1) is different from ethylenediamine (en) due to the additional propyl group and trimethoxysilane moiety. It will most probaly induce some differences on the metal coordination environment comparison to en. Thus, in this chapter, molecular Ni(II) complexes with ethylenediamine (en), *N*-propylethylenediamine (Pren) and *N*-(2-aminoethyl)-3- aminopropyltriymethoxysilane (L^1) ligand are firstly investigated. In a second part, the incorporating of Ni(II)-*N*-(2-aminoethyl)-3-aminopropyltriymethoxysilane (L^1) complexes (n_{L1}: n_{Ni}=1, 2, 3) into the framework of a mesostructured porous silica is described using a novel one-pot synthesis route in the absence of any organic solvent. It includes i) basic conditions, to favor ligand coordination to the metal ion, ii) aqueous sodium silicate solution as silica source, and iii) pure water as single solvent. For comparison, Ni(II)-L^1 complexes have been grafted in the channels of mesostructured porous silicas using a post-synthesis route already

described for Ru(III), Cu(II) and Eu(II) complexes.[22, 160] The structure of the materials has been investigated using XRD, N_2 sorption isotherms and TEM techniques. The nature and quantity of the loaded species has been determined from FT-IR, EA (elemental analysis), ICP-MS and TGA measurements. Furthermore, the metal exchange ability of Ni(II) by Cu(II) has been tested in both types of materials using EPR spectroscopy. Finally, a complete UV-visible study is reported in order to determine the coordination environment of the metal ion for both PMOs and post-synthesis materials.

4.2 Study of the nickel complex precursors in solution

From *N*-propylethylenediamine (Pren) to N-(2-aminoethyl)-3- aminopropyltriymethoxysilane (L^1), this evolution satisfies the need of immobilization of the ligand on solids and makes the active center reusable in the area of catalysis and adsorption. However, the question is coming: are the structure and the coordination environment of the metal ion different in Ni-L^1 and Ni-Pren complexes? Indeed, they are closely related to both preparation of PMOs materials and elucidation of the metal coordination environment in the framework of PMOs (*cf.* 3.3).

4.2.1 Results and discussion

4.2.1.1 Structure of the Ni(II) -Pren complexes

Structure Solution and Refinement

Complex 1 crystallizes in the monoclinic system. According to the observed systematic extinctions, the structure has been solved in the C2/*c* space group. Crystallographic data and refinement details are summarized in **Table 4.1**. Selected inter-atomic bond lengths and bond angles are listed in **Table 4.2**.

Table 4.1 Crystal data and structure refinement for **complex 1**, **2** and **3**

	1	**2**	**3**
	$Ni(pren)_2(H_2O)_2$•2A•$2H_2O$	**$Ni(pren)_2(NO_3)_2$**	**$Ni(pren)_3$•2(NO_3)**

Refined formula	$C_{24}H_{50}N_4Ni_1O_8S_2$	-	-
Molecular weight (g.mol^{-1})	674.88	-	-
Crystallographic system	monoclinic	triclinic	triclinic
Space group	C2/*c* (No. 15)	P-1 (No. 2)	P-1 (No. 2)
Temperature (K)	293	293	293
Z	4	-	-
a (Å)	26.640 (2)	6.96 (3)	15.935 (1)
b (Å)	10.0382 (9)	7.31 (5)	19.260 (2)
c (Å)	12.423 (1)	30.2 (2)	19.432 (2)
α (deg.)	90	95.7 (3)	99.217 (4)
β (deg.)	101.240 (5)	91.54 (8)	105.938 (4)
γ (deg.)	90	112.08 (5)	104.075 (4)
Volume (Å^3)	3258.4 (5)	14010 (16)	5395.2 (9)
D (g.cm^{-3})	1.316	-	-
μ (mm^{-1})	0.771	-	-
Crystal size (mm^3)	0,051 * 0,053 * 0,059	0,021 * 0,029 * 0,032	0,125 * 0,145 * 0,273
Crystal colour	Blue	Blue	Blue
Crystal shape	Cube	Cube	Aiguille
No. of ind. refl.	3818	-	-
R_{int}	0.034	-	-
R (I/σ(I) > 3)	0.0581	-	-
R_w (I/σ(I) > 3)	0.0663	-	-
GOF on *F*	1.23		
$\Delta\rho_{max}$ (e$^-$.Å^{-3})	0.44		
$\Delta\rho_{max}$ (e$^-$.Å^{-3})	-0.50	-	-

Table 4.2 Selected bond lengths [Å] and bond angles [°] for **complex 1**

Bond lengths			
Ni1 - N1	2.096 (4)	Ni1 - N4	2.129 (5)
Ni1 - O11	2.085 (3)		

Bond angles			
N4 - Ni1 - N1	82.3 (2)	N4 - Ni1 - O11	90.7 (2)
N1 - Ni1 - O11	91.1 (2)	N4 - Ni1 - N1	97.7 (2)
N1 - Ni1 - N1	180	O11 - Ni1 - N1	88.9 (2)
N4 - Ni1 - N4	180	N1 - Ni1 - N4	97.7 (2)
O11 - Ni1 - N4	89.3 (2)	N1 - Ni1 - N4	82.3 (2)
N4 - Ni1 - O11	90.7 (2)	N1 - Ni1 - O11	88.9 (2)
O11 - Ni1 - O11	180	N1 - Ni1 - O11	91.1 (2)

Structural description

Complex 1 is built from a Ni(II) cation located in a quasi perfect octahedral environment in terms of Ni-N,O bond lengths and N,O-Ni-N,O bond angles (**Figure 4.1 a**, **Table 4.2**). The basal plane (the metallic atom is located on the inversion centre) is composed by four nitrogen atoms (N1 and N4) belonging to the two *pren* ligands whereas the top position of the octahedron are occupied by two water molecules coordinated to the metallic center, forming then a cationic entity $[Ni^{II}(Pren)_2(H_2O)_2]^{2+}$. In order to assume the electroneutrality of the whole structure, two A^- anions ($A=C_7H_7SO_2$) co-crystallize. Note that two free water molecules also crystallize in the unit-cell. Therefore, the refined formula is then $[Ni(pren)_2(H_2O)_2]\bullet 2A\bullet 2H_2O$, which is consistent with the result of elemental analysis.

There are also a lot of hydrogen bonds between the cationic metallic entity, the counter-anions and the free water molecules (**Figure 4.1b**) forming neutral planes in the (*b*,*c*)-plan of the unit-cell (**Figure 4.2a**). These plans stack one on the other one along the a-axis of the unit-cell to form a sheet structure (**Figure 4.2b**).

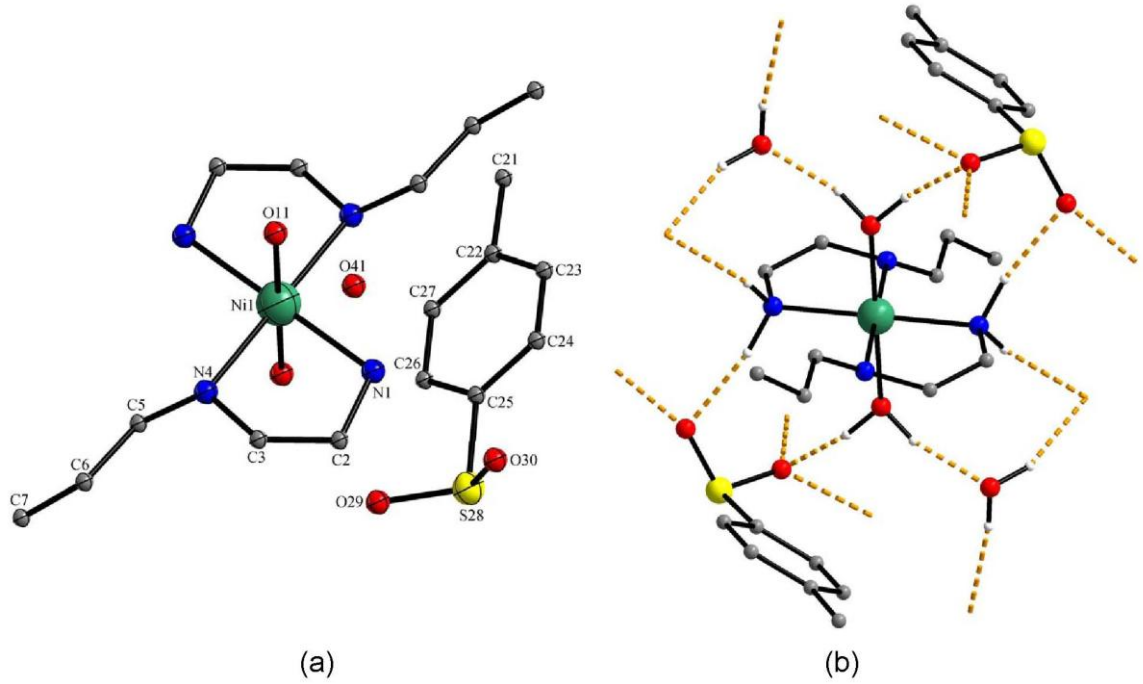

Figure 4.1 (a) Asymmetric unit of **complex 1**, $[Ni(pren)_2(H_2O)_2]\bullet 2A\bullet 2H_2O$, ($A=C_7H_7SO_2$), with atom labelling. Ellipsoids are represented with a probability of 30%. Hydrogen atoms have been removed for clarity; (b) hydrogen bonds present in the structure of **complex 1** and hydrogen atoms are not involved in.

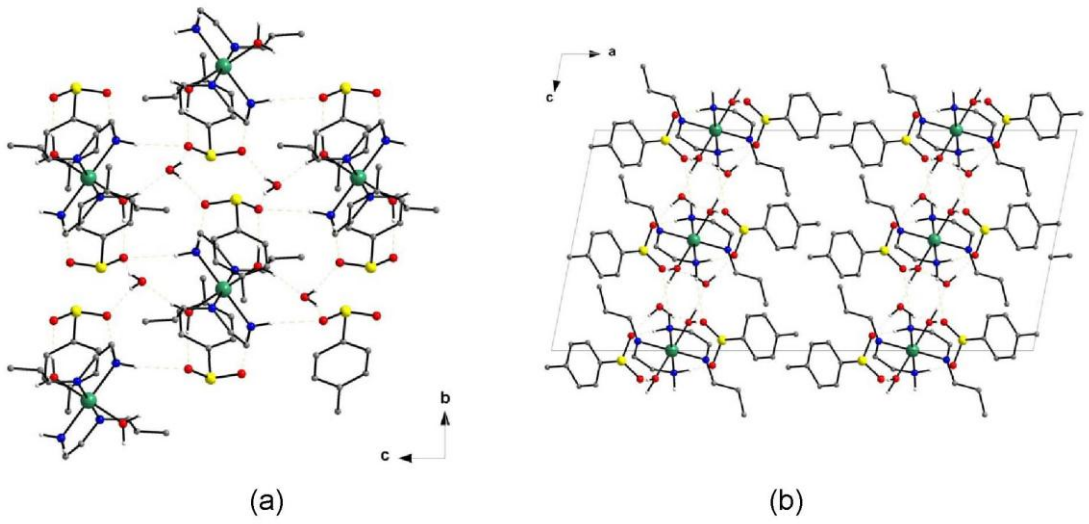

Figure 4.2 (a) Neutral plan of **complex 1** in the (*b*,*c*)-plan of the unit-cell built from hydrogen bonds (orange dash lines); (b) projection in the (*a*,*c*)-plan of the unit-cell of **complex 1** packing (including hydrogen bonds). Hydrogen atoms are not involved in and any hydrogen bonds have been removed for clarity.

For complex 2, despite several attempts, it was impossible to obtain a crystal structure of sufficient quality. This was certainly due to (i) the small size of the crystal and (ii) its low

diffracting power in large angles. However, with data collected during a measurement, it was possible to find a solution to present its model below.

This complex crystallizes in the triclinic crystal system (**Table 4.1**). In agreement with the observed systematic extinctions, the solution was found in space group P-1 (No. 2). Unlike the **complex 1** previously described, it is a neutral entity since the NO_3^- anions replace water molecules of the **complex 1** by coordination via an oxygen atom (**Figure 4.3**). The metallic Ni(II) is located in a distorted octahedral environment. The square of this environment is composed of four nitrogen atoms from two cis-Pren ligands position. The fifth and sixth positions on both sides of the square are occupied by two oxygen atoms from two molecules of NO_3^-. This result is in agreement with the elemental analysis, $Ni(Pren)_2(NO_3)_2$.

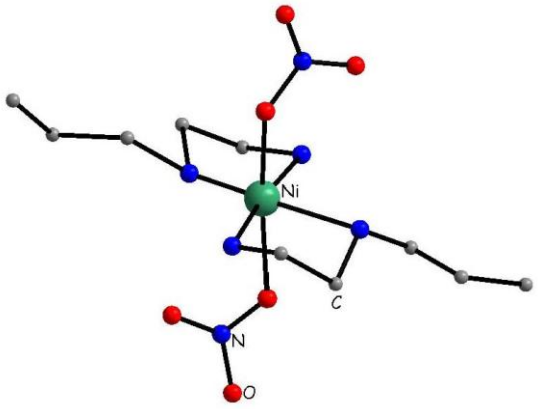

Figure 4.3 Model of the crystal structure of complex $Ni(Pren)_2(NO_3)_2$, **complex 2** (grayer C atom, blue N atom, red O atom, yellow S atom, green Ni(II)).

For **complex 3**, despite several attempts, it was impossible to find a crystal of sufficient quality to obtain diffraction data to completely solve and refine the crystal structure. Indeed, the complex co-crystallized with solvent molecules. The stability of the crystals tested under ambient conditions was not sufficient to achieve a complete record before degradation of the crystal due to evaporation of solvent. However, it was possible to obtain a model by recorded diffraction data.

This complex crystallizes in the triclinic crystal system and the solution was obtained in the space group P-1 (No. 2) (**Table 4.1**). Ni(II) atom is located in a regular octahedral (link lengths Ni-N all roughly equal to 2.15 Á) exclusively composed of nitrogen atoms from

three Pren ligands (**Figure 4.4**). The fifth and sixth positions on both sides of the square are occupied by two oxygen atoms from two molecules of NO_3^-. Projection of the crystal structure of Ni $(Pren)_3$•2 (NO_3) in the plane (a, b) cell (**a**) and in the plane (b, c) cell (**b**) is shown in **Figure 4.5**.

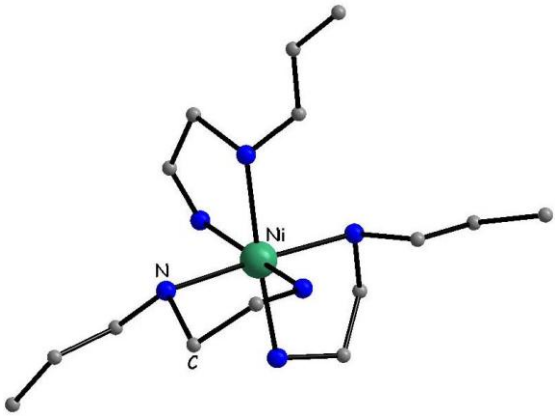

Figure 4.4 Model of the crystal structure of **complex 3**, $[Ni(Pren)_3]^{2+}$ [grayer C atom, blue N atom, red O atom, yellow S atom, green Ni(II)].

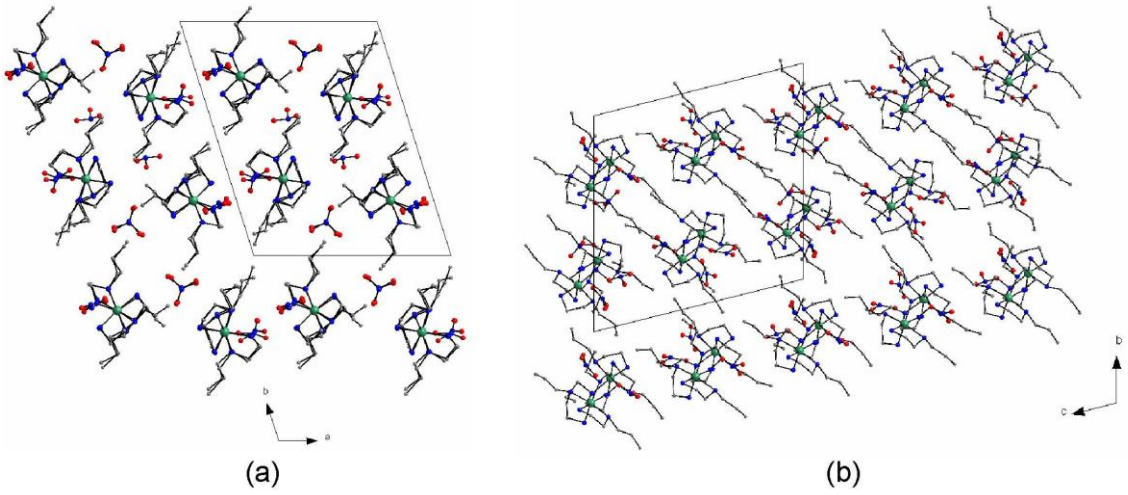

Figure 4.5 Projection of the crystal structure of **complex 3**, Ni $(Pren)_3$•2(NO_3), in the plane (a, b) cell (**a**) and in the plane (b, c) cell (**b**).

4.2.1.2 Comparison Ni(II)-Pren complexes with Ni(II)-L^1 complexes

A series of Ni(II)-en, Ni(II)-Pren and Ni(II)-$\mathbf{L^1}$ ($\mathbf{L^1}$ = N-(2-aminoethyl)-3-aminopropyltriymethoxysilane) complexes with various ligand/Ni(II) molar ratios (1, 2, 3, 4, 6, 9 and 18) were prepared and monitored by UV-visible spectros-

copy. The corresponding data are gathered in **Table 4.3**. All the Ni(II) complexes presented two absorption bands ν_3 and ν_2 in the range of 22000-38000 cm^{-1} (**Figure 4.6**), and a third large band, ν_1, appeared in the NIR region. The bands ν_3, ν_2, ν_1 can be attributed to the spin-allowed electronic transitions of Ni^{2+} ions in an octahedral environment: $^3T_{1g}(P) \leftarrow {}^3A_{2g}$, $^3T_{1g}(F) \leftarrow {}^3A_{2g}$ and $^3T_{2g}(F) \leftarrow {}^3A_{2g}$, respectively (**Scheme 4.1**). From the absorption bands ν_3 and ν_2, the crystal field, Δ, and the nephelauxetic parameter, β, can be obtained through **Formula 4.1**

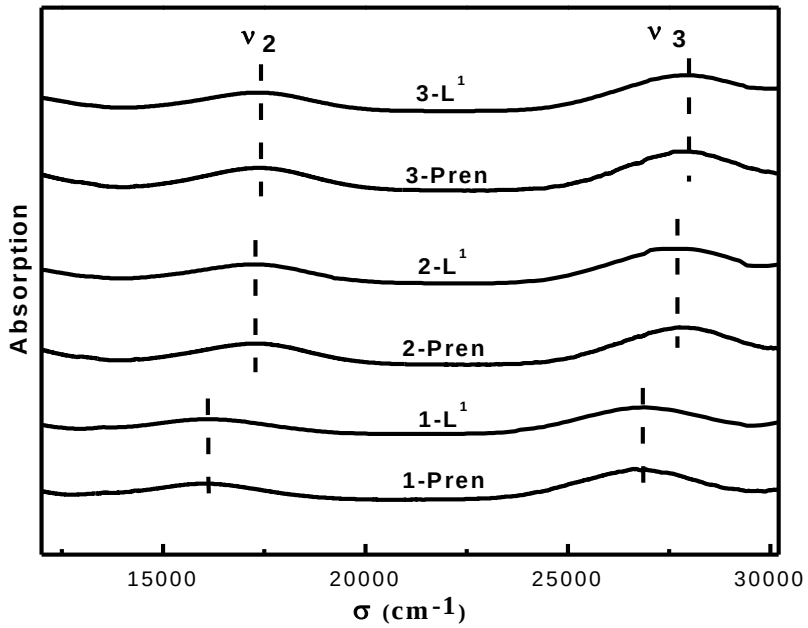

Figure 4.6 UV-visible spectra of 1-Pren, 2-Pren, 3-Pren, 1-L^1, 2-L^1 and 3-L^1.

Formula 4.1 Assuming an octahedral symmetry, Δ,ν_1 and β parameters can be determined from the following formulas: [161]

$\nu_3/\ \nu_2= [15B+3*\Delta+(225*B^2-18*B*\Delta+\Delta^2)^{1/2}]/\ [15B+3\Delta-(225B^2-18*B*\Delta+\Delta^2)]$

$\nu_3/\ B= 1/2*[15+3*\Delta/\ \beta+(225-18*\Delta/\ \beta+\ (\Delta/\ \beta)^2)^{1/2}]$

$\nu_1 = \Delta;\ 10Dq(cm^{-1})= \nu_1\ (cm^{-1})$

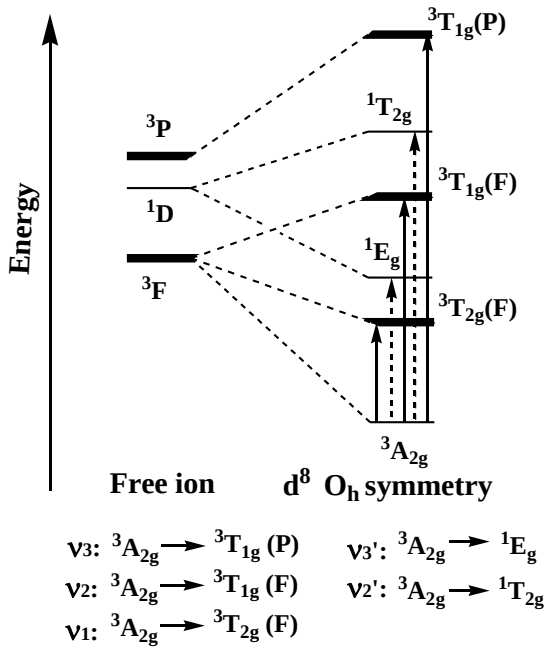

Scheme 4.1 Simplified correlation diagram between the energy levels of the Ni^{2+} free ion (d^8) and those of the same ion subjected to a crystal field of octahedral symmetry. Solid line arrows indicate spin-allowed electronic transitions and dotted line arrows spin-forbidden ones.

Table 4.3 Parameters obtained from UV-visible spectra for Ni containing samples.

Solution	ν_3 ±50 cm^{-1}	ν_2 ±50 cm^{-1}	Δ [a] ±50 cm^{-1}	*Dq* ±50 cm^{-1}	β [b] ± 0.015	pH
1-en [c]	27000	16300	10070	1010	0.84	
2-en [c]	28200	17600	11120	1110	0.80	
3-en [c]	29100	18400	11820	1180	0.77	
1-Pren [c]	26800	16100	9920	990	0.84	
2-Pren [c]	27820	17300	10900	1090	0.80	
3-Pren [c]	28300	17700	11200	1120	0.79	
1-Pren	26800	16100	9920	990	0.84	8.58
2-Pren	27800	17200	10790	1080	0.81	10.20
3-Pren	27930	17360	10930	1090	0.80	11.79
4-Pren	28100	17500	11040	1100	0.80	11.91
6-Pren	28200	17500	11000	1100	0.81	12.19
9-Pren	28300	17600	11090	1110	0.81	12.33

18-Pren	28300	17600	11090	1110	0.81	12.31
1-L[1]	26800	16100	9920	990	0.84	--
2-L[1]	27800	17200	10790	1080	0.81	--
3-L[1]	27930	17360	10930	1090	0.80	--
4-L[1]	28100	17450	10980	1100	0.81	--
6-L[1]	28200	17500	11000	1100	0.81	--
9-L[1]	28300	17600	11090	1110	0.81	--
18-L[1]	28300	17600	11090	1110	0.81	--

a: Δ: calculated crystal field considering *Oh* symmetry; **b**: β, nephelauxetic parameter, $\beta=B/B_0$ (B, B_0 Racah parameter, β calculated from **Formula 4.1**), $B_0=1041$ cm^{-1} (free Ni^{2+} ion); **c**: complexes in absolute ethanol, others in aqueous solution.

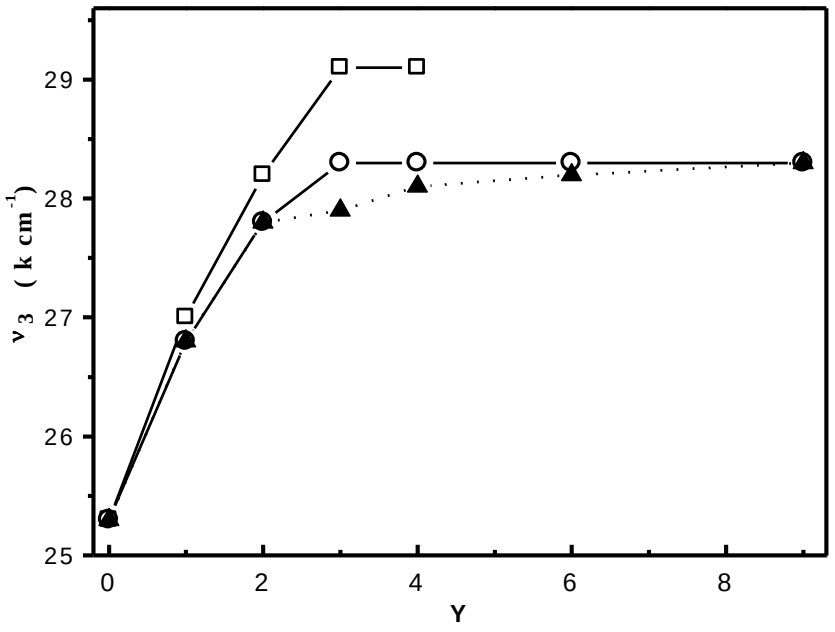

Figure 4.7 ν_3 absorption bands *vs*. Y (Ligand/Ni) molar ratio. "□", Ni-en complexes in water; "○", Ni-Pren complexes in absolute ethanol; "▲", Ni-Pren or Ni-L^1 complexes in water.

The N-monoalkyl-substituted amines become slightly more basic with increasing length of the alkyl chain,[162] propylethylendiame (Pren) is thus a stronger base than ethylenediamine (en). However, absorption bands ν_3 and ν_2 of Ni(II)-Pren complexes decrease (**Table 4.3**, **Figure 4.7**) compared to Ni(II)-en complexes with same ligand/Ni(II) molar ratio in absolute ethanol. and the spectra show a systematic decrease in *Dq* values Furthermore, with

the increase of ligand/Ni(II) (=1, 2, 3), the difference of *Dq* values between 1-Pren, 2-Pren and 3-Pren and 1-en, 2-en and 3-en become progressively great. All these results indicate that the steric effect is more important than the inductive effect.[163]

The ratio of the energy of the ^3P-^3F term splitting in the complex to the free Ni^{2+} ion value (B_0=1041 cm^{-1}) is the nephelauxetic parameter β. β correlates the extent to which the d-electrons of the metal are delocalized on the ligand orbitals. The more electrons delocalized, the smaller nephelauxetic parameter β is. The β values of both the Ni(II)-Pren complexes and Ni(II)-en complexes decrease with the increase of ligand/Ni(II) molar ratio (=1, 2, 3). When Ni(II)-Pren complexes were compared to Ni(II)-en complexes in the same ligand/Ni(II) molar ratio, similar β values are observed (**Table 4.3**). Thus the nephelauxetic parameter seems less sensitive to steric interaction than the *Dq* value. Therefore, β is primarily dependent on inductive and polarization factors.

The absorption bands ν_3 and ν_2 of both Ni(II)-Pren complexes and Ni(II)-L^1 complexes shift to lower energy values in aqueous solutions, specially the complexes with ligand/Ni(II) ≥ 3 (**Table 4.3**, **Figure 4.7**). When Ni(II)-L^1 complexes in aqueous solution were compared to Ni(II)-Pren complexes, similar absorption bands ν_3 and ν_2 and *Dq* values and nephelauxetic parameter β are observed (**Figure 4.6**, **Table 4.3**), indicating that there are no effect on the trimethoxysilane in L^1 ligand. For the Ni-L^1 solutions, a blue shift of the two transitions was observed when Y was increased. Comparing the 1-L^1 complex with 2-L^1, absorption bands ν_3 and ν_2 are significantly shifted, from 26800 cm^{-1} and 16100 cm^{-1} to 27800 cm^{-1} and 17200 cm^{-1}, respectively. Concomitantly, the crystal field Δ increases from 9910 cm^{-1} to 10790 cm^{-1} and the nephelauxetic parameter β decreases from 0.84 to 0.81. For Y= 3, 4, 6, 9 and 18 the position of the ν_3 band was shifted to 27930, 28100, 28200 , 28300 and 28300 cm^{-1}(**Table 4.3**, **Figure 4.7**), and the band ν_2 was shifted do 17360, 17450, 17500, 17600 and 17600 cm^{-1}, respectively. The β decreases from 0.85 to 0.81 with the increase of the ligand number, indicating that the electron of Ni (II) delocalize to the ligand. Thus, the progressive blue-shift of the absorption bands upon increase of the L^1 loading from Y = 3 to Y = 9 could be in agreement with the presence of a mixture of $[Ni(L^1)_2]^{2+}$ and $[Ni(L^1)_3]^{2+}$, which should be richer in the latter species upon increase of the L^1 loading. Absorption bands ν_3 and ν_2 of 28300 cm^{-1} and 17600 cm^{-1} could probably be assigned to that of

$Ni(L^1)_3^{2+}$. This progressive blue-shift is also observed in that of Ni(II)-Pren complexes in aqueous solution, whereas, the absorption bands ν_3 and ν_2 can reach to 28300 cm^{-1} and 17700 cm^{-1} when Pren/Ni = 3 in absolute ethanol. Therefore, in aqueous solution, the general shift of the absorption bands is most probably due to the complexity of aqueous solutions of amine coordination compounds [163] or the pH effect of solution.

4.2.1.3 Conclusions

The crystal structure of bis(propylethylenediamine) nickel(II) and tris(propylethylenediamine) nickel(II) complexes indicate that the Ni(II)-Pren complexes possess octahedral structures as that of Ni(II)-en complexes. The d-d transitions ($^3T_{1g}(P) \leftarrow {}^3A_{2g}$, $^3T_{1g}(F) \leftarrow {}^3A_{2g}$) of Ni(II) -Pren complexes shift to low energy values compared to Ni(II)-en complexes, probably due to the steric effect indicated by *Dq* values.

On the other hand, the d-d transitions [$^3T_{1g}(P) \leftarrow {}^3A_{2g}$, $^3T_{1g}(F) \leftarrow {}^3A_{2g}$] of Ni(II)-Pren complexes shift to lower energy from absolute ethanol to aqueous solution. Ni(II)-Pren complexes and Ni(II)-L^1 complexes possess similar spectra in aqueous solution, indicating that the trimethoxysilane in L^1 ligand has no effect for the Ni(II) coordination environment. In addition, when Y=1 (Y= L^1/Ni molar ratio), the main species are $[Ni(L^1)]^{2+}$, when Y=2, the main species are $[Ni(L^1)_2]^{2+}$, while Y = 3, the species are mixture of $[Ni(L^1)_2]^{2+}$ and $[Ni(L^1)_3]^{2+}$ and an excess of ligand is required to obtain the $[Ni(L^1)_3]^{2+}$ species.

4.3 Incorporation of the nickel precursors in the wall of nanostructured-porous silica

4.3.1 Results

4.3.1.1 Synthesis and characterization of PMOs materials

Nickel (II) nitrate and N-(2-aminoethyl)-3-aminopropyltriymethoxysilane (L^1) have

been used as starting reactants to form in a first step a $Ni(L^1)_y$ complex which is in a second step used as a molecular organic block to build the PMO material. Indeed, these organic blocks have been condensed with silicate oligomers in the presence of a surfactant as template in order to obtain a mesostructured porous material of the type LUS (Laval University Silica), which possesses a similar 2D hexagonal structure as MCM-41.[110, 164]

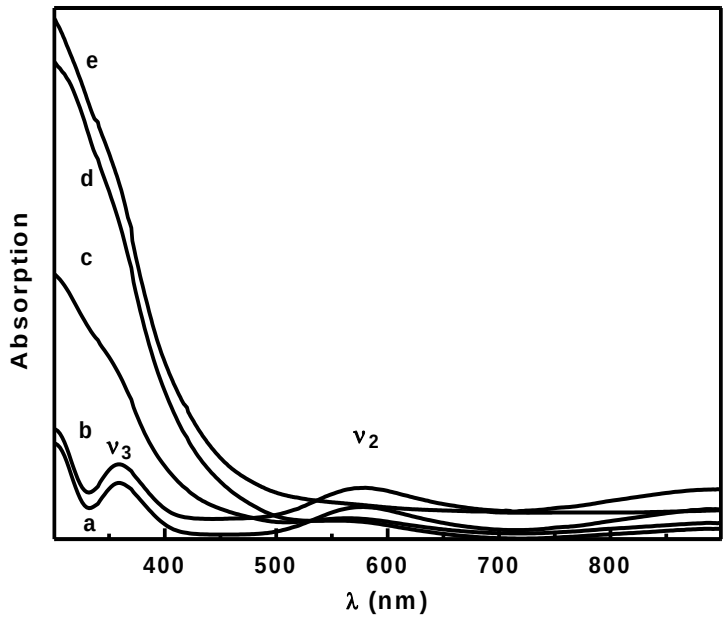

Figure 4.8 UV-visible spectra of the Ni-L^1 complex (**X**=3) in aqueous solution at room temperature (**a)**, 60 °C (**b**), 80 °C (**c**), 100 °C (**d**) and 130 °C (**e)**.

In order to synthesize the PMOs materials in the presence of the Ni-L^1 complexes using the above protocol, a study of the stability of Ni(II) complexes at different temperatures was performed. Therefore, the optimization of the synthesis conditions was mainly about finding a suitable temperature for obtaining the hexagonal structure corresponding to a mesostructured porous material while keeping the metal complex inside the walls. A series of reaction temperatures (between 25°C to 130 ºC for 24 h) was investigated to test the stability of the Ni complex. UV-visible spectroscopy was used to monitor the ν_3 and ν_2 absorption bands which are characteristic of the Ni-L^1 complexes (**Figure 4.8**). The optimal temperature was found to be 60 ºC, and it was

considered as the optimal temperature to synthesize the PMOs materials. A blanc, *i.e.* LUS without the Ni complex, was therefore synthesized at 60 ºC for 24 h. The obtained solid, M, presented a well-ordered hexagonal mesostructure as shown by XRD (*vide infra*, **Figure 4.9**).

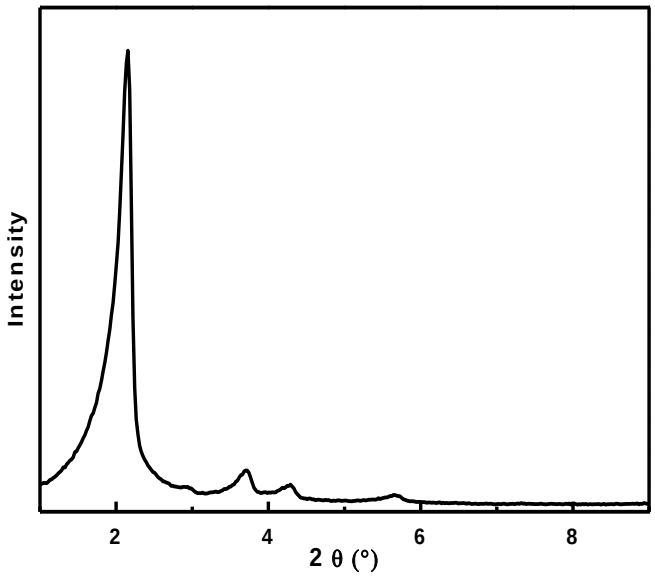

Figure 4.9 X-ray diffraction pattern of **M**.

A gel with the following molar ratio was prepared: Y L^1 : 1 $Ni(NO_3)_2$: 100 SiO_2 : 4.5 CTATos : 500 NaOH : 77500 H_2O, Y= 1, 2 and 3 for materials M-OP-Ni(L^1), M-OP-Ni($2L^1$) and M-OP-Ni($3L^1$), respectively. The initial amount of Ni(II) ion was kept constant in all the syntheses and the L^1 ligand loading was varied. During the synthesis of the PMOs materials three solutions were prepared: a solution of sodium silicate, a solution of CTATos (template) and solution of Ni-L^1 complex. The order of mixing of these three solutions was important: Ni-L^1 complex was added into the solution of CTATos, and once the complex was homogenously dispersed, the solution of sodium silicate was dropwise added, since a precipitate would have been produced if the solution of Ni(II) complex was in contact with the solution of sodium silicate. In all cases, about 80 % of the Ni(II) ions in the mother gel were incorporated in the final hybrid material M-OP-Ni(YL^1) (Y = 1, 2, 3) (*vide infra*, **Table 4.4**).

Extraction of the surfactant in PMOs materials

Approaches reported for the extraction of cationic surfactants in PMOs materials are mainly as follows: HCl, NH_4Cl or NaCl in ethanol solution.[165] If the inappropriate amount of HCl is used for the extraction of the surfactant for materials M-OP-Ni(YL^1), the L^1 ligand can be protonated, promoting metal leaching.[166] Salts, like NH_4Cl and NaCl, can remove the surfactant, but easily destroy the hexagonal structure of the material, which was proved by XRD data. For SBA-3 based Rh-PMOs, synthesized in acidic media, treatment with hexamethyldisilazane (HDMSA) evolves NH_3 by reaction with surface silanol groups; the templating surfactant is therefore displaced by neutralization of the protonated silanol groups.[15] Here, the same reasoning prompt us to use chlorotrimethylsilane (CTMS) that is better suited for solids synthesized in basic conditions. Then the HCl evolved neutralizes the silanolate groups and displaces the surfactant. This treatment has a stabilizing effect on the structure.[167, 168] Indeed, the trimethylsilyl groups [-Si(CH_3)$_3$ = TMS] so-obtained cover the internal surface of the material by capping the silanol groups and produce concommitantly a stabilization of the fragile siliceous network.

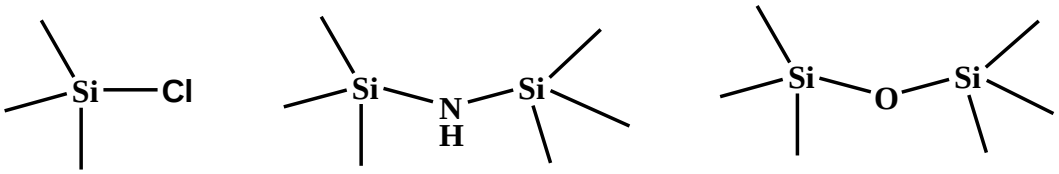

CTMS **HMDSA** **HMDSO**

Scheme 4.2 Structure of three silanes **CTMS**, **HMDSA** and **HMDSO**.

To our knowledge, slianes, such as CTMS, HMDSA or HMDSO (**Scheme 4.2**), can remove surfactant while maintaining the mesoporous structure.[167, 168] Then, three methods denoted as for *TA*, *TO* and *T* were tested to find out the safer way for simultaneous surfactant extraction and silanol capping (see experimental part). The preservation of the coordination state of nickel (II) was taken as the first condition to fulfill; ν_2 and ν_3 absorption bands were taken as UV-visible fingerprints of the complex. Data are reported for material M-OP-Ni($3L^1$) (**Table A**), note that the same conclusions

can be drawn from the treatment of material M-OP-Ni(L^1) and M-OP-Ni($2L^1$).

Table A UV-visible fingerprints of the complex before and after surfactant extraction according to methods *TA*, *T* and *TO*.

Sample	ν_3 ±50 cm^{-1}	ν_2 ±50 cm^{-1}
M-OP-Ni($3L^1$)	27400	17000
M-OP-Ni($3L^1$)-TA	27400	16900
M-OP-Ni($3L^1$)-T	26000	15700
M-OP-Ni($3L^1$)-TO	24450	14300

Comparing the bands position of M-OP-Ni($3L^1$) and M-OP-Ni($3L^1$)-TA, before and after treatment according to method *TA* using an equimolar mixture of CTMS and HMDSA, reveals no significant shift (**Table A**). On the contrary, when hexamethyl-disiloxane (HDMSO) is the silylating agent, the ν_3 = 24450 cm^{-1} and ν_2 =14300 cm^{-1} values observed for M-OP-Ni($3L^1$)-TO are close to the values reported for nickel phyllosilicate (ν_3= 24040 cm^{-1}).[107] This is reminiscent of a profound surface modification, which is likely due to the evolution of water during the reaction of HMDSO with silanol groups. When CTMS was employed instead leading to M-OP-Ni($3L^1$)-T, ν_3, ν_2 were also shifted in an intermediate position indicating that the evolution of HCl is also detrimental to the integrity of the nickel complexes.

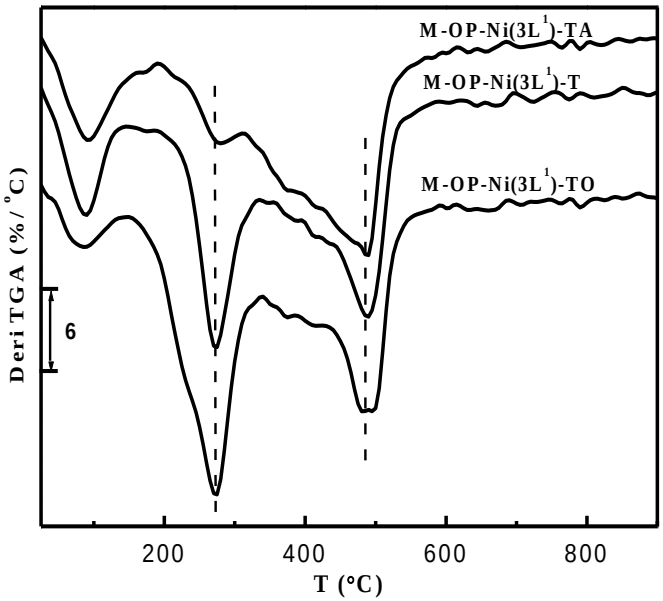

Figure 4.10 TGA diagram of M-OP-Ni($3L^1$)-TA, M-OP-Ni($3L^1$)-T and M-OP-Ni($3L^1$)-TO.

Besides, the differential TGA profile of sample M-OP-Ni(3L^1)-TA (**Figure 4.10**) presents one major weight loss centered at 492 ºC, consistent with the presence of grafted TMS groups and L^1 ligand bound to Ni that both appear to decompose in the same range of temperatures. Again, both M-OP-Ni(3L^1)-T and M-OP-Ni(3L^1)-TO materials present different features, *i.e.*, an additional weight loss centered at about 267 ºC, most likely due to the decomposition of the protonated and non-complexed L^1 ligand.

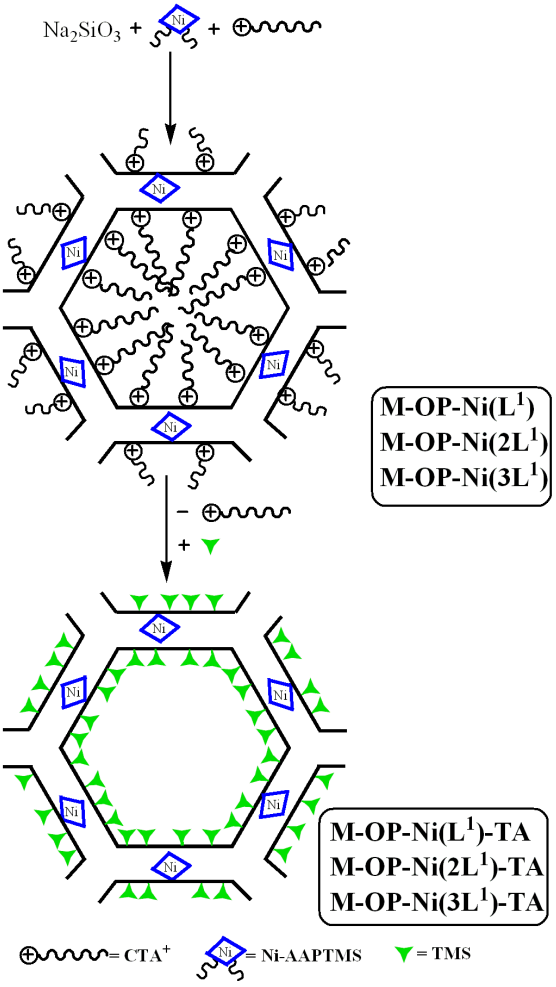

Scheme 4.3 Synthesis route of PMOs M-OP-Ni(YL^1)-TA (Y= 1, 2, 3) (above).

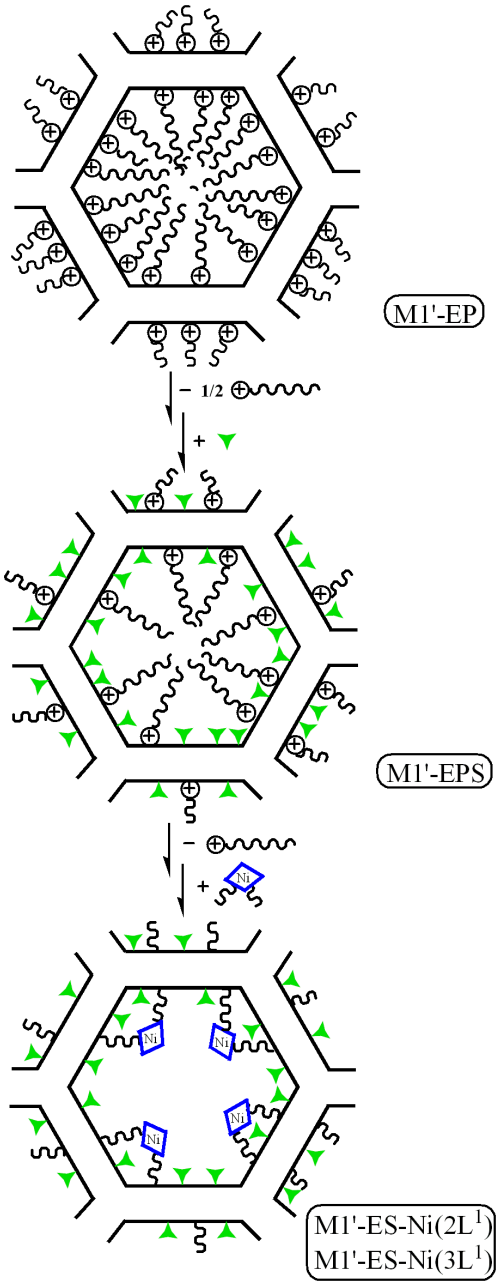

Scheme 4.4 Synthesis route of materials post-synthesized M1'-ES-Ni(YL^1) (Y= 2, 3) (right).

These results indicate that the best method for surfactant removal without mofication

of the metal environment is the method *TA*. Therefore, we will focus on materials M-OP-Ni(L^1)-TA, M-OP-Ni($2L^1$)-TA and M-OP-Ni($3L^1$)-TA in the following.

Characterization of PMOs materials

XRD. The mesostructure of all the materials was characterized by XRD. All the samples present a well-ordered mesoporous hexagonal structure as shown for M-OP-Ni($2L^1$), M-OP-Ni($2L^1$)-TA, M-OP-Ni($3L^1$) and M-OP-Ni($3L^1$)-TA in **Figure 4.11**. Three peaks assigned to <100>, <200> and <210> reflections based on a hexagonal unit were observed, indicating the presence of uniformly sized pores. The d_{100} value for M-OP-Ni($2L^1$) and M-OP-Ni($3L^1$) is about 4.2 nm which is similar to that found for M (4.1 nm). The intensity of XRD patterns increases upon decrease of the L^1 ligand content. The extracted and TMS capped materials M-OP-Ni($2L^1$)-TA and M-OP-Ni($3L^1$)-TA exhibit a much higher intensity due to the larger change in electron densities by the removal of the surfactant assemblies. Furthermore, they show a silghtly higher d_{100} value than the corresponding as made materials, M-OP-Ni($2L^1$) and M-OP-Ni($3L^1$). This is probaly due to the trimethylsilyl groups on the surface which may expand the lattice structure.

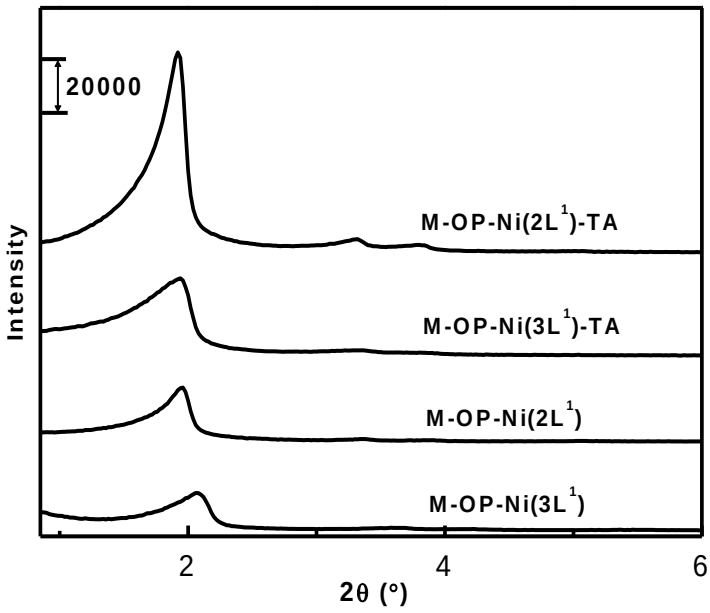

Figure 4.11 XRD patterns of M-OP-Ni($2L^1$), M-OP-Ni($3L^1$), M-OP-Ni($2L^1$)-TA and M-OP-Ni($3L^1$)-TA.

TEM. A transmission electron microscopy (TEM) study was performed on M-OP-Ni($3L^1$)-TA material which clearly shows the formation of ordered mesoporous channels and a hexagonal structure (**Figure 4.12A**). As a comparison, the reference M-H, *i.e.*, the extracted solid without the Ni-L^1 complex, was also analyzed (Figure **Figure 4.12B**). Both solids present mainly as spherical particles, and some fibers are also observed. For M-OP-Ni($3L^1$)-TA a group of fibers is observed on the right of **Figure 4.12A**. The two lonely fibers perpendicular to this group of fibers are around 20 nm thickness and clearly show the typical longitudinal channels of LUS. In addition, on the top of the figure, a transversal view of one fiber is presented, where the hexagonal channels are clearly shown. Finally, some defects are observed in the central lonely fiber (cavities about twice larger than the regular channels). However, for material M-H larger particles and fibers were observed without defects (**Figure 4.12B**). In addition, the channel ordering was obseved in longer distance than for the Ni containg sample M-OP-Ni($3L^1$)-TA.

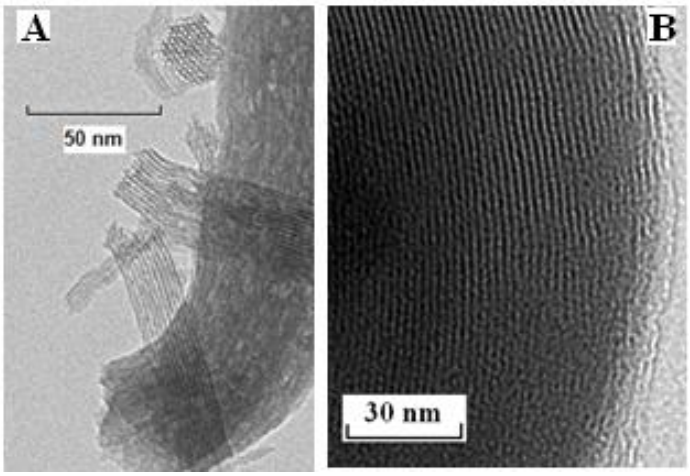

Figure 4.12 TEM of M-OP-Ni($3L^1$)-TA (A) and M-H (B).

IR. In the IR spectrum of M-OP-Ni($3L^1$), bands at 2850 cm^{-1} and 2918cm^1 are assigned to the ν_s(C-H) and ν_{as}(C-H) stretching vibrations of the -CH_2- groups of the surfactant, respectively (**Figure 4.13**). After surfactant removal, these two bands disappear in the spectrum of M-OP-Ni($3L^1$)-TA, which means that surfactant was efficently removed by using the CTMS and HMDSA mixture. Bands at 2962 cm^{-1} and 2903 cm^{-1} are assigned to the ν_s(C-H) and ν_{as}(C-H) of –CH_3 groups of thimethylsilane

[-Si(CH_3)$_3$] on the surface of M-OP-Ni(3L^1)-TA, due to the capping process concomitant with the surfactant removal. Indeed, a band at 850 cm^{-1}, attributed to the ν(Si-C) stretching vibration, observed in the spectrum of M-OP-Ni(3L^1)-TA attests for the presence of [Si-(CH_3)$_3$], as shown in **Figure 4.14**. The absence of the peak characteristic for NO_3^- (1385 cm^{-1}) in both M-OP-Ni(3L^1) and M-OP-Ni(3L^1)-TA materials (**Figure 4.14**) is also in agreement with the presence of other ions such as OH^- or SiO^- groups to counterbalance the positive charge of the Ni(II) ions.

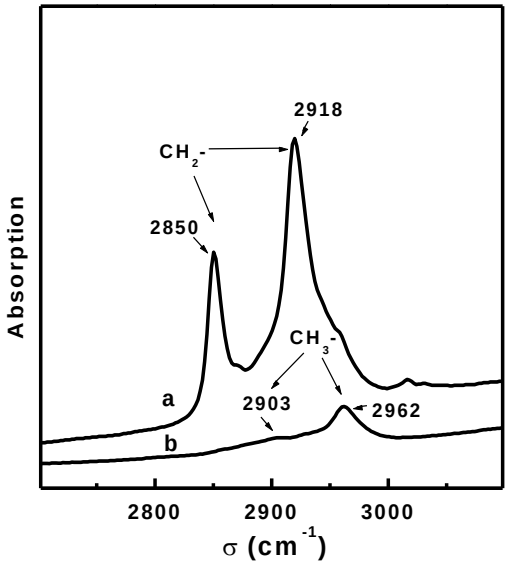

Figure 4.13 FT-IR spectra of (a) M-OP-Ni(3L^1) and (b) M-OP-Ni(3L^1)-TA.

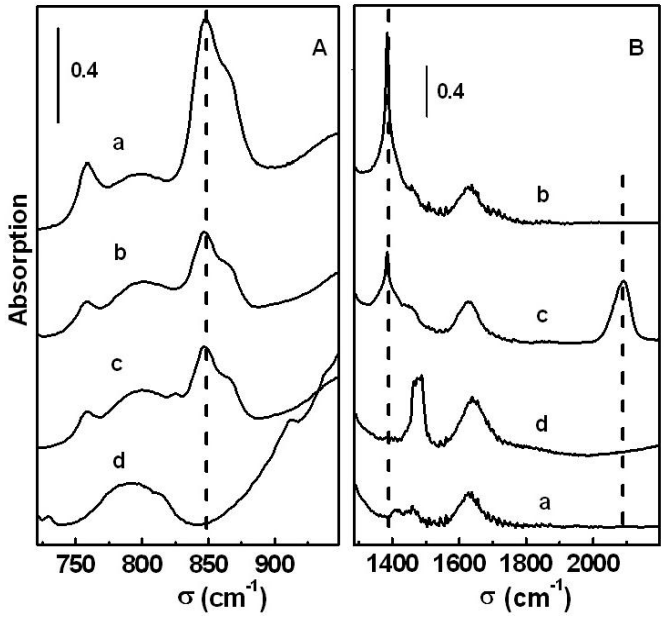

Figure 4.14 FT-IR spectra of (**a**) M-OP-Ni(3L^1)-TA, (b) M1'-ES-Ni(3L^1), (c) M1'-ES-Ni(3L^1)-NCS and (d) M-OP-Ni(3L^1).

Table 4.4 Nickel content and molar ratios deduced from elemental analyses and weight loss from TGA.

Material	Ni[a] wt% ±0.1	Ni/Si [b] ±0.001	TMS/Si [b] ± 0.01	L^1/Si [b] ± 0.01	L^1/Ni ±0.1
M-OP-Ni(L^1)	1.7	0.036	--	0.03 [c]	0.9
M-OP-Ni($2L^1$)	1.6	0.033	--	0.07 [c]	2.0
M-OP-Ni($3L^1$)	1.5	0.033	--	0.10 [c]	2.8
M-OP-Ni(L^1)-TA	2.2	0.036	0.25	0.03 [d]	1.1
M-OP-Ni($2L^1$)-TA	1.8	0.030	0.22	0.07 [d]	2.3
M-OP-Ni($3L^1$)-TA	1.9	0.034	0.24	0.09 [d]	2.7
M1'-ES-Ni($2L^1$)	2.5	0.038	0.15	0.09 [d]	1.9
M1'-ES-Ni($3L^1$)	2.4	0.040	0.12	0.12 [d]	3.1

a: measured by ICP-MS; b: molar ratio per inorganic silica; the inorganic SiO_2 content is obtained from the residual weight in TGA at 1000 ºC upon subtraction of both NiO and the SiO_2 formed from the grafted organosilanes; c: due to the presence of both surfactant and ligand, both species contributing to the N amount, this value has been calculated starting from the ratio observed for the corresponding M-OP-Ni(YL^1) (Y = 1, 2, 3) samples, d: L^1 ligand is determined from N amount by subtraction of the N corresponding to surfactant M-OP-Ni(YL^1)-TA or the nitrate ions (M1-ES-Ni(YL^1) when present.

EA. Elemental analyses of nickel PMOs materials were preformed to know whether the Ni ion leached during the gel formation and surfactant removal. Ni wt%, Ni/Si (pure inorganic SiO_2) and ligand/Ni molar ratios are gathered in **Table 4.4**. The Ni wt% is around 2% in all the PMOs materials. Indeed, the Ni content in the mother gel was constant for all the materials and the L^1 ligand varied. Ni/Si is equal to 0.033 for M-OP-Ni($3L^1$), which is higher than that of the mother gel which was equal to 0.01. A yield in nickel is *ca*. 78 %, and a yield in silicon is partial (*ca*. 21 %) After the silylation and surfactant removal, Ni/Si_{inorg} of M-OP-Ni($3L^1$)-TA was not significantly modified, indicating no metal leaching. The same behaviour was observed for M-OP-Ni($2L^1$) and M-OP-Ni(L^1) before and after surfactant removal (**Table 4.4**). Moreover, the ligand/Ni molar ratio for M-OP-Ni(L^1)-TA, M-OP-Ni($2L^1$)-TA and M-OP-Ni($3L^1$)-TA is equal to1.1, 2.3 and 2.7 which is similar to the values of M-OP-Ni(L^1), M-OP-Ni($2L^1$) and M-OP-Ni($3L^1$) in as-made materials, respectively. Finally, the TMS/Si_{inorg} ratio

decreases from 0.29 on the Ni(II) free sample M-TA down to *ca*. 0.23 for M-OP-Ni(L^1)-TA, M-OP-Ni($2L^1$)-TA and M-OP-Ni($3L^1$)-TA. This shows that the presence of the complex does affect the surface structure decreasing the OH density by *ca*. 20 %. PMOs materials possess an average 3 Ni-L^1: 24 TMS: 100 SiO_2 (inorganic) molar ratio for (M-OP-Ni(YL^1))-TA in **Scheme 4.3** which was drawn in taking this into account.

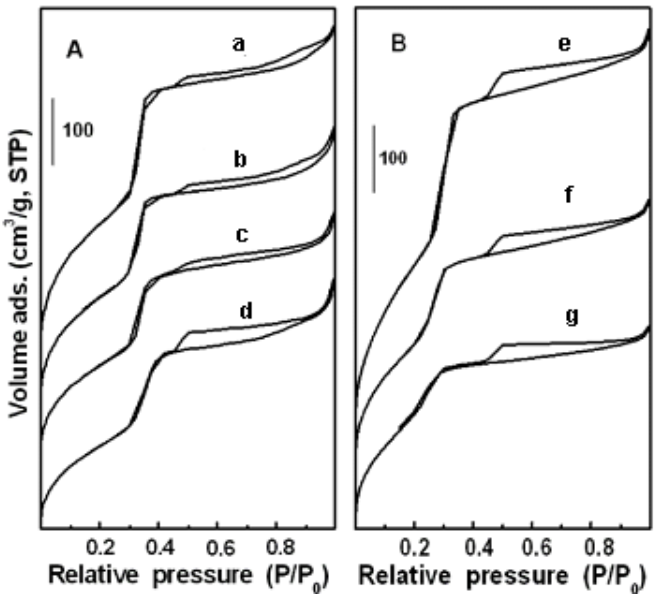

Figure 4.15 Nitrogen adsorption-desorption isotherms at 77 K of one-pot synthesis materials (**a**) M-TA, (**b**) M-OP-Ni(L^1)-TA, (**c**) M-OP-Ni($2L^1$)-TA, (**d**) M-OP-Ni($3L^1$)-TA and post-synthesis materials (**e**) M1'-ES, (**f**) M1'-ES-Ni($2L^1$) and (g) M1'-ES-Ni($3L^1$).

N_2 sorption isotherms. Nitrogen sorption isotherms at 77K and the corresponding pore size distributions are gathered in **Figure 4.15** and **Figure 4.16**, respectively. The obtained isotherms are of type IV according to the IUPAC classification,[38] and are characteristic of materials with uniform mesoscale porosities.[6, 169] Note that the acid extracted metal free materials prepared at 60 or at 130 °C, M-H and M1'-H, present similar surface area and pore volume, which is advantageous for comparison with non-functionalized materials. In addition, M-TA Ni free material treated according to *method TA* provides an appropriate reference for a full capped surface using trimethyl silyl groups. The profiles for M-OP-Ni(L^1)-TA, M-OP-Ni($2L^1$)-TA, M-OP-Ni($3L^1$)-TA and M-TA account for a narrow

pore size distribution and an average pore diameter of 3.7 nm, determined by using the BdB model (**Table 4.5**). The unit cell a_0 parameter for M-OP-Ni(L^1)-TA, M-OP-Ni($2L^1$)-TA, M-OP-Ni($3L^1$)-TA and M-TA is 5.0, 5.0 and 4.9 nm, respectively, which gives an apparent wall thickness of 1.4 ± 0.1 nm in all cases. The fact that both the pore size and the wall thickness are not modified by the incorporation of the Ni-L^1 complex, is in agreement with the presence of the metal complex inside the framework of the silica as previously observed in Rh@PMOs.[15]

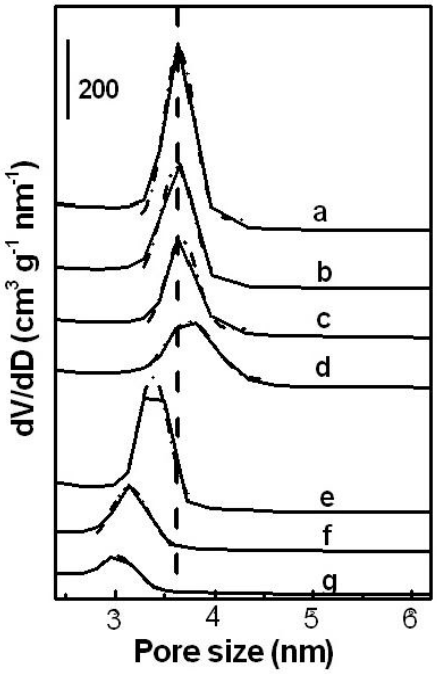

Figure 4.16 Pore-size distribution of (a) M-OP-Ni(L^1)-TA, (b) M-OP-Ni($2L^1$)-TA, (c) M-OP-Ni($3L^1$)-TA, (d) M-TA, (e) M1'-ES, (f) M1'-ES-Ni($2L^1$) and (g) M1'-ES-Ni($3L^1$). Gaussian simulation of the pore size profiles is indicated in dotted line.

However, if the BET specific surface and the total pore volume are compared (**Table 4.5**), a decrease of both parameters is observed for the Ni containg PMOs materials, M-OP-Ni(L^1)-TA, M-OP-Ni($2L^1$)-TA and M-OP-Ni($3L^1$)-TA compared to the metal-free material (M-TA). Indeed, the specific surface and the total pore volume of 730 $m^2.g^{-1}$ and 0.70 $cm^3.g^{-1}$, respectively, in M-TA decrease gradually upon incorporation of the Ni-L^1 complexes down to 470 $m^2.g^{-1}$ and 0.52 $cm^3.g^{-1}$, respectively, in M-OP-Ni($3L^1$)-TA. These values are given per gram of dehydrated material. A

correction considering the presence of the Ni-L^1 complex inside the framework of the silica should be taken into account and it will be discused below (see discusion and **Table 4.6**). In addition, a hysteresis is observed in the isotherms for $P/P_0 > 0.43$, which is more pronounced for the M-OP-Ni($3L^1$)-TA solid. This is likely due to cavitation because of the presence of defects in the porous mesostructure as observed by TEM (**Figure 4.12**).[170, 171] Finally, the microporosity present in the parent M-TA material seems to diminish upon incorporation of the metal complex, as shown for low relative preasures in **Figure 4.15**. Noteworthily, the large adsorption at low pressure ($P/P_0 < 0.1$) due to micropores in classical MCM-41 and also in the parent materials M-H and M1'-H (curve not shown here) is practically absent in silylated materials M-OP-Ni(YL^1)-TA. This feature is hardly seen in **Figure 4.15** because of the offsets used for the sake of clarity; otherwise the curves would have been almost superimposed one with another.

Table 4.5 Textural properties of mesoporous hybrid materials deduced from N_2 sorption isotherms at 77K.

Material	ϕ_{BdB}[a] (nm) ± 0.1	W_t (nm)[b] ± 0.1	S_{BET} ($m^2.g^{-1}$)[c] ± 50	V_p ($cm^3.g^{-1}$)[d] ± 0.02
M-OP-Ni(L^1)-TA	3.7	1.3	600	0.58
M-OP-Ni($2L^1$)-TA	3.6	1.4	530	0.52
M-OP-Ni($3L^1$)-TA	3.8	1.2	470	0.52
M-H[e]	--	--	1048	1.02
M-TA[f]	3.6	1.4	730	0.70
M1'-H[e]	3.7	1.0	1030	0.96
M1'-ES	3.4	1.4	860	0.71
M1'-ES-($2L^1$)	3.1	1.6	600	0.46
M1'-ES-($3L^1$)	2.9	1.8	550	0.35

a: using BJH model instead of the BdB one, the diameter would be 0.8 nm smaller in each case; b: apparent wall thickness is determined using $W_t = 2*d_{100}/3^{1/2} - \phi_{BdB}$; c: measured in the P/P_0 range 0.05-0.25; d: measured at $P/P_0 = 0.98$; e: the surfactant was extracted with an equimolar ethanolic solution of HCl (1 $mol.L^{-1}$) at 0°C; f: M presents an a_0-value of 4.8 nm in XRD.

Table 4.6 Surface area and pore volume considering different residual mass.

Material	S_{BET} [a] ($m^2.g^{-1}$)±50	S_{BET} [b] ($m^2.g^{-1}$)±50	S_{BET} [c] ($m^2.g^{-1}$)±50	V_p [a] ($cm^3.g^{-1}$)±50	V_p [b] ($cm^3.g^{-1}$)±50	V_p [c] ($cm^3.g^{-1}$)±50
M-TA	730	800	940	0.70	0.77	0.90
M-OP-Ni(L^1)-TA	600	750	930	0.58	0.73	0.90
M-OP-Ni($2L^1$)-TA	530	670	920	0.52	0.66	0.90
M-OP-Ni($3L^1$)-TA	470	610	840	0.52	0.67	0.93
M1'-ES-($2L^1$)	600	788	982	0.46	0.60	0.75
M1'-ES-($3L^1$)	550	681	965	0.35	0.43	0.61

a: the reference mass includes all the organic and inorganic matter of the materials except water, measured after treatment of the sample at 80 °C under vacuum overnight (pre-treatment conditions of the N_2 sorption isotherm); b: includes all inorganic matter, *i.e.*, NiO and SiO_2 both Ludox (inorganic) and organosilane (organic), obtained from the residual mass measured from TGA at 1000 °C, *i.e.* residual SiO_2 and NiO; c: includes only inorganic silica.

Synthesis and characterization of post-synthesis materials.

Post-synthesis materials were synthesized to be compared with the PMOs materials. The so-called molecular stencil patterning (MSP) approach developped by some of us [110, 160] was used to achieve an homogeneous distribution of the Ni complexes in the internal surface of the silica (**Scheme 4.4**). Starting from the as-made LUS (M1'), half of the surfactant was removed and trimethylsilyl (TMS) functions were grafted without displacement of the remainging surfactant, obtaining material M1'-EPS. In this material the surfactant molecules are homogeneouly distributed and they are acting as stencil to further incorporate a second function, which is the Ni-L^1 in this study. Therefore, after the removal of the remaining surfactant and grafting of the Ni-L^1 complexes with Y=2-3, materials M1'-ES-Ni($2L^1$) and M1'-ES-Ni($3L^1$) were respectively obtained. The molar composition of the final material M1'-ES-Ni($2L^1$) deduced from EA and TGA, was the following: 89 SiO_2: 12 TMS: 4 $Ni(AAPMS)_2$, and has been taken into account to dessign the **Scheme 4.3**.

The XRD patterns of these materials (**Figure 4.17**) show the characteristic <100>, <110>, <200> reflections of a hexagonal mesostructure with d_{100} = 4.0 nm for

M1'-ES-Ni(3L^1). In both cases, a lower intensity for all the peaks was observed compared to the parent support, M1'-ES, indicating the incorporation of the Ni complex inside the channels of the silica. The IR spectrum of both samples (**Figure 4.14**) presents an absorption peak located at 1385cm^{-1} for M1'-ES-Ni(3L^1). This peak corresponds to NO_3^-, indicating that the conterions of the Ni (II) complex of post-synthesis materials were still the nitrate ions of the initial nickel salt.

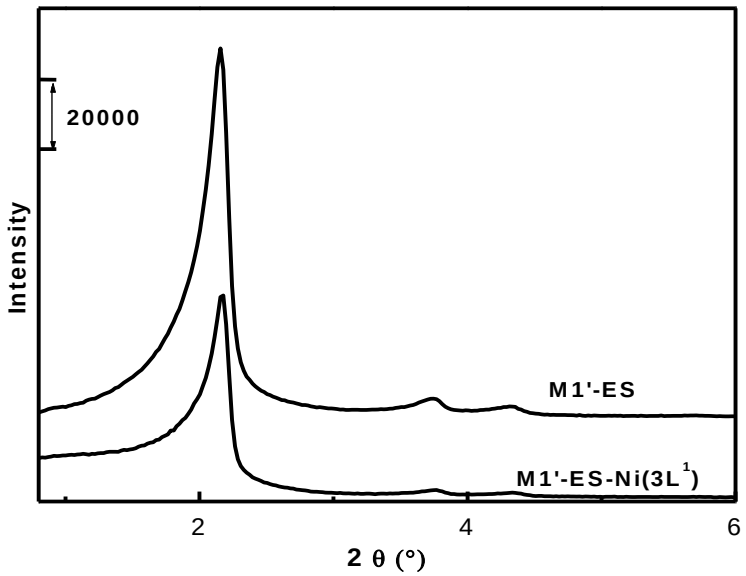

Figure 4.17 XRD patterns of M1'-ES and M1'-ES-Ni(3L^1).

A molar ratio N/Ni of 5.9 and 8.2 were calculated for M1'-ES-Ni(2L^1) and M1'-ES-Ni(3L^1), respectively, from EA. These results match the theoretical values of N/Ni molar ratio for M1'-ES-Ni(2L^1) and M1'-ES-Ni(3L^1) which should correspond to 4 or 6 nitrogen atoms from 2 or 3 ligands, respectively, and 2 nitrogen from 2 nitrate counterions. Therefore, ligand/Ni molar ratio of 1.9 and 3.1 can be deduced for M1'-ES-Ni(2L^1) and M1'-ES-Ni(3L^1), respectively (**Table 4.4**).

In the N_2 sorption isotherm of the post-synthesis samples (**Figure 4.15**), a pronunced decrease of both specific surface and total pore volume was observed upon grafting of the Ni-L^1 complexes: from 860 m^2.g^{-1} and 0.71 cm^3.g^{-1}, respectively, in M1'-ES to 550 m^2.g^{-1} and 0.35 cm^3.g^{-1}, respectively, in M1'-ES-Ni(3L^1). The post-grafting of the Ni complexes on the M1'-ES silica was characterized by a diminution of the pore size from

3.4 nm in M1'-ES down to 3.0 nm in the M1'-ES-Ni(YL^1) (Y=2, 3) materials (**Table 4.5**). These results are all indicating the presence of the metal complexes inside the pore channel for the post-synthesis materials M1'-ES-Ni($2L^1$) and M1'-ES-Ni($3L^1$).[22] Finally, a hysteresis was also observed in the isotherms for $P/P_0>0.42$, which was already present in the parent material M1'-ES. Upon grafting of the Ni complexes, this hysteresis is not modified.

4.3.1.2 Nickel exchange ability and metal displacement

We investigated the metal exchange ability on both one-pot and post-synthesis materials. The stability constants of $Cu(en)_2^{2+}$ and $Ni(en)_2^{2+}$ are $10^{19.6}$ and $10^{14.1}$, respectively,[172] which indicates that copper (II) possess a higher affinity to ethylenediamine (en). Therefore, the solids containing the Ni-L^1 complexes were treated with copper(II) nitrate. Four different experimental procedures were tested.

In *method 1*, an HCl pretreatment was performed: M-OP-Ni($3L^1$)-TA was firstly washed with 10 eq of HCl in order to protonate the AAPS ligand to favour Ni(II) decoordination. Then the solid obtained was neutralized by using tetramethylammonium hydroxide, and it was finally treated with an ethanolic solution of copper (II) nitrate, obtaining material M-OP-Ni($3L^1$)-TA-CuNH. In the *method 2*, M-OP-Ni($3L^1$)-TA was treated in a similar way as in the previous procedure but without HCl pretreatment, and the obtained solid was named M-OP-Ni($3L^1$)-TA-CuN. We noticed that in both process about 15-20% of TMS were lost *via* quantitative IR analysis.[160] **Table 4.7** lists the Ni and Cu weight % measured by ICP-MS and the Cu(II) content measured by EPR analysis. It is worth mentioning that Ni content in M-OP-Ni($3L^1$)-TA-CuNH decreases to 1.4 wt% compared to the parent material, M-OP-Ni($3L^1$)-TA, with 1.9 wt% of Ni, while the Ni content in M-OP-Ni($3L^1$)-TA-CuN is maintained at 1.9 wt%. In addition, in both M-OP-Ni($3L^1$)-TA-CuNH and M-OP-Ni($3L^1$)-TA-CuN materials, a relatively high Cu content of 4.9 wt% and 3.1 wt% was determined, respectively.

Table 4.7 Elemental analysis for the ion exchange tests (wt %).

Material	Ni ± 0.01% (ICP-MS)	Cu ± 0.01% (ICP-MS)	Cu[a] ± 0.01% (EPR)	Yield of metal exchange mol. %
M-OP-Ni(L^1)-TA-CuN	2.1	1.1	0.1	4
M-OP-Ni($2L^1$)-TA-CuN	1.7	1.6	n.a.	n.a
M-OP-Ni($3L^1$)-TA-CuN	1.9	3.1	0.15	7
M-OP-Ni($3L^1$)-TA-CuNH	1.4	4.9	0.5	24
M1'-ES-Ni($2L^1$)-CuN	0.4	3.9	2.4	89
M1'-ES-Ni($2L^1$)-H	0.17	--	--	100
M1'-ES-Ni($2L^1$)-HCu	0.05	4.8	2.3	85

a: Quantification of the EPR signal was performed by double integration after base line correction. Ni content: M-OP-Ni(L^1)-TA, 2.2%; M-OP-Ni($2L^1$)-TA, 1.8%; M-OP-Ni($3L^1$)-TA, 1.9% and M1'-ES-Ni($2L^1$), 2.5% (See **Table 4.4**).

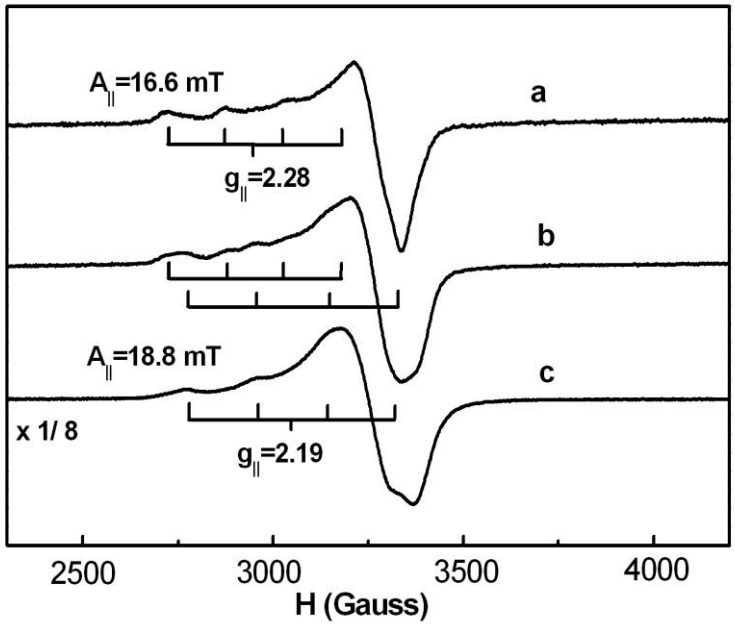

Figure 4.18 EPR spectra at 298 K of (a) M-OP-Ni($3L^1$)-TA-CuN, (b) M-OP-Ni($3L^1$)-TA-CuNH, (c) M1'-ES-Ni($2L^1$)-CuN. Experimental conditions: frequency = 9.35GHz, power = 160 mW (M-OP-Ni($3L^1$)-TA-CuN, M-OP-Ni($3L^1$)-TA-CuNH) and 10 mW (M1'-ES-Ni($2L^1$)-CuN), modulation amplitude: 3 G and modulation frequency: 100 kHz.

The coordination of copper (II) in M-OP-Ni($3L^1$)-TA-CuN and M-OP-Ni($3L^1$)-TA-CuNH was investigated using EPR (**Figure 4.18**). For M-OP-Ni($3L^1$)-TA-CuN the $g_{||}$ and $A_{||}$ parameters are equal to 2.28 and 16.6 mT,

respectively, which corresponds to the EPR signature of a $[Cu(L^1)]^{2+}$ species.[124] M-OP-Ni($3L^1$)-TA-CuNH exhibits two EPR signatures, the first one is the same as in M-OP-Ni($3L^1$)-TA-CuN and the second one appears with roughly a similar intensity as the first one. The EPR fingerprint of the latter, $g_{||}$ = 2.19 $A_{||}$ and $A_{||}$ = 18.8 mT, matches well with a $[Cu(L^1)_2]^{2+}$species.[173] A quantitative analysis shows that alltogether these EPR active species accounts for as 0.15 and 0.5 wt% of Cu in M-OP-Ni($3L^1$)-TA-CuN and M-OP-Ni($3L^1$)-TA-CuNH, only. This is indeed a very small fraction of the copper contained in the materials and far less than the initial Ni content to displace. Most of copper is obviously EPR inactive.

These data suggest that *method 1* is not efficient to displace Ni(II) ions from their sites. On one hand, copper (II) mostly reacts with the silica surface to generate EPR silent silicate like species.[174] The acidic treatment that seems to promote this effect must have some relation with TMS leaching leading to a less protected internal surface (not further studied here). On the other hand, the EPR active species are isolated copper sites stabilized by complexation by a single L^1 grafted ligand, as far as the EPR signal is concerned. These extra L^1 ligands are more likely located in the channel and not complexed by nickel in the mother material M-OP-Ni($3L^1$)-TA. The preliminary acidic treatment of *method 2* seems to displace Ni(II) ions only partially, 0.5 out of 1.9 wt%, resulting 24 mol. % of metal exchange (**Table 4.7**). Since there is only 0.15 wt% of EPR active $Cu(L^1)_2{}^{2+}$, it is difficult to unequivocally correlate these sites with those left by nickel (II). Here, the displacement of nickel is due to partial protonation of L^1 site in the wall apparently not reversed by the treatment with TMAOH. This illustrates how much the nickel sites in the Ni(YL^1)@PMOs series are stabilized inside de framework of the pore wall.

For comparison, replacement of nickel by copper was also tested on M1'-ES-Ni($2L^1$) according to *methods 3* and *4* leading to M1'-ES-Ni($2L^1$)-HCu and M1'-ES-Ni($2L^1$)-CuN, respectively. *Method 3* includes an acidic pretreatment as seen before, that drastically decreases the nickel content from 2.5 wt% down to 0.17 wt% [M1'-ES-Ni($2L^1$)-H], corresponding to 100 mol. % of metal exchange (**Table 4.4**). The sample was then neutralized to deprotonate the L^1 ligand and treated with $Cu(NO_3)_2$,

obtaining the M1'-ES-Ni(2L^1)-HCu material, with a Cu loading of 4.8 wt%. A lower value of 2.3 % of Cu was measured for this material by EPR, which is close to the value of the original Ni content. This sequence of reactions was monitored by UV-visible spectroscopy attesting for the exchange of the Ni(II) by the Cu(II) ion (**Figure 4.19**). Finally, M1'-ES-Ni(2L^1) was directly exchanged with the Cu (II) solution (*method 4*) obtaining M1'-ES-Ni(2L^1)-CuN. The Ni and Cu contents in this sample were 0.4 and 3.9 wt%, respectively. However, the EPR active copper content was 2.4 wt%, corresponding to 89 mol. % of metal exchange. These results indicate that for the post-synthesis materials, the Ni(II) ions can be easly exchanged by the Cu(II) ones. However, an excess of copper is observed compared to the initial Ni amount, due probably either to the formation of diamagnetic copper clusters or to the damage of the internal surface by the formation of copper silicate. This last process could be accelerated by the acid treatment that can promote TMS leaching leading to a less protected internal surface.

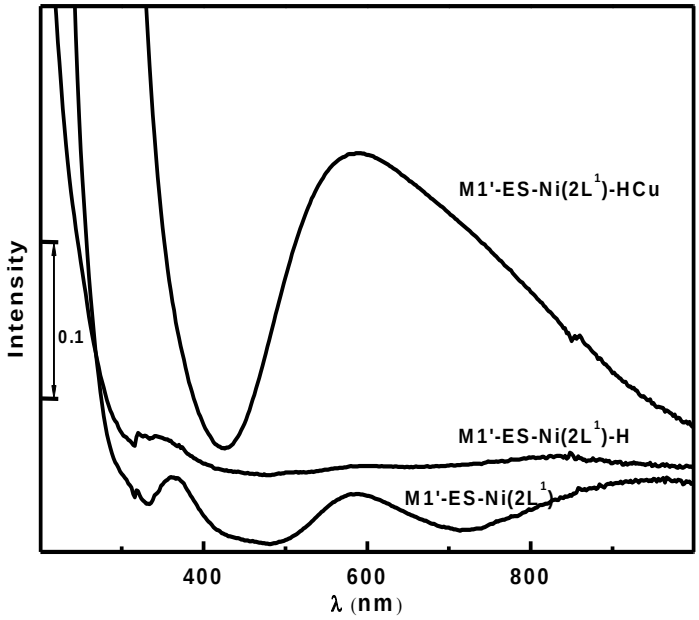

Figure 4.19 UV-visible absorption bands of M1'-ES-Ni(2L^1), M1'-ES-Ni(2L^1)-H, and M1'-ES-Ni(2L^1)-HCu.

4.3.1.3 Coordination state of Ni(II) in the materials

The UV-visible spectra were also recorded for the PMOs solids M-OP-Ni(YL^1) (Y=1-3) and the parameters deduced are gathered in **Table 4.8** and **Figure 4.20**. ν_3 and ν_2 bands for M-OP-Ni(L^1) were observed at 25600 and 15800 cm^{-1}, which were shifted of $\Delta\nu_3$= -1200 cm^{-1} and $\Delta\nu_2$= -300 cm^{-1} respectively, compared to the Ni-Pren solution Y=1 (**Table 4.3**). For material M-OP-Ni($2L^1$) and M-OP-Ni($3L^1$) a $\Delta\nu_3$ shift of -600 cm^{-1} and -530 cm^{-1} was observed compared to the aqueous solution Y= 2 and Y=3, respectively. This shift is an indication of a change in the coordination environment of the Ni ion in the solid, most probably due to the replacement of some water molecules by silanolate or silanol groups (*vide infra*). In agreement, β was shifted for the solids compared to the solution (**Table 4.3** and **Table 4.8**) 0.75 for M-OP-Ni(L^1) compared to 0.85 in solution Y =1, 0.79 for 2 compared to 0.81 in solution Y =2 and 0.79 for M-OP-Ni($3L^1$) compared to 0.80 in solution Y =3. Indeed, this shift was very important for material M-OP-Ni(L^1) compared to M-OP-Ni($2L^1$) and M-OP-Ni($3L^1$), since more water molecules may be replaced by silanolate or silanol groups of the silica in M-OP-Ni(L^1). Finally, the position of the bands in the UV-visible spectra did not change for the capped samples, M-OP-Ni(L^1)-TA, M-OP-Ni($2L^1$)-TA and M-OP-Ni($3L^1$)-TA, indicating that the Ni environment was retained after capping.

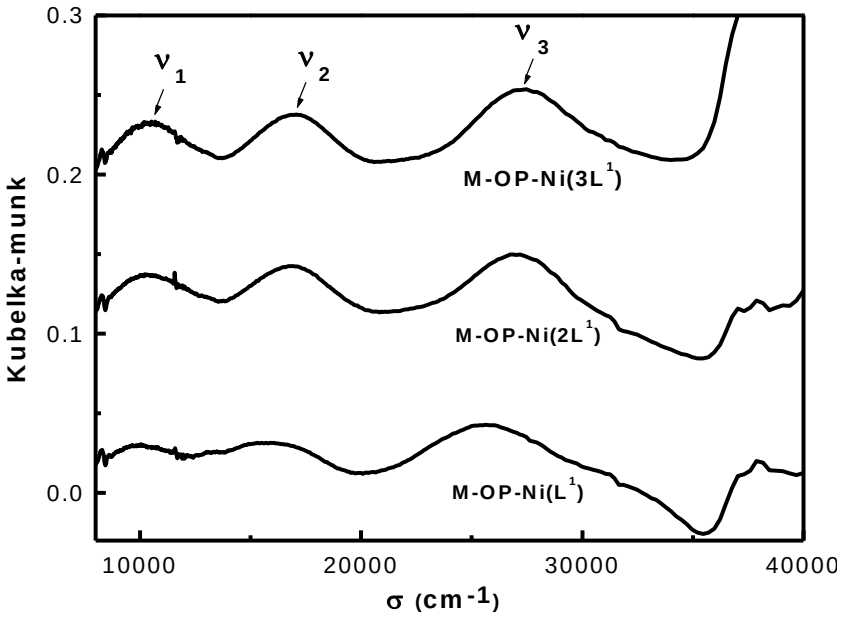

Figure 4.20 UV-visible diffuse reflectance spectra of M-OP-Ni(L^1), M-OP-Ni($2L^1$) and M-OP-Ni($3L^1$).

The UV-visible spectrum for post-synthesis materials M1'-ES-Ni($2L^1$) and M1'-ES-Ni($3L^1$) presents in both cases two absorption bands centered at 27600 cm^{-1} and 17100 cm^{-1} (**Table 4.8**). These values are very close to the ν_3 and ν_2 values observed for the Ni-Pren solution Y=2, *i.e.* 27800 cm^{-1} and 17200 cm^{-1}, respectively, indicating the presence of $[Ni(L^1)_2(H_2O)_2]^{2+}$ as major species, in both solids. Expectingly, β were also very close in these materials and in solution of $[Ni(Pren)_2(H_2O)_2]^{2+}$ 0.80 and. 0.81, respectively.

Table 4.8 Parameters obtained from UV-visible spectra for Ni containing samples.

Sample	ν_3 ±50 cm^{-1}	ν_2 ±50 cm^{-1}	Δ ±50 cm^{-1}	β ± 0.015
M-OP-Ni(L^1)	25600	15800	9370	0.75
M-OP-Ni($2L^1$)	27200	16800	10500	0.79
M-OP-Ni($3L^1$)	27400	17000	10700	0.79
M-OP-Ni(L^1)-TA	25400	15600	9370	0.75
M-OP-Ni($2L^1$)-TA	26900	16600	10400	0.79
M-OP-Ni($3L^1$)-TA	27400	16900	10600	0.80
M-OP-Ni($3L^1$)-TA-SCN	27400	17000	10690	0.79
M1'-ES-Ni($2L^1$)	27600	17100	10740	0.80
M1'-ES-Ni($3L^1$)	27600	17100	10740	0.80
M1'-ES-Ni($3L^1$)-en	28300	17700	11210	0.79
M1'-ES-Ni($3L^1$)-SCN	27900	17500	11110	0.77

Δ: calculated crystal field considering *Oh* symmetry, β: nephelauxetic parameter, $\beta=B/B_0$ (B, B_0 Racah parameter, β caculated from formula S1), B_0=1041 cm^{-1} [free Ni(II) ion].

4.3.1.4 Nickel accessibility

Metal accessibility was tested by using ethylenediamine (**en**) and the thiocyanate ion (SCN^-) as probes on PMOs and post-synthesis materials. Four equivalents of KSCN were added to an ethanolic solution containing M-OP-Ni($3L^1$)-TA or M1'-ES-Ni($3L^1$), and after reaction,

washing and drying, M-OP-Ni($3L^1$)-TA-SCN and M1'-ES-Ni($3L^1$)-SCN were respectively obtained. In the FT-IR spectra, both samples present an absorption band at 2090 cm^{-1}, that can be assigned to the stretching band ν(CN) of SCN^-. The peak intensity was much stronger for M1'-ES-Ni($3L^1$)-SCN than for M-OP-Ni($3L^1$)-TA-SCN. In addition, for M1'-ES-Ni($3L^1$)-SCN the increase of the ν(CN) band was concomitant with a decrease of the peack assigned to NO_3^- (**Figure 4.14**).

From EA, SCN^-/Ni molar ratios were found to be 0.44 and 1.58 for M-OP-Ni($3L^1$)-TA-SCN and M1'-ES-Ni($3L^1$)-SCN, respectively, indicating that SCN^- ions coordinate at least partially nickel in Ni@PMOs and nearly quantitatively in post-synthesis material. In addition the intensity of the band at 850 cm^{-1} indicates that TMS groups were mostly maintained after SCN^- treatment in both cases, as determined form quantitative IR analysis (**Figure 4.14**). This is consistent with EA providing TMS/Si_{inorg} molar ratios were determined to be 0.20 and 0.10 for M-OP-Ni($3L^1$)-TA-SCN and M1'-ES-Ni($3L^1$)-SCN, respectively, which were 0.24 and 0.12 for the respective mother materials M-OP-Ni($3L^1$)-TA and M1'-ES-Ni($3L^1$). The position of the ν_3 and ν_2 bands in the UV-visible spectra was not modified for M-OP-Ni($3L^1$)-TA-SCN compared to M-OP-Ni($3L^1$)-TA, whereas it was shifted to 27900 cm^{-1} and 17500 cm^{-1} for M1'-ES-Ni($3L^1$)-SCN, from 27600 cm^{-1} and 17100 cm^{-1} in M1'-ES-Ni($3L^1$). In addition, β decreased noticingly from 0.80 to 0.77 on the latter case. These results evidence a facile and substential reaction of the SCN^- ligand with Ni(II) ions (SCN^-/Ni=1.58) in the post-synthesis materials with a concomitant displacement of the nitrate counterion. By contrast, in the Ni@PMOs material the thiocyanate does not reach the nickel coordination sphere.

Similarly, the bidentate ethylenediamine ligand can bind nickel centers in material M1'-ES-Ni($3L^1$). According to the blue shift of the electronic d-d transitions observed on the so-obtained M1'-ES-Ni($3L^1$)-en material, one equivalent is enough to reach 28300 cm^{-1} and 17700 cm^{-1}, respectively, for a crystal field Δ of 11210 cm^{-1}, and β of 0.79 consistent with a coordination with a third bidentate diamino ligand en.

4.3.2 General discussion

Specificity of the present synthesis route. Sol-gel synthesis of many oxides including silica are performed via acid or base catalysis below pH of 2 or higher than 8 up to 13. Since polyamines have pK_a ranging from 9 to 11, their choice as complexing agent to stabilize or trap transition metal ions like in the present study, imposes basic routes to avoid competition between protonation and complexation. However, under neutral conditions, amino-ligands such as L^1 can still be used as far as the complexation constant pK is high enough. This is the case for copper(II) as shown by Karakassides *et al*.[158] Nonetheless, they observed that starting from $[Cu(L^1)_2]^{2+}$ complexes a mixture of $[Cu(L^1)]^{2+}$ and $[Cu(L^1)_2]^{2+}$ species is present in the as-made PMOs material. Another synthesis in neutral media was performed by Corriu *et al*. according to a recipe derived from the SBA-15 with tribock copolymers.[17] It implies *cyclam* a strongly complexing tetra aza cycle not sensitive as much as bidentate en, Pren or L^1 ligands at stake here. To our knowledge there is only one report concerning one-pot synthesis of silica-metal complexes hybrid materials in basic media, by Corma *et al*.[119] It is dealing with a vanadyl Schiff base complex introduced in the silica framework using NH_3 (20%) as base source. There is unfortunately little information on the effective location of the complex in the periodic silica. The emphasis is brough rather on the catalytic performance in the enantiomeric excess for carbonyl addition.

The actual work appears to be the first one to fully investigate the specificity of the basic route for the synthesis of a templated silica-metal complex hybrid material. In addition, this is the first one to deal with bidentate ligand showing that conditions may be found to preserve the complex integrity during the sol-gel evolution toward the full elaboration of the structured porous system. The synthesis conditions have been adapted from the known recipe of LUS using cationic surfactant with tosylate as counterion (CTATos).[51, 153, 175] This led to a *P6mm* hexagonal porous structure similar to MCM-41 despite the quite low temperature (60 °C) of ageing.[6, 164] In addition to the low temperature process, the Ni@PMOs synthesis possesses several advantages. First, the sodium silicate solution is a very low coast source of silica and organic free. Second,

the CTATos is also the cheapest cationic surfactant source commercially available, it is used in a low amount and very high yield (> 95% as in LUS). Third, in the Ni@PMOs materials, the yield in Ni is about 80 %. Therefore, our synthesis route is element efficient particularly considering the expensive and polluting precursors.

The point concerning the yield in nickel is surprizing. Indeed, the rate of the hydrolysis and condensation of organotrialkoxysilanes (R'-Si-$(OR)_3$) in basic conditions is slower than that of tetraalkoxysilanes ($Si(OR)_4$) and $Si(OH)_4$).[176] This would be detrimental to the incorporation of the organosilane in the structure. To the contrary, the high yield in Ni suggests here that the Ni-L^1 complexes are likely the fastest to hydrolyze. This striking point is to be related with an activation of the Si-OMe bond by direct linkage of Ni(II) with the methoxy moities. This point needs further investigation, not treated here.

The key point of surfactant removal. The material would have been useless without extraction of the surfactant to liberate the porosity for further applications. To preserve the integrity of the complexes at this stage of the process, one had to avoid also the protonation of L^1 and to prevent the collapse of the porous structure of these solids synthesized at 60°C only. The first reports concerning the stabilization of templated silicas of MCM-41 type were from Tatsumi *et al*. who brought the emphasis on the mechanical resistance. Full silylation was proposed on calcined samples.[58] Later, Jaroniec *et al*. showed that the silylation treatment of MCM-41 using an excess of CTMS performed directly on the as-made silicas led to simultaneous displacement of the surfactant and full surface capping.[59] When HMDSA is used instead, it was thought that silyation occurs only with the external surface by keeping the surfanctant inside the channels. In fact, this is not the case and Badiei *et al*. show that *ca*.1/3 of the surfactant is indeed displaced during the silylation reaction leading to partial surface capping.[177] The retention or the removal of the surfactant is pH dependent and is related to an eventual neutralization of the silanolate groups that retain the cationic surfactant. Therefore, it depends on the nature of the reacting silane.[177]

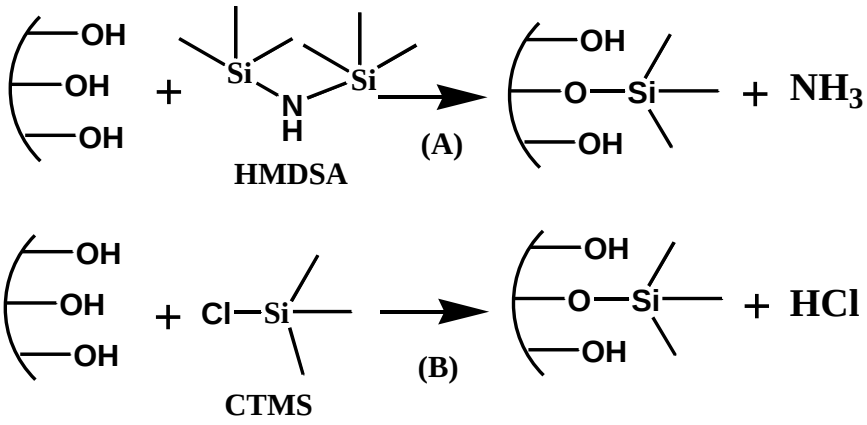

Scheme 4.5 Reactions of HMDSA with silanol groups of materials (A), and CTMS with silanol groups of materials (B).

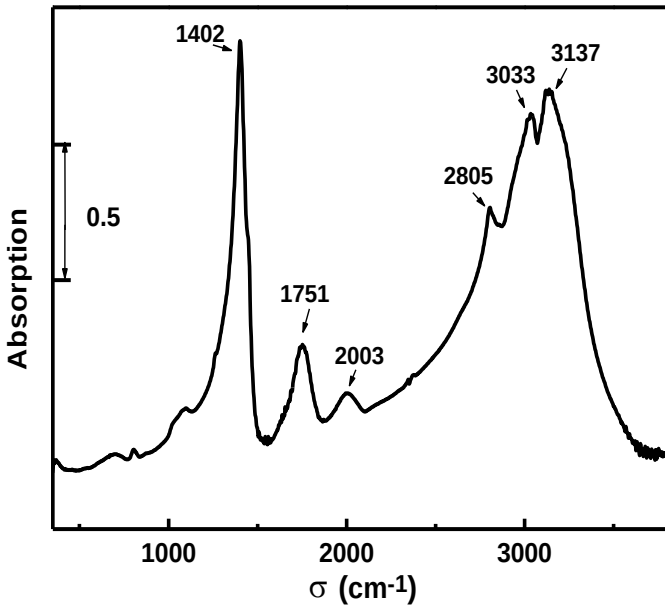

Figure 4.21 FT-IR spectrum of the precipitate (NH_4Cl).

The silylation using the reaction of HMDSA with silanol (≡SiOH) groups evolves the basic NH_3 molecule and avoids the silanolate (≡SiO^-) neutralization, according to **Scheme 4.5A**. By contrast, the reaction using CTMS generates HCl that neutralizes silanolate into silanol groups. Consequently, the cationic surfactant is removed according to **Scheme 4.5**. When HDMSO is the silylating agent, H_2O is produced instead of HCl. In this case, there is no pH change and no surfactant removal expected.[177] To remove the surfactant, and to avoid excessive acidification CTMS was combined with

HMDSA (*method TA*). For comparison, *method T* was tested using CTMS alone and *method TO* was using a mixure of CTMS and HMDSO. In agreement with the expected pH control described above, the best treatment is *method TA*. The last concern was the production of a white colloidal suspension of NH_4Cl as revealed by FT-IR (**Figure 4.21**). Fortunately, a mere filtration sufficed for its elimination (absence of the FT-IR bands of NH_4^+ in M-OP-Ni(YL^1)-TA materials).

Location of nickel (II) in the materials. Here the emphasis is brought on the characteristics that differentiate Ni@PMOs materials from post-synthesis analogues. The first difference shows up on the XRD patterns of the surfactant containing materials with broader XRD peak for Ni@PMOs in comparison with the Ni free sample M. In addition, the peak intensity (integrated area) is increasing from the reference material M to material M-OP-Ni($2L^1$) and M-OP-Ni($3L^1$) indicating a higher XRD contrast. This is expected for nickel located inside the pore walls since it increases the electron density of the wall while the electron density in the empty channel remains low. To the contrary, when the metal is located in the channel the electron density shall increase in the channel leading to a lower difference of electron density between the wall and the channel. This is effectiveley observed in the grafted samples as shown in the series M1'-ES, M1'-ES-Ni($2L^1$) and M1'-ES-Ni($3L^1$).

The yield of the capping reaction measured from the TMS coverage is also an indication of the location of the species. Note that in comparison to the Ni free sample that exhibits a TMS/Si molar ratio of 0.29 (considered here as 100% coverage, materials M-OP-Ni(L^1)-TA, M-OP-Ni($2L^1$)-TA and M-OP-Ni($3L^1$)-TA exhibit a lower coverage of *ca*. 80% (**Table 4.4**). By contrast this coverage drops down more drastically to less than 52 % in the grafted materials M1'-ES-Ni($2L^1$) and M1'-ES-Ni($3L^1$). For the latter, this is consistent with a steric hinderence on the accessibility of the silanol groups that are located nearby or below the grafted species. For the former the slight decrease of surface reactivity suggests a lower silanol density probably in the zone where the complex is underlying inside the wall; this is expected since the pore wall is very thin (~1.4 nm) and about the size of the complex (~1 nm). By contrast, for materials with

grafted Ni complexes, M-OP-Ni($2L^1$) and M-OP-Ni($3L^1$), the unchanged pore size and wall thickness for Ni@PMOs is also a strong evidence for the complex incorporation in the pore wall, according to N_2 sorption isotherms (M-OP-Ni(YL^1)-TA, **Table 4.6**, **Figure 4.15** and **Figure 4.16**). However, as indicated earlier when specific surface and pore volume are compared, the neat decrease of their values in Ni@PMOs need to be commented. A better reference of mass for the specific characteristics may likely be the inorganic SiO_2, instead of the dehydrated material that contains both organosilane ligands and nickel ions contrary to M-TA. The inorganic silica is calculated from residual mass at 1000°C from TGA withdrawing the NiO fraction. After such a correction, both characteristic for Ni@PMOs fall in the range of the metal free reference M-TA (M-TA, 940, m^2g^{-1} and 0.90 cm^3g^{-1}, M-OP-Ni(L^1)-TA, 930 m^2g^{-1} and 0.90 cm^3g^{-1}, M-OP-Ni($2L^1$)-TA, 920 m^2g^{-1} and 0.90 cm^3g^{-1} and M-OP-Ni($3L^1$)-TA, 840 m^2g^{-1} and 0.93 cm^3g^{-1}, **Table 4.6**). For sample M-OP-Ni($3L^1$)-TA the still lower value observed is in agreement with the presence of higher defects concentration seen on the TEM picture (**Figure 4.12A**) as already mentionned, and on the isotherms with the presence of the horizontal hysteresis (**Figure 4.15**). Such defects are most probably induced by the incorporation of Ni-L^1 complexes during the silica growth in the sol-gel process, and also by the presence of none complexed L^1 in M-OP-Ni($3L^1$)-TA. Consistenly, almost no defects were observed for the Ni free material M-H by TEM (**Figure 4.12B**). Similar types of defects have been reported by Mou *et al.*[178] They indicated that the hysteresis is associated with the pore-blocking effect around the embedded voids in the framework structure.[178]

The results of metal exchange ability and accessiblity are evidences of location of the species. The Ni(II) complex in the framework is stable and difficult to exchange by Cu (II). Even using HCl to protonate the amino-ligand, only a small amount of Ni was removed. Indeed, when M-OP-Ni($3L^1$)-TA was exchanged by Cu (II) obtaining M-OP-Ni($3L^1$)-TACuN, the Ni content slightly changed and a high content of Cu was observed (3.9 wt%, with only 0.5 % Cu EPR active). The same behaviour was observed for M-OP-Ni($3L^1$)-TACuH, M-OP-Ni($2L^1$)-TACuN and M-OP-Ni(L^1)-TACuN, with most of the Cu EPR inactive. However, when the post-synthesis materials reacted with

HCl in the same conditions, the color of the obtained solid turned to white, indicating a quantitative decomplexation of the ligand (the Ni concentration tested by ICP-MS decreased from 2.5 % to 0.17 %, **Table 4.7**). In particular, in the case M-OP-Ni($3L^1$)-TACuN, the main Cu (II) species active in EPR was mostly the $[Cu(L^1)]^{2+}$ (**Figure 4.18**), which should correspond to 12 % of the free L^1 ligand being complexed with Cu(II). This value is lower than the free ligand to total ligand ratio observed in M-OP-Ni($3L^1$)-TA, indicating that no nickel was echanged in the PMOs material, and that the only Cu(II) incorporated into the material corresponds to the coordination of the free ligand, the rest of the copper being as copper silicate or copper clusters in the pore-wall interface. However, when a pre-treatment with HCl is previoulsy performed, a mixture of $[Cu(L^1)]^{2+}$ and $[Cu(L^1)_2]^{2+}$ is observed indicating a slight access to the internal metal complexes. Furthermore, Ni (II) in PMOs materials showed a low accessibility to the **SCN^-** ion while Ni (II) in post-synthesis materials can be easily "touched" by SCN^- ion and **en**. These results are also in agreement with the presence of the Ni-L^1 complex in the wall close to the pore, but difficult to access.

Coordination of nickel (II) in the materials. In contrast with the grafted Ni(II) complexes, the most striking properties of the Ni complexes in PMOs are: i) the inaccessibility towards ligand exchange, ii) the unexchangeability of nickel by copper(II) ions and, iii) the resistence to metal leaching under acid treatment in the former materials. This requires some explanation in terms of coordination. **Figure 4.22** was designed to better analyze the frequency shift using the ν_3 electronic transition. Indeed, ν_3 is more sensitive and better characterized than ν_1 and ν_2. The frequency positions are compared with those of $[Ni(H_2O)_{6-2Y}(L^1)_Y]$ species measured in fresh dilute aqueous solution with the same ligand to Ni molar ratio, Y. The arrows of **Figure 4.22** shows the $\Delta\nu_3$ red shift discussed here since it characterizes the change of coordination sphere from the solution to the solid. In materials M-OP-Ni($2L^1$) and M-OP-Ni($3L^1$), the similar shifts are interpreted first since it may easily be discussed in terms of mere ligand exchange.

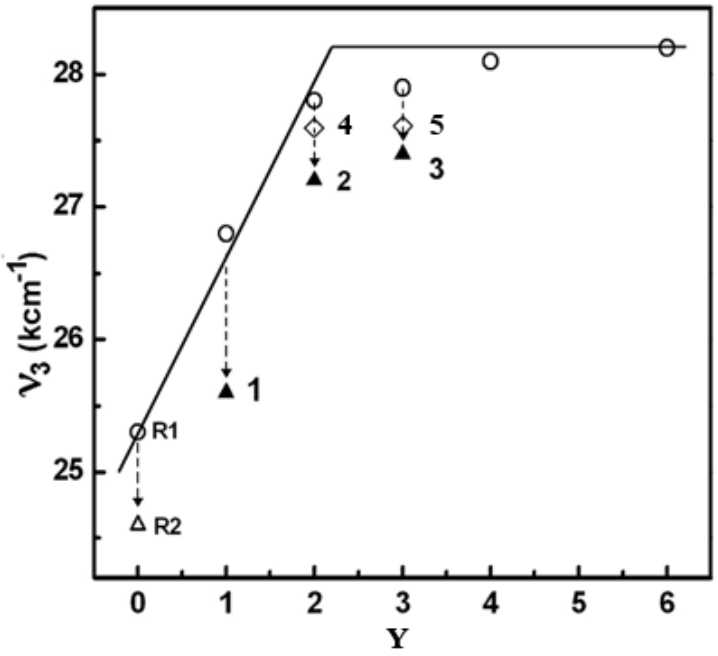

Figure 4.22 Frequency of ν_3 in octahedral Ni^{2+} ion *versus* **Y** = L^1/Ni molar ratio, "○": complexes in solution (**Y**=1, 2, 3, 4, 6); "▲": PMOs [**1**: **M-OP-Ni(L^1)**, **2**: **M-OP-Ni($2L^1$)**, and **3**: **M-OP-Ni($3L^1$)**]; "◇": post-synthesis materials (**4**: **M1'-ES-Ni($2L^1$)** and **5**: **M1'-ES-Ni($3L^1$)**), references R_1 = $[Ni(H_2O)_6]^{2+}$ and R_2 = $[Ni(\equiv SiO)_2(H_2O)_4]$[105]; downward dashlined arrows for the frequency red shift discussed in the text.

In comparison with a solution of $[Ni(H_2O)_2(L^1)_2]^{2+}$, material M-OP-Ni($2L^1$) exhibits a red shift of *ca.* -600 cm^{-1}. A similar shift has been observed when $[Ni(NH_3)_4(H_2O)_2]$ and $[Ni(NH_3)_2(H_2O)_4]$ nickel complexes where adsorbed on amorphous silicas.[105] This was assigned to the formation of $[Ni(NH_3)_2(H_2O)_2(\equiv SiO)_2]$ and $[Ni(NH_3)_4(\equiv SiO)_2]$ surface complexes, respectively. The authors used the average crystal field approximation assuming that the octahedral symmetry is roughly maintained (symmetry change ignored). They concluded that each water molecule substituted by a silanolate moities produces a red shift of -300 cm^{-1} on ν_3 (reference R_1 to R_2, **Figure 4.22**). Applying the same reasoning for the position of ν_3 in material M-OP-Ni($2L^1$) leads to the conclusion that two silanolate groups substituted two water molecules in the mother precursor $[Ni(H_2O)_2(L^1)_2]^{2+}$ yielding a neutral $[Ni(L^1)_2(\equiv SiO)_2]$ complex (**Scheme 4.6**). This hypothesis is fully consistent with the absence of nitrate as revealed in the IR spectra. For material M-OP-Ni($3L^1$), a smaller red shift, of *ca.* -530 cm^{-1} may also be

explained similarly taking into account that the solution with a ligand to nickel ratio **Y**= 3, used for the synthesis of M-OP-Ni($3L^1$), contains a mixture of 76% of $[Ni(H_2O)_2(L^1)_2]^{2+}$ and 26 % of $[Ni(L^1)_3]^{2+}$ species. If one assumes that the aqua ligands of $[Ni(H_2O)_2(L^1)_2]^{2+}$ are the only ones to undergo a substitution by the silanolate moities, then one should have a mixture containing also 76% of $[Ni(\equiv SiO)_2(L^1)_2]$ and 24% of $[Ni(L^1)_3]^{2+}$ species. The final material would exhibit a single broad band with an average position resulting in an intermediate shift of -460 cm^{-1}. The larger shift observed indicates that the actual mixture is closer to *ca.* 90% of the former species and only 10% of the latter.

Along the same line of reasoning, the shift of -1200 cm^{-1} in material M-OP-Ni(L^1) would correspond to the $[Ni(\equiv SiO)_4(L^1)]^{2-}$ species. Such negatively charged species are not likely to form in a thin wall already bearing negatively charged silanolate species. A neutral $[Ni(\equiv SiO)_2(H_2O)_2(L^1)]$ species is much more probable, however, the ν_3 transition would show up at *ca*. 26200 cm^{-1} instead of 25300 cm^{-1}. The formation of a silicate-like phase is an eventuality to take into account since it may form during adsorption or reaction of nickel complexes in basic synthetic media.[179, 180] Then, ν_3 band is expected at 25800 cm^{-1}, which is slightly to high.[181] In addition, the broad linewidth of 5000 cm^{-1} in comparison with an expected value of *ca*. 3100 cm^{-1} indicates the presence of a mixture of species rather than a single type of species. Another type of species may be envisaged assuming that some of the nickel(II) ions underwent the displacement of the last L^1 ligand leading to a species of $[Ni(\equiv SiO)_2(O_L)_4]$ type where O_L stands for meutral *O* donor ligands. The archetype of such a species is the $[Ni(\equiv SiO)_2(H_2O)_4]$ surface complex generated on amorphous silica by adsorption of tetraamminonickel(II) complex followed by thermal removal of the ammino ligands (reference R_2, **Figure 4.22**).[105] Here, the O_L ligand may not only be H_2O but also silanol (≡SiOH) or siloxane (≡SiOSi≡) moities from the amorphous siliceous pore wall. The ν_3 band for such a type of species is expected at *ca*. 24600 cm^{-1} that is too low to represent the only type of species present in material M-OP-Ni(L^1). The rational is a mixture of species such as $[Ni(\equiv SiO)_2(H_2O)_2(L^1)]$ or nickel silicate-like and $[Ni(\equiv SiO)_2(H_2O)_4]$, consistent with an unresolved large band width. An EPR study of material

M-OP-Ni(L^1) prepared with copper(II) instead of nickel(II) shows that about half of the copper is EPR silent as expected for copper engaged in a silicate like phase in agreement with the hypothesis of mixture of species.[182] An EXAFS investigation of such samples may provide more insight in this complex situation, this study is in progress. To the contrary in the post-synthesis materials M1'-ES-Ni($2L^1$) and M1'-ES-Ni($3L^1$), the Ni(II) coordination exhibits the same characteristics than in the $[Ni(H_2O)_2(L^1)_2]^{2+}$ molecular precursor. Furthermore, the presence of NO_3^- ions to counterbalance the charge of the Ni-L^1 complexes as shown by the analysis of FT-IR and EA (**Figure 4.14** and **Table 4.4**) is consistent with a grafted $[Ni(L^1)_2(H_2O)]^{2+}$ species as depicted in **Figure 4.14**. In both cases, the accessibility to en or SCN^- ligand with no displacement of the L^1 grafted moities emphasizes the profound difference of both type of sites (**Scheme 4.6**).

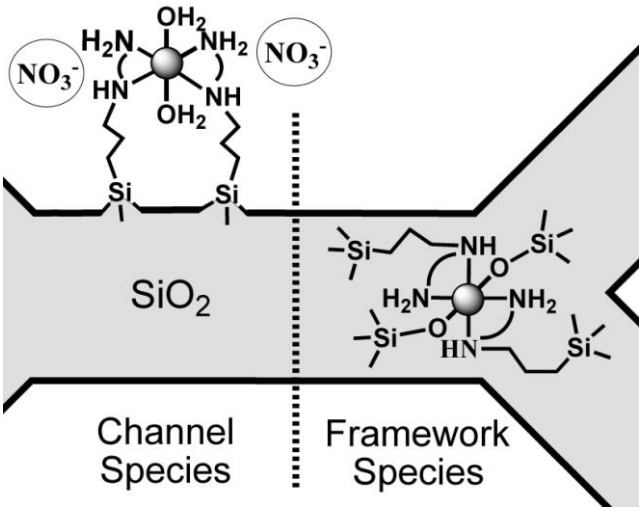

Scheme 4.6 Ni(II) coordination state in material M-OP-Ni($2L^1$)-TA (A) and material M1'-ES-Ni($2L^1$) (B), omitting trimethylsilyl (TMS) groups for simplify.

4.4 Conlusions

In this study $[Ni(L^1)_Y(H_2O)_{6-2Y}](NO_3)_2$ complexes (Y=1-3) were used as molecular organometallic block to built hybrid PMOs materials (M-OP-Ni(L^1), M-OP-Ni($2L^1$), M-OP-Ni($3L^1$). The latter were compared with MCM-41 materials inside the channel of which the same molecular blocks were grafted (M1'-ES-Ni($2L^1$), M1'-ES-Ni($3L^1$)). The

syntheses of the Ni@PMOs were optimized using soft conditions and green reactants (low temperature of 60 °C, sodium silicate as silicon source, NaOH as base and no organic co-solvent). The surfactant extraction were performed using a CTMS-HMDSA mixture which led directly to capped well-ordered materials. XRD, N_2 sorption isotherms and UV-visible spectroscopy showed that in the obtained materials (M-OP-Ni(L^1)-TA, M-OP-Ni($2L^1$)-TA, M-OP-Ni($3L^1$)-TA) both hexagonal mesostructure and Ni(II) coordination state of the mother materials (M-OP-Ni(YL^1)) were maintained. In comparison with the grafted materials, M1'-ES-Ni($2L^1$) and M1'-ES-Ni($3L^1$), the Ni@PMOs materials exhibited much less reduction of pore size, surface area and pore volume consistent with the location of the Ni-L^1 complexes in framework position inside the pore wall of the nanochannel of the PMOs. This is the first time that well defined Ni(II)-amino complexes were introduced in the framework of a mesostructured silica using basic conditions.

These framework functions affect the yield of capping by trimethyl functions (TMS) consistent with their location near the surface and a wall thickness comparable with the inserted complex size. Contrary to grafted species, the framework species exhibit very weak metal exchangeability, strong resistance to acid leaching and ligand inaccessibility, which are reminiscent of the cryptand effect of the siliceous matrix.

In material M-OP-Ni(L^1), poor in the diamino-organosilyl complexing moities (L^1), the framework species are most likely a mixture of species [Ni(L^1)$(SiOH)_2(SiO)_2$] and [Ni($\equiv SiO)_2(O_L)_4$] where O_L stand for a neutral oxygen donor ligand such as H_2O, $\equiv SiOH$ or $\equiv SiOSi \equiv$ and others such as nickel silicate like. In material M-OP-Ni($2L^1$) and M-OP-Ni($3L^1$), the predominant species is the neutral framework complex, [Ni$(L^1)_2(\equiv SiO)_2$]. In material M-OP-Ni($3L^1$), the presence of charged framework species $[Ni(L^1)_3]^{2+}$ is probable but still hypothetical.

Though chemically unaccessible these framework species are potentiel sites for selective optical absorption, electron transfer sites and redox centers. Such properties are very promising in many applications and are under on going investigation.

Chapter 5 Incorporation of copper ethylenediamine and Schiff base complexes in a nanostructured porous silica

5.1 Properties of copper (II)-ethylenediamine complex depending on its location in the nanostructured silica

5.1.1 Introduction

In chapter 4, we have systemically investigated the porosity, morphology and Ni(II) coordination state of Ni(YL^1)@PMOs (L^1: N-(2-aminoethyl)-3-aminopropyltri methoxysilane). However, some of questions are still open: 1) a general nickel species on the PMOs can be drown from UV-visible spectroscopy however no precise distribution of species could be obtained; 2) the template extraction in as-made Ni(YL^1)@PMOs was realized thanks to a treatment by a mixture of CTMS and HMDSA (method *TA*), that also covered the internal surface with trimethylsilyl (TMS) groups; this led to the question on the relation of hydrophobicity and nickel retention in metal exchange process; is a framework metal complex inevitably inaccessible or not? 3) which is the application of framework metal?

To address these questions, Cu(II) has been chosen to be the metal instead of Ni(II). The reasons are: 1) Cu(II)-L^1 complexes are EPR active due to the presence of one unpaired electron of the Cu(II) ion, thus a precise metal coordination state in PMOs can be drawn through EPR; 2) Cu(II)-L^1 complexes possess redox properties that can be investigated by electrochemistry or exploited in redox catalysis chemistry. In addition, two novel methods *HTA* and *H* for template extraction have been developed. These two methods provide different levels of internal surface hydrophobicity: hydrophobic surface using method *TA*, partial hydrophobic surface using method *HTA* and hydrophilic surface using method *H*. Therefore, we can investigate the effect of the surface nature on metal retention property and catalytic behavior.

In this chapter, two types of materials, *i.e.*, Cu(II)-L^1 complexes incorporated in the wall

(Cu(YL^1)@PMOs, **Y=**1, 3) by one-pot synthesis and in the channel [M1'-ES-Cu($2L^1$)] by MSP approach (described in chapter 4), have been prepared. The three methods for template removal were performed on Cu(YL^1)@PMOs, obtaining M-OP-Cu(YL^1)-H, M-OP-Cu(YL^1)-HTA and M-OP-Cu(YL^1)-TA. All materials were investigated using XRD, N_2 sorption isotherm, FT-IR, EPR, UV-visible spectroscopies and elemental analysis. A preliminary study of the electrochemical properties of the hybrid materials was studied. In particular, XRD and FT-IR were used to respectively monitor the difference of hexagonal structure and internal surface property of M-OP-Cu($3L^1$)-H, M-OP-Cu($3L^1$)-HTA and M-OP-Cu($3L^1$)-TA caused by the above three treatments. The copper environment in all materials was characterized by EPR and. Metal accessibility was carried on M-OP-Cu($3L^1$)-H and M-OP-Cu($3L^1$)-TA using acid washing. The primary electrical activity was performed on M-OP-Cu($3L^1$)-TA and M1'-ES-Cu($2L^1$). Furthermore, the catalytic activity of M-OP-Cu($3L^1$)-H, M-OP-Cu($3L^1$)-TA and M'-ES-Cu($2L^1$) was evaluated on the oxidation of 3,5-di-*t*-butylcatechol (DTBC).

5.1.2 Results and discussion

5.1.2.1 Synthesis and porosity characterization

M-OP-XCu(YL^1) (X = Cu/SiO_2 = 1 in sol-gel, Y= L^1/Cu in sol-gel) materials were prepared in the same condition as PMOs containing Ni(II) complexes, *i.e.*, synthesized at 60 ºC for 24 h. A molar composition of synthesis was Y L^1 : 1 $Cu(NO_3)_2$: 100 SiO_2 : 4.5 CTATos : 500 NaOH : 77500 H_2O, Y= L/Cu = 1 and 3 for materials M-OP-Cu(L^1) and M-OP-Cu($3L^1$), respectively. Two novel methods *H* and *HTA* were developed to extract the surfactant (**Scheme 5.1**, **Scheme 5.2**).

The surface of as-made LUS (MCM-41 type) is basic and the cationic heads of template are in the electrostatic interaction with the silanolates of the surface of silica. Therefore, it is possible to use a precise quantity of HCl to remove a known quantity of surfactant of as-made material. In as-made LUS, the surfactant amount is *ca*. 1.4 $mmol \cdot g^{-1}$, which is calculated from the N atom percent in elemental analysis. In method *H*, a equivalent of HCl (1 $mol \cdot L^{-1}$, HCl: CTATos = 1) was used to extract the template, leading to a total hydro-

philic internal surface, the resulting materials referred as M-OP-Cu(YL^1)-H. Quantitative IR spectroscopy was used to monitor this reaction (*vide infra*).

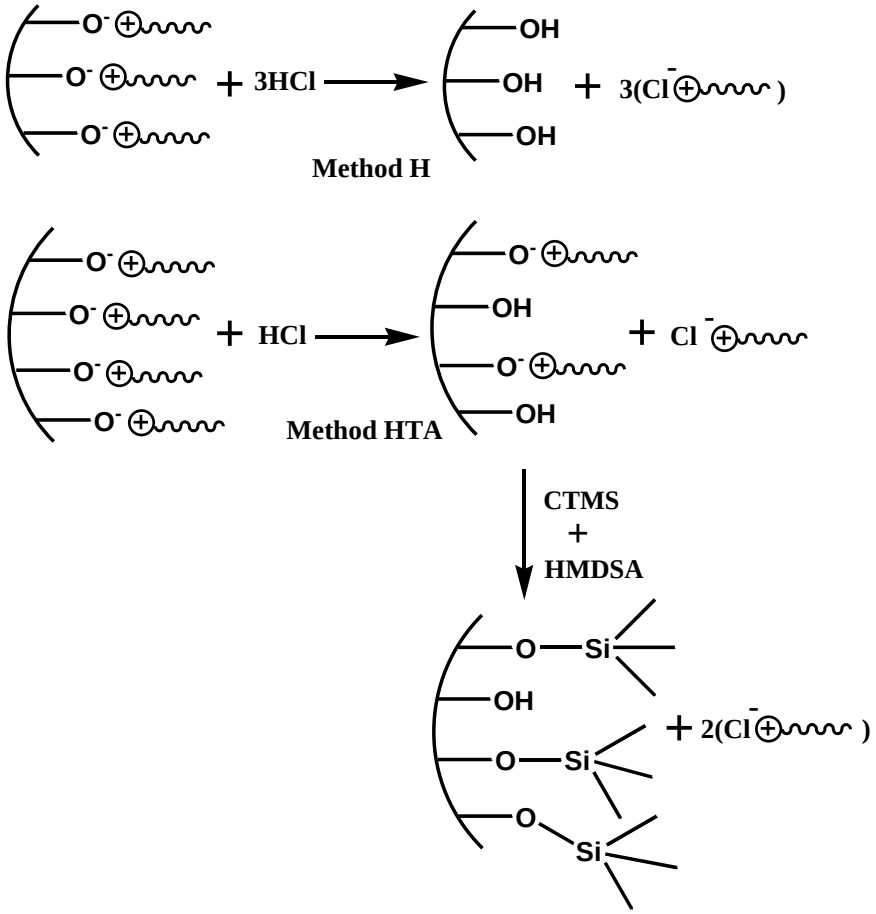

Scheme 5.1 Template removal routes of method H and method HTA.

In method *HTA* half of the surfactant amount was firstly extracted through addition of a certain amount of HCl (1 mol·L^{-1}, HCl: $CTATos_{initial}$ = 0.5), leading to an internal surface with half of the initial surfactant (**Scheme 5.1**, **Scheme 5.2**). Then, a mixture of CTMS and HMDSA was added in the following molar ratios: CTMS: HMDSA: $0.5CTATos_{initial}$ = 1: 1: 1. In this process, the mixture agents both removed the remaining surfactant and concomitantly silylated the internal surface of materials, leading to a partial hydrophilic and hydrophobic surface. The obtained materials were named M-OP-Cu(YL^1)-HTA. The trimethylsilylation percent on the surface was checked by quantitative IR (*vide infra*).

Furthermore, the as-made M-OP-Cu(YL^1) materials were also treated using a mixture of

chlorotrimethysilane (CTMS) and hexamethyldisilazane (HMDSA) (CTMS: HMDSA: CTATos = 6: 6: 1, method *TA*) that simultaneously removed the surfactant and caps the silanol groups leading to materials M-OP-Cu(YL^1)-TA (**Scheme 5.2**).

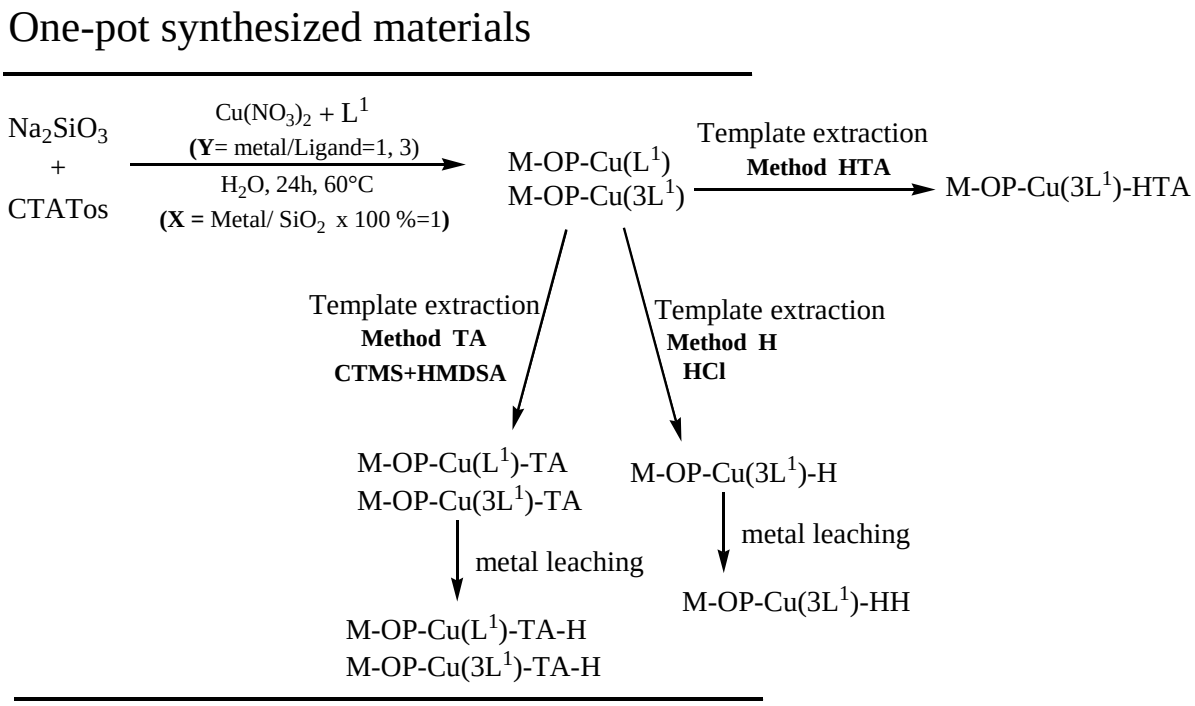

.Scheme 5.2 Synthesized materials.

Therefore, these three methods lead to a progressive decrease on the hydrophilic- hydrophobic properties of the internal surface of the hybrid materials. In addition, the post-synthesized material M1'-ES-Cu(2L^1) was prepared for comparison with the one-pot synthesis materials using the "molecular stencil patterning" (MSP) approach for homogeneous distribution of the metal complexes in the internal channel of mesoporous materials as described in chapter 4.

XRD. The XRD patterns of M-OP-Cu(YL^1) (Y=1, 3) samples with surfactant and without surfactant, M-OP-Cu(L^1)-H, M-OP-Cu(L^1)-HTA and M-OP-Cu(L^1)-TA, are presented in **Figure 5.1**. The XRD patterns of M-OP-Cu(L^1) and M-OP-Cu(3L^1) both show one primary

peak which can be assigned to <100> reflection with d_{100} of 4.3 nm and 4.4 nm, respectively, and a couple of small peaks 2θ between 3 to 5°. These features are typical of uniformly hexagonal pores in the materials. However, the M-OP-Cu($3L^1$) exhibited a much broader d_{100} peak than M-OP-Cu(L^1) due to a higher amount of ligand L^1 added in the sol-gel. After surfactant removal, the XRD patterns of M-OP-Cu($3L^1$)-H, M-OP-Cu($3L^1$)-HTA and M-OP-Cu(YL^1)-TA materials still presented d_{100} reflections, indicating the preservation of hexagonal mesostructures after surfactant removal by using method *H*, method *HTA* and method *TA*. If these three methods are compared, we can find that a progressive increase of the intensity of the d_{100} peak is in the following order: M-OP-Cu($3L^1$)-H < M-OP-Cu($3L^1$)-HTA < M-OP-Cu(YL^1)-TA, indicating that the structure order is affected by the treatments of surfactant removal. Furthermore, M-OP-Cu(YL^1)-TA and M-OP-Cu($3L^1$)-HTA samples showed an increase d_{100} spacing (*ca*. 4.5 nm) compared to the mother material, whereas, a decrease of d_{100} spacing of 4.2 nm was observed for M-OP-Cu($3L^1$)-H. The former is consistent with a surface tension release through silylation process (method *TA* and *HTA*), and the latter is likely due to the condensation of silanol groups through HCl extraction process (method *H*). Therefore, a partial collapse or loss of hexagonal structure may happen in the condensation of silanol groups using method *H*, especially for materials with a high metal loading. This is likely the reason that M-OP-Cu($3L^1$)-H processes a less intensity of d_{100} peak which indicates a less ordered hexagonal structure of the porosity.

For M1'-ES-Cu($2L^1$), the XRD pattern showed the characteristic <100>, <110> and <200> reflections of an hexagonal mesostructure with d_{100} = 4.1 nm, indicating that the MSP method with sequential grafting and acid wash is safe for the hexagonal structure. This is consistent with the results of previous studies.[10, 110, 160, 183]

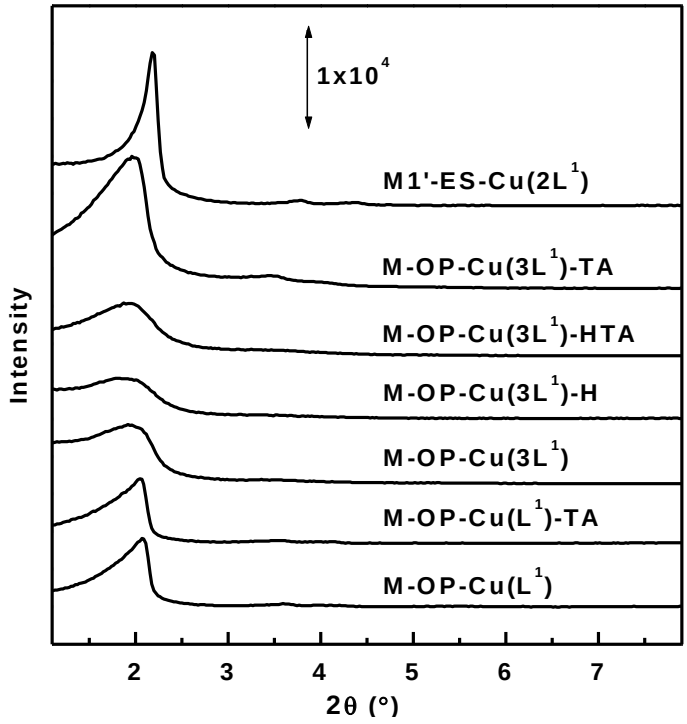

Figure 5.1 XRD patterns of M-OP-Cu(YL^1), M-OP-Cu(YL^1)-TA, M-OP-Cu(YL^1)-HTA and M1'-ES-Cu($2L^1$).

IR. The absorption band at 1381 cm^{-1} assigned to ν(N-O) of NO_3^- is observed in the grafted material M1'-ES-Cu($2L^1$) while it is absent in one-pot synthesis materials despite that NO_3^- ion is the initial counterion of the copper salt added in the sol-gel (**Figure 5.2**). These phenomena was in agreement with the observations in M-OP-Ni(YL^1) and M1'-ES-Ni(YL^1) materials (*cf*. chapter 4).

IR spectra confirmed the efficient surfactant removal on M-OP-Cu($3L^1$)-H, M-OP-Cu($3L^1$)-HTA and M-OP-Cu(YL^1)-TA from the disappearance of the absorption bands of δ(N-C) at 1477 cm^{-1} and the ν_s(C-H) and ν_{as}(C-H) stretching vibrations at 2850 cm^{-1} and 2918cm^{-1}, respectively, of the surfactant (CTATos). Furthermore, for M-OP-Cu(YL^1)-TA and M-OP-Cu($3L^1$)-HTA, IR spectra attested the success of the cap-ping of the surface by trimethylsilyl (TMS) groups due to the absorption bands observed at 850 cm^{-1} and absorption bands at 2962 cm^{-1} and 2903 cm^{-1} assigned to ν(Si-C) and ν(C-H) of trimethylsilyl (TMS), respectively. Furthermore, the intensity of the absorption band at 950 cm^{-1} assigned to ν(Si-O) of silanol groups (≡SiOH) decreased in the order: M-OP-Cu($3L^1$) < M-OP-Cu($3L^1$)-H < M-OP-Cu($3L^1$)-HTA < M-OP-Cu($3L^1$)-TA, con-

firming the change from hydrophilicity to hydrophobicity upon various treatments (see above). Furthermore, the intensities of ν(Si-C) of the TMS groups are not identical in M-OP-Cu($3L^1$)-TA and M-OP-Cu($3L^1$)-HTA spectra. The trimethylsilylation percents of these two materials respectively correspond to 100 % and 65 % coverage of TMS on surface by quantitative IR, considering a total coverage of TMS in M-OP-Cu($3L^1$)-TA material. In other words, it is found that 2/3 of surface is covered by TMS in M-OP-Cu($3L^1$)-HTA. In fact, for the as-made LUS, the molar ratio of CTATos/Si_{inorg} is equal to 0.16, which is calculated from N atom percent and the residual mass in TGA, and the maximal TMS coverage on LUS is 0.24 per Si_{inorg}. The molar ratio of CTATos/≡SiO^- is 2/3 in the as-made LUS. Therefore, the values of 2/3 of TMS coverage on M-OP-Cu($3L^1$)-HTA compared to M-OP-Cu($3L^1$)-TA is consistent with the quantity of agents added for the template removal process and the theoretical values expected.

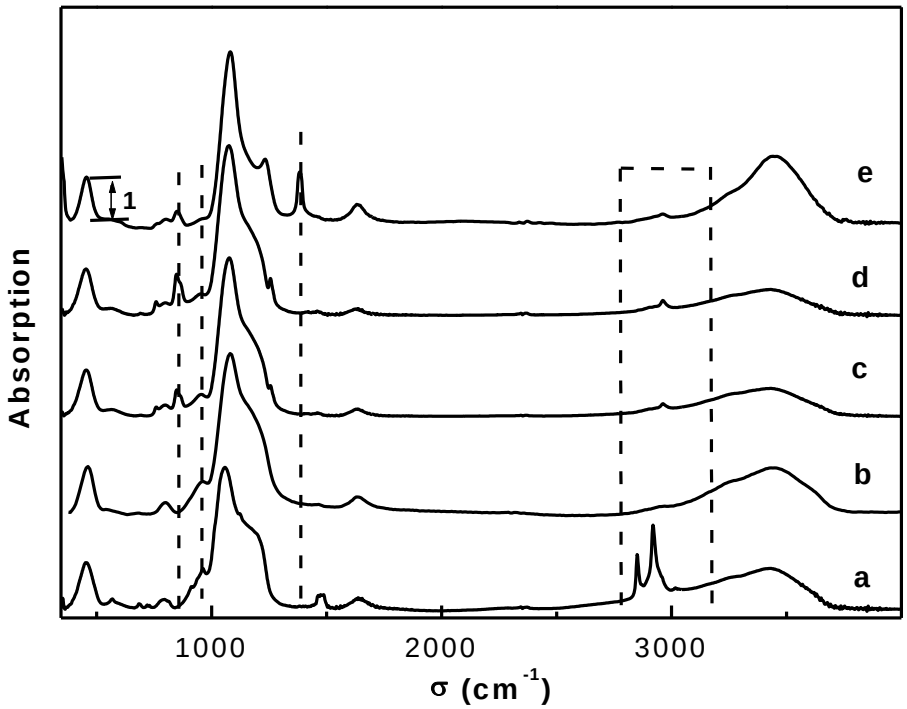

Figure 5.2 FT-IR spectra of a: M-OP-Cu($3L^1$), b: M-OP-Cu($3L^1$)-H, c: M-OP-Cu($3L^1$)-HTA, d: M-OP-Cu($3L^1$)-TA, e: M1'-ES-Cu($2L^1$). IR spectra were after baseline correction.

In a word, IR results reveal that using these methods three different properties of surface were formed: 100 % of hydrophilicity for M-OP-Cu($3L^1$)-H, 35 % of hydrophilicity and

65 % of hydrophobicity for M-OP-Cu($3L^1$)-HTA, and 100 % of hydrophobicity for M-OP-Cu($3L^1$)-TA.

Table 5.1 Copper (II) content and molar ratios deduced from elemental analyses, quantitative EPR and weight loss from TGA.

Sample	Cu [a] wt% ±0.1	Cu [b] wt% ±0.4	Cu/Si [c] ±0.001	L^1/Si [c, d] ± 0.01	L^1/Cu ±0.1	TMS/Si [c] ± 0.01
M-OP-Cu(L^1)	1.8	1.1	0.032	0.03	1.0 [d]	0
M-OP-Cu($3L^1$)	1.7	1.5	0.035	0.08	2.4 [d]	0
M-OP-Cu(L^1)-TA	2.3	1.2	0.032	0.03	1.0 [d]	0.23
M-OP-Cu($3L^1$)-H	2.5	2.2	0.032	0.07	2.3	0
M-OP-Cu($3L^1$)-HTA	2.5	2.2	0.036	0.08	2.2	0.16
M-OP-Cu($3L^1$)-TA	2.3	2.0	0.037	0.08	2.3	0.23
M1'-ES-Cu($2L^1$)	3.0	2.6	0.045	0.90	2.0 [e]	0.15
M-TA	0	0	0	0	0	0.29
M1'-ES	0	0	0	0	0	0.17

a: measured by ICP-MS; **b**: quantification of the EPR signal was performed by double integration after base line correction; **c**: molar ratio per inorganic silica, the inorganic SiO_2 content is obtained from the residual weight in TGA at 1000 °C upon subtraction of both CuO and the SiO_2 formed from the grafted organosilanes; **d**: due to the presence of both surfactant and ligand, both species contributing to the N amount, this value has been calculated starting from the ratio observed for the corresponding samples M-OP-Cu(L^1)-TA, M-OP-Cu($3L^1$) –TA; **e**: L^1 ligand is determined from N amount by subtraction of the N corresponding to surfactant [M-OP-Cu($3L^1$) and M-OP-Cu(L^1)] or nitrate counteranions if present [M1'-ES-Cu($2L^1$)].

EA. The copper weight percentage (wt %), Cu to inorganic silicon molar ratio, trimethyl-silyl (TMS) to inorganic silicon molar ratio, ligand (L^1) to inorganic silicon and ligand (L^1) to Cu molar ratios are reported in **Table 5.1**. The copper loading (*ca.* 1.7 %) in M-OP-Cu(L^1) and M-OP-Cu($3L^1$) is much higher than in the mother gel. For instance, Cu/Si molar ratio is *ca*. 0.033 in M-OP-Cu($3L^1$), while it is 0.01 in the mother gel. Indeed, the yield of copper is 98 %, while a partial yield in silicon (*ca.* 30 %) is observed. After removal of the surfactant using method *H*, *HTA* and *TA*, Cu/Si molar ratios in M-OP-Cu(L^1)-H,

M-OP-Cu($3L^1$)-TA and M-OP-Cu($3L^1$)-HTA were not significantly modified (*ca*. 0.036), indicating that method *H* and method *HTA* are safe for the complexes. In addition, L^1/Cu ratio for M-OP-Cu(L^1)-TA is equal to 1.0 which is in agreement with the initial addition of ligand in the sol-gel, whereas, for Cu($3L^1$)@PMOs is equal to 2.3 and 2.2 which is lower than 3 added in the mother gel, indicating a loss of free L^1. Indeed, the hydrolysis rate of organotrialkoxysilanes (R'-Si-$(OR)_3$) in basic conditions is slower than that of tetraalkoxysilanes ($Si(OR)_4$) and $Si(OH)_4$.[176]

The TMS/Si molar ratio decreased from 0.29 on the Cu-free sample M-TA down to *ca*. 0.23 for M-OP-Cu($3L^1$)-TA, which is probably due to the slightly decrease of surface silanol groups available for capping. The TMS/Si_{inorg} molar ratio for M-OP-Cu($3L^1$)-HTA is equal to 0.16, indicating 69 % of surface coverage with trimethylsilyl groups which is close to the values deduced from quantitative IR spectroscopy (65 %), considering M-OP-Cu($3L^1$)-TA as 100 % TMS coverage. For the post-synthesis material, M1'-ES-Cu($2L^1$), Cu loading was 3.0 % and Cu/Si molar ratio was equal to 0.045. L^1/Cu molar ratio was equal to 2 which is in agreement with the molar ratio in the initial gel (L^1/Cu = 2).

N_2 sorption isotherms. N_2 sorption isotherms at 77 K and the corresponding data are shown in **Figure 5.3** (**a**), (**b**) and **Table 5.2**. The shape of the isotherms is typical of a mesostructured porous material.[6] The steep step of capillary condensation at about 0.33 P/P_0 indicates a narrow pore size distribution for M-TA and M-OP-Cu(L^1)-TA, whereas, a slow step at 0.33 P/P_0 evidences a large pore size distribution for M-OP-Cu($2L^1$)-TA, which is in agreement with the broad d_{100} reflection in XRD patterns (**Figure 5.1**). A diminution of BET surface area and pore volume was observed for M-OP-Cu(L^1)-TA (530 $m^2.g^{-1}$, 0.46 $cm^3.g^{-1}$) and M-OP-Cu($2L^1$)-TA (480 $m^2.g^{-1}$, 0.54 $cm^3.g^{-1}$) compared to M-TA (730 $m^2.g^{-1}$, 0.70 $cm^3.g^{-1}$) (**Table 5.2**). Materials, M-OP-Cu($2L^1$)-TA and M-OP-Cu(L^1)-TA, present similar pore sizes and apparent wall thickness [3.6 nm (BdB model), 1.3 nm] compared to M-TA. By contrast, for M1'-ES-Cu($2L^1$), a pronounced decrease of pore size (2.9 nm) and an increase of the apparent wall thickness (1.8 nm) was observed compared to the metal-free material M1'-ES (3.4 nm, 1.3 nm). In addition, the C-parameter in BET, which is related to

the nature of the internal surface, was found to be *ca.* 20-24 for M-OP-Cu(YL^1)-TA which is similar to the blank M-TA (22), however, it increased to 34 for M1'-ES-Cu($2L^1$). All these results highlight the fact that one-pot synthesized materials possess Cu complexes in the framework, which is in agreement with incorporated Ni(YL^1) complexes into hexagonal mesoporous materials (M-OP-Ni(YL^1)-TA) (*cf.* chapter 4).

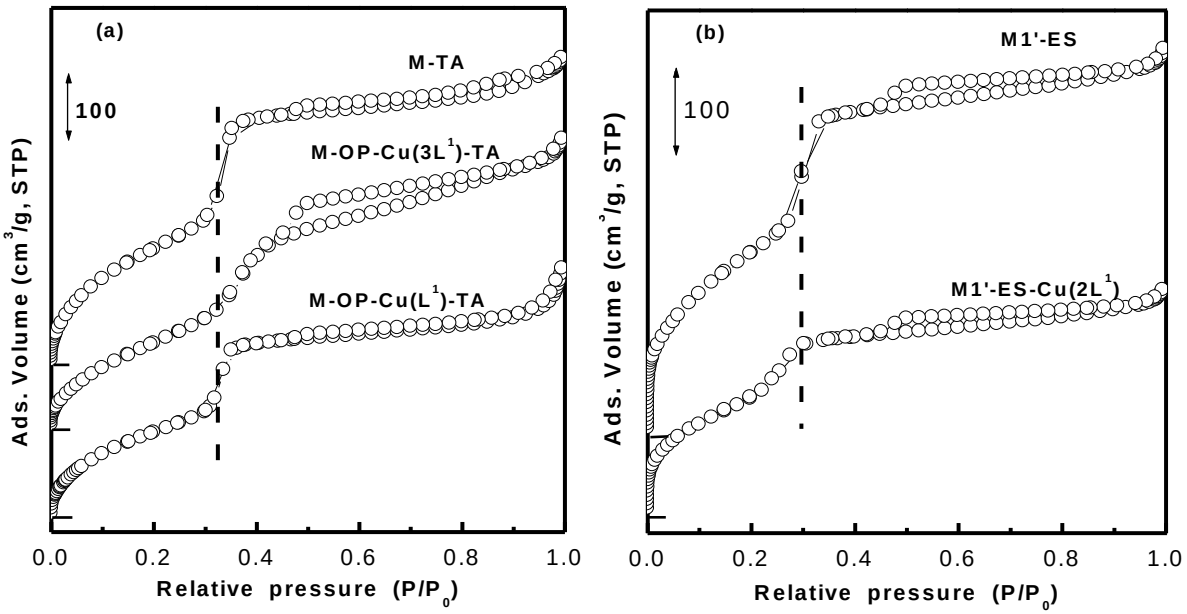

Figure 5.3 Nitrogen adsorption-desorption isotherms at 77 K of one-pot synthesis materials M-TA, M-OP-Cu($3L^1$)-TA, M-OP-Cu(L^1)-TA(a); M1'-ES and grafted material M1'-ES-Cu($2L^1$) (b).

Table 5.2 Textural properties of mesoporous hybrid materials deduced from N_2 sorption isotherms at 77K.

Material	S_{BET} ($m^2.g^{-1}$)[c] ± 50	V_p ($cm^3.g^{-1}$)[a] ± 0.02	ϕ_{BdB}[b] (nm) ± 0.1	a_0[c]	W_t[d] (nm)	C[e]
M-TA	730	0.70	3.6	4.8	1.3	22
M-OP-Cu($3L^1$)-TA	480	0.54	3.7	5.0	1.3	20
M-OP-Cu(L^1)-TA	530	0.46	3.6	4.9	1.3	24
M1'-ES	860	0.71	3.4	4.7	1.3	34
M1'-ES-Cu($2L^1$)	530	0.41	2.9	4.7	1.8	40

a: measured at $P/P_0 = 0.98$; **b**: if BJH model is used instead of BdB one, the diameter would be 0.8 nm smaller in each case; **c**: $a_0 = 2*d_{100}/\sqrt{3}$; **d**: $W_t = a_0 - \phi_{BdB}$; **e**: C values determined from BET.

5.1.2.2 Physicochemical properties of the metal centers

5.1.2.2.1 Cu(II) coordination state characterization

EPR and solid UV-visible spectra. For molecular complex $Cu(L^1)_2$, the g_{ll} and A_{ll} parameters are equal to 2.20 and 19.5 mT (**Table 5.3**), respectively, which are similar to the these of $Cu(en)_2$,[124, 158] indicating a CuN_4 coordination environment for $Cu(L^1)_2$. This result confirms that the g_{ll}-value is mainly affected by electron density on the Cu(II) ion despite that L^1 ligand possesses higher steric hindrance than ethylenediamine ligand, which is consistent with the report by Sakurai *et al*..[123] In addition, this result reveals that the axial coordination of $Cu(L^1)_2$ is most probably H_2O and should not be the Si-OMe or $Si\text{-}O^-$, since A_{ll} is quite sensitive to the axial coordination (*cf*. chapter 2.3.5.1).

Table 5.3 EPR parameters of Cu complexes and materials and wavenumber of the absorption in UV-visible spectroscopy.

Sample	g_{ll}	A_{ll} (mT)	T (K)	ν (cm^{-1})
$Cu(en)_2$ [a]	2.20	19.5	100	18000
$[Cu(L^1)]^{2+}$ [a]	2.28	16.9	100	15650
$Cu(L^1)_2$ [a]	2.20	19.5	100	18000
M-OP-$Cu(L^1)$ [b]	2.26	13.6	298	15100
	2.19	18.8		
M-OP-$Cu(L^1)$-TA [b]	2.26	13.6	298	15100
	2.19	18.8		
M-OP-$Cu(3L^1)$ [b]	2.19	18.8	298, 100	17000
M-OP-$Cu(3L^1)$-H [b]	2.19	18.8	298	17000
M-OP-$Cu(3L^1)$-TA [b]	2.19	18.8	298, 100	16900
M-OP-$Cu(3L^1)$-HTA [b]	2.19	18.8	298	16900
M1'-ES-$Cu(2L^1)$ [b]	2.19	18.8	298	17400

a: in water and glycerol; **b:** solid samples.

For M-OP-$Cu(3L^1)$, the EPR spectra exhibited one primary species with 2.19 for g_{ll} and 18.8 mT for A_{ll} parameters at room temperature and 100 K, indicating the successful immobilization of Cu(II) complexes on the silica (**Table 5.3**). After template removal using method *H*, *HTA* and *TA*, M-OP-$Cu(3L^1)$-H, M-OP-$Cu(3L^1)$-HTA and M-OP-$Cu(3L^1)$-TA exhibit primarily the g_{ll} of 2.19 and A_{ll} of 18.8 mT values to M-OP-$Cu(3L^1)$ [**Figure 5.4** (**a**)], confirming that the Cu environment was maintained during template removal process. If these values are compared to those of the molecular complexes $[Cu(L^1)_2]$, A_{ll} value dimi-

nished from 19.5 mT to 18.8 mT while g_{ll} values are similar (*ca*. 2.19). These results are most probably caused by a change in axial coordination of the framework species. Sakurai *et al*. have found that the axially coordinated square-planar complexes of CuN_4X type present a smaller A_{ll}-value but with a similar g_{ll}-value compared to that of square-planar CuN_4 complexes, which was presented in chapter 2.3.5.1.[123] Therefore, in the solids, it is likely that an axial ligand exists. This ligand is most probably charged and could be the $\equiv SiO^-$ groups which also serve as counterions, substituting both H_2O ligand and the NO_3^- counterion ion, which is consistent with the results of Ni(YL^1)@PMOs.

The d-d absorption bands of Cu($3L^1$)@PMOs in the UV-visible spectra decreased to *ca*. 16900 cm^{-1}, which are much lower in energy than that observed for $Cu(L^1)_2$ (18000 cm^{-1}) (**Table 5.3**). This confirms again the presence of a six-coordinated Cu(II) in Cu($3L^1$)@PMOs, which is induced by Jahn-Teller effect, leading to substitution of the complex and therefore a lower absorption band in UV-visible spectra.

For M1'-ES-Cu($2L^1$), the g_{ll} and A_{ll} parameters are equal to 2.20 and 19.5 mT, respectively. The absorption band in UV-visible spectra is observed at 17400 cm^{-1}. The IR spectrum and EA indicated the presence of NO_3^- ion in M1'-ES-Cu($2L^1$) with a NO_3^-/Cu(II) molar ratio equal to 2. All these results allow us to propose that the Cu-L^1 complex grafted in silica is also six-coordinated and that two NO_3^- are most probably coordinated to the metal ion in axial position, playing also the role as counterion, which leads to a small A_{ll}-value and lower absorption band. However, the effect of NO_3^- is different than that of $\equiv SiO^-$, leading to a different absorption bands between M-OP-Cu($3L^1$)-HTA and M1'-ES-Cu($2L^1$).

EPR spectra of M-OP-Cu(L^1) and M-OP-Cu(L^1)-TA exhibit two species [**Figure 5.4(b)**]: one with g_{ll} = 2.26 and A_{ll} = 13.6 mT, another with g_{ll} = 2.19 for and A_{ll} = 18.8 mT. The first species is most probably attributed to CuN_2 type complex,[124] the second is likely the aforementioned CuN_4 complex. The absorption band in UV-visible spectra is equal to 15100 cm^{-1}, which is much lower than M-OP-Cu($3L^1$) (**Table 5.3**), indicating that the CuN2 species is major. The CuN_2 complex may probably have two $\equiv SiO^-$, $\equiv SiOH$ or H_2O as ligand and counterion besides one L^1 coordinated to one Cu(II), which is a similar situation as that of M-OP-Ni(L^1)-TA (*cf*. chapter 4).

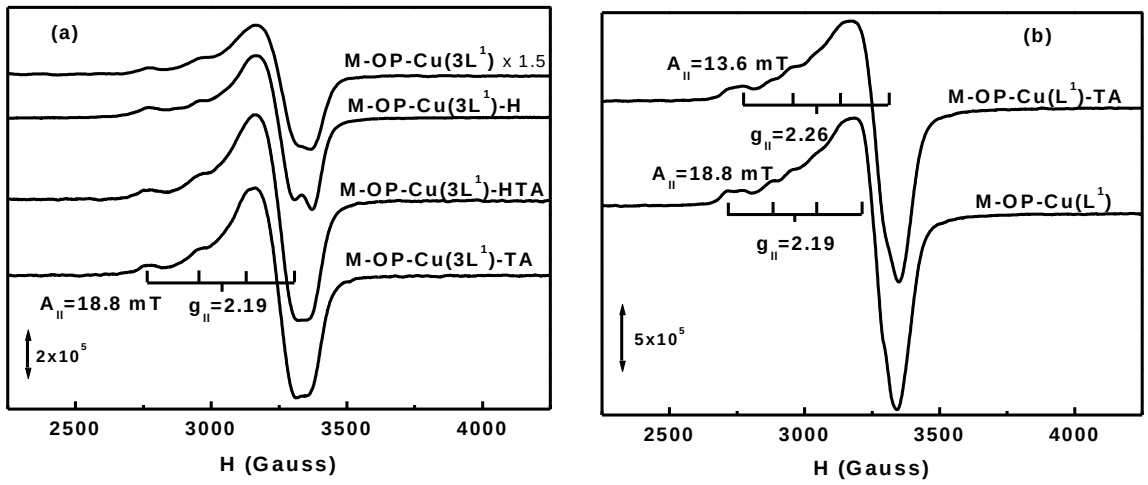

Figure 5.4 EPR spectra at 298 K of M-OP-Cu($3L^1$) (expanded 1.5 times), M-OP-Cu($3L^1$)-TA and M-OP-Cu($3L^1$)-HTA (**a**); M-OP-Cu(L^1) and M-OP-Cu(L^1)-TA (**b**). Experimental conditions: frequency = 9.35GHz, power = 10 mW for (**a**) and 16 mW for (**b**), modulation amplitude: 3 G and modulation frequency: 100 kHz.

Quantitative EPR was employed to quantify the active Cu(II) in Cu(YL^1)@PMOs (*cf.* Appendix B) (**Table 5.1**). For Cu($3L^1$)@PMOs, the EPR active Cu wt. % are 1.5 % for M-OP-Cu($3L^1$), 2.0 % for M-OP-Cu($3L^1$)-TA and 2.2 % for M-OP-Cu($3L^1$)-TA, which correspond to 88 % of EPR active Cu(II) to total Cu determined from ICP-MS. In addition, the EPR active Cu(II) for M'-PS-Cu($2L^1$) is 88 % of total Cu(II). These results indicate that in both Cu($3L^1$)@PMOs and grafted material copper is mainly present as monomer. For Cu(L^1)@PMOs, the EPR active Cu is *ca*. 55 % of the total Cu for M-OP-Cu(L^1) (1.1 % in EPR, 1.8 % in ICP-MS) and for M-OP-Cu(L^1)-TA (1.2 % in EPR, 2.3 % in ICP-MS). These results reveal that the Cu(II) states in Cu(L^1)@PMOs is complicate: half of the copper monomers correspond to $[Cu(L^1)]^{2+}$ and Cu($2L^1$), and the other half is likely dinuclear Cu(II) complexes. Note that this point can be expressed more directly compared to the results of Ni(YL^1)@PMOs (*cf.* chapter 4). These results will be checked by EXAFS (analysis in progress).

5.1.2.2.2 Cu displacement

Metal accessibility was evaluated using HCl extraction. HCl (1 $mol \cdot L^{-1}$, HCl: Cu = 4: 1) was added to extract the Cu(II) on M-OP-Cu($3L^1$)-H, M-OP-Cu($3L^1$)-HTA and

M-OP-Cu(L^1)-TA in ethanolic solution at 40 ºC, obtaining M-OP-Cu($3L^1$)-HH, M-OP-Cu($3L^1$)-TA-H and M-OP-Cu(L^1)-TA-H (**Table 5.4**). The Cu wt % is 2.3 % for M-OP-Cu($3L^1$)-HH, 2.1 % for M-OP-Cu($3L^1$)-TA-H and 2.0 % for M-OP-Cu(L^1)-TA-H, corresponding 8 %, 9 % and 13 % of metal leaching, respectively. Note that in M-OP-Cu(YL^1)-TA-H (L^1 = 1, 3) materials *ca*. 20 % TMS was removed during the metal extraction process. Indeed, in all these materials *ca*. 90 % of Cu was retained. These results indicate that the Cu(II) ions are an accessible situation with no effect from the coverage of TMS on the internal surface of PMOs and they are completely embedded in the siliceous pore walls.

Table 5.4 Copper (wt %) of hybrid materials.

Material	Cu ± 0.1% (ICP-MS)	Yield of metal leaching %
M-OP-Cu($3L^1$)-HH	2.3	8
M-OP-Cu($3L^1$)-TA-H	2.1	9
M-OP-Cu(L^1)-TA-H	2.0	13

M-OP-Cu($3L^1$)-H, Cu 2.5 %; M-OP-Cu($3L^1$)-TA, Cu 2.3 %;
M-OP-Cu(L^1)-TA, Cu: 2.3 %, see in **Table 5.1**.

5.1.2.3 Preliminary study of the electrochemical properties by cyclic voltammetry

These inaccessible framework species are potential sites for selective optical absorption, electron transfer and redox centers. Therefore, the electrochemical properties of Cu($3L^1$)@PMOs were preliminarily studied by cyclic voltammetry. The working electrode was papered by taking a 1: 1 weight ratio of complex precursor or hybrid materials and fine graphite and dispersed in 1 mL of water, which was ultrasonicated for 10 min. Several aliquots of this dispersion were coated on platinum disk (1 mm diameter) and 5 µL of 5 % polystyrene. The electrolyte was a solution of tetrabutylammonium hexafluorophosphate (TBAP, 0.1 M) in CH_2Cl_2. However, during the analysis process, we found that the complex precursor or hybrid materials were gradually decoated on the working electrode, due

to the easy dissolution of polystyrene in CH_2Cl_2.

The response in cyclic voltammetry of the molecular complex $[Cu(L^1)_2(NO_3)_2]$, and the hybrid materials, M-OP-Cu($3L^1$)-TA and M1'-ES-Cu($2L^1$), is shown in **Figure 5.5**. The voltammogram of neat complex exhibited an obvious peak at -0.51 mV and a peak at -0.13 mV, which was recorded in a three-electrode cell. The voltammogram of M-OP-Cu($3L^1$)-TA exhibits a peak at -0.51 mV and a peak at 0.43 mV. The voltammogram of M1'-ES-Cu($2L^1$) exhibited only one peak at -0.53 mV. The scan rates were altered, however, the peaks are not reproducible. In our opinion, the big problem here is that the experimental condition is not the suitable for these materials. Thus, we also have tried the electrochemical measurements on a home-built potentiostat equipped with efficient ohmic drop compensation in a three-electrode cell. However, the results are still not good. Furthermore, Martinez-Ferrero *et al*. have reported to a dip-coating method to measure the electrochemical property on silica-based materials and they have obtained good responses in cyclic voltammogram.[184] This study is in process in our group.

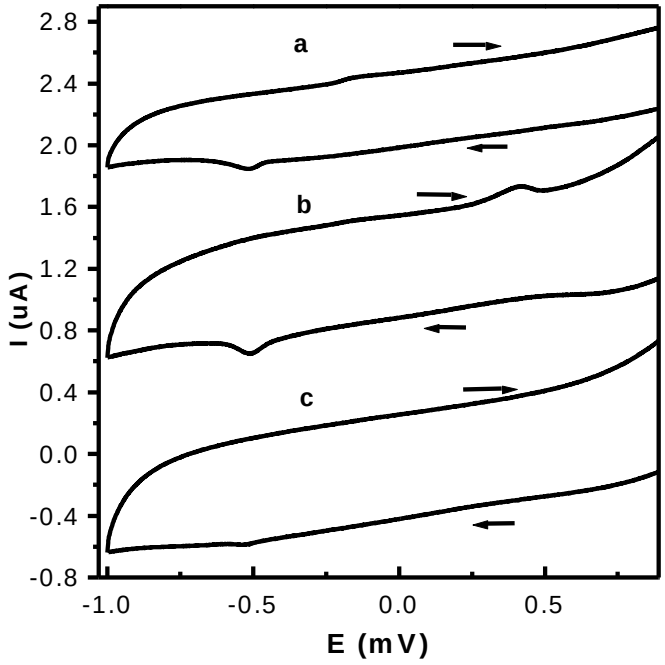

Figure 5.5 Cyclic voltammogram of $Cu(L^1)_2$ (a), M-OP-Cu($3L^1$) (b), M1'-ES-Cu($2L^1$) (c) at scan rate 0.4 $V \cdot s^{-1}$.

5.1.2.4 Compared catalytic activity of copper (II) complex in the wall

and in the channel

The activity of Cu(3L[1])@PMOs and M1'-ES-Cu(2L[1]) was evaluated on the oxidation of 3,5-di-*t*-butylcatechol (DTBC), in which oxygen is used as oxidant (**Scheme 5.3**, **Table 5.5**). For comparison, two blank experiments, *i.e.*, partially silylated metal-free material (M1'-ES), and for EtN_3 without catalyst, were carried out. The conversions of DTBC over M1'-ES and Et_3N are 18 % and 44 %, respectively, however, yields of 3,5-di-t-butylquinone (DTBQ) are 0.5 mol. % and 6 mol. % and DTBQ selectivities are 3 % and 14 %, respectively. The by-products are most probably products of the polymerization of catechol.[185] These results indicate that the oxidation of DTBC to DTBQ can not occur in the absence of Cu(II)-containing catalysts, whereas, the polymerization of catechol can take place in the presence of Et_3N and oxygen.

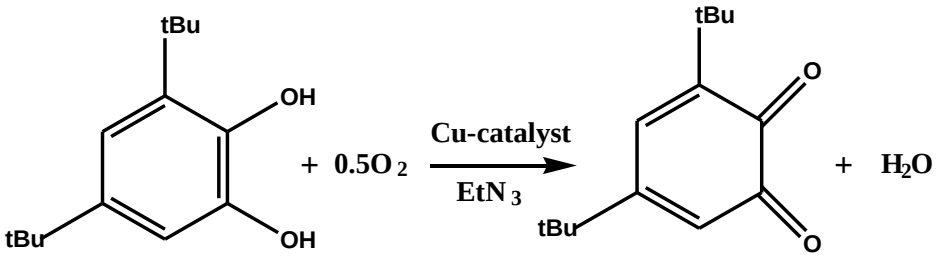

Scheme 5.3 Catalyzed oxidation of 3,5-di-*t*-butylcatechol (DTBC) to 3,5-di-t-butylquinone (DBTQ).

Table 5.5 Catalytic results.

Catalysis	DTBC conversion %	DTBQ yield (mol %)	DTBQ selectivity %
Et_3N [a]	44	6	14
M1'-ES [b]	18	0.5	3
M-OP-Cu(3L[1])-H [c]	50	4	8
M-OP-Cu(3L[1])-TA[c]	76	7	10
M1'-ES-Cu(2L[1]) [c]	69	59	86

Reaction conditions: [a] [Cu]: [DTBC]: [Et_3N] = 1: 23: 0.004, acetonitrile as solvent, room temperature, t = 6 h; [b] without catalyst; [c] without EtN_3. DTBC: 3,5-di-*t*-butylcatechol; DTBQ: 3,5-di-t-butylquinone.

The catalytic activity of M-OP-Cu(3L[1])-H and M-OP-Cu(3L[1])-TA gave a high DTBC

conversion (50 %, 76 %), but low DTBQ yield (4 %, 7 %) and DTBQ selectivity (8 %, 10 %). However, M1'-ES-Cu($2L^1$) exhibited a high activity, giving 69 % of DTBC conversion, 69 mol. % of DTBQ yield and 86 % of DTBQ selectivity. The DTBQ selectivity in post-syntheized material is silghtly higher than that reported by Louloudi *et al*. who claimed a DTBQ selectivity of 83 % using a immobilized Cu(II)-propyl-thiazol-2-ylmethylene-amine complexes on amphrous SiO_2 as catalyst.[151] In our study, a much simpler ligand has been used to afford similar results than Louloudi *et al*.

It can be seen that Cu(II) complex immobilized on mesostructured silica by one-pot synthesis show an obvious different behaviours on oxidation of DTBC compared to post synthesized materials. The drastic difference of the catalytic activity between one-pot synthesized materials and post-synthesized materials is most probably related to the different location of Cu(II) complex, *i.e.*, one in the wall for Cu($3L^1$)@PMOs, another in the channel for M1'-ES-Cu($2L^1$). For the former species, the six-coordinated Cu(II) complex by two L^1 ligands and two $\equiv SiO^-$ groups in the wall could hinder the coordination of extral spieces, thus losing the formation of intermediate spiece in catalytic cycle. For the latter species, although Cu(II) complex in the M1'-ES-Cu($2L^1$) is also six-coordinated by two L^1 ligands and two NO_3^- in the axial direction, NO_3^- is a good leaving group. Thus it is prossible to form intermidate species in the catalytic cycle.

5.1.3 Conclusions

PMOs incorporating Cu(II)-L^1 complexes (M-OP-Cu(YL^1), Y = Ligand/metal = 1, 3) have been synthesized under similar conditions as described for Ni(YL^1)@PMOs (*cf.* chapter 4). The template removal of as-made materials has been achieved using method *TA*, and two novel methods *HTA* and *H*, obtaining M-OP-Cu(YL^1)-TA (-HTA, -H) materials**.** These materials presented well-ordered hexagonal structures with trimethylsilyl (TMS) coverage from 100 % to 0 %, which were determined by XRD, quantitative IR and EA. IR spectra indicated that the counterion NO_3^- is absent in PMOs M-OP-Cu($3L^1$), while it presented in grafting material M1'-ES-Cu($2L^1$). Elemental analysis showed that L^1/Cu molar ratio is equal to 1 for M-OP-Cu(L^1), whereas, it is 2.4 for M-OP-Cu($3L^1$) despite that this value is

equal to 3 in the initial sol-gel. After surfactant removal by using method *H* and *HTA* and *TA*, Cu/SiO_2 molar ratios of $Cu(YL^1)$@PMOs maintained the same as the corresponding as-made materials M-OP-$Cu(L^1)$ and M-OP-$Cu(3L^1)$, respectively, indicating that the two novel methods have developed suitable to remove the template of M-OP-$Cu(YL^1)$.

The comparative study of the N_2 sorption isotherms of M-OP-$Cu(3L^1)$-TA and M-OP-$Cu(L^1)$-TA proves that Cu(II) complexes are indeed in the framework of the PMOs materials, which is in agreement with the results of $Ni(YL^1)$@PMOs (*cf*. chapter 4).

Reduction of solid UV-visible absorption bands of M-OP-$Cu(L^1)$ and M-OP-$Cu(3L^1)$ compared to $[Cu(L^1)]^{2+}$ and $[Cu(L^1)_2]$ complexes suggested a change of metal coordination environment in the axial direction. The quantitative EPR study, for the M-OP-$Cu(L^1)$, allows us to propose that half EPR active species may correspond to the $[Cu(L^1)(\equiv SiO)_2(\equiv SiOH)_2]^{2+}$ complex and $[Cu(L^1)_2(\equiv SiO)_2]$. The EPR silent species are probably $[Ni(\equiv SiO)_2(O_L)_4]$ where O_L stands for a neutral oxygen donor ligand such as *H_2O*, ≡*SiOH* or ≡*SiOSi*≡. For M-OP-$Cu(3L^1)$, the major Cu(II) species is the EPR active and predominant metal state is $[Cu(L^1)_2(\equiv SiO)_2]$ complex.

$Cu(YL^1)$@PMOs materials, [M-OP-$Cu(3L^1)$-H, M-OP-$Cu(3L^1)$-HTA and M-OP-$Cu(3L^1)$-TA], with hydrophilic or hydrophobic internal surface all exhibited a high metal retention property (*ca*. 90 %). This high metal retention is likely due to the nature of incorporated complexes and not related to the internal surface properties (hydrophobic or hydrophilic).

$Cu(YL^1)$@PMOs and the corresponding grafted material [M1'-ES-$Cu(2L^1)$] have been both tested on the oxidation of 3,5-di-*t*-butylcatechol. Only the grafted material [M1'-EP-$Cu(2L^1)$] exhibited an important activity while the PMOs material showed almost no activity, which is most probably due to the different coordination state and different location of the Cu(II) complexes in the material.

5.2 Incorporation of Schiff base complex (Cu-L^2) with 2N2O coordination sphere using a one-pot synthesis

5.2.1 Introduction

In chapter 4 and chapter 5.1, we found that in the Ni(YL^1)@PMOs and Cu(YL^1)@PMOs the metal is inaccessible due to the additional coordination of silanolate groups from the inorganic support to the charged metal-amino complexes.[18] Thus, how can we make the framework metal complexes accessible?

Schiff base copper(II) complexes have been extensively studied due to their applicability as catalyst for oxidation reactions.[186-191] Here, bis(salicylaldimine) copper (II) complex was chosen to be incorporated in the mesoporous material. From the structural point of view, bis(salicylaldimine) copper (II) complexes are usually prone to be hydrophobic due to the aromatic rings on the structure. Furthermore, Schiff base with negative charge from phenolate can make neutral complex. Thus, these two parameters are supposed to be strong driving forces to favour the location of the complexes in the organic side of the electrical pallisade between the micelle and the aqueous solution during the initial steps of the silicate and organosilane moities condensation. Therefore, the neutral bis(salicylaldimine) copper (II) complexes [Cu(L^2)$_2$, L^2= salicylaldimine-N-propylamine- trimethoxysilane] can be expected to be located near the pore using a one-pot synthesis. This should increase the accessibility to metal and therefore exhibit the catalytic activity. Indeed, a few examples using one-pot synthesis to immobilize Schiff base complexes with two alkyltrialkoxysilane arms on mesoporous materials are reported.[119, 121] One example is from Corma *et al*. They have reported PMOs containing vanadyl-salen and chiral vanadyl-salen complexes which exhibit catalytic activity on cyanosilylation reaction of aldehydes with trimethylsilyl cyanide (TMSCN). To our knowledge, there are no reports on mesoporous hybrid materials incorporating copper (II)-salicylaldimine complexes [Cu(L^2)$_2$] *via* one-pot synthesis.

Here, we described the synthesis of hybrid materials incorporating [Cu(L^2)$_2$] complexes with different metal loading using similar conditions as that for Ni(YL^1)@PMOs and Cu(YL^1)@PMOs. For well elucidation of the ligand effect, Ni(YL^1)@PMOs with a similar metal loading has also been synthesized. Surfactant extraction methods (*TA* and *H*) were employed on these materials in order to find a suitable method for surfactant extraction while keeping the integrity of the metal complexes. The obtained materials have been tested in

terms of metal accessibility through a metal extraction study. The porosity and morphology of these materials have been investigated using XRD, TEM and N_2 sorption isotherms techniques. The nature and quantity of the loaded species have been determined from FT-IR, EA (elemental analysis), ICP-MS, UV-visible and EPR spectroscopies. Finally, the catalytic performances of the hybrid materials incorporating $[Cu(L^2)_2]$ complexes have been tested in the hydroxylation of phenol.

In order to characterize the metal environment in the solid hybrid materials, a preliminary study of the Cu-L2 complexes in solution was performed using IR, UV-visible and EPR spectroscopy.

5.2.2 Study of the copper-L^2 complexes in solution

The salicylaldimine-N-propylamine-trimethoxysilane (L^2) with 1N1O coordination sphere is a bidentate Schiff base. The $Cu(L^2)_2$ complex presents therefore a 2N2O coordination sphere around the Cu(II) ion,[192] which is different from the known tetradentate salen complex with 2N2O coordination sphere where the two N atoms are connected by an alkyl bridge. Incorporation of the Cu-L^2 complex into the mesoporous material was performed in the presence of surfactant (CTATos) in basic aqueous solution at 60 ºC for 24 h. Thus, the parameters of the sol-gel process, water, surfactant, temperature, pH and reaction time, have probably an influence on the integrity of Cu-L^2 complex. Thus, it is necessary to monitor the stability of Cu-L^2 complex in these systems. Furthermore, it can allow us to understand if there is any change between the immobilized complex and the molecular species.

5.2.2.1 Results and discussion

Synthesis

Although there are various types of copper (II) sources, copper (II) acetate $[Cu(OAc)_2]$ was chosen as the copper source for the coordination to salicylaldimine, instead of $Cu(NO_3)_2$, $CuCl_2$ and $Cu(ClO_4)_2$. The reason is that the all nitrate, the chloride and the perchlorate copper salts generate rather acidic solutions most likely due to traces of the corresponding acid (HNO_3, HCl or $HClO_4$, respectively) presented as impurities in the commercial

sources. Thus, the imine (C=N) bond in L^2 is easily hydrolyzed in such acidic solutions which was observed by us and others.[112, 193, 194] Here, the Cu-L^2 complex was synthesized by the condensation of $Cu(OAc)_2$ and L^2) (L^2/Cu = 2) in absolute ethanol under reflux (**Scheme 5.4**), and it was named 2-L^2 complex. In addition, the reaction of molar equivalent $Cu(OAc)_2$ and L^2 (L^2/Cu = 1) was carried out, leading to the 1-L^2 complex.

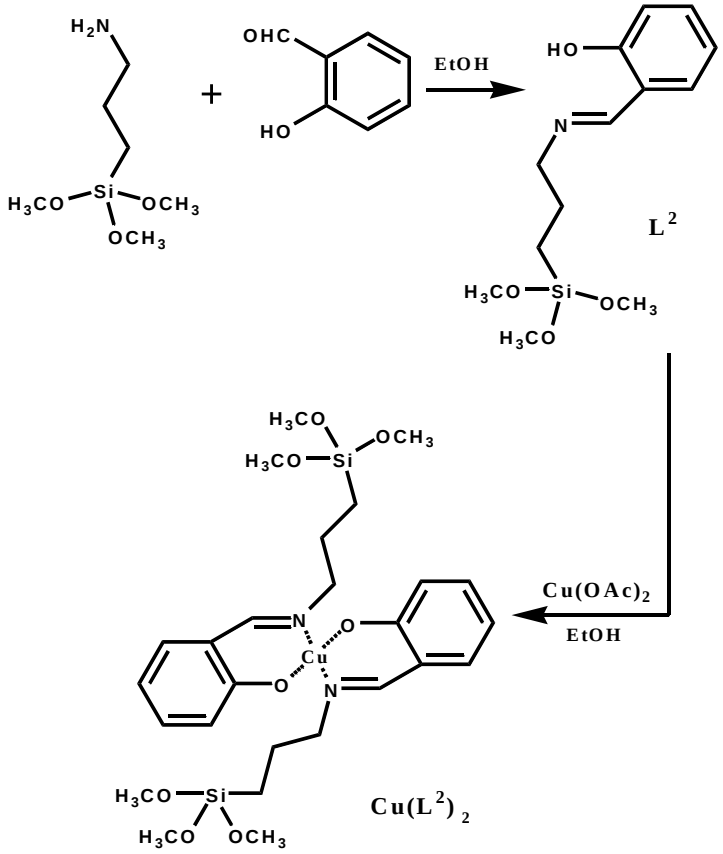

Scheme 5.4 Synthesis route for [Cu(L^2)$_2$] complex

IR spectra L^2 ligand and 2-L^2 complex were studied using IR spectroscopy. A band at 1633 cm^{-1} can be attributed to ν(C=N) of the azomethine group in the free ligand L^2, whereas, it appears at a lower frequency (1623 cm^{-1}) in the IR spectra of the 2-L^2 complex (**Table 5.6**), indicating the coordination of the imino nitrogen to the metal atom.[195]

Table 5.6 IR, UV-visible data of the ligand and complexes.

Samples	IR (KBr)	UV-visible spectra, λ_{max} (nm)						
	$\nu_{(C=N)}$ (cm^{-1})							
L^{2} [a]	1633	217	254	279	314	404		
2-L^{2} [a]	1623	225	242	271	309		360	622
L^{2}_11 [b]		219	239	275		391		
L^{2}_7 [b]		219	239	275		391		
L^{2}_6 [b]		219	239	275		391		
2-L^{2}_11 [b]		219	240	275	313		384	
2-L^{2}_7 [b]		219	240	274			378	
2-L^{2}_6 [b]		219	240	275			391	

a: UV-visible spectra of L^{2} and 2-L^{2} were measured in absolute ethanol; b: L^{2} and 2-L^{2} were dissolved in aqueous solution with pH = 6 (phosphate buffer solution), 6.8 (deionized water) and 11 (sodium hydroxide solution).

UV-visible spectra The stability of the ligand in different solutions (ethanol and water) and various pH from basic to acid aqueous solutions was investigated. Their UV-visible spectra were recorded (**Figure 5.6**), and the corresponding data are gathered (**Table 5.6**). The free L^{2} ligand and 2-L^{2} complex in EtOH present several absorption bands in the ultraviolet region (200-380 nm) and visible region (380-780 nm). For L^{2} ligand in ethanol, the absorption bands below 279 nm can be attributed to π - π^* transitions of the benzene ring and the absorption band at 279 nm corresponds to the π - π^* transitions in azomethine (-C=N) groups of ligand.[112,196, 197] The absorption band observed at 314 nm can be interpreted as a charge-transfer transition in which the azomethine group acts as an electron acceptor and phenyl ring (Ph-O^{-}) as an electron donor.[198] The absorption band observed at 404 nm is most probably due to the transition of n - π^* of (-C=N**:**) of the azomethine group of the ligand. In addition, the yellow color of the ligand may be attributed to this n - π^* transition in the visible region.[199] For the 2-L^{2} complex in EtOH, the π - π^* transitions in the benzene ring and azomethine (-C=N) group of ligand are also observed but shifted of ± 5 cm^{-1}, confirming the coordination of the ligand to the metal ion. In addition, the two absorption bands observed at 309 and 360 nm can be attributed to the metal-ligand charge transition

(MLCT) transitions,[197, 198, 200, 201] the former is assigned to the MLCT transition of Cu→N, and the latter is attributed to the MLCT transition of Cu→O. A shoulder observed at 420 nm is probably attributed to n-π* transition of azomethine.[198] The absorption band centered at 622 nm at lower energy with lower intensity can be attributed to the d-d transition of Cu(II) ion (d_{xy}-d_x^2-$_y^2$ and d_z^2-d_x^2-$_y^2$). All these results suggest that the **L^2** ligand was successfully coordinated to Cu(II) ions.

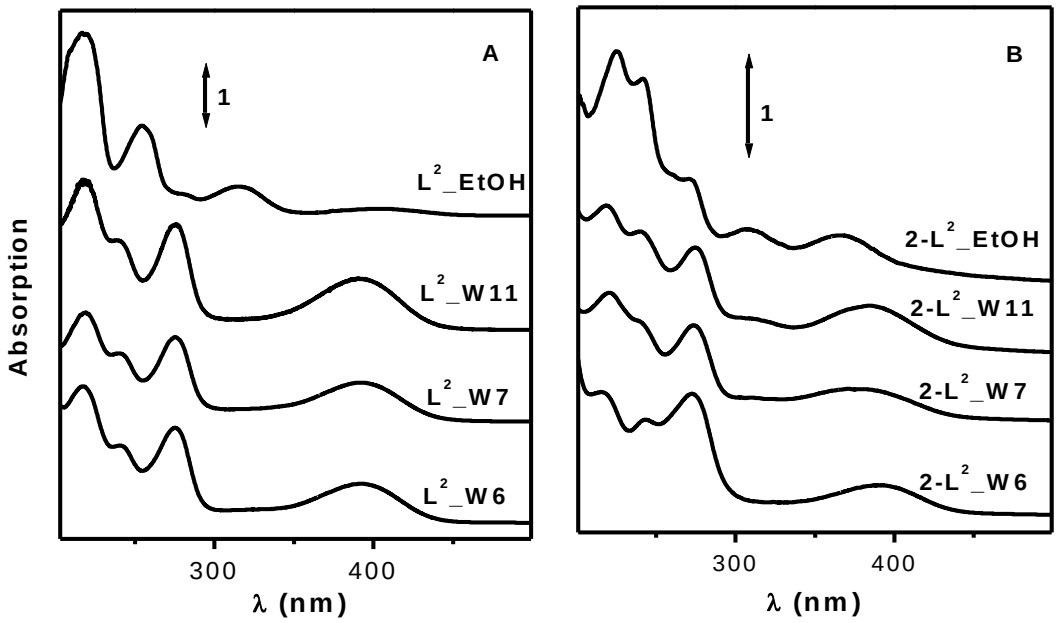

Figure 5.6 UV-visible spectrum of (**A**) L^2 in absolute ethanol and aqueous solutions at various pH (pH =11, 7, 6); (**B**) 2-L^2 in absolute ethanol and aqueous solutions at various pH (pH = 11, 7, 6). (pH=6, phosphate buffer solution; pH = 6.8, deionized water; pH = 11, sodium hydroxide solution)

The L^2 ligand in basic, neutral and acid aqueous solutions displayed similar absorption bands, but slightly different to that of L^2 ligand in the EtOH (**Figure 5.6A**). One absorption band at 275 nm appears much stronger, whereas, the charge-transfer transition band at 314 nm disappeared. Indeed, the latter absorption band is considered sensitive to solvent. In the visible region, a broad band centered at 391 nm was observed for the different pH solutions, which may be assigned to the n - π* transition of (-C=N**:**) of azomethine groups of the ligand. Furthermore, all these solutions with L^2 ligand exhibited yellow color as the L^2 ligand in EtOH. These results suggest that the L^2 ligand is stable in the pH range from 11 to

6 without the hydrolysis of the imine bond.

Parallel experiments were performed on the 2-L^2 complex. The comparison of the UV-visible spectrum of the complex in water at various pH with that in EtOH shows a red-shift of the absorption bands below 300nm assigned to the benzene ring and azomethine (-C=N) groups. The intensity of the absorption band at 309 nm observed in ethanol, which is assigned to MLCT (Cu→N) transition, dramatically decreased in aqueous solution. Furthermore, the intensity was slightly diminished upon reduction of pH in aqueous solution. In addition, the intensity of the MLCT (Cu→O) transition band at 360 nm in ethanol was also decreased upon lowering the pH in aqueous solution. In addition, the broad absorption band centered at 391 nm may be assigned to a mixture of transitions such as MLCT (Cu→O) transition and n - π* of (-C=N**:**) of the azomethine group.

When the UV-visible spectrum of the 2-L^2 complex is compared to that of the L^2 ligand in aqueous solutions at the same pH, a slight blue shift of absorption bands was observed and the intensity of absorption bands are different (**Table 5.6** and **Figure 5.6B**), indicating the existence of Cu-L^2 complexes in aqueous solution. In addition, the color of these solutions with 2-L^2 complexes is turquoise, which is different from the brown color of the complex in ethanol. These results suggest that the 2-L^2 complex in aqueous solutions may be partially decomposed. This hypothesis will be confirmed by the study of ERP spectroscopy.

EPR spectroscopy. Ethanolic solutions of 1-L^2 and 2-L^2 were characterized by EPR spectroscopy (**Figure 5.7**). For 2-L^2, one main species was observed. The $g_{\|}$ and $A_{\|}$ parameters of 2-L^2 are equal to 2.23 and 16.7 mT respectively (**Table 5.7**), which corresponds to $[Cu(L^2)_2]$ complex with a 2N2O structure of copper(II) center.[202] Furthermore, it is reported that the coordination geometry of the $[Cu(L^2)_2]$ complex is most probably planar at room temperature.[192, 194] For 1-L^2, there are two species: one with $g_{\|}$ of 2.23 and $A_{\|}$ of 16.7 mT corresponding to $[Cu(L^2)_2]$ complex; another possesses $g_{\|}$ of 2.30 and $A_{\|}$ of 15.9 mT, which is assigned to 1N3O structure of copper (II) center, and should be a mono-L^2 copper complex of $[Cu(L^2)]^{2+}$ type.[202] From the gaussian fit, the molar ratio of bis-L^2 copper to mono-L^2 copper complexes can be deduced, which is 2.8 in the 1-L^2 ethanolic solution. Considering that Cu^{2+} concentration is equal to the L^2 ligand, we got that the concentration

of $[Cu(L^2)]^{2+}$, $[Cu(L^2)_2]$ and $Cu(OAc)_2$ can be determined, which are respectively 15.2 %, 42.4 % and 42.4 %.

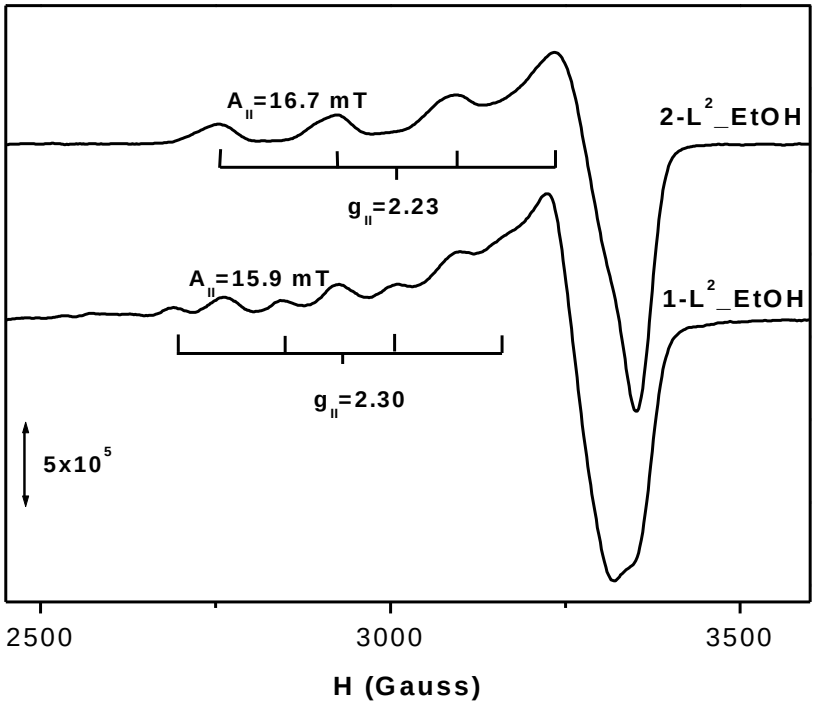

Figure 5.7 EPR spectra of 1-L^2 and 2-L^2 at 130 K in 20 % glycerine/80 %EtOH with L^2/Cu(II)=1 and 2, respectively.

Table 5.7 EPR data of Cu(II) complexes at 130 K.

Sample	pH	solution	$g_{\|}$	$A_{\|}$ (mT)	$g_{\perp}$
$[Cu(L_2)]^{2+}$	--	EtOH	2.30	15.9	2.06
$Cu(L_2)_2$	5.37	EtOH	2.23	16.7	2.04
$Cu(OAc)_2$	--	H_2O	2.37	14.5	2.05
$CuSO_4$	6.89	H_2O	2.41	12.1	2.65

The stability of $[Cu(L^2)_2]$ complex in both aqueous solution and template-containing aqueous solution was studied using EPR spectroscopy to investigate the effect of water, time, temperature and CTATos on the complex. The ethanolic solution of 2-L^2 was treated with either solution A [5H_2O/1EtOH (v/v)] or solution B [5H_2O/1EtOH (v/v) with 0.09 mol/L CTATos] at room temperature, obtaining EPR spectra 2-L^2_solution A_0h and

2-L^2_solution B_0h [**Figure 5.8 (1)**, **(2)**]. Then both solutions were stirred at 60 ºC for 24 h, obtaining the EPR spectra 2-L^2_solution A_24h and 2-L^2_solution B_24h [**Figure 5.8 (1)**, **(2)**]. The EPR spectra showed a mixture of species in all cases, probably $Cu(L^2)_2$, $[Cu(L^2)]^{2+}$ and $Cu(OAc)_2$. Indeed, in the initial 2-L^2 complex in ethanol, there are mainly two species: $[Cu(L^2)_2]$ complex (**Figure 5.7**, 2-L^2_EtOH) and CH_3COOH (AcOH, produced in the complex preparation process). When the ethanolic solution of 2-L^2 was added in solution A or solution B, the $Cu(L^2)_2$ complex partially decomposed in aqueous solution. The ligand exchange reaction took place as shown in **Scheme 5.5**, since the acidic property of HL^2 (pKa = 8.89) is lower than AcOH (pKa = 4.75). However in absolute ethanol, the following reactions are displaced to left direction due to the high pKa of absolute ethanol, leading to the $[Cu(L^2)_2]$ as main species.

$$Cu(L^2)_2 + AcOH \overset{H_2O}{\rightleftharpoons} Cu(L^2)(OAc) + HL^2 \quad (A)$$

$$Cu(L^2)(OAc) + AcOH \overset{H_2O}{\rightleftharpoons} Cu(OAc)_2 + HL^2 \quad (B)$$

Scheme 5.5 Ligand exchange reaction of $[Cu(L^2)_2]$ with CH_3COOH (AcOH) in aqueous solution.

When the EPR spectra of 2-L^2 complex in solution A and solution B at RT for 0 h were compared to that of after heating at 60 ºC for 24 h (**Figure 5.8** 2-L^2_solution A_0h, 2-L^2_solution A_24h; 2-L^2_solution B_0h, 2-L^2_solution B_24h), a shift to higher g-values was observed in both cases. It can be observed a change of ratio among the $[Cu(L^2)_2]$ and $[Cu(L^2)]^{2+}$ spices and a decrease of $Cu(OAc)_2$ species after 24 h reaction. This is probably due to a displacement of the equilibrium in the above two reactions (**Scheme 5.5**), affected by the temperature and reaction time. Furthermore, the EPR results suggest that the position of equilibrium should shift to the right, leading to produce more $Cu(OAc)_2$ and HL^2. The former $Cu(OAc)_2$ could form dinuclear species which are EPR inactive. The produced HL^2 could push the position of the equilibrium to the left, leading to the increase of $[Cu(L^2)_2]$ species (**Scheme 5.5**). This is why in EPR the amount of $[Cu(L^2)_2]$ species increased than that of $[Cu(L^2)]^{2+}$ at 60 ºC for 24 h. In addition, the EPR spectrum of solution A at 24 h (**Figure 5.8 b'**) exhibited less $[Cu(L^2)_2]$ amount than that of solution B (**Figure 5.8**

b). This is probably due to a partial stabilization of the complex by the surfactant micelles (CTA^+).

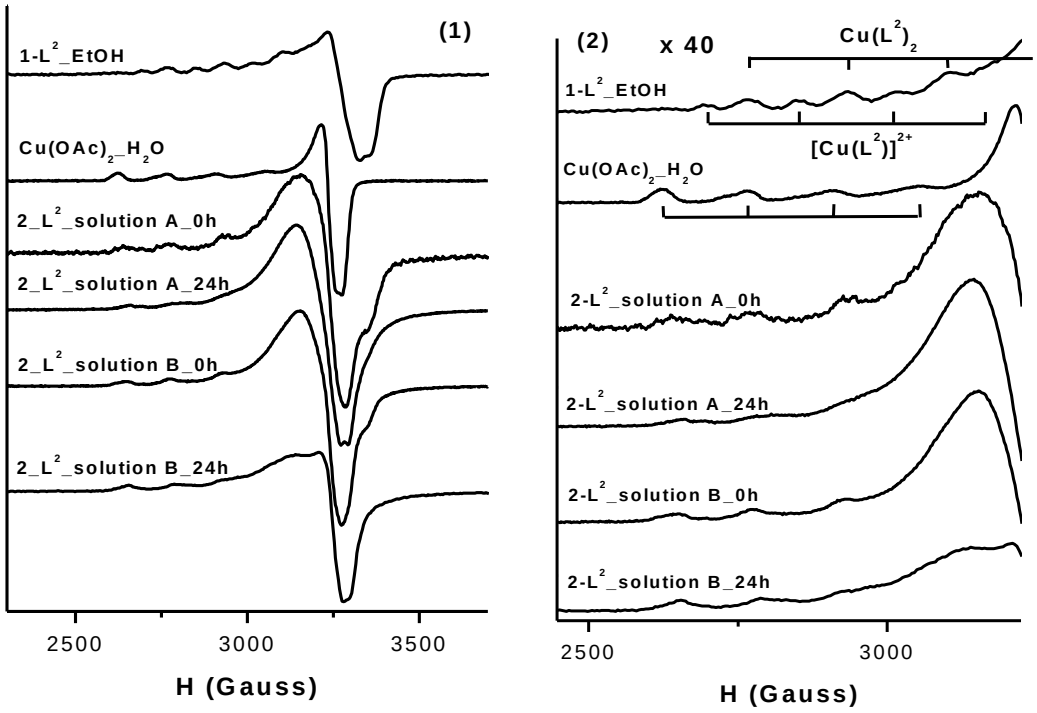

Figure 5.8 EPR spectra of 1-L^2_EtOH (1-L^2 complex in absolute ethanol), $Cu(OAc)_2$_H_2O [$Cu(OAc)_2$ in water], 2-L^2_solution A_0h (ethanolic solution of 2-L^2 complex was added in solution A at RT), 2-L^2_solution A_24h [ethanolic solution of 2-L^2 complex was added in solution A and stirred at 60 °C for 24 h], 2-L^2_solution B_0h [ethanolic solution of 2-L^2 complex was added in solution B at RT], 2-L^2_solution B_24h [ethanolic solution of 2-L^2 complex was added in solution B and stirred at 60 °C for 24 h]. Conditions: 130 K, *ca*. 20 v/v % glycerin. (**1**): original EPR spectra; (**2**): EPR spectra enlarged 40 times.

5.2.2.2 Conclusions

2-L^2 complex in absolute ethanol consists of mainly [$Cu(L^2)_2$] species. It is gradually decomposed in aqueous solution in the pH range from 11 to 6, due to a ligand exchange reaction [**Scheme 5.5**(**A**), (**B**)]. The reaction temperature and reaction time can affect the extent of the ligand exchange in aqueous solution. The presence of CTATos surfactant can influence the above reaction and displace the equilibrium to prevent the decomposition [$Cu(L^2)_2$] complex.

5.2.3 Mesoporous hybrid materials incorporation Cu(II)-L^2 complex us-

ing one-pot synthesis

5.2.3.1 Synthesis and characterization

Hybrid materials incorporating $[Cu(L^2)_2]$ complexes were synthesized though the condensation of sodium silicate and the metal complexes in the presence of CTATos under basic conditions at 60 ºC for 24 h, obtaining M-OP-XCu(YL^2) (Y = L^2/Cu=2, X = Cu/SiO_2 * 100 % in sol-gel). Indeed, the synthesis conditions chosen are similar to Ni(YL^1)@PMOs and Cu(YL^1)@PMOs. The reasons are the following: 1) the $[Cu(L^2)_2]$ complex is stable at 60 ºC; 2) the metal-free material with complex (M) exhibits a good hexagonal structure determined from XRD patterns[203]; and 3) the porosity and metal accessibility of all of the one-pot synthesized materials in this thesis can be therefore compared.

Indeed, the molar composition of the sol-gel was the following: 2X L^2 : X $Cu(OAc)_2$: 100 SiO_2 : 4.5 CTATos : 500 NaOH : 77500 H_2O. Three X = 0.1, 0.2 and 0.5 were studied, obtaining the following materials: M-OP-0.1Cu($2L^2$), M-OP-0.2Cu($2L^2$) and M-OP-0.5Cu($2L^2$). In addition, M-OP-0.3Ni($2L^1$) was synthesized in the same conditions except for the addition of 0.3 % of $Ni(L^1)_2$ in the initial sol-gel (**Scheme 5.6**).

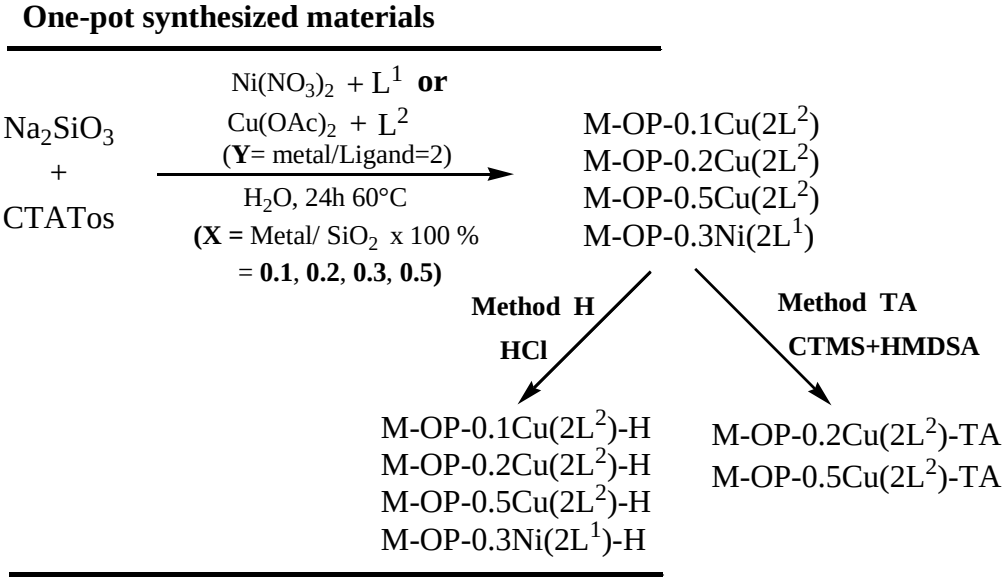

Scheme 5.6 One-pot synthesized materials.

Two methods, method *H* and method *TA* (*cf.* chapter 5.1), for surfactant removal were performed on M-OP-XCu($2L^2$) (X = 0.2 and 0.5), obtaining M-OP-XCu($2L^2$)-H and

M-OP-XCu($2L^2$)-TA, respectively. The surfactant in M-OP-0.3Ni($2L^1$) was performed by method *H*, obtaining M-OP-0.3Ni($2L^1$)-H. All samples can keep the hexagonal structures using these two methods for surfactant removal (**Figure 5.9** and **Figure 5.10**). Comparing the UV-visible spectra of M-OP-0.5Cu($2L^2$) and M-OP-0.5Cu($2L^2$)-H, the absorption bands are no significant shifted. By contrast, when method *TA* was used, in M-OP-0.5Cu($2L^2$)-TA the absorption bands assigned to MLCT (Cu→N) and d-d transition of Cu(II) ion showed a lower intensity compared to as-made material (**Figure 5.15**, **Figure 5.16** and **Table 5.12**). Two new absorption bands at 312 nm and 420 nm appeared. The same results were also obtained on M-OP-0.2Cu($2L^2$)-H and M-OP-0.2Cu($2L^2$)-TA materials. Furthermore, from the results of elemental analysis (**Table 5.9**), Cu/SiO_2 (total SiO_2) molar ratio is 0.016 for M-OP-0.5Cu($2L^2$), and 0.013 for M-OP-0.5Cu($2L^2$)-H, whilst a decrease to 0.002 is observed for M-OP-0.5Cu($2L^2$)-TA. For M-OP-0.2Cu($2L^2$), Cu/SiO_2 molar ratio is not modified, after method *H* treatment, M-OP-0.2Cu($2L^2$)-H (0.006), while it decreased to 0.002 for M-OP-0.2Cu($2L^2$)-TA.

These results indicate that the best method for surfactant removal and protection of metal environment is the method *H*. Therefore, we will focus on materials, M-OP-0.1Cu($2L^2$)-H, M-OP-0.2Cu($2L^2$)-H and M-OP-0.5Cu($2L^2$)-H in the following. M-OP-0.3Cu($2L^1$)-H and M-OP-Cu($3L^1$)-H were used to compare the metal accessibility and complex location to M-OP-XCu($2L^2$)-H.

XRD. One-pot synthesized materials, M-OP-XCu($2L^2$) and M-OP-XCu($2L^2$)-H (X = 0.1, 0.2, 0.5) were characterized by XRD (**Figure 5.9**). All the samples present the <100>, <200> and <210> reflections, indicating hexagonal mesostructure of the porosity. The d_{100} values of M-OP-XCu($2L^2$) are all around 4.1 nm which is similar to that of the metal-free material **M** (**Table 5.8**). After the surfactant removal, the intensity of materials M-XCu($2L^2$)-H in XRD patterns becomes much higher than the corresponding material M-XCu($2L^2$), which is probably due to the larger change on electron density between the channel and the framework by the removal of the surfactant assemblies. The intensity of XRD patterns decrease with the increase of Cu content (**Figure 5.9**). Furthermore, the d_{100} values of M-XCu($2L^2$)-H are reduced to *ca*. 3.8 nm (**Table 5.8**). This phenomenon is attributed to the

condensation of silanol groups when the surfactant was extracted through acid treatment.

M-OP-0.3Ni($2L^1$) and M-OP-0.3Ni($2L^1$)-H exhibited three peaks assigned to <100>, <200> and <210> reflections, which is consistent with well ordered hexagonal array of channels as in MCM-41 type of materials (**Figure 5.9**).[6, 204]

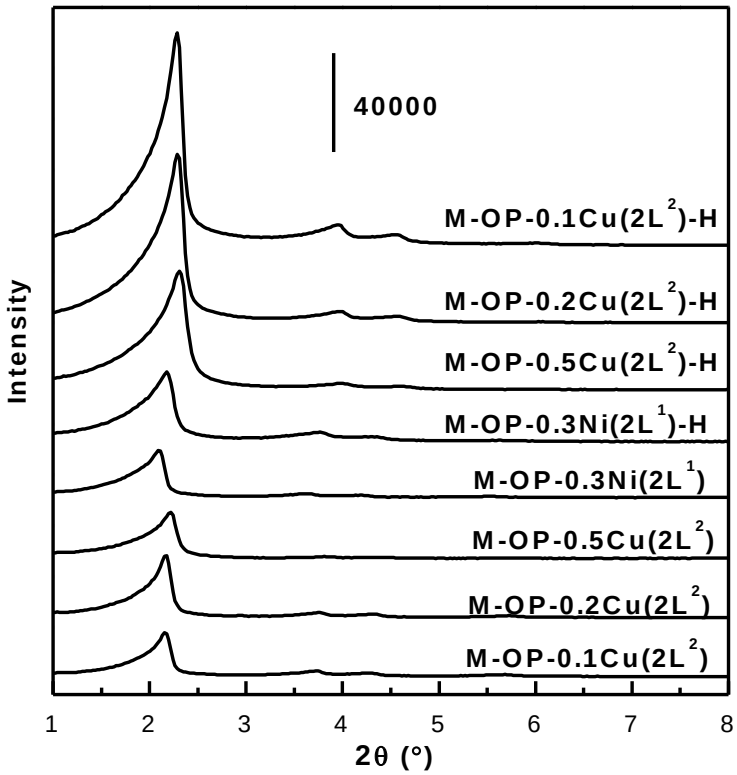

Figure 5.9 XRD patterns of M-OP-XCu($2L^2$), M-OP-XCu($2L^2$)-H (X = 0.1, 0.2, 0.5), M-OP-0.3Ni($2L^1$) and M-OP-0.3Ni($2L^1$)-H.

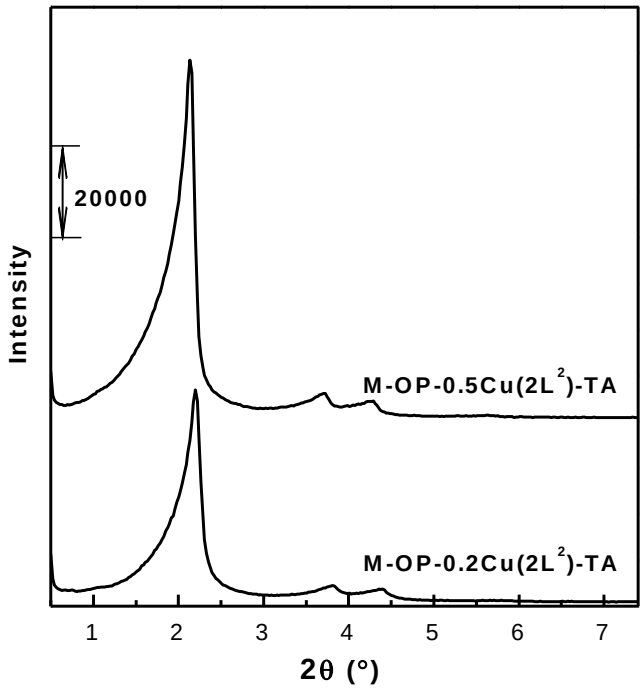

Figure 5.10 XRD patterns of M-OP-0.2Cu(2L^2)-TA and M-OP-0.5Cu(2L^2)-TA.

Table 5.8 Lattice factors of hybrid materials.

Sample	d_{100} (nm)	a_0 [a] (nm)
M	4.2	4.8
M-H	4.1	4.7
M-OP-0.1Cu(2L^2)	4.1	4.7
M-OP-0.2Cu(2L^2)	4.1	4.7
M-OP-0.5Cu(2L^2)	4.0	4.6
M-OP-0.3Ni(2L^1)	4.2	4.9
M-OP-0.1Cu(2L^2)-H	3.9	4.5
M-OP-0.2Cu(2L^2) -H	3.7	4.5
M-OP-0.5Cu(2L^2) -H	3.8	4.4
M-OP-0.3Ni(2L^1)-H	4.1	4.7
M-OP-0.2Cu(2L^2) -TA	4.1	4.8
M-OP-0.5Cu(2L^2) -TA	4.0	4.6

a: $a_0 = 2 * d_{100}/(3)^{1/2}$

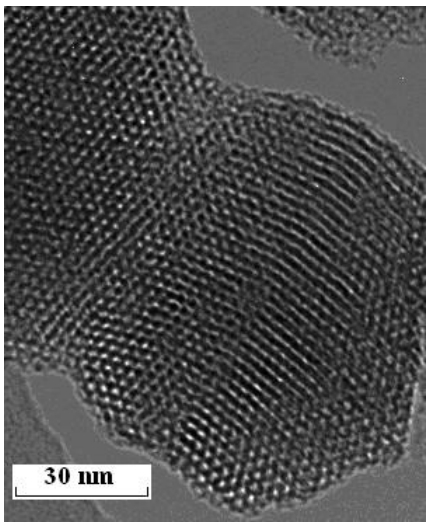

Figure 5.11 TEM of M-OP-0.5Cu($2L^2$) –H.

TEM TEM was performed on sample M-0.5Cu($2L^1$)-H, which possesses the highest Cu content in their family (Cu: 1.1 %). As shown in **Figure 5.11**, this sample presents a well-ordered hexagonal structure (on the left part) and longitudinal channels (on the right side), which are typical features of MCM-41 type of materials.[6]

IR. Samples M-OP-XCu($2L^2$) and M-OP-XCu($2L^2$)-H were studied by IR spectroscopy (**Figure 5.12**). The IR spectrum of M-OP-XCu($2L^2$) present absorption bands of δ(N-C) at 1477 cm^{-1} and the ν_s(C-H) and ν_{as}(C-H) stretching vibrations at 2850 cm^{-1} and 2918 cm^1 of the surfactant (CTATos). After surfactant removal (*method H*), the above bands were absent, indicating that the surfactant removal was efficient although a gentle HCl extraction was performed. The disappearance of the bands corresponding to ν_s(C-H) and ν_{as}(C-H) stretching vibrations of the surfactant also was also observed on M-OP-0.3Ni($2L^1$)-H.

The baseline of the IR spectra was corrected and each spectrum was normalized to the absorption band of the valence angle of tetrahedral SiO_4 units of δ(O-Si-O) at 450 cm^{-1} (*cf.* Appendix A) (**Figure 5.12**). The absorption band centered at 1650 cm^{-1} of all M-OP-XCu($2L^2$)-H samples exhibits a higher intensity than that of M-H without the metal complex. The intensity of this band increase progressively with the increases of [Cu(L^2)$_2$] complex incorporated on the material. Furthermore, when M-OP-0.5Cu($2L^2$) was treated with an excess of HCl (HCl: surfactant = 2: 1), the resulting material,

M-OP-0.5Cu($2L^2$)-2H, with 0.06 wt % of Cu exhibits a much lower absorption band at 1650 cm^{-1}. These results strongly suggest that the imine group (C=N) present in the M-OP-XCu($2L^2$)-H samples. However, this band is observed at 1623 cm^{-1} for the molecular $[Cu(L^2)_2]$ complex.

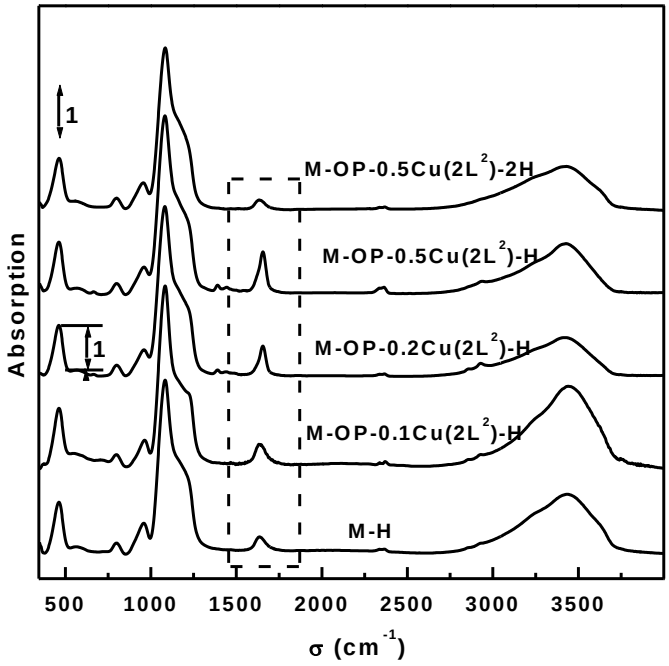

Figure 5.12 IR spectra of M-OP-XCu($2L^2$)-H (X=0.1, 0.2, 0.5).

EA. Cu weight percentage and Cu to total silicon molar ratios are presented in **Table 5.9**. Cu/Si molar ratios in the mother gel are 0.1%, 0.2 % and 0.5 % and increased up to 0.4 %, 0.6 % and 1.6 % in the final materials M-OP-0.1Cu($2L^2$), M-OP-0.2Cu($2L^2$) and M-OP-0.5Cu($2L^2$). Ni/Si molar ratio is 1.2 % in M-OP-0.3Ni($2L^1$). Indeed, for M-OP-XCu($2L^2$), the yield of silicon at such low temperature of synthesis was only *ca*. 28 %, while the yield of copper was ~ 100 %. For M-OP-0.3Ni($2L^1$), the yield in Ni was 78 % and the yield in silicon was also partial (*ca*. 21 %).

After the gentle template extraction by *method H* (1 eq. HCl/template, technical ethanol at 40 °C), the Cu/Si molar ratios are 0.3 % for M-OP-0.1Cu($2L^1$)-H, 0.6 % for M-OP-0.2Cu($2L^1$)-H and 1.3 % for M-OP-0.5Cu($2L^1$)-H. The Ni/Si molar ratio was 1.0 % in M-OP-0.3Ni($2L^1$)-H (**Table 5.9**). These results indicated that the copper(II) and nickel(II)

are mainly kept after HCl extraction using *method H*.

Table 5.9 Metal content and molar ratios deduced from elemental analysis and weight loss from TGA.

Sample	Si [a] wt%	Cu [b] wt%	Cu/Si [c]	M [d] yield%	Si yield %	Cu [e] wt%
M-OP-0.1Cu($2L^2$)	51.28	0.2	0.004	99	25	--
M-OP-0.2Cu($2L^2$)	52.83	0.4	0.006	96	26	0.4
M-OP-0.5Cu($2L^2$)	52.24	0.9	0.016	99	31	0.9
M-OP-0.3Ni($2L^1$)	51.91	0.6	0.012	78	21	--
M-OP-Cu($2L^1$)	48.93	1.7	0.032	97	30	--
M-OP-0.1Cu($2L^2$)-H	89.23	0.3	0.003	--	--	--
M-OP-0.2Cu($2L^2$)-H	79.12	0.5	0.006	--	--	0.4
M-OP-0.5Cu($2L^2$)-H	82.84	1.1	0.013	--	--	1.0
M-OP-0.3Ni($2L^1$)-H	85.53	0.9	0.010	--	--	--
M-OP-Cu($2L^1$)-H	80.58	2.5	0.029	--	--	2.3
M-OP-0.2Cu($2L^2$)-TA	85.76	0.2	0.002	--	--	--
M-OP-0.5Cu($2L^2$)-TA	85.85	0.2	0.002	--	--	--

a: the weight percent of total silicon (inorganic and organic) is obtained from the residual weight in TGA at 1000 ºC upon subtraction of CuO; b: copper weight content was measured by ICP-MS; c: Cu/Si molar ratio; d: M: Ni(II) and Cu(II); e: determined from quantitative EPR measurement. Quantification of Cu(II) species was performed using crystals of $CuSO_4.5H_2O$ as calibration reference.

5.2.3.2 N_2 sorption isotherms of hybrid materials

The nitrogen sorption isotherms for the M-H, M-OP-0.5Cu($2L^2$)-H and M-OP-0.3Ni($2L^1$)-H are presented in **Figure 5.13** and the corresponding textural data are gathered in **Table 5.10**. The isotherms of all the materials are of type IV according to the IUPAC classification.[38] The steep step of the capillary condensation at about 0.38 P/P_0 evidenced a narrow pore size distribution.[6, 169] Strikingly, the pore diameter, calculated from the BdB model, for materials M-OP-0.3Ni($2L^1$)-H and M-OP-Cu($2L^1$)-H and the metal-free M-H are within 0.1 nm the same, while it is much smaller for M-OP-0.5Cu($2L^2$)-H (**Table 5.10**).

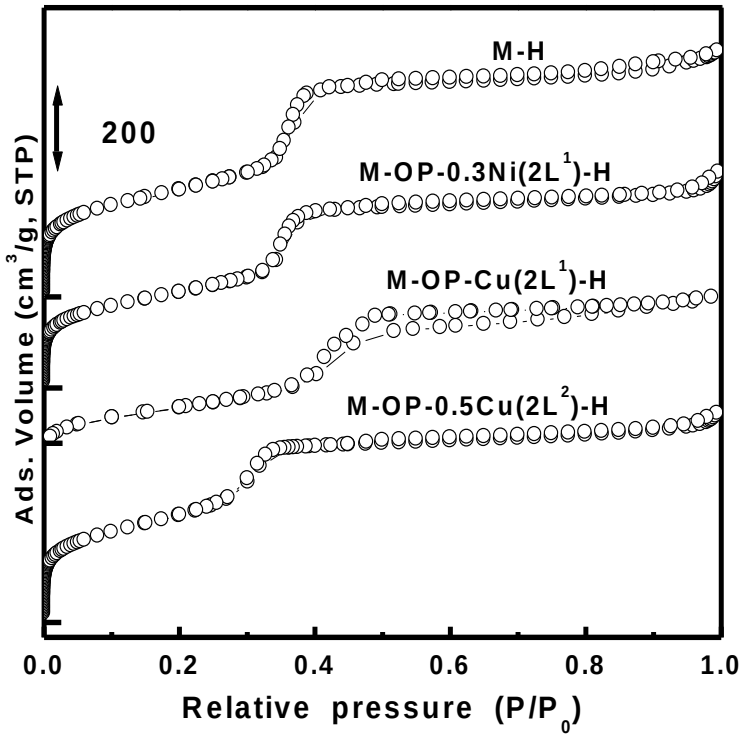

Figure 5.13 Nitrogen adsorption-desorption isotherms at 77 K of one-pot synthesis materials.

If the BET specific surface and the total porous volume are compared, a slight modification was observed for both M-OP-0.3Ni(2L^1)-H (S_{BET} = 910 m^2g^{-1}, V_p= 0.85 cm^3g^{-1}) and M-OP-0.5Cu(2L^1)-H (S_{BET} = 1010 m^2g^{-1}, V_p= 0.83 cm^3g^{-1}) compared to the blank M-H, (S_{BET} = 1050 m^2g^{-1}, V_p= 1.02 cm^3g^{-1}) whereas a more prononunced diminution was observed for M-OP-Cu(2L^1)-H (S_{BET} = 650 m^2g^{-1}, V_p= 0.76 cm^3g^{-1}), which possesses a higher metal content (**Table 5.10**). These parameters are not trivial to be compared, since defects due to the presence of the metal complex could be possible in such materials, and this effect should be more important for higher metal content. Moreover, similar copper-amino complexes grafted in the channels of the same silica support and containing about 1 wt% copper,[204] lead to ϕ_{BdB}~3.3 nm, S_{BET} ~ 600 m^2g^{-1} and V_p~ 0.4 cm^3g^{-1} which are values considerable lower that those found for the present materials. In addition, in the present study the wall thickness W_t is roughly the same for all materials. These data strongly suggest that the metal complexes are not located in the mesoporous channel in all these materials contrary to grafted species. Again, the C-parameter calculated from BET, which is related to the nature of the internal surface,

is about the same (104 ± 5) for M-OP-0.3Ni($2L^1$)-H and M-OP-Cu($2L^1$)-H, respectively, which is similar to the blank M-H (108), indicating that the chemical nature of the internal surface was equivalent. However, for M-OP-0.5Cu($2L^2$)-H dealing with the salicylaldimine ligand, the C parameter is definitively smaller (83), showing that the nature of the ligand does affect the chemistry of the surface in this case.

Table 5.10 Textural properties of mesoporous hybrid materials.

Sample	S_{BET} ($m^2 \cdot g^{-1}$)	V_{BJH} ($cm^3 \cdot g^{-1}$)	ϕ_{BdB} (nm)	W_t [a] (nm)	C [b]
M-H	1050	1.02	3.8	0.9	108
M-OP-0.5Cu($2L^2$)-H	1010	0.83	3.5	0.9	83
M-OP-0.3Ni($2L^1$)-H	910	0.85	3.8	0.9	106
M-OP-Cu($2L^1$)-H	650	0.76	3.9	0.9	99

a: apparent wall thickness is determined using $W_t = 2*d_{100}/(3)^{1/2} - \phi_{BdB}$; b: C value determined from BET.

5.2.3.3 Cu (II) coordination state characterization

EPR. EPR spectra for M-OP-XCu($2L^2$) and M-OP-XCu($2L^2$)-H were recorded at room temperature (**Figure 5.14**). The corresponding spectral parameters are summarized in **Table 5.11**. A closer examination reveals $g_{\parallel} > g_{\perp} > 2.0023$ in all the cases, which is consistent with $d_{x^2-y^2}$ ground state as the magnetic orbital and with an elongated square pyramidal or elongated octahedral environment for Cu(II).[205, 206]

Table 5.11 g and A values deuced from EPR spectra at 298 K.

Materials	$g_{\parallel}$	$A_{\parallel}$ (mT)	$g_{\perp}$
M-OP-0.1Cu($2L^2$)	2.31	13.9	2.04
	2.22	17.2	2.01
M-OP-0.2Cu($2L^2$)	2.31	13.9	2.04
	2.22	17.2	2.01
M-OP-0.5Cu($2L^2$)	2.31	13.9	2.04
	2.22	17.2	2.01

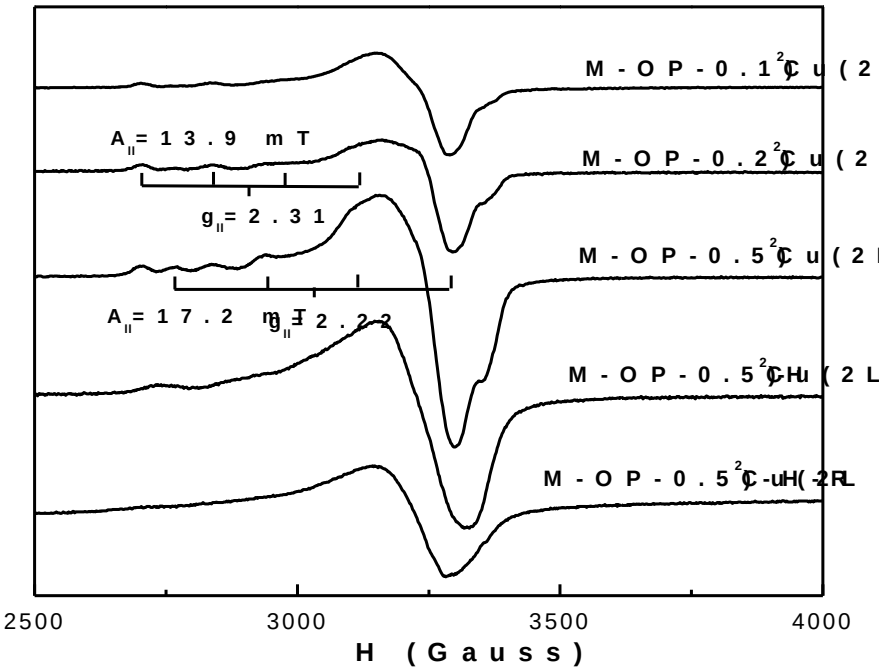

Figure 5.14 EPR spectrum of M-OP-XCu($2L^2$), M-OP-XCu($2L^2$)-H and M-OP-0.5Cu($2L^2$)-H-R at 298 K.

The EPR spectra of M-OP-0.1Cu($2L^2$), M-OP-0.2Cu($2L^2$) and M-OP-0.5Cu($2L^2$) all exhibited two species. The intensity of these two species increases with the increase of Cu loading. In the EPR spectrum of M-OP-0.5Cu($2L^2$), these two species can be well observed and distinguished: one presents $g_{\|}$ of 2.31 and $A_{\|}$ of 13.9 mT, and the other presents $g_{\|}$ of 2.23 and $A_{\|}$ of 17.2 mT, which respectively correspond to a 1N3O environment and a 2N2O environment of Cu(II).[192, 202] This result indicates that two type complexes, mono(salicylaldimine) copper(II) $[Cu(L^2)]^+$ and bis(salicylaldimine) copper(II) $[Cu(L^2)_2]$, present in the M-OP-XCu($2L^2$) materials. The reason of the formation of these two complexes are likely that the initial bis(salicylaldimine) copper(II) complex in the sol-gel partially decomposed and formed $[Cu(L^2)]^+$ and $[Cu(L^2)_2]$ complexes, which has been elucidated in the study of copper-L^2 complexes in solution (*cf.* 5.2.2). After template extraction using HCl washing, M-OP-XCu($2L^2$)-H exhibit a broader signal which is probably due to overlapping of $[Cu(L^2)]^+$ and $Cu(L^2)_2$ species. Thus in the M-OP-XCu($2L^2$) materials, the surfactant likely plays a role of isolation these species, which make the above mentioned two species, distinguished. The studied of Murphy *et al*. can support this point.[117] They ob-

served a broad EPR signal of xero- and aerogels containing N, N'-ethylenebis(salicylidenaminato) (salen) Cu(II) complexes which were synthesized *via* sol-gel method under slight acid conditions.[118] Furthermore, the aerogels exhibited a dramatic reduction activity for isophorone oxidation. From observing the data of Murphy *et al*., Baleizão *et al*. have doubted the change of coordination sphere of the initial copper(II) complex with 2(NO) sphere in the obtained aerogels.[207] Indeed, it is most probably that the coordination environment around the metal is different from that proposed 2N2O, which can be supported by this thesis.

Active Cu(II) complexes in EPR were quantified and the results are presented in (*cf.* Appendix B) (**Table 5.9**). The active Cu(II) species in EPR are 0.4 % for M-OP-0.2Cu($2L^2$) and 0.9 % for M-OP-0.5Cu($2L^2$), which are close to the Cu(II) content determined from ICP-MS (0.4 % and 0.9 %, respectively). After surfactant removal, the EPR active Cu(II) species are 0.4 % for M-OP-0.2Cu($2L^2$)-H and 1.0 % for M-OP-0.5Cu($2L^2$)-H, which are consistent with the result from ICP-MS (0.5 % and 1.1 %). All these results reveals that there is no dinuclear or polynuclear Cu(II) species on these hybrid materials but mononuclear Cu(II) species on M-OP-XCu($2L^2$). Furthermore, these results revealed that in the initial bis-L^2 copper(II) complex only one L^2 replaced by one OAc^- [**Scheme 5.5(A)**] or one $\equiv SiO^-$ in the sol-gel process, due to the highly basic conditions (pH = 11.5) or the stabilization by template which make the behavior of complex is different from the corresponding molecular species.

UV-visible spectra

The UV-visible spectra of hybrid materials, M-OP-XCu($2L^2$) and M-OP-XCu($2L^2$)-H, have been recorded (**Figure 5.15** and **Figure 5.16**), and the corresponding data are gathered (**Table 5.12**). The materials show several intense absorptions in the ultraviolet region (200-380 nm) and visible region (380-780 nm). The M-OP-XCu($2L^2$) exhibits several absorption bands below 270 nm, attributed to π - π^* transition in the benzene ring and the π - π^* transitions of the azomethine (-C=N) groups, that are already observed in the spectrum of [Cu(L^2)$_2$] molecular complex. M-OP-XCu($2L^2$) presented two absorption bands of *ca.* 306 nm and

368 nm, which are assigned to MLCT (Cu→O and Cu→N) transitions. In addition, the shoulder at *ca*. 450 nm is mostly probably attributed to n - π* transitions of azomethine (-C=N) group.

Table 5.12 Absorption bands in the UV-visible spectra for hybrid materials.

Sample	λ_{max} (nm)					
L^{2} [a]	217,	254,	279,	314,	404	
$Cu(L^{2})_2$ [a]	225,	242,	271,	309,	360,	622
M-OP-0.1Cu($2L^{2}$)	224,	244,	270,	306,	368,	634
M-OP-0.2Cu($2L^{2}$)	226,	268,	306,	368,	633	
M-OP-0.5Cu($2L^{2}$)	232,	248,	268,	308,	368,	633
M-OP-0.3Ni($2L^{2}$)	368,	595				
M-OP-0.1Cu($2L^{2}$)-H	224,	238,	268,	306,	362,	633
M-OP-0.2Cu($2L^{2}$)-H	210,	240,	270,	310,	364,	633
M-OP-0.5Cu($2L^{2}$)-H	212,	240,	270,	308,	368,	637
M-OP-0.5Cu($2L^{2}$)-2H	220,	244,	276,	396,	686	
M-OP-0.5Cu($2L^{2}$)-HH	216,	244,	278,	398,	890	
M-OP-0.3Ni($2L^{2}$)-H	372,	602				
M-OP-0.2Cu($2L^{2}$)-TA	218,	246,	274,	312,	370,	639
M-OP-0.5Cu($2L^{2}$)-TA	218,	248,	274,	312,	376,	630

a: determined in ethanol.

The absorption band centered at *ca*. 634 nm at lower energy and in lower intensity is attributed to the d-d transition of Cu(II) ion (d_{xy}-$d_{x^2-y^2}$; d_{z^2}-$d_{x^2-y^2}$), which is at lower energy than the [$Cu(L^{2})_2$] molecular complex (622 nm). The reason is highly likely the formation of a mixture of species such as mono(salicylaldimine) copper(II) and bis(salicylaldimine) copper(II) complexes in the hybrid materials. Therefore, these results confirm again that the copper-salicylaldimine complexes have been successfully introduced in the hybrid materials. M-OP-XCu($2L^{2}$)-H materials display similar absorption bands to those of M-OP-XCu($2L^{2}$), and the intensity of bands were maintained (**Figure 5.15** and **Figure 5.16**, **Table 5.12**). There results reveal that the copper species are not modified during the surfactant removal process using the gentle HCl washing (*method H*). In addition, these results indicate again that method *H* is a suitable approach to both maintain the hexagonal struc-

ture and the complex integrity after template removal.

Two M-OP-0.5Cu($2L^2$)-2H and M-OP-0.5Cu($2L^2$)-HH were obtained by using an excess of HCl (1 mol·L^{-1}, HCl: surfactant = 2: 1) treatment. Their UV-visible spectra are presented in **Figure 5.15** and **Figure 5.16**. They exhibit totally different UV-visible spectra to M-OP-0.5Cu($2L^2$), especially because of the absence of the absorption bands attributed to MLTC transitions and d-d transition of the Cu(II) ion, indicating the leaching of Cu(II) complex, which is consistent with the low Cu content on materials checked by ICP-MS.

M-OP-0.3Ni($2L^1$) and M-OP-0.3Ni($2L^1$)-H exhibit absorption bands ν_3 and ν_2 of 368 nm and 595 nm, 372 nm and 602 nm, which is in agreement with the results presented in chapter 4, indicating NiN_4 coordination sphere of complex.

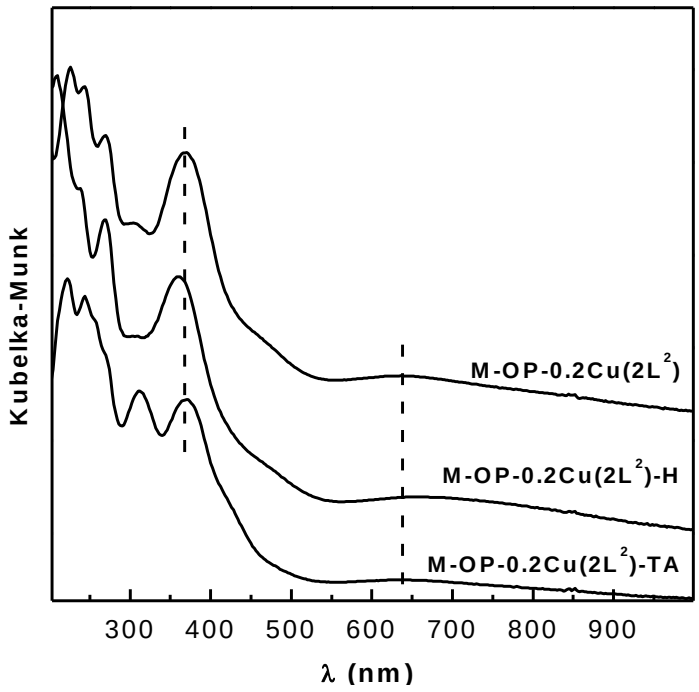

Figure 5.15 Solid state UV-visible spectra of M-OP-0.2Cu($2L^2$), M-OP-0.2Cu($2L^2$)-H and M-OP-0.2Cu($2L^2$)-TA.

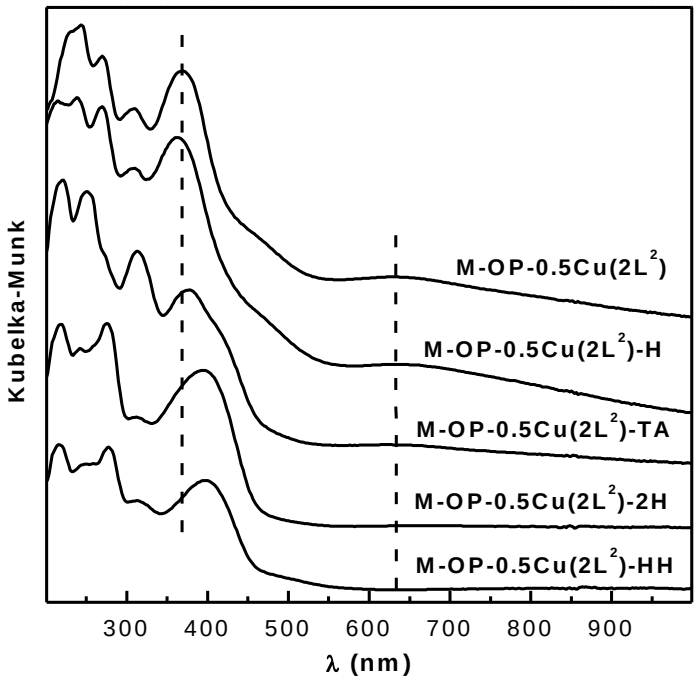

Figure 5.16 Solid state UV-visible spectra of M-OP-0.5Cu($2L^2$), M-OP-0.5Cu($2L^2$)-H, M-OP-0.5Cu($2L^2$)-TA, M-OP-0.5Cu($2L^2$)-2H and M-OP-0.5Cu($2L^2$)-HH.

5.2.3.4 Metal displacement

The metal extraction was tested by using an excess of HCl, and the results are presented in **Table 5.13**. The M-OP-0.5Cu($2L^2$) material was washed with an excess of HCl (1mol·L^{-1}, HCl: metal = 8: 1) in technical ethanol (the indicative pH is equal to 3), the obtained solid is named M-0.5Cu($2L^2$)-2H. From the ICP-MS analysis, the Cu content decreases to 0.06 wt %, which corresponds to 95 % Cu(II) leaching.

M-0.5Cu($2L^2$)-H material without surfactant was treated once again by HCl (1mol·L^{-1}, HCl: metal = 4: 1), the resulted material is referred to as M-0.5Cu($2L^2$)-HH. The Cu(II) content of M-0.5Cu($2L^2$)-HH is equal to 0.04 %, corresponding to 96 % of Cu(II) leaching. However, only 0.58 % of Ni(II) is observed for M-0.3Ni($2L^1$)-HH and 2.27 % of Cu(II) is found for M-0.5Cu($3L^1$)-HH, which shows a quantitative Cu(II) removal of *ca*. 70 % and 90 %, respectively.

Table 5.13 Elemental analysis for metal accessibility tests (wt %).

Materials	Cu wt % (ICP-MS)	Cu leaching mol. %
M-OP-0.5Cu($2L^2$)-2H	0.06	95
M-OP-0.5Cu($2L^2$)-HH	0.04	96
M-OP-0.3Ni($2L^1$)-HH	0.58	30
M-OP-Cu($2L^1$)-HH	2.27	8

5.2.3.5 Location of metal complexes on PMOs

Hence in solids M-OP-0.3Ni($2L^1$)-H and M-OP-Cu($2L^1$)-H, the $[Ni(en)_2]^{2+}$ and $[Cu(en)_2]^{2+}$ complexes are located in a non leaching position in the framework of the silica. Surprinzingly, this is the charged bisethylenediamine type of complex obtained from en that is "embedded" in the wall of the pore (**Scheme 5.7**). The local neutrality is likely due to silanolate moities. This would explain the strong retention under the acid leaching test. Similarly, the $[Cu(L^2)_2]$ and $[Cu(L^2)XL]$ complexes (X = SiO^- or OH^- and, L = H_2O or silanol ligands) in material M-OP-XCu($2L^2$), are both likely located in the wall according to the pore wall thickness and the high value of the pore volume. However, their weak resistance to the acid leaching test attests for their accessibility to proton attack and their propensity to be removed from their polydentate sites. It is proposed here that both sites are "showing on" the porewall surface like outcrops and called as such in **Scheme 5.7**. The rational for such difference between L^1 and L^2 resides both in the more hydrophobic nature and in the neutrality of the complexes formed by the latter in comparison with the former. Indeed, both parameters are strong driving forces to locate the complexes in the micelles during the initial steps of the sol-gel condensation of the silicate and organosila ne moities.

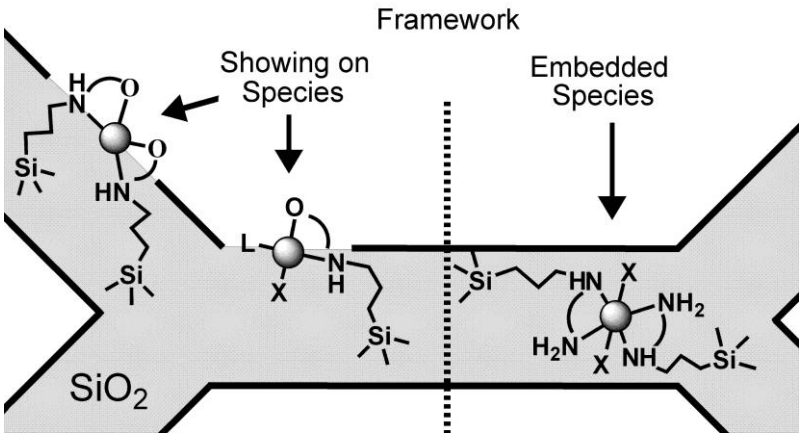

Scheme 5.7 "Showing on" and "embedded" framework species in materials M-OP-XCu($2L^2$) and, M-OP-0.3Ni($2L^1$) or M-OP-Cu($2L^1$), respectively: L is any neutral ligand such as water or silanol whilst X is any negatively charged ligand such as silanolate or hydroxyde.

5.2.3.6 Catalytic hydroxylation of phenol

Catalytic activities and selectivities in phenol hydroxylation by H_2O_2 over M-OP-XCu($2L^2$) were studied (**Table 5.14**). Blank experiments with M-H as catalyst exhibited no activity toward phenol hydroxylation. Under the same conditions (phenol: Cu = 130: 1, phenol: H_2O_2 = 3: 1), M-OP-XCu($2L^2$) catalyst showed activity on phenol hydroxylation, 19.4 % for M-OP-0.1Cu($2L^2$), 25.3 % for M-OP-0.2Cu($2L^2$) and 16.5 % for M-OP-0.5Cu($2L^2$). In addition, the tar selectivity decreased from 62.4 % for M-OP-0.1Cu($2L^2$) to 37.5 % for M-OP-0.2Cu($2L^2$) and 14.5 % for M-OP-0.5Cu($2L^2$). In all cases, catechol (CAT) was the predominant product. However, Ray *et al*. have reported that the predominant product is the hydroquinone and no benzoquinone was formed when the catalyst the bis(salicylaldimine) copper(II) complexes immobilized in the channel of MCM-41, while the characterization of catalyst is very poor.[126] Other Cu(II) ion incorporated in mesoporous materials, such as Cu-SBA-15,[128] Cu-HMS[127] and Cu exchanged Y,[131] favor the formation of catechol, while TS-1 and Cu-CMM favor the formation of hydroquinone. A possible reason for a preference of catechol is probably that two-dimensional mesostructure shows a non-shape-selective oxidation for hydroxylation of phenol.

After the first run, M-OP-0.5Cu($2L^2$)-H was recovered by filtration, and then washed with ethanol and acetone, and dried at 60 °C for 18 h. This obtained material was named

M-OP-0.5Cu($2L^2$)-H and was characterized by EPR spectroscopy (**Figure 5.14**). A change of the EPR spectrum was observed. The EPR active Cu(II) species after reaction was 0.8 wt %, which was 1.0 wt % in the initial solid M-OP-0.5Cu($2L^2$)-H. This result indicates a leaching Cu(II) species during the reaction. This may be due to either weak binding constant of Cu(II)-L^2 complexes or hemolytic decomposition of the H_2O_2 forming ·OH radical.

Table 5.14 Catalytic activities and selectivity in phenol hydroxylation with H_2O_2 over various catalysts [a].

Sample	Phenol: H_2O_2	Phenol conv. (mol%)	H_2O_2 eff. conv %[b]	Products selectivity [c] (%)		diphenols selectivity (mol%)
				CAT	HQ	
M-H	1: 1	0	0	0	0	0
M-OP-0.1Cu($2L^2$)-H	3.0: 1	19.4	38	65.4	34.6	38
M-OP-0.2Cu($2L^2$)-H	3.0: 1	25.3	45	64.8	35.2	62
M-OP-0.5Cu($2L^2$)-H	3.0: 1	16.5	42	64.0	36.0	85

a: Reaction condition : solvent: buffer solution pH = 6, phenol: 0.0989 g, phenol: Cu = 130:1, t = 2 h, T = 80 ºC, [phenol] = 0.15 mol/L

b: the efficiency conversion of H_2O_2 was calculated as follows: H_2O_2 eff. Conv = 100 x H_2O_2 (mol) consumed in formation of CAT and HQ / H_2O_2 (mol) converted. H_2O_2 conversion was determined by the iodometry titration.

c: CAT = catechol, HQ = hydroquinone, and BQ = benzoquinone. The product of tar is not included, and the product selectivity is CAT (or HQ or BQ)/(CAT+HQ+BQ).

5.2.3.7 Conclusions

A novel synthesis of hybrid materials with Cu-Schiff base complexes has been optimized at 60 °C using sodium silicate as silicon source for co-condensation with various contents of Cu(L^2)$_2$ (L^2: N-salicylaldimine-propylamine-trimethoxysilane) complexes and using NaOH as the base source in the presence of cetyltrimethylammonium tosylate (CTATos) without any organic co-solvent, obtaining materials M-OP-XCu($2L^2$) [X = 0.1, 0.2, 0.5, 2 = L^2/Cu*100% in the sol-gel]. A mixture of chlorotrimethysilane (CTMS) and hexamethyldisilazan (HMDSA) (*method TA*) or an appropriate amount of HCl (*method H*) have been tested for the surfactant extraction from the as-made materials. From the results of elemen-

tal analysis and UV-visible spectra, using *method H* for template extraction, the obtained M-OP-0.1Cu($2L^2$)-H (0.3 wt % Cu content), M-OP-0.2Cu($2L^2$)-H (0.5 wt % Cu content) and M-OP-0.5Cu($2L^2$)-H (1.1 wt % Cu content) materials can not only keep the hexagonal mesostructure but also preserve the integrity of metal complex.

The EPR and UV-visible study revealed that Cu(II)-Schiff base complexes are successfully incorporated into the mesoporous materials *via* one-pot synthesis, but the Cu(II) species on solid consists of a mixture of $[Cu(L^2)]^+$ and $[Cu(L^2)_2]$ complexes despite of the initial $[Cu(L^2)_2]$ complexes added in the sol-gel process. This result is most probably caused by a partial decomplexation of the L^2 ligand in aqueous solution.

For comparison, M-OP-0.3Ni($2L^1$)-H (0.9 wt % Ni content) and M-OP-Cu($2L^1$)-H (2.5 wt % Cu content) materials were presented in this study. The wall thickness W_t is roughly the same for all materials deduced from isotherms. In addition, for M-OP-XCu($2L^2$)-H materials, their weak resistance to the acid leaching test attests for their accessibility to proton attack and their propensity to be removed from their polydentate sites compared to M-OP-0.3Ni($2L^1$)-H, M-OP-Cu($2L^1$)-H. All these results allow us to propose that the location of Cu(II)-L^2 complexes are most probably "showing on" the porewall surface like outcrops, and charged bisethylenediamine type of M(II)-L^1 complexes are "embedded" in the wall of the pore. Furthermore, the M-OP-XCu($2L^2$)-H materials exhibit activity on phenol hydroxylation in the presence of H_2O_2, indicating again that the complexes are accessible to a substrate. These results open novel opportunities for the design of multifunctionnel materials.

5.3 Schiff base complex with 3N1O coordination sphere in the channel

5.3.1 Introduction

Catalytic hydroxylation of phenol, which is an important reaction for production of fine chemicals like catechol and hydroquinone, has been intensively investigated. Heterogeneous catalysts play an important role in the hydroxylation reaction of phenol for their excellent recovery ability and some environmentally friendly properties. Researchers have

used many strategies for preparing heterogeneous catalysts one of these consists to introduce different types of transition metal ion into microporous/mesoporous materials. For example, TS-1 has exhibited attractive activity of hydroxylation, which was first realized in commercial application by Enichem in 1986 in Italy[208] and was extensively investigated in the effect of various parameters by Ratnasamy *et al.*[209] and Tatsumi *et al.*,[210] but their synthesis is to some extent complicated and high cost. On the other hand, the Cu (II) ion has been planted into different mesoporous materials since the Cu(II) owns a well redox property and the mesoporous materials possess high surface area. Reported mesostructured catalysts like CuMCM-41[129], CuSBA-15[128], CuHMS[127] and CuCMM[130] exhibit a good activity for phenol hydroxylation reaction, however, they carry some weaknesses. As we realized so far, the selectivity to diphenols and to so-called "tar" is not clearly provided in these previous data. Furthermore, the activities of such catalysts significantly decrease on the second run, and the unique way to recover the activity is to regenerate the catalysts by calcination.

Another available strategy is to introduce the metal complexes in the micro/mesoporous solids, either by encapsulation or by grafting (post-synthesis). Many types of metal complexes have been encapsulated according to the former methodology, such as M(H2hybe)/Y with M = Cr(III), Fe(III) or Bi(III) where H2hybe is 1,2-bis(2-hydroxybenzamido)ethane,[211] $CuCl_{l6}$Pc/ZSM-5 with phthalocyanine as Pc,[212] Cu(salen)/Y and Cu(5-Cl-salen)/Y where salen is *N*,*N*'-ethylenebis (salicylidenaminato)[209] and [Fe(II)phen]/MCM-41.[213] They all exhibited activity toward phenol hydroxylation, the reaction activity is limited by the leaching of the metal complexes out of the pores. The second methodology making the use of covalent can minimize the leaching thanks to the covalent bonding linkage of the metal complexes to the supports through a tether. Only few examples are reported on such approach for mesoporous materials with application to phenol catalytic hydroxylation.[126, 214] In the actual chapter 5.2, Cu(II)-L^2 complexes incorporated according to the one-pot synthesized hybrid materials have been primarily applied on phenol hydroxylation. Due to the lower affinity of L^2 for Cu(II) in comparison with L^1, we treat also in this section the case of a tetradentate-Schiff base copper(II) complex [Cu(L^3)(CH_3COO)] (L^3: N-(salicylaldimine)- (N'-propyltrimethoxylsilane)- diethylene-

triamine).

Cu-L^3 complex linked via a single siloxane moieties will be immobilized on mesoporous materials through the "molecular stencil patterning" technique to ensure as best as we could an even distribution of Cu(II) complex [Cu(L^3)(CH_3COO)] in the channel (**Scheme 5.8**). The textural and chemical properties of the intermediate samples (M2', M2'-ES) and the final sample (M2'-ES-CuL^3) material will be investigated following a similar approach as described before. The latter material will be tested in phenol hydroxylation reaction with H_2O_2 as oxidant. Various reaction factors such as reaction time, H_2O_2/substrate, pH and solvent will be investigated and phenol conversion and products selectivity will also be provided. A preliminary study of the stability of the Cu-L^3 complexes in solution will be also performed.

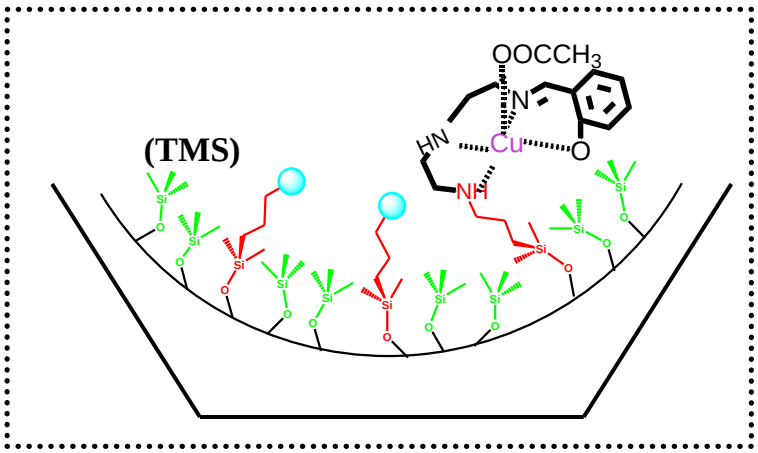

Scheme 5.8 Trimethylsilyl (TMS) and Cu(II) complex [Cu(L^3)(CH_3COO)] functionalized LUS (MCM-41 type) via molecular stencil patterning method.

5.3.2 Stability study of L^3_{ref} and 1-L^3_{ref} in aqueous solution

Here, tetradentate-Schiff base was chosen as the ligand (L^3_{ref}) with a 3N1O coordination sphere. This ligand was reacted with one equivalent $Cu(OAc)_2$ in absolute ethanol, obtaining the so-called 1-L^3_{ref} complex. The expected environment around the metal center in 1-L^3_{ref} is constituted of 3N and 2O from L^3_{ref} ligand and OAc^- ion ([Cu(L^3_{ref})(CH_3COO)], **Scheme 5.9 right**). Theoretically, this complex possesses a higher affinity toward Cu(II) ion than bis(salicylaldimine) copper(II) complex and copper(II) salen complex with 2N2O coordina-

tion sphere due to higher chelate effect of L^3_{ref} ligand and a 3N1O coordination sphere.

Some reports have revealed that salen type complex is stable in aqueous solution. However, there is no systemic investigation on 1-L^3_{ref} complex in aqueous solutions at various pH. Indeed, phenol hydroxylation is usually carried out in the neutral or acid aqueous solutions at certain temperature and reaction time. Thus, functionalized heterogeneous catalyst with metal complex needs to possess a high metal affinity in the above solutions to avoid metal leaching during the reaction, despite that there are other reasons that may promote metal leaching. Therefore, a investigation of the stability of 1-L^3_{ref} in various pH aqueous solutions was required. The effects of pH, temperature and reaction time for ligand (L^3_{ref}) and 1-L^3_{ref} complex are presented in the following.

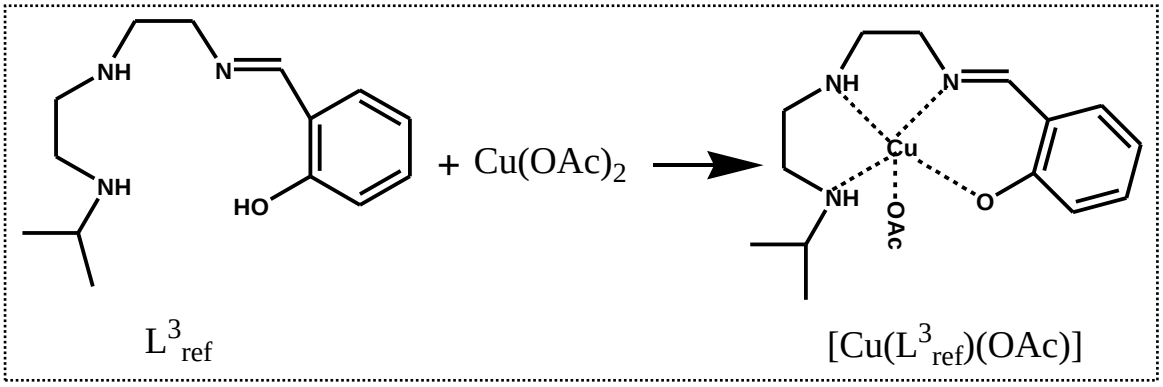

Scheme 5.9 Synthesis route of Cu(L^3_{ref})(OAc) complex.

5.3.2.1 Structural study of the Cu-L^3_{ref} complex

To our knowledge, there is no report on the crystal structure of Cu(II)-L^3_{ref} complex. We have tried to obtain good quality monocrystals, but have not yet gotten it. However, we can propose the structure from many other clues.

The crystal structure of Schiff base analogues of HL^3_{ref} are 2-(2,5,8-triaza-l-octenyl)phenol (Hsaden) and *N*-(2-hydroxyphenylmethenylimino)-1,5-diamine-3-azapentane (HDA), and their corresponding Cu(II) complexes have already been reported.[215-217] Haber *et al*. have studied a copper (II) complex with Hsaden ligand using XPS spectroscopy. This ligand in the complex Cu(Hsaden)ClO_4 is coordinated to the metal ion in a tetradentate fashion, via a 3N1O donor set. Interestingly, the 1S peak in XPS was asymmetric and appeared to consist of

two components. The weaker component at a lower binding energy is attributed to the azomethine N atom, while the higher one was attributed to the two amino groups.[215] Zhu *et al*. have synthesized a copper(II) complex with HAD ligand. From the crystal structure determination, the Cu(II) ion is coordinated by three N and two O atoms form HAD and a water molecule in a distorted square-pyramidal geometry (**Figure 5.17**).[217]

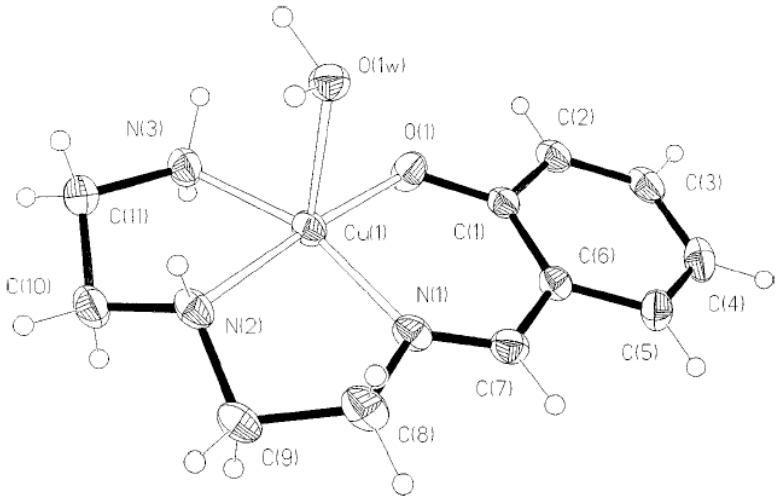

Figure 5.17 Ortep view (35 % probability displacement) of the [Cu(HDA)(H_2O)]Cl complex.[217]

Here, we proposed that the Cu(II) ion in 1-L^3_{ref} complex possesses a coordination sphere composed 3N1O from the tetradentate L^3_{ref} ligand and one acetate ion acting as ligand or counterion, *i.e.*, Cu(L^3_{ref})(OAc) (**Scheme 5.9**). This hypothesis will be supported by the combined results of UV-visible and EPR spectra of the molecular complex (1-L^3_{ref}) and the grafted complex [M2'-ES-Cu(L^3)].

5.3.2.2 Stability study of L^3_{ref} and Cu(II)-L^3_{ref} complex

UV-visible spectra. The stability of L^3_{ref} and 1-L^3_{ref} complex in aqueous solutions at various pH was studied by UV-visible spectroscopy (**Figure 5.18** and **Figure 5.19**, **Table 5.15**). For salicylaldimine (L^3_{ref}) ligand in absolute ethanol, the absorption bands below 279 nm can be attributed to π - π^* transitions in the benzene ring and π - π^* transitions in the azomethine (-C=N) groups of ligand.[112,196, 197] The absorption band observed at 308 nm can be interpreted as a charge-transfer transition.[198] The absorption band observed at 406 nm is most probably

due to the transition of n - π* of the azomethine group (-C=N**:**) of the ligand which give a yellow color.[199]

The L^3_{ref} ligand in basic aqueous solution displayed slightly different bands from that of L^3_{ref} ligand in EtOH. A band at 279 nm appears much stronger and the band at 308 disappeared. The absorption band attributed to n -π* transitions of -C=N**:** exhibited a blue shift to 390 nm, which is most probably due to the solvochromic effect. In our case, it is likely that the ground state can be stabilized in polar water than ethanol, thus leading to an increase of the energy gap between the ground and the excited states, observing a blue shift of n -π* transitions of -C=N**:**. With the decrease of pH from 7 to 6, the intensity of the absorption bands at 275 and 390 nm decrease, but new absorption bands at 255 and 330 nm appears and their intensity increases with the reduction of pH. Indeed, these two bands are a contribution of salicylaldehyde (**Table 5.15**): the absorption band at 255 nm corresponds to the π - π* transitions of aldehyde (-C=O**:**) function in the ligand, and the band at 330 nm can be attributed to the n -π* transitions of -C=O**:**. These results suggest that L^3_{ref} is hydrolyzed in aqueous solution below pH = 7.

For 1-L^3_{ref} complex in absolute EtOH, except the absorption bands from π - π* transitions in the benzene ring and of the azomethine (-C=N) group of the ligand, new absorption bands in the range of 320-390 nm may be attributed to the metal charge transition (MLCT) of Cu→O and Cu→N.[197, 198, 200, 201] The absorption band at 579 nm at lower energy and in lower intensity can be attributed to the d-d transition of Cu(II) ion (d_{xy}-$d_x{}^2$-$_y{}^2$ and $d_z{}^2$-$d_x{}^2$-$_y{}^2$). All these results suggest that the L^3_{ref} ligand coordinates to Cu(II) ion.

Parallel experiments of the pH effect were performed on the 1-L^3_{ref} complex in water [**Figure 5.19** (**A**), (**B**), **Table 5.15**]. Comparison of the UV-visible spectrum of the complex in aqueous solution at various pH with that of the complex in absolute EtOH shows that the similar UV-visible spectra are similar, indicating that the 1-L^3_{ref} complex is stable in aqueous solution from basic pH (pH = 11) to acidic (pH = 5). An additional experiment was carried out: the 1-L^3_{ref} complex was introduced in the solution at pH=6, and then the mixture was stirred at 80 °C for 2 h. The UV-visible spectra of this complex is similar to that of 1-L^3_{ref} in solution of pH = 6. These results suggest that after complexation with Cu(II) the imine bond (-C=N-) of L^3_{ref} ligand become much stable. The reason is likely that the free

electrons on the imine nitrogen (-C=N**:**) serve as electron donor to the Cu(II) ion, thus the extra proton can hardly attack the imine bond of the ligand. Furthermore, the tetradentate coordinated Cu(II) complex has a high stability constant.

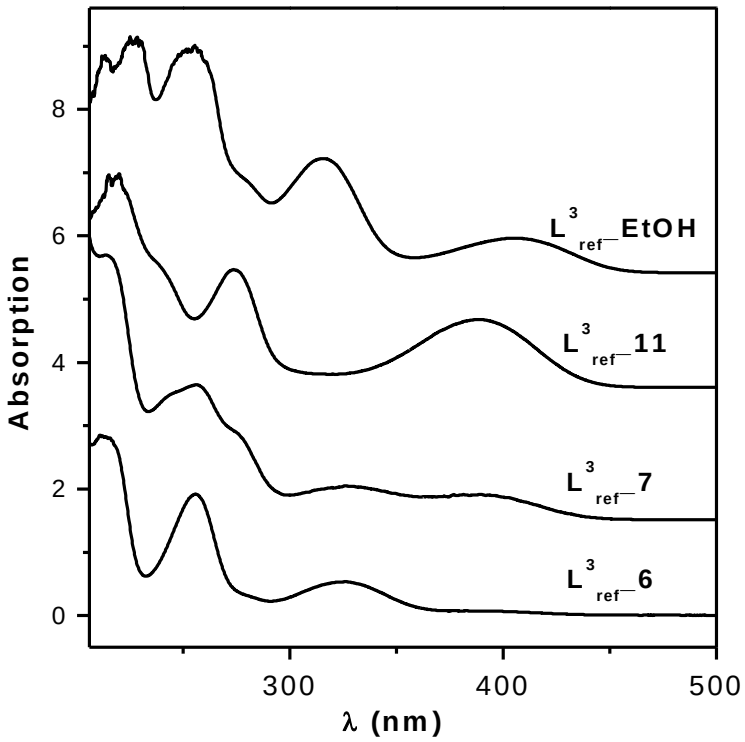

Figure 5.18 UV-visible spectra of ligand (L^3_{ref}) in absolute EtOH and aqueous solutions at various pH (pH = 11, 7, 6).

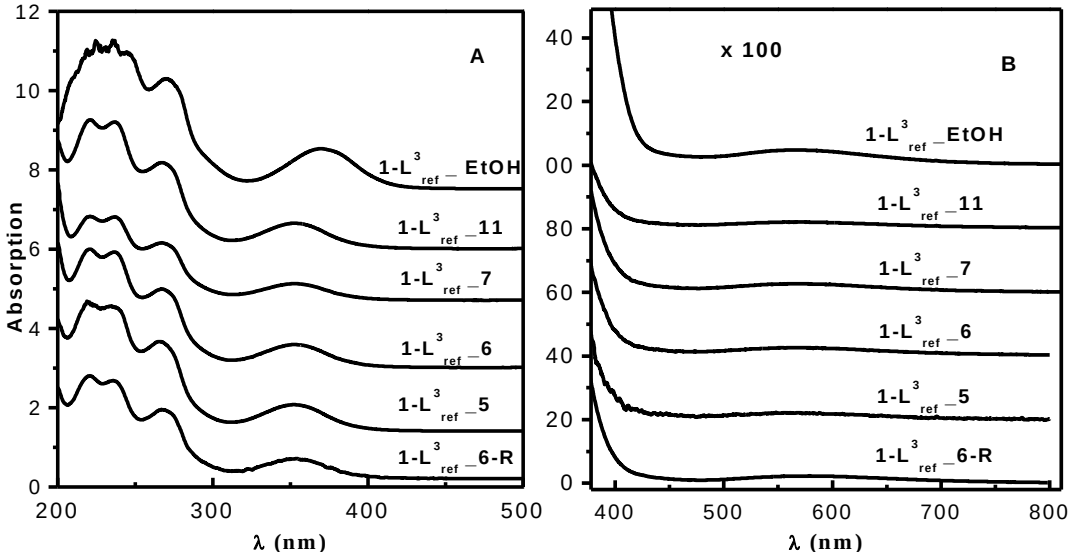

Figure 5.19 UV-visible spectra of complex (1-L^3_{ref}) in absolute EtOH and aqueous solutions at various pH (pH = 11, 7, 6 and 5). (A): 200-500 nm; (B): 380-810 nm, enlarged 100 times.

1_L^3_{ref}_6-R: 1_L^3_{ref} complex was added in aqueous solution at pH = 6 and stirred at 80 °C for 2 h.

Table 5.15 UV-visible data of ligand (L^3_{ref}) and their copper complex 1-L^3_{ref}.

Sample	solvent	pH	Wavelength (λ_{max} / (nm))
Salicylaldehyde	H_2O		255, 326
Salicylaldehyde	EtOH		255, 326
L^3_{ref}	EtOH		279, 308, 406
	H_2O	11[a]	274, 390
	H_2O	7 [b]	255, 274, 330, 390
	H_2O	6 [b]	256, 324, 390
	H_2O	0.3 [c]	256, 280, 338
1_L^3_{ref}	EtOH		266, 353, 579
	H_2O	11 [a]	267, 354, 570
	H_2O	7 [b]	266, 353, 571
	H_2O	6 [b]	268, 353, 570
	H_2O	5 [b]	267, 353, 573

a: NaOH solution; **b**: phosphate buffer solution, **c**: HCl solution.

EPR spectra

The EPR spectra of 1-L^3_{ref} complex in absolute ethanol or in deionized water were checked (**Figure 5.20**). In ethanol, there is only one species with g_1 of 2.19, A_{ll} of 19.6 mT, which is close to the reported bis(ethylenediamine) copper(II) with 4N coordination (*cf.* chapter 5.1). However, in the synthesis process, one molar equivalent of L^3_{ref} and copper(II) acetate were added. Consequently, if any bis(L^3_{ref}) copper(II) complex was formed, then this will result in the presence of $Cu(OAc)_2$ remaining in the solution. This is not the case according to EPR spectroscopy. In addition, UV-visible spectra of the solution exhibited the presence of the (Cu→O) metal to ligand electronic transition at 353 nm. This evidenced the full tetradentate action of L^3_{ref} via not only both amino groups but also via the imino and the phenolate moieties. Therefore, this species should be mono(salicylaldimine) copper(II) with 3N1O coordination and acetate acting as ligand or counterion (**Scheme 5.9**). By analogy with similar complexes (**Figure 5.17**),[215-217] the acetate ion could play the role of the 5th ligand since absolute ethanol is a poor ionizing solvent.

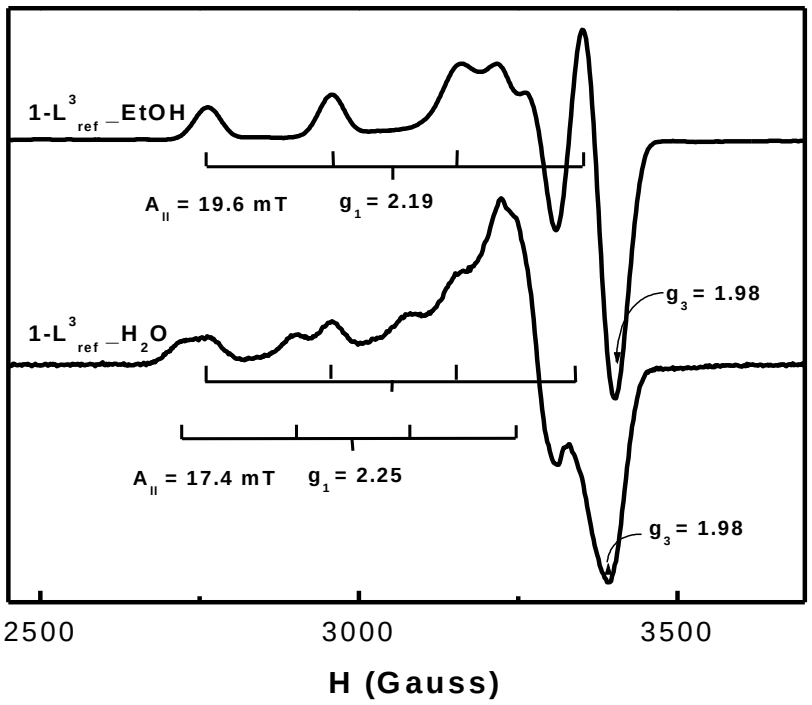

Figure 5.20 EPR spectra of 1-L^3 in absolute ethanol or deionized water (without buffer) at 130 K.

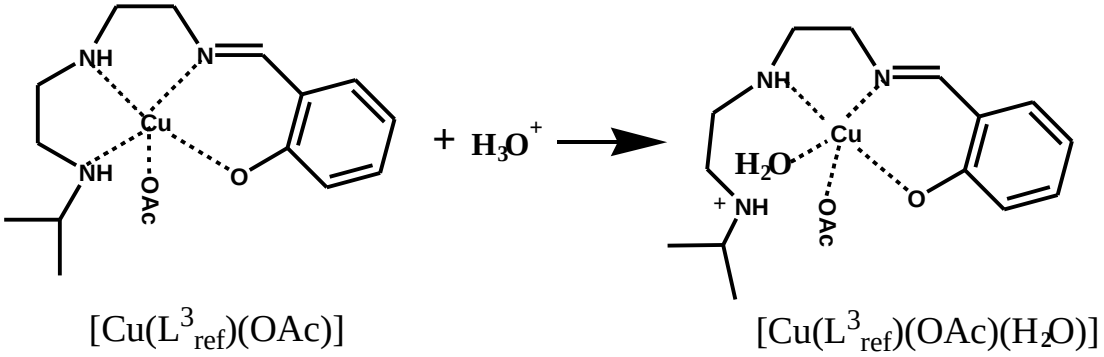

Scheme 5.10 Coordination evolution of Cu-L3ref complex in acidic water.

By contrast with the previous observation, in water there are two species formed for the same L^3_{ref}/Cu=1 molar ratio. One species is the same as the above-mentioned with the same EPR parameters. The second species possesses g_1 of 2.25 and $A_{\|}$ of 17.4 mT, which corresponds to 2N2O environment of Cu(II). This evolution of coordination state of copper in the presence of water clearly showed that this tetradentate L^3_{ref} complex undergone some kind of hydrolysis. However, the striking stability of the L^3_{ref} molecule in the presence of copper strongly suggested that the imino group stayed linked to copper(II). Furthermore,

the 2N2O environment indicated that one N chromophore was removed. The decomplexation of this amino group was replaced by a water molecule coordinated to copper as illustrated in (**Scheme 5.10**). The driving force for such a change is certainly the protonation of the ligand. Nonetheless, the absence of other species like tetra aquo or bis(acetate) copper(II) complexes illustrated the higher stability of $[Cu(L^3_{ref})]^+$ over $[Cu(L^2)_2]$ complex.

5.3.2.3 Conclusions

The complex with one N-(salicylaldimine)-(N'-isopropyl)-diethylenetriamine (L^3_{ref}) was obtained in absolute ethanol through the reaction of L^3_{ref} with bis(acetate) copper complex. The coordination of Cu(II) ion in the 1-L^3_{ref} complex in absolute ethanol is likely of the 3N1O type from the tetradentate L^3_{ref} ligand plus 1O coming from one acetate ion. When the pure ligand is solvated in water, it was found unstable below pH 7, since the imino group was hydrolyzed under acid catalysis. However, this molecule is stabilized down to pH 5 in the presence of copper(II) since this imino group engaged a direct bond with this metal ion. Nonetheless, EPR and UV-visible spectroscopies revealed that the tetradentate L^3_{ref} ligand may evolve toward a tridentate state under partial protonation.

5.3.3 Grafting complex $[Cu(L^3)]^+$ onto mesoporous material

5.3.3.1 Synthesis and characterization of hybrid materials

1-L^3 complex [L^3: N-(salicylaldimine)-(N'-propyltrimethoxylsilane)-diethylenetriamine] linked one side with an alkyltrialkoxysilane arm was synthesized through the condensation of equivalent $Cu(OAc)_2$ and HL^3 (similar as 1-L^3_{ref}). 1-L^3 complex was grafted on mesoporous material through a so-called molecular stencil pattering (MPS) approach developed in our group,[110] obtaining M2'-ES-Cu(L^3) material. The detailed synthesis step is provided in (**Scheme 5.11**). In the first step, the cationic template (CTA^+) as stencil covering the surface of M2' material was partially removed using a suitable amount of HCl (1 $mol \cdot L^{-1}$) extraction, obtaining M2'-E material. In the second step, trimethylsilyl groups (TMS), which act as hydrophobic isolating function, are introduced in the empty place without removal of

the remaining template molecules, leading to M2'-ESP. In the third step, the remaining template molecules are extracted by a suitable amount of HCl in gentle conditions, giving M2'-ES. Finally, the 1-L^3 complex is grafted. An appropriate ratio of TMS/1-L^3 is required to lead to isolated metal complexes totally surrounded by TMS functions, obtaining M2'-ES-Cu(L^3). This technique offers the advantage of affording a homogeneous dispersion of two functions at high loading. In addition, all synthesis steps were carried out under anhydrous conditions in order to avoid pre-hydrolysis of silane or the decomposition of the Cu-L^3 complex (*cf.* 5.3.2.2).

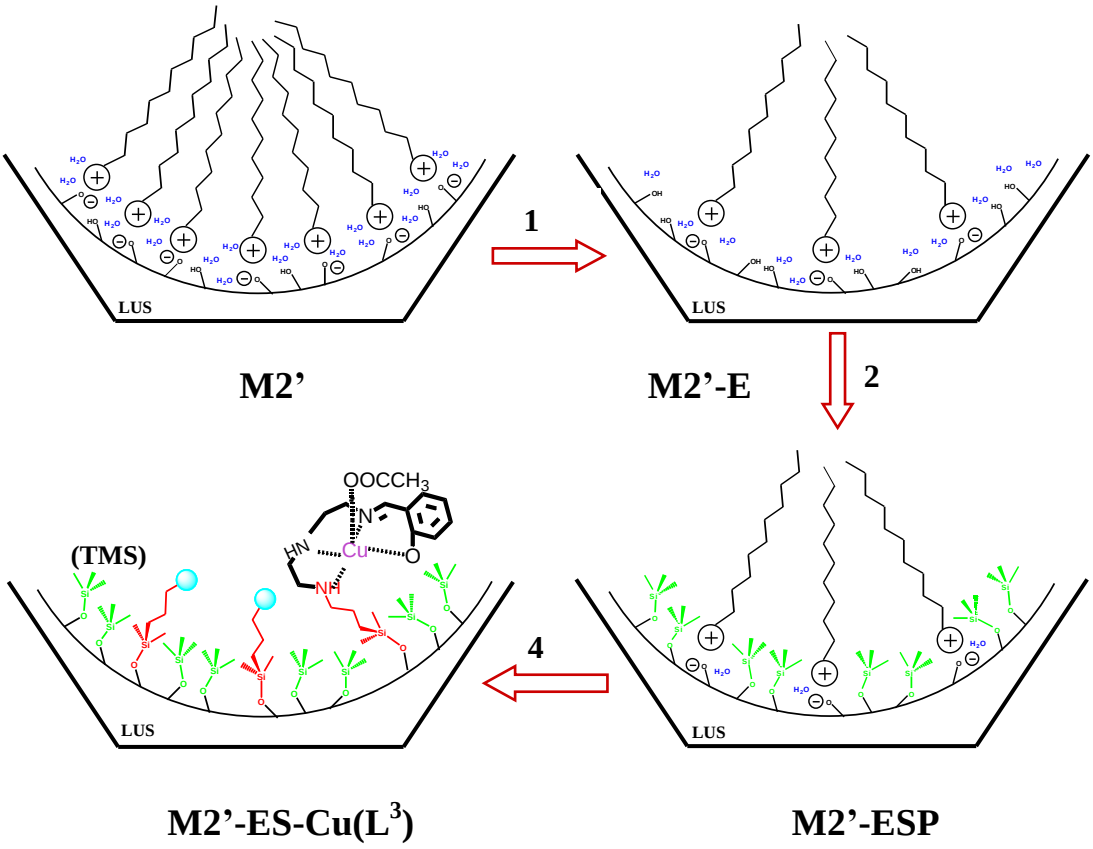

Scheme 5.11 Synthesis route of M2'-ES-Cu(L^3) through "MSP" method based on sequential grafting.

XRD. The XRD patterns of materials M2', M2'-ES and M2'-ES-Cu(L^3) are presented in **Figure 5.21**. All materials, M2', M2'-ES and M2'-ES-Cu(L^3), exhibit three peaks assigned to <100>, <200>, <210> reflections based on a well-ordered 2D hexagonal unit, indicating that acid extraction, silylation and grafting of 1-L^3 are safe for the mesoporous hexagonal structure. The d_{100} values for M2'-ES and M2'are about 4.0 nm, it decreases to 3.8 nm for

M2'-ES-Cu(L^3), suggesting the incorporation of copper complex on the mesoporous material. Furthermore, the intensity of d_{100} peak of M2'-ES-Cu(L^3) is much lower than that of M2'-ES, which is due to the larger change in electron densities between channel and framework, indicating the successfully grafting of the1-L^3 complex.

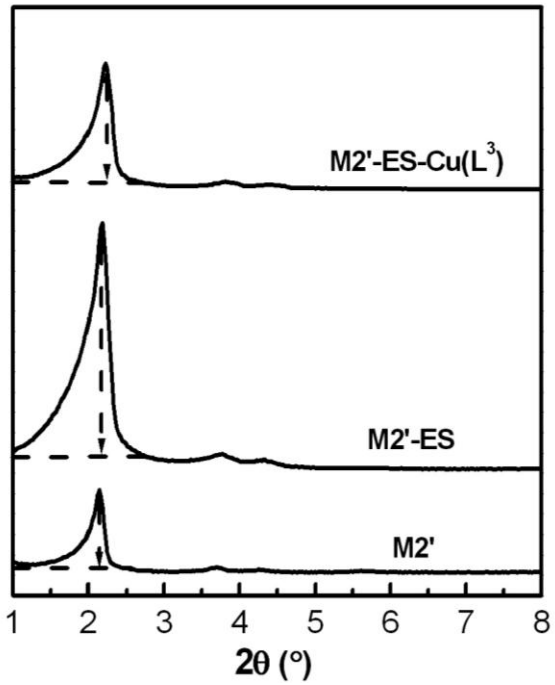

Figure 5.21 XRD patterns of M2', M2'-ES and M2'-ES-Cu(L^3).

IR spectra.

IR spectra of M2'-ES and M2'-ES-Cu(L^3) were baseline corrected and normalized using the band at 450 cm^{-1} assigned to the δ(O-Si-O) of valence angle of tetrahedral SiO_4 (*cf.* Appendix A) (**Figure 5.22**). The band at 850 cm^{-1} attributed to the ν(Si-C) of trimethylsilyl [-Si(CH_3)$_3$] is used to quantify the surface coverage with the trimethylsilyl (TMS) functions. The TMS coverage to toal surface is 52 % for M2'-ES, decreases to 46 % after grafting of the [Cu(L^3)]$^+$ complex for M2'-ES-Cu(L^3), losing *ca*. 12 % of TMS groups. In the IR spectra of M2'-ES-Cu(L^3) the band observed at 1542 cm^{-1} may be assigned to N-H bending vibration. The band at 1450 and 1605 cm^{-1} can be attributed to the ν(C=O) of unidentate acetate since the ν(C=O) of ionic acetate are at 1414 and 1578 cm^{-1}.[218] These results suggest that the 1-L^3 complex was successfully grafted and acetate ion is most probably coordi-

nated to the metal central to neutralize the charge of Cu(II).

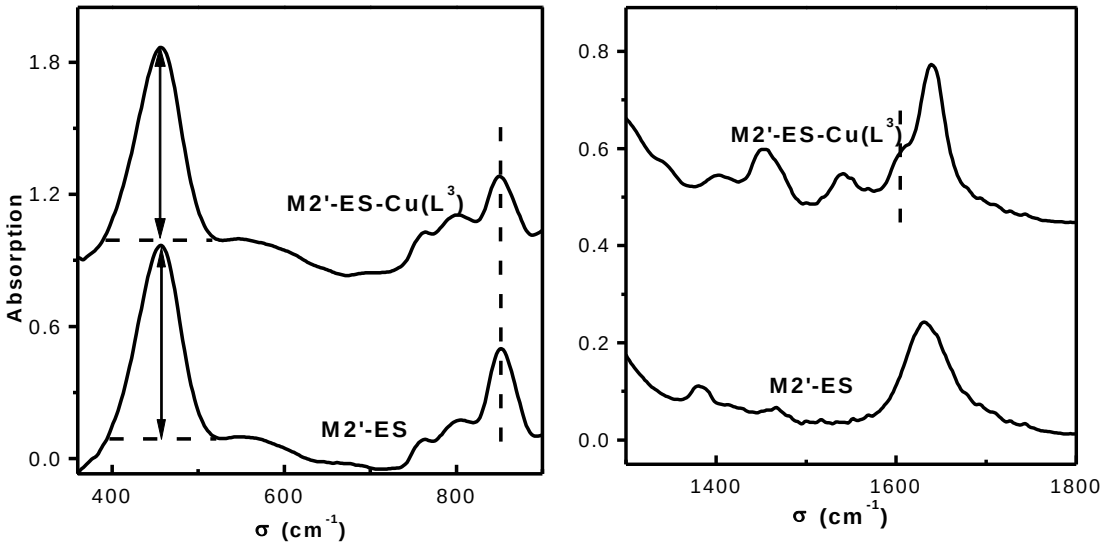

Figure 5.22 FT-IR spectra of M2'-ES and M2'-ES-Cu(L^3).

EA. The elemental analysis of M2'-ES and M2'-ES-Cu(L^3) are listed in **Table 5.16**. For M2'-ES-Cu(L^3), the TMS functions to inorganic SiO_2 molar ratio is equal to 0.16, corresponding to about 70% of surface coverage, considering that a totally trimethylsilylated surface gives a TMS/SiO_2 of 0.23. The treatment of this material with the copper complex to obtain the M2'-ES-Cu(L^3) material slightly displaced some of the TMS groups, leading to 0.14 of TMS/SiO_2 molar ratio, indicating *ca*. 12 % of lost of TMS, which is in agreement with the result of the quantitative IR. The L/SiO_2 molar ratio was 0.043. In addition, the copper content determined by ICP-MS was 2.79 wt%, which corresponds to 0.042 Cu/SiO_2, indicating that all the ligand was complexed to the metal ion. Finally, a N/Cu ratio of L^3 was observed for M2'-ES-Cu(L^3), which discard a possible hydrolysis of the imine function of the L ligand during the synthesis of the hybrid material and the formation of the bis(salicylaldimine) copper(II) complex.

Table 5.16 Elemental analysis for M2'-ES and M2'-ES-Cu(L^3).

Sample	Cu wt % (ICP-MS)	Cu wt % (EPR)	SiO_2 [b]	L^3/ SiO_2 [b]	TMS/ SiO_2 [b]	N/ Cu
M2'-ES	--	--	77.89	--	0.16	
M2'-ES-Cu(L^3)	2.8	2.6 [a]	64.52	0.043	0.14	3.1

a: quantification of the EPR signal was performed by double integration after baseline correction and the crystals of $CuSO_4.5H_2O$ were used as calibration reference (*cf.* Appendix B). b: molar ratio per inorganic silica; the inorganic SiO_2 content is obtained from the residual weight in TGA at 1000 °C upon subtraction of both CuO and the SiO_2 formed from the grafted organosilanes.

BET For M2'-ES and M2'-ES-Cu(L^3) materials, all the nitrogen sorption isotherms (**Figure 5.23**) are of type IV according to the IUPAC classification.[38] The steep step of the capillary condensation at about 0.38 P/P_0 evidenced a narrow pore size distribution.[6, 169] A pronounced decrease of both specific surface and total pore volume from 820 m^2g^{-1}, 0.66 cm^3g^{-1} in M2'-ES down to 661 m^2g^{-1}, 0.45 cm^3g^{-1} in M2'-ES-Cu(L^3) was observed (**Table 5.17**). In addition, the pore size, calculated from the BdB model was significantly reduced from 3.2 nm in M2'-ES to 2.8 nm in M2'-ES-Cu(L^3), respectively. These results strongly indicate that the location of the metal complex is in the pore channel for M2'-ES-Cu(L^3).

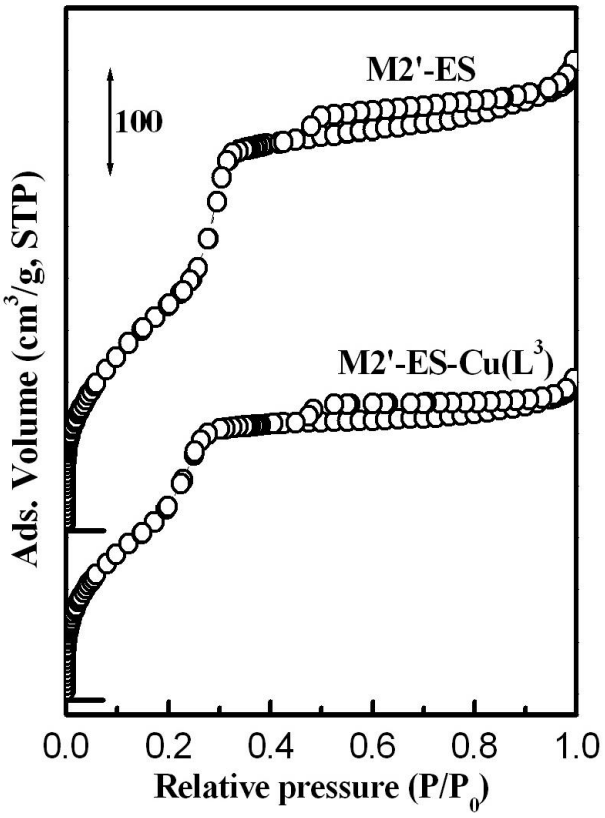

Figure 5.23 N_2 sorption isotherms at 77 K of M2'-ES and M2'-ES-Cu(L^3).

Table 5.17 Textural properties of M2'-ES and M2'-ES-Cu(L^3) deduced from N_2 sorption isotherms at 77 K.

Sample	S_{BET} (m^2g^{-1})	V_p [a] (cm^3g^{-1})	ϕ_{BdB} [b] (nm)	a_0 [c] (nm)	W_t [d] (nm)	C [e]
M2'-ES	820	0.66	3.2	4.8	1.4	35.2
M2'-ES-Cu(L^3)	661	0.45	2.8	4.7	1.9	37.7

a: measured at $P/P_0 = 0.98$; **b**: using BJH model instead of the BDB one, the diameter would be 0.8 nm lower in each case; **c**: $a_0 = 2*d_{100}/(3)^{1/2}$; **d**: apparent wall thickness is determined using $W_t = 2*d_{100}/3^{1/2} - \phi_{BdB}$; **e**: C parameters from BET equation.

5.3.3.2 Cu(II) coordination state

As it was introduced in the chapter 2, direct grafting approach used here to synthesize M2'-ES possesses an advantage of avoidance of modification of metal complex during the grafting process compared to indirect grafting (*cf.* chapter 2.3.2.1). Therefore, 1-L^3 complex was functionalized M2'-ES material through direct grafting approach. The Cu(II) coordination state of the grafted complex on mesoporous material was checked by UV-visible and EPR spectroscopy. For a better comprehensive M2'-ES-Cu(L^3), HL^3 ligand and 1-L^3 molecular complex were also studied as references using the above spectroscopies.

UV-visible spectra of HL^3, 1-L^3 and M2'-ES-Cu(L^3) were recorded in the range of 200-900 nm and presented in **Figure 5.24**. The corresponding data are gathered in **Table 5.18**. In the UV-visible spectra of HL^3 and 1-L^3 complex, the observed absorption bands below 277 nm are attributed to the π - π^* transition in the benzene ring and the absorption band *ca*. 277 nm corresponds to the π - π^* transitions in the azomethine (-C=N) group of ligand. For HL^3 ligand, the strong absorption band at 311 nm can be attributed to the charge-transfer transition in which the azomethine group acts as an electron acceptor and phenyl ring ($Ph\text{-}O^-$) as an electron donor.[198] The observed absorption band at 395 nm is assigned to the transition of n - π^* of the azomethine in the ligand. For the 1-L^3 complex and M2'-ES-Cu(L^3), a broad absorption band observed in the range of 320-390 nm may be attributed to the metal to ligand charge-transfer transitions (MLCT) of Cu→N and Cu→O. And an absorption band at 588 nm at low lower energy and in lower intensity were all observed, which can be assigned to the d-d transitions (d_{xy}-$d_{x^2-y^2}$; d_{z^2}-$d_{x^2-y^2}$).

Table 5.18 UV-visible characteristic of the samples.

Samples	UV-visible spectra, λ_{max} (nm)						
$HL^{3\,a}$	213	248	273	311	395		
$1\text{-}L^{3\,a}$	221	247	277	305		369	590
M2'-ES-Cu(L^3)						368	586

a: HL^3 and $1\text{-}L^3$ complex were recorded in absolute EtOH.

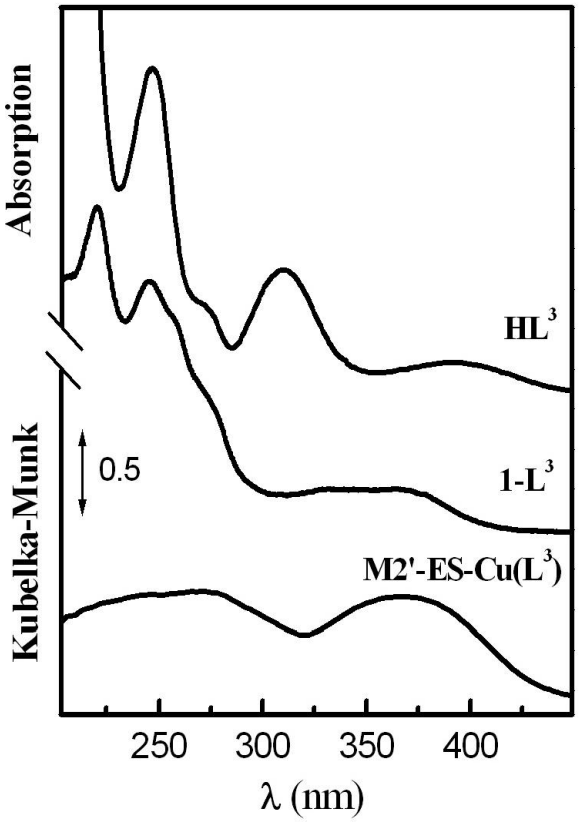

Figure 5.24 Liquid UV-visible spectra of HL^3 and $1\text{-}L^3$ in absolute ethanol. Solid diffuse reflectance UV-visible spectra of M2'-ES-Cu(L^3).

The EPR spectrum for $1\text{-}L^3$ complex was recorded as ethanol glass at 130 K, and the spectrum of the M2'-ES-Cu(L^3) was recorded both at 130 K and at room temperature. The corresponding spectral parameters are summarized in **Table 5.19**. Often g_2 and g_3 are close one to another, so we may assume that they represent the perpendicular ($g_2 \approx g_3 = g_\perp$) plan while g_1 can be assimilated to $g_\parallel$. In both samples, $g_\parallel$ value is bigger than $g_\perp$ value, which is typical of d^9 complexes with d_{x2-y2} ground state and elongated square pyramidal or elongated octahedral environment for Cu(II). The values of $g_\parallel$, $g_\perp$ and $A_\parallel$ of M2'-ES-Cu(L^3) are

equal to 2.18, 1.99 and 19.4 mT at room temperature, and slightly changed to 2.20, 1.98 and 19.5 mT at 130 K, which are similar to that of 1-L^3_{ref} and 1-L^3 complexes at 130 K. In addition, EPR spectra become broaden at low temperature (130 K) (**Figure 5.25**). The reason is most probably that at low temperature the grafted complex has low mobility and is blocked in various conformations due to the heterogeneity of the silanol and TMS position in its vicinity.

The different parameters of $g_{\|}$ and $A_{\|}$ of Cu(II) complexes in EPR spectra can be attributed to a varying number of nitrogen and oxygen coordinating sites and to a change in the symmetry around the metal center. Moreno-Carretero *et al*. have reported that 6-amino-l,3-dimethyl-5-nitrosouracilato (N^5, N^6)-aqua-2,2'-bipyridine *(N, N')* - copper(II) perchlorate hydrate and 2, 2'-bipyridine (*N, N'*)-chloro-l,3-dimethylviolurato (N^5, O^6)-copper(II) hemihydrate complexes display axial EPR powder spectra with $g_{\perp}$= 2.03 and $g_{\|}$ = 2.25 and $g_{\perp}$= 2.03 and $g_{\|}$ = 2.20, respectively, proposing a $(4N)_{xy}+O_z$ and $(3N1O)_{xy}+O_z$ environment around the Cu(II).[219] Abry *et al*. have observed that N, N'-bis(2-pyridinylmethyl)-ethane-1,2-diamine copper(II) trifluoromethanesulfonate complex with tetradentate ligand grafted in mesoporous silica exhibits low g values with $g_{\|}$ = 2.219 and g_3 = 1.994. Combining EPR spectra with EXAFS analysis, they proposed the Cu complexes with a 2N2O environment. For M2'-ES-Cu(L^3), it seems that a $(3N1O)_{xy}+O_z$ environment around copper is more reasonable than $(2N2O)_{xy}$ and the coordination geometry is rather pentacoordinated.

Table 5.19 g and A parameters for complexes and solid.

Sample	$g_{\|}$	$g_{\perp}$	A_{ll} (mT)	T (K)
1-$L^{3\,a}$	2.20	1.98	19.5	130
M2'-ES-Cu(L^3)	2.20	1.98	19.5	130
M2'-ES-Cu(L^3)	2.18	1.99	19.4	298

a : recorded at 130 K in 80 % absolute ethanol/ 20 % glycerol.

Furthermore, the $g_{\|}$ of 2.19 and A_{ll} of 19.6 mT is close to the reported bis(ethylenediamine) copper(II) with 4N coordination (*cf*. chapter 5.1). In the synthesis process, equivalent molar amounts of L^3 and copper(II) acetate were added. Moreover,

there is no species attributed to $Cu(OAc)_2$ in EPR spectrum. These results are in agreement with molecular complex that of 1-L^3_{ref} (*cf.* 5.3.2.2). Therefore, for M2'-ES-Cu(L^3), it is probably that the Cu center is in a $(3N1O)_{xy}+O_z$ environment.

Quantitative EPR was performed on M2'-ES-Cu(L^3) solid. The EPR active copper (II) species was determined to be 2.6 % which is close to 2.8 % of the total Cu content determined by ICP-MS (**Table 5.16**), confirming that the copper complexes are isolated on the surface of mesoporous material.

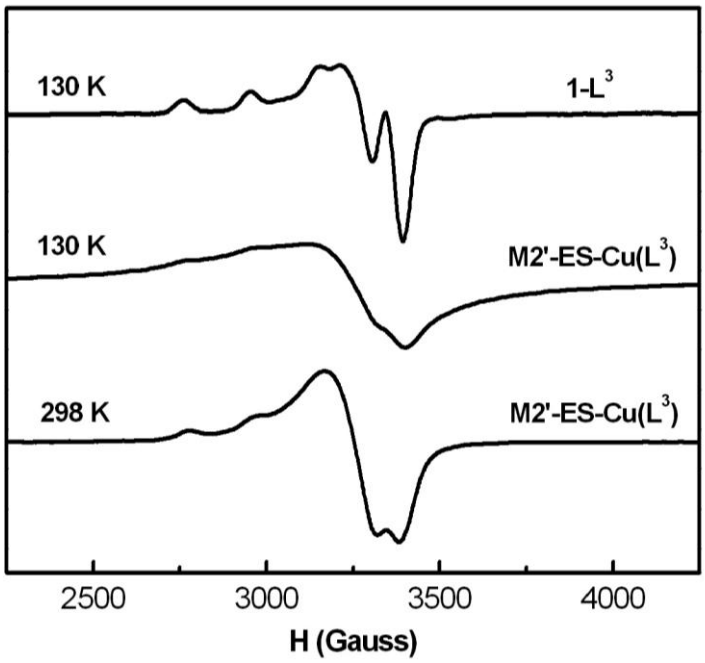

Figure 5.25 EPR spectra of 1-L^3 and M2'-ES-Cu(L^3). EPR spectra of 1-L^3 and M2'-ES-Cu(L^3) were recorded at 130 K for the former, and 130 K and room temperature for the latter, with the following parameters: frequency: 9.35 GHz; power: 10.1 mW, 32 mW and 10 mW, respectively; modulation amplitude: 6G, 15G and 1G respectively; modulation frequency: 100 kHz.

5.3.4 Catalytic hydroxylation of phenol

M2'-ES-Cu(L^3) catalyst was evaluated in the phenol hydroxylation with H_2O_2. The formed products were determined using HPCL. The detail treatment of data from HPLC is provided in Appendix C. In addition to the catechol (CAT), hydroquinone (HQ) and 1,4-benzoquinone (BQ), tar was also observed,[135, 220] which exhibit much higher polarity and are brown color. These products could be possibly the deep oxidation products such as

maleic acid, acrylic acid, acetic acid, oxalic acid and oligomerization products.[221] Various reaction factors such as reaction time, H_2O_2/substrate ratio, pH and solvent, have been investigated on the effect of phenol conversion and products selectivity.

5.3.4.1 Comparison of the heterogeneous catalyst and its homogeneous analogue

Catalytic activities and selectivities in phenol hydroxylation with H_2O_2 over blank experiments, heterogeneous catalyst [M2'-ES-Cu(L^3)] and homogeneous analogue (1-L^3) as well as two blank experiments are listed in **Table 5.20**. There are no activity on phenol hydroxylation in the blank experiments with metal-free solid (M2'-ES) and without the solid. Under the same conditions, the heterogeneous catalyst M2'-ES-Cu(L^3) showed lower phenol conversion (48.1 %) than the homogenous 1-L^3_{ref} (52.0 %), but with higher selectivity to diphenols (76.1 % compared to 69.5 %). CAT/HQ molar ratio over M2'-ES-Cu(L^3) was 1.73, which is higher than that of the homogenous 1-L^3_{ref} (1.55). However, no 1, 4-benzoquinone (BQ) was observed over the M2'-ES-Cu(L^3) catalyst. This result could be caused by the different mobility of the active species on homogenous and heterogeneous.

We also tested the influence of the copper content on phenol hydroxylation. As shown in **Table 5.20**, the phenol conversion decreases with the diminution of copper content added, and the selectivity of diphenols also diminishes. This result suggests that the solid catalyzes this reaction.

Table 5.20 Catalytic activity and selectivity in phenol hydroxylation by H_2O_2 over **M2'-ES-Cu(L^3)** and others.

Sample	Phenol conv. (%)	Diphenols slectivity [a] (%)	Product selectivity (%)			CAT/HQ
			CAT	HQ	BQ	
No catalyst	10.7	0	0	0	0	0
M2'-ES	11.9	0	0	0	0	0
1-L^3_{ref}	52.0	69.5	60.7	39.1	0.2	1.55
M2'-ES-Cu(L^3)	48.1	76.1	63.4	36.6	0	1.73

M2'-ES-Cu(L^3)[b]	44.4	52.9	62.1	37.9	0	1.90

a: Diphenols selectivity = yield of CAT and HQ and BQ (mol) % / total phenol coversion (mol) %. Yield of CAT and HQ and BQ (mol) % are dertermined from HPLC.
Reaction condition: pH = 6, phosphate buffer solution as solvent, temperature 80°C, phenol: Cu = 100:1 (molar ratio), phenol: H_2O_2 = 1: 1.2, reaction time 2h. **b**: phenol: Cu = 200:1
CAT: Catechol; HQ: Hydroquinone; BQ: 1, 4-benzoquinone.

5.3.4.2 Reaction time

The activity and selectivity in phenol hydroxylation by H_2O_2 for various reaction times over M2'-ES-Cu(L^3) were investigated and the results presented in the **Table 5.21**. The phenol conversion was 38.4 % at 1 h, increased to 48.1 % at 2 h, and continued to increase to 51.2 % at 4 h. However, the diphenols selectivity decreased with the increase of reaction time: 82.2 % for 1 h, 76.1 % for 2 h, and 70.5 % for 4 h. In fact, the yield of diphenols was 31.6 % at 1 h, and enhanced to 36.6 % at 2 h, and then this value was maintained at 4 h. These results indicate that the increase in phenol conversion is due to the formation of tar. The CAT/HQ molar ratio slightly decreased from 1.77 at 1 h to 1.73 at 2 h. This value was maintained to 1.73 until 4 h. By the titration of H_2O_2 concentration, it was found that at 2 h the H_2O_2 conversion already reached to 97 %. Thus, the reaction time during 2 h is the key step for taking place the phenol hydroxylation.

Table 5.21 Catalytic activity and selectivity in phenol hydroxylation by H_2O_2 over M2'-ES-Cu(L^3) with reaction time.

Time (h)	Phenol conv. %	Diphenols selectivity [a] %	CAT/ HQ
1	38.4	82.2	1.77
2	48.1	76.1	1.73
4	51.2	70.5	1.73

Other reaction conditions are the same as those indicated in Table 5.15.

5.3.4.3 Effect of the H_2O_2 addition mode

It was reported that H_2O_2 addition mode has influence on both activity and selectivity for the oxidation reaction.[135, 222] Here, H_2O_2 addition modes were investigated on the phenol

hydroxylation over M2'-ES-Cu(L^3). Two modes of addition were studied: 1) H_2O_2 was added at once at the reaction temperature; 2) H_2O_2 was sequentially added in a period of 1 h at the reaction temperature (**Table 5.22**). It was found that phenol conversions were 43.0 % for the one-pot addition mode and 40.7 % for the sequential addition mode. The main difference appears on the selectivity on diphenols, which was much higher in the first mode (73.0 %) than in the second mode (55.0 %). Furthermore, for the second mode, CAT/HQ molar ratio was 1.69 which is higher than that observed in first mode (1.60). These results suggest that in the sequential addition mode catechol and hydroquinone are most probably are further oxidized and therefore more tar is produced.

Table 5.22 Effect of the H_2O_2 addition mode on the catalytic activity and selectivity in phenol hydroxylation over M2'-ES-Cu(L^3).

Mode of addition	Phenol conv. %	Diphenols selectivity [a] %	CAT/HQ
1) one-pot addition	43.0	73.0	1.60
2) sequential addition	40.7	55.0	1.69

Reaction conditions: pH = 6, phosphate buffer solution as solvent, temperature 80 °C, phenol: Cu = 100:1 (molar ratio), phenol: H_2O_2 = 1: 1, reaction time 2h.

5.3.4.4 pH effect

Various buffer solutions with different pH were tested on the phenol hydroxylation with H_2O_2 over M2'-ES-Cu(L^3) (**Table 5.23**). Here, the pH of the buffer solutions was chosen in the range from 7 to 5, where the1-L^3 complex is stable in these solutions (*cf*. chapter 5.3.2). Anyway, the basic solution is out of our investigation. The reasons are the following: 1) hydrogen peroxide decomposes faster in basic conditions than acid conditions; 2) the generation of OH^- species in basic condition probably approach the active center and thereby inhibiting the absorption of hydrogen peroxides to the active site. In fact, Wu *et al.*[223] and Kannan *et al.*[132, 133] have respectively reported that no activity on phenol hydroxylation was observed in the basic conditions (pH = 9 or pH = 11) over hydrotalcite-like compounds (CuAlCO3-HTLc) and ternary hydrotalcites (CuNiAl or CuCoAl).

Here, buffer solutions with different pH can not only effect the phenol conversion but

also the product selectivity. The phenol conversion increased with the decrease of pH: 21.1 % for pH 7, 43.0 % for pH 6, and 50.7 % for pH 5. However, the diphenols selectivities were low at pH 7 (40.3 %) and pH 5 (48.6 %). The highest diphenols selectivity was 73.0 % at pH 6. Therefore, we considered that pH 6 is the best condition for phenol hydroxylation considering both the high conversion of phenol and high selectivity to diphenols. Wang *et al*. and Liu *et al*. have observed an increased activity of phenol conversion in acid aqueous solution.[131, 224] They consider the reason that hydroxyl radical is more easily formed in a weak acidic medium. Indeed, the suitable pH for this reaction varies with the catalysts used. For example, Zhu *et al*.[223] have claimed a maximum phenol conversion (53.5 %) at 7.0 over $CuAlCO_3$-HTLc catalyst; Kannan *et al*.[133] have reported no significant difference in phenol conversion between pH 7 (20.8 %) and pH 5 (22.1 %) over CuCoAl ternary hydrotalcites. However, in both cases only phenol conversion is considered while the distribution of diphenols and tar is out of consideration (detail results were presented in Table 2.4).

For elucidation of the effect of phosphate used as better solution, we also studied the activity of phenol hydroxylation over M2'-ES-Cu(L^3) in deionized water. The phenol conversion was 38.1 % and diphenols selectivity is 67.8 %, which is higher than in buffer solution at pH 7 (21.1 % and 40.3 %, respectively). This result appears to indicate the negative effect of phosphate on phenol conversion and diphenols selectivity at pH 7. A further study needs to be carried out. Nonetheless, here, a slight acidification in the presence of buffer remains favorable for both phenol conversion and diphenols selectivity as in absence of buffer.[131, 224]

Table 5.23 Catalytic activity and selectivity in phenol hydroxylation by H_2O_2 over M2'-ES-Cu(L^3) with different pH buffer solutions

pH	Phenol conv. %	Dipehnols selectivity %	CAT/ HQ
7 [a]	21.1	40.3	2.62
6 [a]	43.0	73.0	1.60
5 [a]	50.7	48.6	1.51

7 [b]	38.1	67.8	1.64

Other reaction conditions are the same as those in **Table 5.22**, H_2O_2 one-pot addition.
a: phosphate buffer solution ; **b**: deionized water without phosphate.

5.3.4.5 Substrate / oxidant effect

Various molar ratios of phenol/H_2O_2 were studied on phenol hydroxylation with H_2O_2 over M2'-ES-Cu(L^3). The obtained phenol conversion and product selectivity were presented in **Table 5.24**. With the increase of phenol: H_2O_2 molar ratio, phenol conversion enhanced while the efficiency of H_2O_2 decreased, and a reduction of diphenols selectivity was observed. These results are in good agreement with the previous works reported by Lee *et al.*,[131] and Xiao *et al.*[135, 225] and Ratnasamy *et al.*[209] However, the diphenols selectivity was maintained (*ca.* 73 %) below phenol/H_2O_2 molar ratio of 1.2. The molar ratio of CAT to HQ was not very sensitive to the change of phenol to H_2O_2 molar ratio. This result is opposite to those reported on TS-1, where the molar ratio of CAT to HA decreased sharply with the increase of the molar ratio of phenol to H_2O_2 from 1 to 3.[209]

Table 5.24 Catalytic activity and selectivity in phenol hydroxylation with H_2O_2 over M2'-ES-Cu(L^3) with different phenol/H_2O_2 molar ratio.

Phenol: H_2O_2	Phenol conv. %	H_2O_2 eff. conv.[a] %	Diphenols selectivity %	CAT/HQ
3: 1	15.2	34	73.0	2.00
1: 1	43.0	31	73.0	1.60
1: 1.2	48.1	31	76.1	1.77
1: 2.2	72.9	25	52.0	1.63

[a] The efficiency conversion of H_2O_2 was calculated as follows: H_2O_2 eff. conv. = H_2O_2 (mol) consumed in formation of diphenols and benzoquinone / H_2O_2 (mol) converted. H_2O_2 conversion was determined by the iodometry titration.

5.3.4.6 Solvent effect

It has been reported that solvent significantly affects the phenol conversion and product selectivity in the presence catalysts such as CuSBA-15 and copper hydroxyl phosphate.[128, 135] Herein, organic solvent acetonitrile was chosen to be compared with water on the phenol hydroxylation with H_2O_2 over M2'-ES-Cu(L^3) (**Table 5.25**). When CH_3CN was used as

solvent, phenol conversion is very low (1.6 %), the only formed product is 1, 4-benzoquinone (BQ). However, when water was employed as solvent, phenol conversion significantly increass (43 %), and the main formed products are diphenols (CAT and HQ). This result is consistent with the previous reports.[128, 131, 135] However, acetone is the best solvent for TS-1 instead of water.[209, 220] The key point here is that water is a cheap, clean, safe and environmental kindly solvent.

Table 5.25 Catalytic activity and selectivity in phenol hydroxylation with H_2O_2 over M2'-ES-Cu(L^3) with different solvent.

Solvent	Phenol conv. %	Product selectivity %			CAT/ HQ
		CAT	HQ	BQ	
CH_3CN	3.7	0	0	100	0
H_2O [a]	43.0	61.5	38.5	0	1.60

Reaction condition: pH = 6, phosphate buffer solution as solvent, temperature 80°C, phenol: Cu = 100:1 (molar ratio), phenol: H_2O_2 = 1: 1, reaction time: 2h.

5.3.4.7 Recycle tests

The catalytic activity of M2'-ES-Cu(L^3) was monitored for three runs of the reaction, and the obtained data are shown in **Table 5.26**. The activity of M2'-ES-Cu(L^3) was maintained between the first run (43%) and the second run (42.5 %). The catalyst was only generated after the first run by washing using ethanol and acetone, and then drying at 60 °C overnight. Indeed, in the second run, the Cu wt. % determined by ICP-MS was 2.2 %, which is close to that of initial catalyst M2'-ES-Cu(L^3) (2.3 %, with subtraction of weight of trimethyl). In third run, the activity diminished from 20.3 %, which is probably due to the partial Cu leaching.

Table 5.26 Catalytic activity and selectivity in phenol hydroxylation by H_2O_2 over M2'-ES-Cu(L^3) with catalyst recycle.

Run	Cu wt. %	Phenol conv. %	H_2O_2 eff. conv. %	Diphenols selectivity %	CAT: HQ
First run	2.3 [a]	43.0	32	73.0	1.60
Second run	2.2 [b]	42.5	30	70.6	1.67

Third run	--	33.0	20	62	1.90

Reaction condition: pH = 6, phosphate buffer solution as solvent, temperature 80°C, phenol: Cu = 100:1 (molar ratio), phenol: H_2O_2 = 1: 1, reaction time 2h.

[a] Cu wt. % is corrected by taking out of the weight from trimethylsilyl (TMS) groups; [b] determined by ICP-MS, TMS was totally removed during the reaction process as checked by infrared spectroscopy.

5.3.4.8 Characterization of the recovered catalyst

The catalysts M2'-ES-Cu(L^3)_7 and M2'-ES-Cu(L^3)_6, which were respectively after the first run in reactions at pH = 6 and pH = 7, were checked by UV-visible spectroscopy. A broad absorption band from 200 nm to 800 nm was observed. This is probably due to the adsorption of tar on the solid, which is in agreement color change of the catalyst from indigo to dark brown after the reaction. The IR spectra revealed that the isolating function trimethyl were *ca*. 99 % lost. The recovered catalysts were also characterized using EPR spectroscopy to monitor the Cu(II) coordination state. M2'-ES-Cu(L^3)_7 and M2'-ES-Cu(L^3)_6 samples displayed $g_{\|}$ of 2.20 and $A_{\|}$ of 19.4 mT (**Figure 5.26**), which are the same g and A values as for the grafted 1-L^3 complex on M2'-ES-Cu(L^3), indicating that the Cu(L^3)(OAc) complex is stable in the neutral and slight acid conditions during the oxidation reaction.

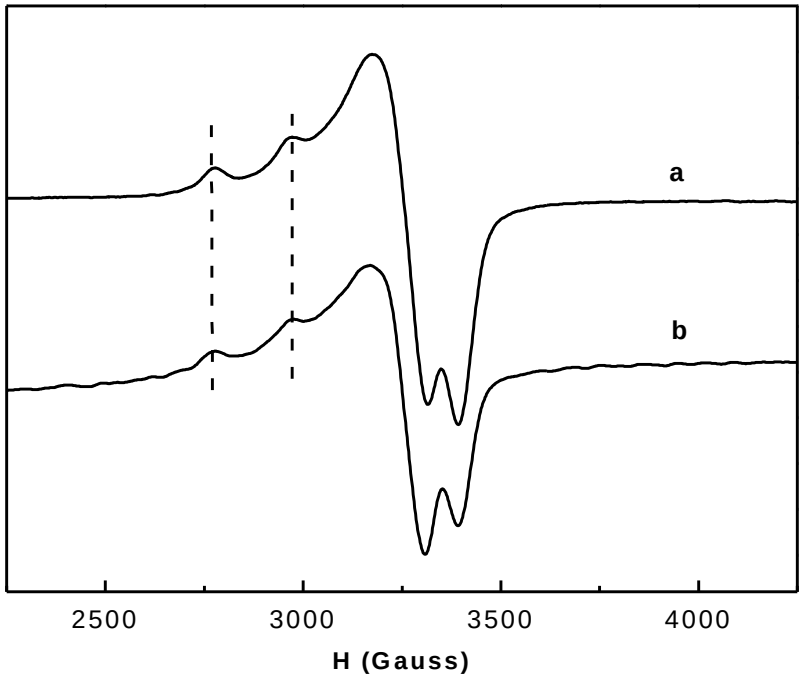

Figure 5.26 EPR spectra of catalyst M2'-ES-Cu(L^3) after the reaction. **a**: catalyst recovered in pH=7 condition [M2'-ES-Cu(L^3)_7]; **b**: catalyst recovered in pH=6 condition [M2'-ES-Cu(L^3)_6].

5.3.4.9 Mechanism proposed

For Cu(II) functionalized materials used as heterogeneous catalysts in the hydroxylation of phenol with H_2O_2 as oxidant, until now, there is no mechanism proposed about mono copper complex as catalyst on this reaction. However, there are mainly two types of proposed mechanisms for copper oxide based catalysts (**Scheme 5.12**, **Scheme 5.13**) in the literatures. The two mechanisms both consider that the production of hydroxyl radical (·OH) corresponds to the formation of catechol and hydroquinone. However, they are different in the way to form the hydroxyl radical (·OH) by the redox reaction of Cu(II) and H_2O_2.

The mechanism (**1**) (**Scheme 5.12**) is supported by Wang *et al.*,[128] Wu *et al.*,[226] Zhang *et al.*,[127] He *et al.*[130] and Robbins *et al.*.[227] In this proposed mechanism, the active center Cu(II) and H_2O_2 yield ·OH and HO_2· radical species, via redox cycling of Cu(II) and Cu(I) (process A). Then ·OH species attacks phenol to in form the products catechol and hydroquinone (process B). Benzoquinone is the further oxidized products by the attack of ·OH to the diphenols. Tar can be produced by over oxidation. *P*-benzoquinone/hydroquinone redox couple can be formed by the reaction of benzoquinone and hydroquinone as shown in the process D. In addition, oxygen and H_2O can be formed by the decomposition of H_2O_2 (process C).

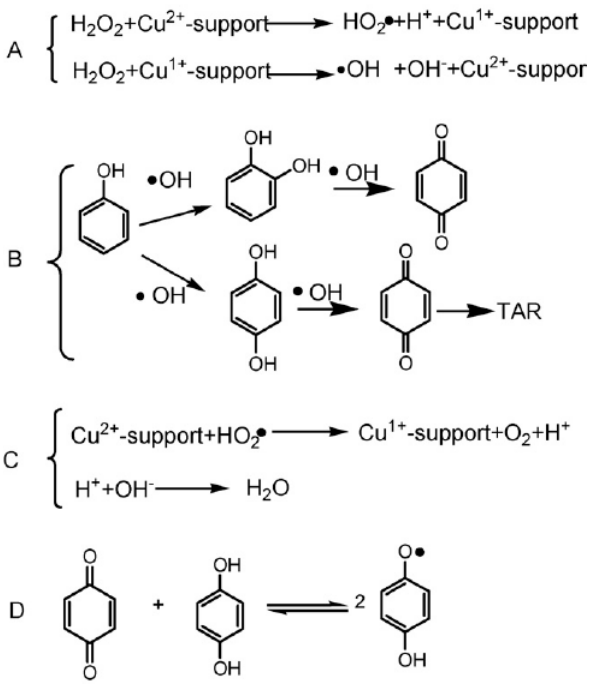

Scheme 5.12 Proposed mechanism (**1**) for phenol hydroxylation.[128]

The mechanism (**2**) (**Scheme 5.13**) is approved by Xiao *et al*[135] and Wu *et al*.[228] In this mechanism, the interaction of Cu(II) and H_2O_2 results in the generation of ·OH and HO_2· radicals, via redox cycling of Cu(II) and Cu(III). Catechol and hydroquinone are then produced in parallel processes by the attack of ·OH radicals to the aromatic ring and hydroquinone can be oxidized to form benzoquinone and over oxidized to form tar.

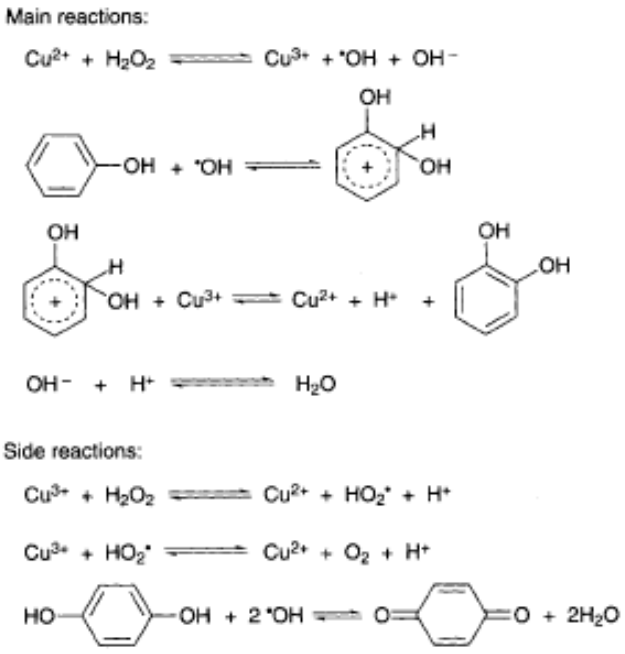

Scheme 5.13 Proposed mechanism (**2**) for phenol hydroxylation.[228]

5.3.5 Conclusions

A novel catalyst of M2'-ES-Cu(L^3) with N-(salicylaldimine)-(N'-propyltrimethoxylsilane)- diethylenetriamine copper (II) complex Cu(L^3)(CH_3COO) complex was synthesized *via* the "MSP" technique to achieve a homogeneous dispersion the metal complex (1-L^3). The M2'-ES-Cu(L^3) and its intermediate materials (M2' and M2'-ES) were characterized by XRD, FT-IR, EA, UV-visible and EPR spectroscopies. These analyses indicate that M2'-ES-Cu(L^3) with copper content of 2.8 % processes a well-ordered hexagonal structure. The copper (II) ion presents most probably a 3N2O coordination environment from the L^3 ligand and an acetate ion as a ligand or counterion. 2.6 % of copper (II) ion is EPR active indicating that the Cu ion presents as monomeric species. This material has been evaluated the catalytic activity on the phenol hydroxylation. The effect of reaction time, H_2O_2/substrate ratio, pH and solvent was investigated. This material exhibits good activity on phenol hydroxylation with phenol conversion at *ca*. 48 % and diphenols selectivity at *ca*. 76 %. The H_2O_2 concentration changes the phenol conversion and product selectivity. Solvent has a profound effect on phenol hydroxylation over M2'-ES-Cu(L^3): in aqueous solution the catalyst activity is much higher than in organic solvents like acetonitrile. The recycle tests show that the catalyst can maintain the same activity between the first and the second run, and a slight decrease is observed after the third run.

Results suggest that M2'-ES-CuL^3 catalyst exhibit a highest activity in aqueous solution. The recycle tests show this novel catalyst can keep the same activity on second run without the process of calcination regeneration.

Chapter 6 General conclusions and perspectives

6.1 General conclusions

In this dissertation, we have developed a novel methodology to control the location of a metal complex and its accessibility either in "framework" or in channel position in periodic mesostructured organicsilicas. This is examplified using Ni(II) ions as a spectroscopic probe and copper(II) to test the porous solids in catalytic hydroxylation of phenol.

Three ligands were used: N-(2-aminoethyl)-3-aminopropyltrimethoxysilane (L^1), N-salicylaldimine-propylamine-trimethoxysilane (L^2) and N-(salicylaldimine)-(N'-propyltrimethoxylsilane)-diethylenetriamine (L^3). In addition, Ni(II) ion was used as probe. These complexes were incorporated in 2D mesostructured templated silica through two synthetic routes, either the one-pot synthesis or the post-synthesis grafting. The one-pot synthesis route was optimized using soft conditions and green reactants (low temperature of 60 °C, sodium silicate as silicon source, NaOH as base and no organic co-solvent). The Ni(II)-L^1, Cu(II)-L^1 and Cu(II)-L^2 complexes were co-condensed with sodium silicate using the one-pot synthetic route in the presence of

cetyltrimethylammonium tosylate as templating agent and NaOH as the base source at 60 °C to built well-ordered periodic mesoporous organosilicas (PMOs) of MCM-41 type, obtaining materials M-OP-XNi(YL^1), M-OP-XCu(YL^1) and M-OP-XCu(YL^2) [X= Metal/SiO_2 * 100% in the sol-gel, Y= L/Metal in the sol-gel]. The post-synthesis route was based on a sequential grafting using the so-called "molecular stencil pattern" in order to evenly distribute the metal complexes in the pores of mesoporous silica. The Ni(II)-L^1, Cu(II)-L^1 and Cu(II)-L^3 complexes have been respectively grafted in the preformed mesoporous silica.

For Ni(II)-L^1 complexes, three materials M-OP-Ni(L^1), M-OP-Ni($2L^1$) and M-OP-Ni($3L^1$) with different molar ratios of ligand to metal (Y = Ligand/metal = 1, 2 and 3, respectively) have been prepared *via* one-pot synthesis. The template of the as-made materials was extracted using a mixture chlorotrimethysilane (CTMS) and hexamethyldisilazane (HMDSA) (*method TA*), leading to materials M-OP-Ni(L^1)-TA, M-OP-Ni($2L^1$)-TA and M-OP-Ni($3L^1$)-TA (~ 2 wt % Ni content). XRD, N_2 sorption isotherms and DRUV spectroscopy showed that all the obtained hybrid materials [M-OP-Ni(YL^1)-TA] are hexagnal mesostructured porous organosilicas. The coordination states of Ni(II) has been found the same as the as-made materials [M-OP-Ni(YL^1)] but different from the molecular complexes $Ni(L^1)_Y(H_2O)_{6-2Y}(NO_3)_2$ (Y = 1-3). The comparative study of the N_2 sorption isotherms strongly support the idea that the Ni(II)-L^1 complexes are indeed located in the framework for the PMOs materials while they are obviously occupying the pore volume in the post-synthesis solids. This is the first time that well defined Ni(II)-amino complexes were introduced in the framework of a mesostructured silica using basic conditions.

The Ni(YL^1)@PMOs materials exhibited a very low metal exchange ability while Ni(II) can be totally exchanged by Cu(II) under the same conditions for the post-synthesized material M1'-EP-Ni($2L^1$). With the DRUV study, in material M-OP-Ni(L^1), poor in the diamino-organosilyl complexing moities (L^1), the framework species are most likely a mixture of species [Ni(L^1)$(SiOH)_2(SiO)_2$] and [Ni(≡

$SiO)_2(O_L)_4]$ where O_L stands for a neutral oxygen donor ligand such as H_2O, $\equiv SiOH$ or $\equiv SiOSi \equiv$ and others such as nickel silicate like. In material M-OP-Ni($2L^1$) and M-OP-Ni($3L^1$), the predominant species is the neutral framework complex, $[Ni(L^1)_2(\equiv SiO)_2]$. In material M-OP-Ni($3L^1$), the presence of charged framework species $[Ni(L^1)_3]^{2+}$ is probable but still hypothetical.

For Cu(II)-L^1 complexes, two materials M-OP-Cu(L^1) and M-OP-Cu($3L^1$) (Y = 1, 3) have been synthesized via one-pot synthesis. The template removal of as-made materials has been achieved by method *TA*, and two novel methods *HTA* and *H* using combination of HCl washing and mixture of CTMS-HMDSA or a mere gentle acidification, respectively. These treatments lead to full extraction with or without concomitant capping of the silanol. The comparative N_2 sorption studies of M-OP-Cu($3L^1$)-TA and M-OP-Cu(L^1)-TA prooved that Cu(II) complexes were indeed in the framework for the PMOs materials in agreement with the results on the Ni(YL^1)@PMOs series. The bathochrome shift of the d-d electronic transition of copper(II) ion in M-OP-Cu(L^1) and M-OP-Cu($3L^1$) compared to $[Cu(L^1)]^{2+}$ and $[Cu(L^1)_2]$ complexes suggested a modification of coordination like in the wall of Ni(II) ion, *i.e.*, involving $\equiv SiO^-$ groups in environment in the z axis. Qualitative and quantitative EPR study, for the M-OP-Cu(L^1), half of EPR active species was of $[Cu(L^1)(\equiv SiO)_2(\equiv SiOH)_2]^{2+}$ and $[Cu(L^1)_2(\equiv SiO)_2]$ types. The EPR silence species were assumed to be $[Cu(\equiv SiO)_2(O_L)_4]$ where O_L stand for a neutral oxygen donor ligand such as H_2O, $\equiv SiOH$ or $\equiv SiOSi \equiv$. In M-OP-Cu($3L^1$), most of the Cu(II) species was EPR active and the predominant coordination state was $[Cu(L^1)_2(\equiv SiO)_2]$.

The framework sites in M-OP-Cu($3L^1$)-TA, M-OP-Cu($3L^1$)-HTA and M-OP-Cu($3L^1$)-H materials with hydrophobic or hydrophilic internal surface all exhibited high metal retention property (*ca*. 90 %). This indicated that high metal retention was due to the nature of incorporated complexes and was not related to the internal surface property (hydrophobe or hydrophile). Cu(YL^1)@PMOs and grafted material [M1'-EP-Cu($2L^1$)] have been tested in catalytic oxidation of 3, 5-di-*t*-butylcatechol. Only grafted material [M1'-EP-Cu($2L^1$)] exhibited activity while the PMOs material showed no activity at all, most probably due to the inaccessibility of copper like in the nickel materials studied in the previous chapter.

With the ligand L^2, three materials M-OP-0.1Cu($2L^2$), M-OP-0.2Cu($2L^2$) and M-OP-0.5Cu($2L^2$) with different Cu(II) loading (X = metal/SiO_2 = 0.1, 0.2 and 0.5 in sol-gel, respectively) have been prepared accrording to the one-pot synthesis route. A mixture agent of chlorotrimethysilane (CTMS) Upon the extraction treatment including method *TA* a large fraction of the metal was extracted, only the method *H* applied no acid excess was found efficient for selective extractration of the surfactant, keeping most of the copper in the materials. The metal integrity was also maintained during latter treatment for the L^2/Cu ratio of 2. The Cu(II)-L^2 complex was successfully incorporated in the mesoporous silica, while the Cu(II) state on solid is a mixture of $[Cu(L^2)]^{2+}$ and $[Cu(L^2)_2]$ complexes due to the partial decomposition of $[Cu(L^2)_2]$ complexes in aqueous solution. In parallel, M-OP-0.3Ni($2L^1$)-H [0.9 wt % of Ni(II)] and M-OP-Cu($2L^1$)-H [2.5 wt % of Cu] materials have been prepared and extracted according to method *H*. All the PMOs, M-OP-XCu($2L^2$)-H, M-OP-0.3Ni($2L^1$)-H and M-OP-Cu($2L^1$)-H, exhibited the same apparent wall thickness deduced from isotherms, consistent with the location of Cu-L^2 species in the framework.

For M-OP-XCu($2L^2$)-H materials, their weak resistance to the acid leaching test attests for their accessibility to proton attack and their propensity to be removed from their polydentate sites compared to M-OP-0.3Ni($2L^1$)-H, M-OP-Cu($2L^1$)-H. All these results allow us to propose that the location of Cu(II)-L^2 complexes are most probably "showing on" the porewall surface like outcrops, and charged bisethylenediamine type of M(II)-L^2 complexes is "embedded" in the wall of the pore. Furthermore, M-OP-XCu($2L^1$)-H exhibited catalytic activity on phenol hydroxylation.

The influence of reaction factors were investigated on a novel catalyst of M2'-ES-Cu(L^3) with N-(salicylaldimine)-(N'-propyltrimethoxylsilane) -diethylenetriamine copper (II) complex, since tetradentate-Schiff base copper(II) complex $[Cu(L^3)(CH_3COO)]$ with a 3N1O coordination sphere prossesses a higher affinity to Cu(II) than $[Cu(L_2)^2]$ with a 2(NO) coordination sphere. M2'-EP-Cu(L^3) has been synthesized *via* the "MSP" technique for homogeneous dispersion the function

group (CuL^3) on the internal surface of mesoporous material. XRD patterns suggested that the final M2'-EP-Cu(L^3) exhibited a well ordered hexaganol structure. EA, DRUV and EPR spectra indicated that the copper (II) coordination state is most likely of a 3N1O type and with an acetate ion as a ligand or a counterion, and all the Cu(II) species grafted in the solid are EPR active (2.6 wt % active for 2.8 wt % measured from ICP-MS). This material exhibited catalytic activity in phenol hydroxylation. The infulence of the reaction time, the H_2O_2/substrate, the pH and the solvent on the phenol conversion and product selectivity has been investigated. In aqueous buffer solution the catalyst activity is much higher than in organic solvent like acetonitrile. CAT/HQ molar ratio can be 2.62 by changing the pH of aqueous solution. The recycle tests showed that the catalyst can keep the same activity between the first run and the second run while a decrease in the third run was observed.

6.2 Perspectives

The results of this manuscript pen a wide area of development. Some can be suggested such as:

1) For the salen of a better coordination accessibility control on showing on site, one may suggest the use of a mono or bidentate protecting ligand during the one-pot synthesis.
2) To further tailor the redox properties of the embedded framework species one may envisage other metal such as manganese, other ligands such as those containing sulfur donating groups or eventually dimmers or any small metal clusters.
3) To generated a variety of "showing on" framework species, one should investigate the use of many other hydrophobic ligands of catalytic or adsorption or optical properties.
4) In line with the design of multifunctional materials, one should also demonstrate that it is possible to combine both framework sites of different nature and grafted sites to tailor catalyst on demand, for instance, the combination of Cu(II) and Fe(III) complex within the same material might be efficient for successive hydroxylation and ring opening of phenol into environment friendly diacids. Other metal complexes with aromatic ring and higher affinity to metal can be incorporated into mesoporous silica to built periodic mesoporous organosilicas (PMOs). These PMOs materials are expected

to be “showing” on the framework with accessible site. They can be applied in catalytic reaction.

5) Synthesis of multifunctional hybrid materials with redox species in the framework and active site in the channel for catalytic reaction in a “single-step”.

Appendix A: IR quantitative treatment

- Original IR spectra of **M’** (LUS) (**Figure A.1**)

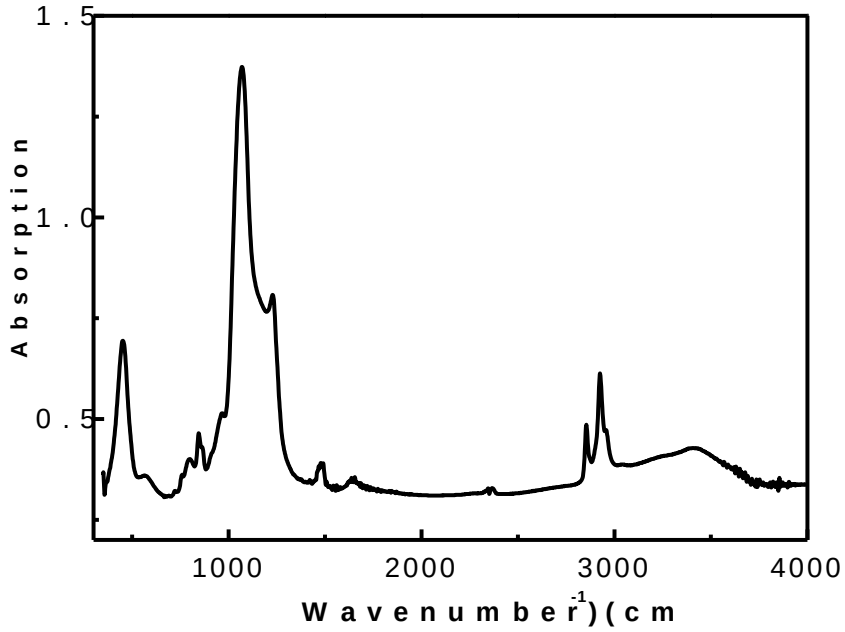

Figure A.1 Original IR spectrum of **M’**.

- Chose certain points which belong to the baseline part (**Table A.1**).

Table A.1 Chosen points in FT-IR spectra.

Wavenumber (cm^{-1})	Absorption
356.768	0.312
2044.187	0.31
2499.308	0.316
3995.808	0.338

- Simulate a line according to these points, obtaining the new correction line (solid line) (**Figure A.2**).
- Subtracte the original IR data from the baseline corrected data, obtaing a new absorption data.

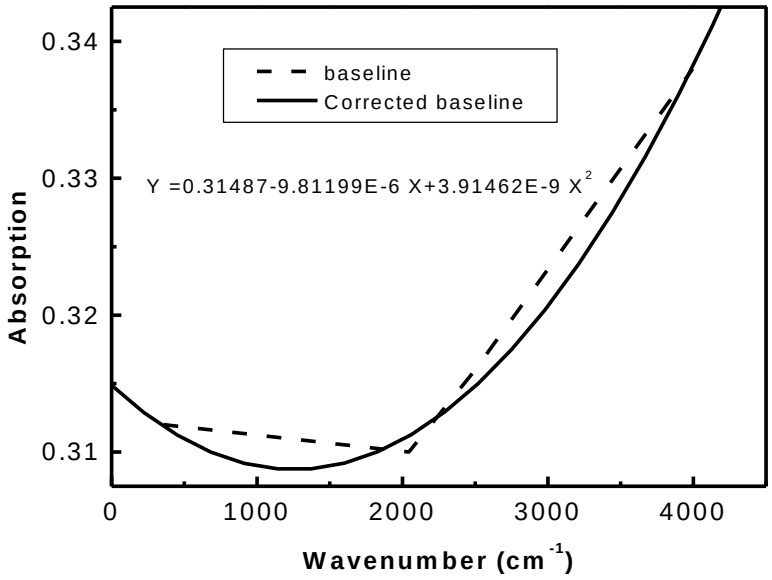

Figure A.2 Baseline correction.

- Draw the corrected spectra through the wavenumber and the new absorption data (solid line, **Figure A.3**).

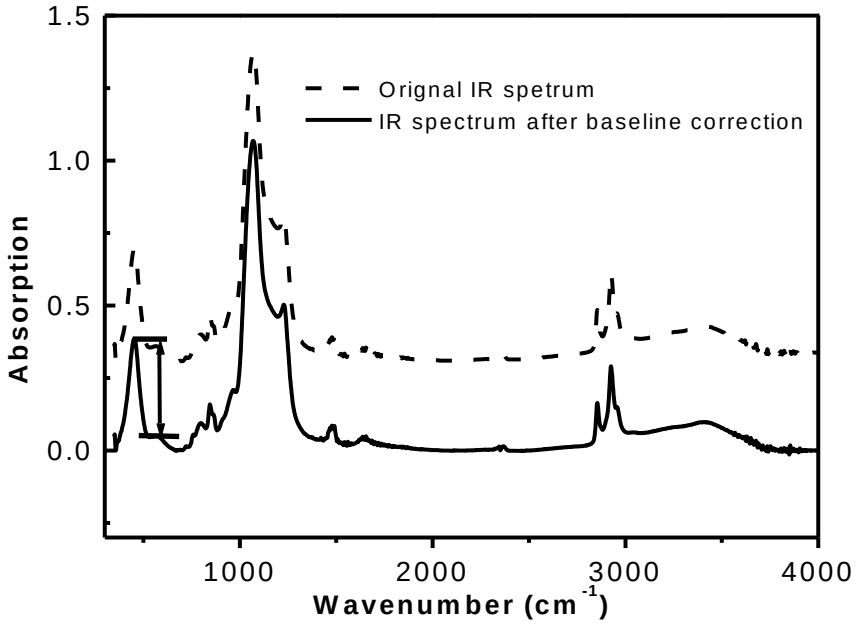

Figure A.3 IR spectrum after baseline correction.

- Normalize the IR spectrum by taking the absorption bands of δ(O-Si-O) of the valence angle of tetrahedral SiO_4 units located at 450 cm^{-1}.

Appendix B: EPR quantitative treatment

- Use $CuSO_4.5H_2O$ crystals as calibration reference, obtaining several EPR spectra.
- Double integration after base line correction of EPR spectra, obtaining the figure regarding Cu amount *vs* intensity (**Figure B.1**).
- Measure EPR active Cu(II) species among sample.

1) Weight certain sample mass (~ 2 mg), and then put them in EPR tube

2) Put EPR tube in a suitable place of cavity in order to get the maximal EPR signal after double integration

3) Use the relation between Cu amount and intensity (**Figure B.1**) to obtain the EPR active Cu among sample.

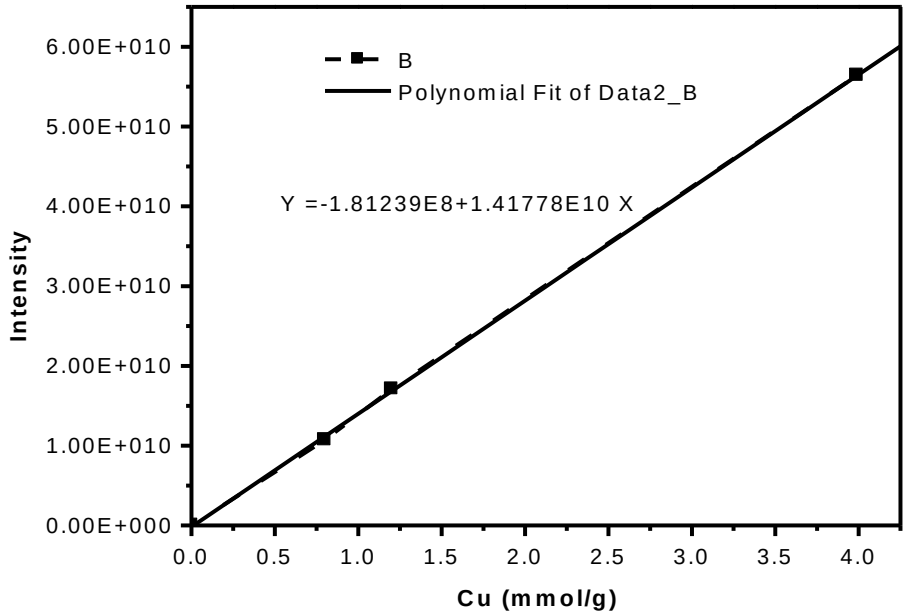

Figure B.1 Experimental conditions: frequency = 9.35GHz, power = 10 mW, modulation amplitude: 0.6 G and modulation frequency: 100 kHz.

Appendix C: Conversion of reactant and yield of product determined from GC and HPLC

C.1 Internal standard approach for calculation of DTBC conversion and DTBQ yield from GC determination

An internal standard is inert during the reaction, thus it is considered as a constant product with no consumption. Here, naphthalene is chosen as internal standard in the oxidation of 3,5-di-*t*-butylcatechol (DTBC). Therefore, the DTBC conversion can be calculated in the following way:

S_{D0}: retention surface area of initial DTBC; S_{I0}: retention surface area of initial naphthalene; S_{Dt}: retention surface area of DTBC at t h; S_{It}: retention surface area of naphthalene at t h;

$DTBC_{conversion}$ % = (S_{Dt}/ S_{It} - S_{D0}/S_{I0})/ (S_{D0}/S_{I0})

DTBQ yield was calculated in the following way:

- Prepare several concentrations of authentic DTBQ and naphthalene in acetonitrile
- Inject these aliquots into GC, obtaining certain retention surface areas which correspond to the certain sample concentration. Obtain the average DTBQ/naphthalene corresponding factor (r) in GC
- The yield of DTBQ at t h can be obtained in the following way:

  Yield of DTBQ (mol) = $n_{napthalene}$ (mol) * S_{Qt} / S_{It} / r

  S_{It}: retention surface area of initial naphthalene; S_{Qt}: retention surface area of DTBQ at t h;

C.2 Calculation approach for phenol conversion and product yield from HPLC determination

1) Prepare different concentrations of authentic products (phenol, catechol, hydroquinone) in water

2) Inject these aliquots into HPCL, obtaining certain retention surface areas

3) Draw the diagram of retention surface area (**S**) *vs* sample concentration (**C**) (**Figure C.1**).

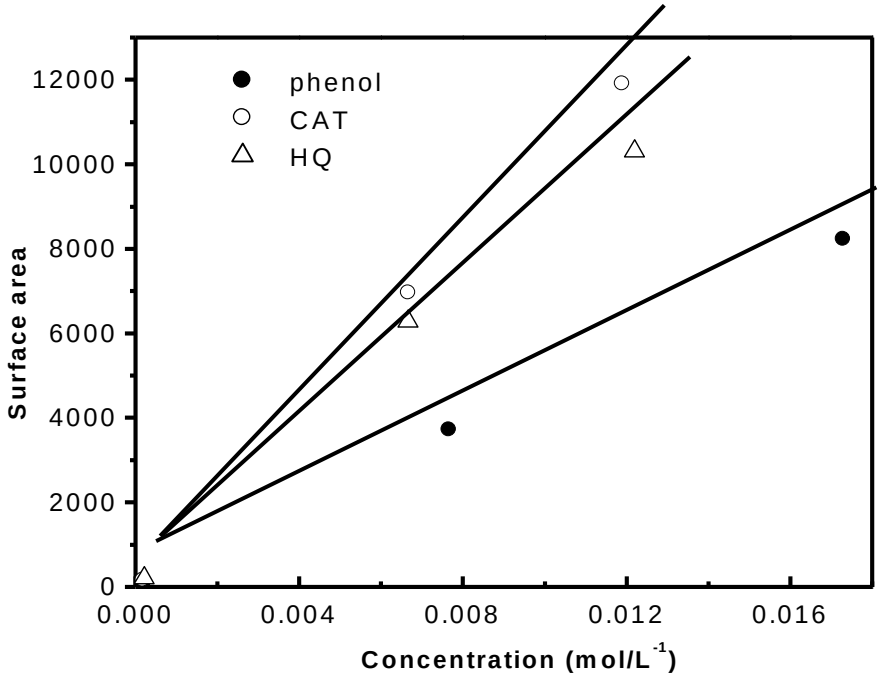

Figure C.1 Calibration line of authentic phenol, CAT and HQ.

4) Calculate retention surface area/concentration (**S/C**) values (**Table C.1**)

For example, phenol:

S/C = [101/0.00021 + 3706/0.00767 + 8216/0.173 + (3706-101)/(0.00767-0.00021) + (8216-101)/(0.0173-0.00021) + (8216-3706)/(0.0173-0.00767)] / 6 = 477577

Table C.1 Retention surface area *vs* concentration.

Authentic sample	Concentration (mol/L)	Surface area in HPLC	S/C [a]
Phenol	0.00021	101	477577
	0.00767	3706	
	0.0173	8216	
Catechol (CAT)	0.000187	155	977815
	0.00667	6945	
	0.0119	11898	
Hydroquinone (HQ)	0.000218	208.2	875661
	0.00666	6277.7	
	0.0122	10304.6	

[a] S/C = surface area/ concentration

5) Phenol conversion and CAT yield (mol) can be obtained in the following formulas:

Sp_0: retention surface area of initial Phenol; Sp_t: retention surface area of Phenol at t h; S_{Ct}: retention surface area of CAT at t h; [Phenol]: concentration of phenol; [CAT]: concentration of CAT.

$[Phenol]_0 = Sp_0 / [S/C]_{phenol}$

$[Phenol]_t = Sp_t / [S/C]_{phenol}$

$Phenol_{conversion}$ mol % = $([Phenol]_0 - [Phenol]_t) / [Phenol]_0 \times 100\ \% = (Sp_0 - Sp_t) / Sp_0 \times 100\ \%$

$[CAT]_t = S_{Ct} / [S/C]_{CAT}$

CAT_{yield} mol % = $[CAT]_t / [Phenol]_0 = S_t \times [S/C]_{phenol} / [S/C]_{CAT} / Sp_0 \times 100\ \%$

References

1. Gates B. C., *Cataytic. chemistry*, Wiley, 1992.
2. M. Boudart, *La cinétique des réactions en catalyse hétérogène*, Masson,1982.
3. Thomas J. M., *Principles and practice of heterogeneous catalysis, VCH*, 1997.
4. M. G. Clerici, G. Bellussi, U. Romano, *J. Catal.*, 1991, **129**, 159-167.
5. S. Gontier, A. Tuel, *J. Catal.*, 1995, **157**, 124-132.
6. J. S. Beck, J. C. Vartuli, W. J. Roth, M. E. Leonowicz, C. T. Kresge, K. D. Schmitt, C. T. W. Chu, D. H. Olson, E. W. Sheppard, S. B. McCullen, J. B. Higgins, J. L. Schlenker, *J. Am.Chem.. Soc.*, 1992, **114**, 10834-10843.
7. S. Inagaki, Y. Fukushima, K. Kuroda, *J. Chem. Soc. Chem. Comm.*, 1993, 680-682.
8. C. P. Jaroniec, M. Kruk, M. Jaroniec, A. Sayari, *J.Phys. Chem. B*, 1998, **102**, 5503-5510.
9. T. J. Terry, T. D. P. Stack, *J. Am. Chem. Soc.*, 2008, **130**, 4945-4953.
10. S. Abry, F. Lux, B. Albela, A. Artigas-Miquel, S. Nicolas, B. Jarry, P. Perriat, G. Lemercier, L. Bonneviot, *Chem. Mater.*, 2009, **21**, 2349-2359.
11. S. Inagaki, S. Guan, Y. Fukushima, T. Ohsuna, O. Terasaki, *J. Am. Chem. Soc.*, 1999, **121**,

9611-9614.
12. T. Asefa, M. J. MacLachan, N. Coombs and G. A. Ozin, *Nature*, 1999, **402**, 867-871.
13. B. J. Melde, B. T. Holland, C. F. Blanford, A. Stein, *Chem. Mater.*, 1999, **11**, 3302-3308.
14. C. Baleizao, B. Gigante, H. Garcia, A. Corma, *J. Catal.*, 2003, **215**, 199-207.
15. V. Dufaud, F. Beauchesne, L. Bonneviot, *Angew. Chem. Inter. Ed.*, 2005, **44**, 3475-3477.
16. G. Dubois, R. J. P. Corriu, C. Reye, S. Brandes, F. Denat, R. Guilard, *Chem. Comm.*, 1999, 2283-2284.
17. R. J. P. Corriu, A. Mehdi, C. Reye, C. Thieuleux, *Chem. Comm.*, 2002, 1382-1383.
18. R. J. P. Corriu, A. Mehdi, C. Reye, C. Thieuleux, *Chem. Comm.*, 2003, 1564-1565.
19. S. Itoh, M. Taki, P. Holland, W. B. Tolman, L. Que, S. Fukuzumi, *J. Inorg. Biochem.*, 1999, **74**, 33-33.
20. S. Mahapatra, J. A. Halfen, E. C. Wilkinson, L. Que, W. B. Tolman, *J. Am. Chem. Soc.*, 1994, **116**, 9785-9786.
21. G. Battaini, E. Monzani, A. Perotti, C. Para, L. Casella, L. Santagostini, M. Gullotti, R. Dillinger, C. Nather, F. Tuczek, *J. Am. Chem. Soc.*, 2003, **125**, 4185-4198.
22. S. Abry, A. Thibon, B. Albela, P. Delichere, F. Banse, L. Bonneviot, *New J. Chem.*, 2009, **33**, 484-496.
23. K. Zhang, B. Albela, M. Y. He, Y. M. Wang, L. Bonneviot, *Phys. Chem. Chem. Phys.*, 2009, **11**, 2912-2921.
24. B. Notari, *Advances in Catalysis, Vol 41*, 1996, **41**, 253-334.
25. R. Ravindra, Z. Shuang, H. Gies, R. Winter, *J. Am. Chem. Soc.*, 2004, **126**, 12224-12225.
26. C. H. Lei, Y. S. Shin, J. Liu, E. J. Ackerman, *J. Am. Chem. Soc.*, 2002, **124**, 11242-11243.
27. W. G. Madden, E. D. Glandt, *J. Stat. Phys.*, 1988, **51**, 537-558.
28. S. L. Zhao, W. Dong, Q. H. Liu, *J. Chem. Phys.*, 2006, **125**.
29. W. R. Zhao, J. L. Gu, L. X. Zhang, H. R. Chen, H. R. Chen, J. L. Shi, *J. Am. Chem. Soc.*, 2005, **127**, 8916-8917.
30. S. Giri, B. G. Trewyn, M. P. Stellmaker, V. S. Y. Lin, *Angew. Chem.Inter. Ed.*, 2005, **44**, 5038-5044.
31. H. Yoshitake, T. Yokoi, T. Tatsumi, *Chem. Mater.*, 2003, **15**, 1713-1721.
32. T. Kang, Y. Park and J. Yi, *Industrial & Engineering Chemistry Research*, 2004, **43**, 1478-1484.
33. E. J. Connolly, G. M. O'Halloran, H. T. M. Pham, P. M. Sarro and P. J. French, *Sensors and Actuators a-Physical*, 2002, **99**, PII S0924-4247(0901)00885-00888.
34. A. Corma, *Chem. Rev.*, 1997, **97**, 2373-2419.
35. J. W. Zhao, F. Gao, Y. L. Fu, W. Jin, P. Y. Yang, D. Y. Zhao, *Chem. Comm.*, 2002, 752-753.
36. S. H. Park, Y. N. Xia, *Adv. Mater.*, 1998, **10**, 1045-+.
37. K. Maex, M. R. Baklanov, D. Shamiryan, F. Iacopi, S. H. Brongersma, Z. S. Yanovitskaya, *J. Appl. Phys.*, 2003, **93**, 8793-8841.
38. K. S. W. Sing, D. H. Everett, R. A. W. Haul, L. Moscou, R. A. Pierotti, J. Rouquerol, T. Siemieniewska, *Pure Appl. Chem.*, 1985, **57**, 603-619.
39. G. Ferey, *Chem. Mater.*, 2001, **13**, 3084-3098.
40. T. Yanagisawa, T. Shimizu, K. Kuroda, C. Kato, *Bull. Chem. Soc. Jpn.*, 1990, **63**, 988-992.
41. R. Ryoo, S. H. Joo and S. Jun, S. Jun, *J. Phys. Chem. B*, 1999, **103**, 7743-7746.
42. R. Ryoo, C. H. Ko, M. Kruk, V. Antochshuk, M. Jaroniec, *J. Phys. Chem. B*, 2000, **104**, 11465-11471.
43. A. Stein, M. Fendorf, T. P. Jarvie, K. T. Mueller, A. J. Benesi, T. E. Mallouk, *Chem. Mater.*, 1995, **7**,

304-313.
44. P. T. Tanev and T. J. Pinnavaia, *Science*, 1995, **267**, 865-867.
45. P. V. Braun, P. Osenar and S. I. Stupp, *Nature*, 1996, **380**, 325-328.
46. J. Q. Li, L. Delmotte, H. Kessler, *Chem. Comm.*, 1996, 1023-1024.
47. S. Oliver, A. Kuperman, N. Coombs, A. Lough and G. A. Ozin, *Nature*, 1995, **378**, 47-50.
48. G. A. Ozin, S. Oliver, *Adv. Mater.*, 1995, **7**, 943-&.
49. A. Sayari, P. Liu, *Microporous Mater.*, 1997, **12**, 149-177.
50. C. T. Kresge, M. E. Leonowicz, W. J. Roth, J. C. Vartuli and J. S. Beck, *Nature*, 1992, **359**, 710-712.
51. L. Bonneviot, M. Morin and A. Badiei, *Patent WO 01/55031 A 1*, 2001.
52. R. Ryoo, J. M. Kim, C. H. Ko, C. H. Shin, *J. Phys. Chem.*, 1996, 1996, **100**, 17718-17721.
53. S. A. Bagshaw, E. Prouzet and T. J. Pinnavaia, *Science*, 1995, **269**, 1242-1244.
54. Q. S. Huo, D. I. Margolese, U. Ciesla, P. Y. Feng, T. E. Gier, P. Sieger, R. Leon, P. M. Petroff, F. Schuth and G. D. Stucky, *Nature*, 1994, **368**, 317-321.
55. D. Y. Zhao, J. L. Feng, Q. S. Huo, N. Melosh, G. H. Fredrickson, B. F. Chmelka and G. D. Stucky, *Science*, 1998, **279**, 548-552.
56. L. Mercier, T. J. Pinnavaia, *Chem. Mater.*, 2000, **12**, 188-196.
57. S. R. Hall, C. E. Fowler, B. Lebeau, S. Mann, *Chem. Comm.*, 1999, 201-202.
58. K. A. Koyano, T. Tatsumi, Y. Tanaka, Y. Tanaka, S. Nakata, *J. Phys. Chem. B*, 1997, **101**, 9436-9440.
59. V. Antochshuk, M. Jaroniec, *Chem. Comm.*, 1999, 2373-2374.
60. S. Kawi, M. W. Lai, *Chem. Comm.*, 1998, 1407-1408.
61. W. Z. Zhang, T. R. Pauly, T. J. Pinnavaia, *Chem. Mater.*, 1997, **9**, 2491-2498.
62. S. Inagaki, Y. Fukushima, K. Kuroda, K. Kuroda, *J. Colloid Interface Sci.*, 1996, **180**, 623-624.
63. A. Monnier, F. Schuth, Q. Huo, D. Kumar, D. Margolese, R. S. Maxwell, G. D. Stucky, M. Krishnamurty, P. Petroff, A. Firouzi, M. Janicke and B. F. Chmelka, *Science*, 1993, **261**, 1299-1303.
64. D. M. Antonelli, J. Y. Ying, *Angew. Chem. Int. Ed.*, 1996, **35**, 426-430.
65. F. Hoffmann, M. Cornelius, J. Morell, *Angew. Chem Int. Ed.*, 2006, **45**, 3216-3251.
66. (a) H. Yang, N. Coombs, G. A. Ozin, *Nature*, 1997, **386**, 692-696; (b) H. Yang, N. Coombs, G. A. Ozin, *Adv. Mater.*, 1997, **9**, 811-814; (c) S. Che, Y. Sakamoto, O. Terasaki, T. Tatsumi, *Chem. Mater.*, 2001, **13**, 2237-2229.
67. F. Y. Qu, G. S. Zhu, H. M. Lin, W. W. Zhang, J. Y. Sun, S. G. Li, S. L. Qiu, *J. Solid State Chem.*, 2006, **179**, 2027-2035.
68. P. Y. Feng, X. H. Bu, G. D. Stucky, D. J. Pine, *J. Am. Chem. Soc.*, 2000, **122**, 994-995.
69. A. Galarneau, J. Lapichella, D. Brunel, F. Fajula, Z. Bayram-Hahn, K. Unger, G. Puy, C. Demesmay, J. L. Rocca, *J. Sep. Sci.*, 2006, **29**, 844-855.
70. H. P. Lin, C. Y. Mou, *Acc. Chem. Res.*, 2002, **35**, 927-935.
71. J. Babin, J. Iapichella, B. Lefevre, C. Biolley, J. P. Bellat, F. Fajula, A. Galarneau, *New J. Chem.*, 2007, **31**, 1907-1917.
72. Q. S. Huo, D. I. Margolese, G. D. Stucky, *Chem. Mater.*, 1996, **8**, 1147-1160.
73. A. Sayari, P. Liu, M. Kruk, M. Jaroniec, *Chem. Mater.*, 1997, **9**, 2499-2506.
74. T. Kimura, Y. Sugahara, K. Kuroda, *Chem. Comm.*, 1998, 559-560.
75. P. Schmidt-Winkel, W. W. Lukens, D. Y. Zhao, P. D. Yang, B. F. Chmelka, G. D. Stucky, *J. Am. Chem. Soc.*, 1999, **121**, 254-255.
76. J. S. Lettow, Y. J. Han, P. Schmidt-Winkel, P. D. Yang, D. Y. Zhao, G. D. Stucky and J. Y. Ying, *Langmuir*, 2000, **16**, 8291-8295.

77. B. Lefevre, A. Galarneau, J. Iapichella, C. Petitto, F. Di Renzo, F. Fajula, Z. Bayram-Hahn, R. Skudas, K. Unger, *Chem. Mater.*, 2005, **17**, 601-607.
78. A. Sayari, Y. Yang, M. Kruk, M. Jaroniec, *J. Phys. Chem. B*, 1999, **103**, 3651-3658.
79. A. Corma, Q. B. Kan, M. T. Navarro, J. PerezPariente, F. Rey, *Chem. Mater.*, 1997, **9**, 2123-2126.
80. J. Liu, Q. Yang, X. S. Zhao, L. Zhang, *Microporous Mesoporous Mater.*, 2007, **106**, 62-67.
81. A. Sayari, M. Kruk, M. Jaroniec, I. L. Moudrakovski, *Adv. Mater.*, 1998, **10**, 1376-+.
82. C. F. Cheng, W. Z. Zhou, D. H. Park, J. Klinowski, M. Hargreaves, L. F. Gladden, *J. Chem. Soc. Faraday Trans.*, 1997, **93**, 359-363.
83. M. Widenmeyer, R. Anwander, *Chem.Mater.*, 2002, **14**, 1827-1831.
84. X. S. Zhao, G. Q. Lu, A. K. Whittaker, G. J. Millar, H. Y. Zhu, *J. Phys. Chem. B*, 1997, **101**, 6525-6531.
85. N. Moll, F. Banse, K. Miki, M. Nierlich, J. J. Girerd, *Eur. J. Inorg. Chem.*, 2002, 1941-1944.
86. S. Shylesh, A. P. Singh, *Microporous Mesoporous Mater.*, 2006, **94**, 127-138.
87. I. K. Mbaraka, B. H. Shanks, *J. Catal.*, 2005, **229**, 365-373.
88. E. P. Barrett, L. G. Joyner, P. P. Halenda, *J. Am. Chem. Soc.*, 1951, **73**, 373-380.
89. Broekhof.Jc, J. H. Deboer, *J. Catal.*, 1968, **10**, 377-&.
90. S. Brunauer, P. H. Emmett and E. Teller, *Journal of the American Chemical Society*, 1938, **60**, 309-319.
91. A. Stein, B. J. Melde, R. C. Schroden, *Adv. Mater.*, 2000, **12**, 1403-1419.
92. L. Mercier, T. J. Pinnavaia, *Adv. Mater.*, 1997, **9**, 500-&.
93. X. Feng, G. E. Fryxell, L. Q. Wang, A. Y. Kim, J. Liu and K. M. Kemner, *Science*, 1997, **276**, 923-926.
94. A. Walcarius, N. Luthi, J. L. Blin, B. L. Su, L. Lamberts, *Electrochim. Acta*, 1999, **44**, 4601-4610.
95. H. Yoshitake, T. Yokoi, T. Tatsumi, *Chem. Mater.*, 2002, **14**, 4603-4610.
96. I. Diaz, F. Mohino, J. Perez-Pariente, E. Sastre, *Appl. Catal. A: Gen.*, 2001, **205**, 19-30.
97. D. Das, J. F. Lee, S. F. Cheng, *Chem. Comm.*, 2001, 2178-2179.
98. D. J. Macquarrie, D. B. Jackson, *Chem. Comm.*, 1997, 1781-1782.
99. D. Brunel, *Microp. Mesop. Mater.*, 1999, **27**, 329-344.
100. T. Asefa, *Dissertation*.
101. S. Che, Z. Liu, T. Ohsuna, K. Sakamoto, O. Terasaki and T. Tatsumi, *Nature*, 2004, **429**, 281-284.
102. S. Inagaki, S. Guan, T. Ohsuna and O. Terasaki, *Nature*, 2002, **416**, 304-307.
103. C. Nozaki, C. G. Lugmair, A. T. Bell, T. D. Tilley, *J. Am. Chem. Soc.*, 2002, **124**, 13194-13203.
104. K. L. Fujdala, T. D. Tilley, *J. Catal.*, 2003, **216**, 265-275.
105. L. Bonneviot, O. Legendre, M. Kermarec, D. Olivier, M. Che, *J. Colloid Interface Sci.*, 1990, **134**, 534-547.
106. M. Che, Z. X. Cheng, C. Louis, *J. Am. Chem. Soc.*, 1995, **117**, 2008-2018.
107. K. Q. Sun, E. Marceau, M. Che, *Phys. Chem. Chem. Phys.*, 2006, **8**, 1731-1738.
108. G. E. Fryxell, J. Liu, T. A. Hauser, Z. M. Nie, K. F. Ferris, S. Mattigod, M. L. Gong, R. T. Hallen, *Chem. Mater.*, 1999, **11**, 2148-2154.
109. S. Abry, *These*, 2007, 239.
110. S. Abry, B. Albela and L. Bonneviot, *C. R. Chim.*, 2005, **8**, 741-752.
111. S. A. Raynor, J. M. Thomas, R. Raja, B. F. G. Johnson, R. G. Bell, M. D. Mantle, *Chem. Comm.*, 2000, 1925-1926.
112. X. G. Zhou, X. Q. Yu, J. S. Huang, S. G. Li, L. S. Li, C. M. Che, *Chem. Commun.*, 1999, 1789-1790.

113. R. I. Kureshy, I. Ahmad, N. H. Khan, S. H. R. Abdi, K. Pathak, R. V. Jasra, *J.Catal.*, 2006, **238**, 134-141.
114. K. B. Hansen, J. L. Leighton, E. N. Jacobsen, *J. Am. Chem. Soc.*, 1996, **118**, 10924-10925.
115. W. Zhang, J. L. Loebach, S. R. Wilson, E. N. Jacobsen, *J. Am. Chem. Soc.*, 1990, **112**, 2801-2803.
116. R. Irie, T. Hashihayata, T. Katsuki, M. Akita,Y. Moro-oka, *Chem. Lett.*, 1998, 1041-1042.
117. E. F. Murphy, L. Schmid, T. Burgi, M. Maciejewski, A. Baiker, D. Gunther, M. Schneider, *Chem. Mater.*, 2001, **13**, 1296-1304.
118. E. F. Murphy, A. Baiker, *J. Mol. Catal. A: Chem.*, 2002, **179**, 233-241.
119. C. Baleizao, B. Gigante, D. Das, M. Alvaro, H. Garcia, A. Corma, *J. Catal.*, 2004, **223**, 106-113.
120. C. Baleizao, B. Gigante, H. Garcia and A. Corma, *Tetrahedron*, 2004, **60**, 10461-10468.
121. C. Baleizao, B. Gigante, D. Das, M. Alvaro, H. Garcia and A. Corma, *Chem. Commun.*, 2003, 1860-1861.
122. L. Que, *Physical methods in bioinorganic chemistry: spectroscopy and magnetism*, University Science Books, c2000.
123. T. Sawada, K. Fukumaru, H. Sakurai, *Chem. Pharm. Bull.*, 1996, **44**, 1009-1016.
124. M. A. J. Burton Lewis W. , Morgan L. O., *J. Chem. Phys.*, 1966, **45**, 4003-4010.
125. J. M. Holland, X. M. Liu, J. P. Zhao, F. E. Mabbs, C. A. Kilner, M. Thornton-Pett, M. A. Halcrow, *J. Chem. So. Dalton Trans.*, 2000, 3316-3324.
126. S. Ray, S. F. Mapolie, J. Darkwa, *J. Mol. Catal. A: Chem.*, 2007, **267**, 143-148.
127. Z. H. Fu, J. H. Chen, D. L. Yin, D. H. Yin, L. X. Zhang, Y. Y. Zhang, *Catal. Lett.*, 2000, **66**, 105-108.
128. L. P. Wang, A. G. Kong, B. Chen, H. M. Ding, Y. K. Shan, M. Y. He, *J. Mol. Catal.A: Chem.*, 2005, **230**, 143-150.
129. I. Sobczak, M. Ziolek, M. Renn, P. Decyk, I. Nowak, M. Daturi, J. C. Lavalley, *Microp. Mesop. Mater.*, 2004, **74**, 23-36.
130. H. L. Tang, Y. Ren, B. Yue, S. R. Yan, H. Y. He, *J. Mol. Catal. A: Chem.*, 2006, **260**, 121-127.
131. J. Wang, J. N. Park, H. C. Jeong, K. S. Choi, X. Y. Wei, S. I. Hong, C. W. Lee, *Energy Fuels*, 2004, **18**, 470-476.
132. A. Dubey, V. Rives, S. Kannan, *J. Mol. Catal. A: Chem.*, 2002, **181**, PII S1381-1169(1301)00360-00360.
133. V. Rives, A. Dubey, S. Kannan, *Phys. Chem. Chem. Phys.*, 2001, **3**, 4826-4836.
134. Y. M. Liu, S. T. Liu, K. Z. Zhu, X. K. Ye, Y. Wu, *Appl. Catal. A: Gen.*, 1998, **169**, 127-135.
135. F. S. Xiao, J. M. Sun, X. J. Meng, R. B. Yu, H. M. Yuan, J. N. Xu, T. Y. Song, D. Z. Jiang, R. R. Xu, *J. Catal.*, 2001, **199**, 273-281.
136. C. H. Wang, J. W. Lu, H. H. Wei and M. Takeda, *Inorganica Chimica Acta*, 2007, **360**, 2944-2952.
137. S. J. Lippard and J. M. Berg, *Principles of Bioinorganic Chemistry*, University Science Books, Mill Valley, CA, 1994.
138. C. Eicken, B. Krebs and J. C. Sacchettini, *Curr. Opin. Struct. Biol.*, 1999, **9**, 677-683.
139. C. Gerdemann, C. Eicken and B. Krebs, *Accounts Chem. Res.*, 2002, **35**, 183-191.
140. A. Volbeda and W. G. J. Hol, *J. Mol. Biol.*, 1989, **209**, 249-279.
141. I. A. Koval, P. Gamez, C. Belle, K. Selmeczi and J. Reedijk, *Chem. Soc. Rev.*, 2006, **35**, 814-840.
142. E. I. Solomon, M. J. Baldwin and M. D. Lowery, *Chem. Rev.*, 1992, **92**, 521-542.
143. E. I. Solomon, U. M. Sundaram and T. E. Machonkin, *Chem. Rev.*, 1996, **96**, 2563-2605.
144. E. A. Lewis and W. B. Tolman, *Chem. Rev.*, 2004, **104**, 1047-1076.
145. L. M. Mirica, X. Ottenwaelder and T. D. P. Stack, *Chem. Rev.*, 2004, **104**, 1013-1045.

146. L. Que, W. B. Tolman, *Angew. Chem.-Int. Edit.*, 2002, **41**, 1114-1137.
147. M. Louloudi, Y. Deligiannakis, N. Hadjiliadis, *Inorg. Chem.*, 1998, **37**, 6847-6851.
148. M. Louloudi, Y. Deligiannakis, N. Hadjiliadis, *J. Inorg. Biochem.*, 2000, **79**, 93-96.
149. M. Louloudi, K. Mitopoulou, E. Evaggelou, Y. Deligiannakis, N. Hadjiliadis, *J. Mol. Catal. A: Chem.*, 2003, **198**, 231-240.
150. D. Zois, C. Vartzouma, Y. Deligiannakis, N. Hadjiliadis, L. Casella, E. Monzani, M. Louloudi, *J. Mol. Catal. A: Chem.*, 2007, **261**, 306-317.
151. G. Grigoropoulou, K. C. Christoforidis, M. Louloudi, Y. Deligiannakis, *Langmuir*, 2007, **23**, 10407-10418.
152. C. H. Lee, S. T. Wong, T. S. Lin, C. Y. Mou, *J. Phys. Chem. B*, 2005, 2005, **109**, 775-784.
153. L. Bonneviot, A. Badiei, N. Crowther, *Patent WO 02216267*, 2002.
154. NONIUS, *Kappa CCD Program Package: COLLECT, DENZO, SCALEPACK, SORTAV; Nonius BV: Delft,The Netherlands*, 1999.
155. D. J. Watkin, C. K. Prout, J. R. Carruthers, P. W. Betteridge, *CRYSTALS Issue 11; Chemical Crystallography Laboratory: Oxford, U.K.,*, 1999.
156. G. Cascarano, A. Altomare, C. Giacovazzo, A. Guagliardi, A. G. G. Moliterni, D. Siliqi, M. C. Burla, G. Polidori, M. Camalli, *Acta Crystallogr., Sect. A* 1996, **52**, C-79.
157. K. Z. Hossain, L. Mercier, *Adv. Mater.*, 2002, **14**, 1053-1056.
158. M. A. Karakassides, A. Bourlinos, D. Petridis, L. Coche-Guerente, P. Labbe, *J. Mater. Chem.*, 2000, **10**, 403-408.
159. A. B. P. Lever, *Inorganic Electronic Spectroscopy*, Elsevier, 1984.
160. S. Calmettes, B. Albela, O. Hamelin, S. Menage, F. Miomandre, L. Bonneviot, *New J. Chem.*, 2008, **32**, 727-737.
161. S. F. A. Kettle, Physic-Chimie Inorganique Une Approche Basée Sur La Chimie De Coordination, Deboeck université, 1999.
162. F. Basolo, R. K. Murmann, *J. Am.Chem. Soc.*, 1952, **74**, 2373-2374.
163. S. F. Pavkovic, D. W. Meek, *Inorg. Chem.*, 1965, **4**, 20-&.
164. L. Bonneviot, M. Morin, A. Badiei, *Patent WO 01/55031 A 1*, 2001.
165. F. C. E. Hall S. R., Lebeau B., Mann S., *Chem. Comm,*, 1999.
166. M. C. Burleigh, S. Dai, E. W. Hagaman, J. S. Lin, *Chem. Mater.*, 2001, **13**, 2537-2546.
167. T. Tatsumi, K. A. Koyano, Y. Tanaka, S. Nakata, *Mesoporous Molecular Sieves 1998*, 1998, **117**, 143-150.
168. T. Tatsumi, K. A. Koyano, N. Igarashi, *Chem. Comm.*, 1998, 325-326.
169. C. T. Kresge, J. C. Vartuli, W. J. Roth and M. E. Leonowicz, in *Mesoporous Crystals and Related Nano-Structured Materials*, 2004, pp. 53-72.
170. G. A. Coasne B., Di Renzo F., Pellenq R.J.M, *Langumuir*, 2006, **22**.
171. G. A. Coasne B., F. Di Renzo , R.J.M. Pellenq, *J. Phys. Chem.*, 2007, **111**.
172. M. Bernard and F. Busnot, *Usuel de Chimie Générale et Minérale*, Dunod, Paris, 1984.
173. R. Ganesan, B. Viswanathan, *J. Phys. Chem. B*, 2004, **108**, 7102-7114.
174. O. Clause, L. Bonneviot, M. Che, M. Verdaguer, F. Villain, D. Bazin, H. Dexpert, *J. Chimi. Phys. Phys. Chimi. Biol.*, 1989, **86**, 1767-1775.
175. A. R. Badiei, L. Bonneviot, *Inorg. Chem.*, 1998, **37**, 4142-4145.
176. J. H. Z. dos Santos, H. T. Ban, T. Teranishi, T. Uozumi, T. Sano, K. Soga, *Appl. Catal. A: Gen.*, 2001, **220**, 287-302.

177. A. Badiei, L. Bonneviot, N. Crowther, G. M. Ziarani, *J. Organomet. Chem.*, 2006, **691**, 5911-5919.
178. H. P. Lin, S. T. Wong, C. Y. Mou, C. Y. Tang, *J. Phys. Chem. B*, 2000, **104**, 8967-8975.
179. O. Clause, M. Kermarec, L. Bonneviot, F. Villain, M. Che, *J. Am. Chem. Soc.*, 1992, **114**, 4709-4717.
180. O. Clause, L. Bonneviot, M. Che, *J. Catal.*, 1992, **138**, 195-205.
181. A. Manceau, G. Calas, A. Decarreau, *Clay Miner.*, 1985, **20**, 367-387.
182. W. J. Zhou, *unpublished data*.
183. S. Abry, F. Lux, B. Albela, G. L. Lemercier, A. Artigas-Miquel, B. Jarry, P. Perriat, L. Bonneviot, *chem. mater.*, 2009, **21**, 2349-2359.
184. E. Martinez-Ferrero, D. Grosso, C. Boissiere, C. Sanchez, O. Oms, D. Leclercq, A. Vioux, F. Miomandre, P. Audebert, *J. Mater. Chem.*, 2006, **16**, 3762-3767.
185. Y. Kong , S. L. Mu, *Chinese J. Chem.*, 2003, **21**, 630-637.
186. J. L. van Wyk, S. F. Mapolie, A. Lennartson, M. Hakansson, S. Jagner, *Inorg. Chimi. Acta*, 2008, **361**, 2094-2100.
187. K. J. Oconnor, S. J. Wey, C. J. Burrows, *Tetrahedron Lett.*, 1992, **33**, 1001-1004.
188. B. B. De, B. B. Lohray and P. K. Dhal, *Tetrahedron Letters*, 1993, **34**, 2371-2374.
189. M. Palucki, P. Hanson, P. K. Dhal, *Tetrahedron Lett.*, 1992, **33**, 7111-7114.
190. K. Noda, N. Hosoya, K. Yanai, R. Irie, T. Katsuki, *Tetrahedron Lett.*, 1994, **35**, 1887-1890.
191. M. Yamada, S. Ochi, H. Suzuki, A. Hisazumi, S. Kuroda, I. Shimao, K. Araki, *J. Mol. Catal.*, 1994, **87**, 195-202.
192. R. C. Rosenberg, C. A. Root, P. K. Bernstein, H. B. Gray, *J. Am. Chem. Soc.*, 1975, **97**, 2092-2096.
193. D. E. Fenton, G. P. Westwood, A. Bashall, M. McPartlin, I. J. Scowen, *J. Chem. Soc. Dalton Trans.*, 1994, 2213-2214.
194. H. Elias, C. Hasserodttaliaferro, L. Hellriegel, W. Schonherr, K. J. Wannowius, *Inorg. Chem.*, 1985, **24**, 3192-3198.
195. D. K. Rastogi, S. K. Sahni, V. B. Rana, S. K. Dua, *Transition Met. Chem.*, 1978, **3**, 56-60.
196. E. Tas, A. Kilic, N. Konak and I. Yilmaz, *Polyhedron*, 2008, **27**, 1024-1032.
197. I. Kuzniarska-Biernacka, A. Bartecki and K. Kurzak, *Polyhedron*, 2003, **22**, 997-1007.
198. K. Kurzak, , I. Kuzniarska-Biernacka, B. Zurowska, *J. Solution Chem.*, 1999, **28**, 133-151.
199. S. Nagakura, A. Kuboyama, *J. Am. Chem. Soc.*, 1954, **76**, 1003-1005.
200. T. Tanaka, *J. Am. Chem. Soc.*, 1958, **80**, 4108-4110.
201. I. Kuzniarska-Biernacka, K. Kurzak, B. Kurzak, J. Jezierska, *J. Solution Chem.*, 2003, **32**, 719-741.
202. E. F. Murphy, D. Ferri, M. Baiker, S. Van Doorslaer, A. Schweiger, *Inorg. Chem.*, 2003, **42**, 2559-2571.
203. W. J. Zhou, B. Albela, M. Ou, P. Perriat, M. Y. He, L. Bonneviot, *J. Mater. Chem., In press*.
204. S. Abry, A. Thibon, B. Albela, P. Delichère, F. Banse,L. Bonneviot, *New J. Chem.*, 2009, **33**, 484-496.
205. A. H. Maki, A. Davison, N. Edelstein, R. H. Holm, *J. Am. Chem. Soc.*, 1964, **86**, 4580-&.
206. M. J. Bew, B. J. Hathaway , R. J. Fereday, *J. Chem. Soc. Dalton Trans.*, 1972, 1229-&.
207. C. Baleizao, H. Garcia, *Chem. Rev.*, 2006, **106**, 3987-4043.
208. A. Esposito, M. Taramasso, C. Neri, *U. S. Patent 4,396,783,*, 1983.
209. A. Thangaraj, R. Kumar, P. Ratnasamy, *J. Catal.*, 1991, **131**, 294-297.
210. T. Yokoi, P. Wu, T. Tatsumi, *Catal. Comm.*, 2003, **4**, PII S1566-7637(1502)00228-00225.
211. M. R. Maurya, S. J. J. Titinchi, S. Chand, *J. Mol. Catal. A: Chem.*, 2004, **214**, 257-264.

212. S. S. Shevade, R. Raja, A. N. Kotasthane, *Appl. Catal. A: Gen.*, 1999, **178**, 243-249.
213. C. B. Liu, X. K. Ye,Y. Wu, *Catal. Lett.*, 1996, **36**, 263-266.
214. C. W. Lee, D. H. Ahn, B. Wang, J. S. Hwang, S. E. Park, *Microporous Mesoporous Mater.*, 2001, **44**, 587-594.
215. V. Haber, P. Ptacek, *Inorg. Chimi. Acta*, 1991, **179**, 267-270.
216. V. Haber, J. Loub, J. Podlahova, J. Kopf and E. Weiss, *Acta Crystallographica Section C-Crystal Structure Communications*, 1988, **44**, 1905-1907.
217. H. L. Zhu, S. Y. Li, Z. D. Wang, F. Yang, *J. Chem. Crystallogr.*, 2004, **34**, 203-206.
218. K. Nakamoto, *Infrared and raman spectra of inorganic and coordination compounds. Part B: applications in coordination, organometallic, and bioinorganic chemistry*, Wiley, 1992.
219. F. Belanger-Gariepy, R. Faure, F. Hueso-Urena, M. N. Moreno-Carretero, J. A. Rodriguez-Navarro and J. M. Salas-Peregrin, *Polyhedron*, 1998, **17**, 1747-1753.
220. J. A. Martens, P. Buskens, P. A. Jacobs, A. Vanderpol, J. H. C. Vanhooff, C. Ferrini, H. W. Kouwenhoven, P. J. Kooyman, H. Vanbekkum, *Appl. Catal. A: Gen.*, 1993, **99**, 71-84.
221. A. Santos, P. Yustos, A. Quintanilla, S. Rodriguez, F. Garcia-Ochoa, *Appl.Catal. B: Env.*, 2002, **39**, 97-113.
222. F. Song, Y. M. Liu, H. H. Wu, M. Y. He, P. Wu, T. Tatsumi, *J. Catal.*, 2006, **237**, 359-367.
223. K. Z. Zhu, C. B. Liu, X. K. Ye, Y. Wu, *Appl. Catal. A: Gen.*, 1998, **168**, 365-372.
224. C. B. Liu, Y. J. Shan, X. G. Yang, X. K. Ye, Y. Wu, *J. Catal.*, 1997, **168**, 35-41.
225. J. M. Sun, X. J. Meng, Y. H. Shi, R. W. Wang, S. H. Feng, D. H. Jiang, R. R. Xu, F. S. Xiao, *J. Catal.*, 2000, **193**, 199-206.
226. C. Liu, K. Zhu, Y. Shan, X. Ye, R. Zhan , Y. Wu, *Chin. Appl. Chem.*, 1996, **14**, 10.
227. M. H. Robbins and R. S. Drago, *J. Catal.*, 1997, **170**, 295-303.
228. C. B. Liu, Z. Zhao, X. G. Yang, X. K. Ye, Y. Wu, *Chem. Commun.*, 1996, 1019-1020.